OPTICAL PARAMETRIC AMPLIFIERS USING CHIRPED QUASI-PHASE-MATCHING GRATINGS

A DISSERTATION
SUBMITTED TO THE DEPARTMENT OF ELECTRICAL ENGINEERING
AND THE COMMITTEE ON GRADUATE STUDIES
OF STANFORD UNIVERSITY
IN PARTIAL FULFILLMENT OF THE REQUIREMENTS
FOR THE DEGREE OF
DOCTOR OF PHILOSOPHY

Mathieu Charbonneau-Lefort

June 2007

I certify that I have read this dissertation and that, in my opinion, it is fully adequate in scope and quality as a dissertation for the degree of Doctor of Philosophy.

(Martin M. Fejer) Principal Co-Advisor

I certify that I have read this dissertation and that, in my opinion, it is fully adequate in scope and quality as a dissertation for the degree of Doctor of Philosophy.

(Bedros Afeyan) Principal Co-Advisor

I certify that I have read this dissertation and that, in my opinion, it is fully adequate in scope and quality as a dissertation for the degree of Doctor of Philosophy.

(Stephen E. Harris)

Approved for the University Committee on Graduate Studies.

Abstract

Several scientific and technological applications require short optical pulses with large peak power. Optical amplifiers are critical components of these high-power ultrafast laser systems. Conventionally, this role is played by solid-state optical amplifiers, but increasingly, optical parametric amplifiers (OPAs) are being used. The amplification of femtosecond pulses with OPAs often requires an effort to broaden the amplification bandwidth. The approach explored in this work consists in using chirped quasi-phase-matching (QPM) gratings.

We first describe a 1-D model, which, in the case of linearly chirped QPM gratings, predicts a flat gain over a wide bandwidth. We also explore more general phase-matching profiles, such as apodized profiles for reducing the gain and phase ripple, periodically modulated profiles for selective frequency amplification and a tandem grating design for simultaneous gain and group delay control.

We carried out a simple experiment to verify these predictions. The experiment revealed two unexpected effects: the presence of stronger parametric fluorescence than anticipated from the 1-D model and different behavior associated with positive and negative chirp rates. These phenomena can be explained by a 2-D model which includes non-collinear interactions and transverse localization of the gain due to the finite diameter of the pump beam. This model reveals the existence of localized growing modes, which can be amplified over the entire length of the grating and offer a gain much larger than expected in a 1-D model.

The existence of large-gain noncollinear growing modes imposes constraints to the design of chirped-QPM grating OPAs. We formulate design guidelines to suppress those undesired effects.

Acknowledgements

I once heard it said that a PhD is not so much about the destination as it is about the journey.

Clearly, arriving at a destination matters: finding answers, understanding new phenomena and exploring unknown territory are among the most rewarding moments in the career of a researcher. They are the reason we chose to be scientists in the first place. But the years spent as a student leave such a strong impression that it is hard to overstate the importance of the journey.

The analogy makes even more sense when it comes time to acknowledge the people who contributed to my education. Some of these people taught me to walk; some were road companions. Others could not come with me on the trip but were watching from a distance.

My research advisor, Professor Martin Fejer, made all this possible when he agreed to include me in his group. Marty is an incredibly resourceful advisor. His extremely broad knowledge extends far beyond the field of optics. I am immensely grateful that he gave me the freedom of carrying out a research project of theoretical flavor.

Dr. Bedros Afeyan has been my mentor throughout this journey. I met Bedros at a conference a few months before coming to Stanford. I was far from thinking that he would later play such a critical role in my life. He cared about my education, directed my readings, and from his vast experience gave me advice regarding both work and my personal life. A countless number of times he invited me to his home and we would discuss our research projects as well as physics in general.

I also want to thank Professor Steve Harris. I heard about his research on slow light before coming to Stanford. It is a great honor to have him on my thesis committee.

I am indebted to my professors from the departments of Electrical Engineering, Applied Physics and Physics, who taught me at the Master's and PhD levels. In particular, I am grateful to Professors Robert Byer, Steve Harris, Yoshihisa Yamamoto, David Miller, James Harris, Steve Chu and Alexander Fetter.

My colleagues played an important role in my studies. Andrew Schober taught me how to conduct optics experiments; he was also an excellent friend. The experiments reported in this thesis were carried out on a setup that he built. Carsten Langrock, Rostislav Roussev and David Hum were also colleagues and friends who helped in the lab and with whom I had many insightful discussions.

I want to thank my new family here in the Bay Area for their support: the Fahmys, the Gads and the Lopez.

My family in Quebec are among those who watched me embark on the journey from far away. Myriam, Etienne and Elisabeth probably wished I did not choose a graduate school so far from home; I am grateful for their encouragements in spite of the distance. Ultimately, it is thanks to my parents, Nicole and Jacques, that I was able to come to Stanford. Education has always been their first priority. As I grew older and pursued studies in physics, they might not have understood in detail what I was doing, but I have always known that I could count on their unconditional support.

Above all, I am thankful to my wife, Sara. Her mere presence makes me so much happier. She helps me put the occasional frustrations of work into perspective. I am most excited to have her at my side as I am entering my post-Stanford life.

Contents

List of Tables

List of Figures

Chapter 1

Introduction

Several scientific and technological applications require short optical pulses with large peak power [1]. Titanium-doped sapphire, thanks to its large gain bandwidth, has enabled the development of mode-locked femtosecond lasers [2]. However, for many applications the pulse energy produced by these lasers is not sufficient. Most high-energy, ultrafast laser systems make use of *optical amplifiers* to bring the pulse energy from the nanojoule to the millijoule level and higher [2]. The chirped-pulse amplification technique [3], which avoids the undesired effects associated with large peak power by first stretching the optical pulse and then recompressing it after the amplification stage, made possible amplification over nine orders of magnitude while enabling high pulse energies.

Solid-state optical amplifiers have played a major role in the development of high-power laser systems [1, 2]. However a limitation of solid-state laser amplifiers lies in the fact that their gain spectrum is dictated by a narrow atomic transition. This determines the operating wavelength and limits the amplification bandwidth.

Optical parametric amplifiers (OPAs) provide a solution to this problem. OPAs allow a wider choice of pump and signal wavelengths. Their large single-pass gain avoids the need for complex multi-pass or regenerative configurations. Moreover, parametric amplifiers do not rely on optical absorption as a pumping mechanism, thus eliminating the problem of thermal lensing common to high average-power systems. Their use as femtosecond pulse amplifiers [4, 5, 6] and in chirped-pulse amplification

systems [7] has been successfully demonstrated.

There are two techniques commonly used to broaden the amplification bandwidth of OPAs. The first one is to operate at degeneracy, where the signal and idler wavelengths are equal. In this case the group velocities of the waves are matched, which leads to a broad amplification bandwidth. Chirped-pulse amplification systems using this technique are described in Ref. [8, 9, 10]. A drawback of operating at degeneracy is that it requires the wavelength of the pump laser to be fixed. Another disadvantage is that the bandwidh, although larger than in a non-degenerate case, remains limited by the dispersion of the material.

The second bandwidth-broadening technique involves a non-collinear geometry [11]. The input signal beam is dispersed angularly using diffraction gratings in order to ensure simultaneously phase matching and group velocity matching between the signal and idler waves. Amplification of pulses as short as 5 fs was achieved using this method [12, 13].

A less complicated approach, still collinear in nature, is to use *chirped quasi-phase-matching gratings* in order to build broadband OPAs. This is the technique explored in this thesis.

The quasi-phase-matching (QPM) technique consists in a periodic reversal of the sign of the nonlinear coefficient in order to compensate for the accumulated phase mismatch [14]. Since the period of the sign reversal is a controlled parameter, quasi-phase-matched devices operate equally well over a range of wavelengths. QPM allows more freedom over the polarization of the waves, enabling the use of the largest component of the nonlinear susceptibility tensor. For these reasons, QPM gratings have become a widely used alternative to traditional birefringent phase matching. In particular, femtosecond-pulse amplifiers based on quasi-phase-matched materials have been successfully demonstrated [15, 16, 17].

In addition to the benefits mentioned above, QPM offers a distinct advantage over conventional nonlinear crystals: it allows the engineering of non-uniform phase-matching profiles, which can be used to obtain desirable and highly tunable gain and phase spectra. For instance, chirped QPM gratings were used to broaden the second-harmonic acceptance bandwidth [18] and to manipulate the phase of the generated

wave in order to achieve pulse compression [19, 20, 21, 22, 23]. Previous work in the context of OPA includes the calculation of the single-pass gain [24], the use of aperiodic QPM gratings in optical parametric oscillators [25] and the proposal of a tandem-grating design for the simultaneous control of the gain and group delay [26].

This work is an investigation of the properties of chirped QPM gratings used as broadband OPAs. The easiest model by which to describe OPAs is the Rosenbluth model [32], which is presented in chapter 2. We give expressions for the amplitude and phase response of any slowly-varying QPM grating profile, and explore a variety of designs. We begin by looking at the linear phase-matching profile in depth. It is the most important in practice because it allows one to achieve an essentially constant gain over a wide bandwidth. We also consider apodization techniques to reduce the gain and phase ripple. We then explore the effect of a sinusoidal modulation of the grating profile, which provides selective amplification at certain frequencies. Finally, we describe a tandem-grating design which achieves constant gain and constant group delay across the spectrum. We conclude chapter 2 by giving a numerical example of an actual design. We also give a short discussion of parametric amplification in the low-gain regime, showing the connection with the work done the context of second-harmonic generation and difference-frequency generation [22, 23].

Chapter 3 contains an analysis of the space-time formulation of optical parametric amplification. We first review the case of a uniform phase-matching medium, and show that the Green's functions can be expressed in terms of modified bessel functions. Then we investigate the linear phase-matching profile. In this case, the Green's functions can be calculated exactly in terms of integrals over parabolic cylinder functions. Finally, we use those Green's functions to calculate the shape of long and short amplified pulses.

Following this exposition of the 1-D models in the frequency and time domains, we describe the experiments that were conducted to confirm the theoretical predictions. Chapter 4 discusses the design of the experiment, including the design and fabrication of aperiodically-poled lithium niobate (PPLN) crystals. Chapter 5 is an account of the experimental results. While experiments confirmed the basic results predicted by the model, they also revealed two unexpected phenomena. First, the emitted parametric

fluorescence was much more intense than expected; second, positive and negative chirp rates behaved differently. These empirical observations are in direct conflict with the 1-D model. Chapter 6 shows how to interpret these results by appealing to a 2-D model in which non-collinear propagation, diffraction and lateral localization of the pump beam play critical roles.

Details of the 2-D model are given in chapter 7. Solutions found by numerical simulations are presented in chapter 8. Chapter 9 describes the experiment carried out to directly probe one transverse mode at a time, well above the parametric fluorescence floor. Chapter 10 gives approximate analytic solutions of the 2-D model and compares the results with both numerical simulations and experiments. We show that laterally-localized gain-guided modes can exist in chirped QPM gratings. We also show that diffraction can balance phase deaccumulation in the case of negative chirp rates, which can lead to a gain much larger than that predicted by the Rosenbluth model. In chapter 11 we formulate design guidelines to suppress these undesired transverse effects.

Chapter 2

1-D Model

In this chapter we present the analysis of the 1-D model for optical parametric amplification in chirped quasi-phase-matching (QPM) gratings. We give expressions for the amplitude and phase responses of general, slowly-varying QPM grating profiles. In the case of a locally linear profile (section 2.3.2), we recover the Rosenbluth gain formula [32].

2.1 OPA in Non-Uniform QPM Gratings

A diagram illustrating optical parametric amplification (OPA) in non-uniform quasi-phase-matching (QPM) gratings is shown in Fig. 2.1.

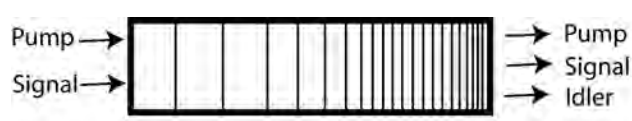

Figure 2.1: Illustration of OPA in a chirped QPM grating.

We consider three co-propagating waves, the pump, signal and idler, with frequencies ω_p, ω_s and ω_i, respectively. In order for their coupling to be most efficient, these three waves must satisfy the frequency-matching condition $\omega_p = \omega_s + \omega_i$. We denote by $\delta\omega \equiv \omega_s - \omega_{s0}$ the frequency shift with respect to the nominal frequency

ω_{s0}. Due to the dispersive properties of the material, the three wavenumbers will not necessarily be matched [27]. We define $\Delta k(\delta\omega) \equiv k_p - k_s - k_i$ to be the intrinsic k-vector mismatch. In $\chi^{(2)}$ materials, perfect wave vector matching also guarantees optimal 3-wave coupling conditions.

The contribution of the QPM grating cancels most of the intrinsic wavevector mismatch. We consider rather general grating profiles. The only requirement that we impose on the grating period $\Lambda(z)$ is that it be a piece-wise slowly-varying function of position. We define $K_g(z) = 1/\Lambda(z)$ the associated grating wavenumber. The overall wavenumber mismatch, κ, is the difference between the intrinsic mismatch and the potentially spatially non-uniform QPM grating:

$$\kappa(z, \delta\omega) = \Delta k(\delta\omega) - K_g(z). \tag{2.1}$$

The chirp rate $\kappa'(z)$ is the rate of change of the wavenumber mismatch in the axial direction:

$$\kappa'(z) = \frac{\partial\kappa(z, \delta\omega)}{\partial z} = -\frac{dK_g(z)}{dz}. \tag{2.2}$$

We define the perfect phase-matched point (PPMP) to be at the position z_{pm} where $\kappa(z_{pm}, \delta\omega) = 0$.

The usual treatment of OPAs makes use of the slowly-varying envelope approximation. The signal and idler envelope functions $E_{s,i}$ are obtained from the electric fields $\widetilde{E}_{s,i}$ by extracting their fast carrier phases, namely, $\widetilde{E}_{s,i} = E_{s,i} \exp\{i[k_{s,i}(\omega_{s,i})z - \omega_{s,i}t]\}$. The wave numbers $k_{s,i}(\omega_{s,i})$ introduced here are frequency dependent: they account for material dispersion. (An alternative definition includes dispersion in the envelope rather than in k-vector; see Ref. [22] for a discussion of these two approaches.) We normalize the optical fields to make them proportional to the photon fluxes by introducing $A_{s,i} = (n_{s,i}/\omega_{s,i})^{1/2} E_{s,i}$, where $n_{s,i}$ are the refractive indices at the respective frequencies of the two waves. We treat the pump as an undepleted, monochromatic plane wave. The resulting steady-state rate equations for the spatial evolution of a pair of signal and idler frequency components are [27, 28]:

$$\frac{dA_s}{dz} = i\gamma(z, \delta\omega) A_i^* e^{i\phi(z,\delta\omega)} \tag{2.3}$$

$$\frac{dA_i^*}{dz} = -i\gamma(z,\delta\omega)A_s e^{-i\phi(z,\delta\omega)}. \tag{2.4}$$

The coupling coefficient is $\gamma(z,\delta\omega) = (\omega_s\omega_i/n_s n_i)^{1/2}\,(d_{eff}(z)/c)\,|E_p|$, where d_{eff} is the amplitude of the effective nonlinear coefficient of the QPM grating (i.e. the amplitude of the Fourier coefficient of the spatially modulated structure), $|E_p|$ is the magnitude of the pump wave electric field and c is the speed of light in vacuum. We allow the coupling coefficient γ to vary slowly with position and frequency. The phase mismatch accumulated between the three waves is then given by

$$\phi(z,\delta\omega) = \int_{z_0}^{z} \kappa(z',\delta\omega)dz', \tag{2.5}$$

where z_0 is the position of the input plane of the grating. We will in general allow both signal and idler waves to be incident on the crystal at z_0, with amplitudes A_{s0} and A_{i0}, respectively.

With the change of variables $A_{s,i} = a_{s,i}\gamma^{1/2}e^{i\phi/2}$, we combine the coupled-mode equations (2.3) and (2.4) to eliminate one of the fields, leading to a second-order linear ODE in standard form [34]:

$$\frac{d^2a_{s,i}}{dz^2} + Q(z)a_{s,i} = 0, \tag{2.6}$$

where

$$Q(z) = \left(\frac{\kappa}{2} - \frac{i}{2}\frac{\gamma'}{\gamma}\right)^2 - \gamma^2 + \frac{i\kappa'}{2} + \frac{1}{2}\left(\frac{\gamma'}{\gamma}\right)', \tag{2.7}$$

and where prime denotes differentiation with respect to z.

The solutions to Eq. (2.6) will have an oscillatory character when $\mathrm{Re}(Q) > 0$, and be exponentials when $\mathrm{Re}(Q) < 0$. The two regimes are separated by the turning points, given by the condition $\frac{1}{2}|\kappa| \approx \gamma$ (here we assume that γ'/γ is small and can be neglected). Located on either side of the PPMP, the turning points define the limits of the amplification region. A typical grating profile $\kappa(z,\omega)$ is shown in Fig. 2.2, together with the location of the PPMP and two turning points, which define the extent of the amplification region.

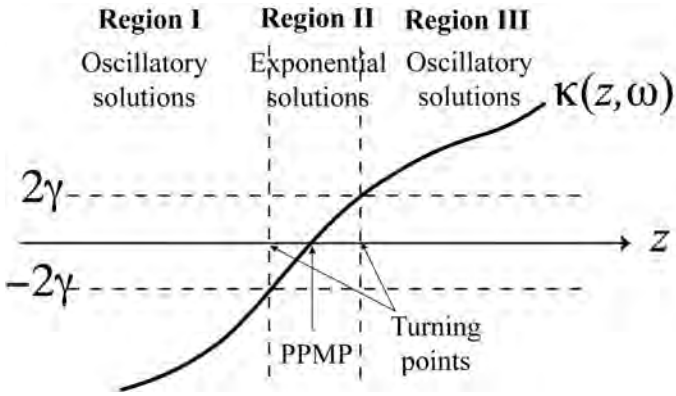

Figure 2.2: Non-uniform grating profile, showing the perfect phase-matched point (PPMP), the turning points and nature of the solutions in each region.

Table 2.1 lists the physical quantities used in the 1-D model.

ω_p, ω_s, ω_i	Pump, signal and idler frequencies
ω_{s0}, ω_{i0}	Signal and idler nominal frequencies
$\delta\omega \equiv \omega_s - \omega_{s0}$	Input frequency shift
$k_p(\omega_p)$, $k_s(\omega_s)$, $k_i(\omega_i)$	Pump, signal and idler wave vectors
$k_{s0}(\omega_{s0})$, $k_{i0}(\omega_{i0})$	Signal and idler nominal wave vectors
$\Delta k \equiv k_p - k_s - k_i$	Intrinsic wave vector mismatch
$K_g(z)$	Grating wavevector
$\kappa(z) \equiv \Delta k - K_g$	Total wave vector mismatch
$\kappa'(z) \equiv \partial\kappa/\partial z$	Chirp rate
z_0	Input plane position
z_{pm}	Phase-matched point
$\phi(z) = \int_{z_0}^{z} \kappa(z')\, dz'$	Phase mismatch
$\gamma(z)$	Coupling coefficient
A_{s0}, A_{i0}	Signal and idler inputs

Table 2.1: Symbols used in the 1-D OPA model

2.2 Practical Formulas for OPA Design

2.2.1 WKB Solution

We use the WKB formalism and notation developed by Heading [29]. In this notation, the end points of the phase integrals as well as the order of dominance of the solutions is easily conveyed. We set the phase reference level at one of the complex turning points, where the function Q vanishes. There exist two such turning points, z_{tp1} and z_{tp2}, located in the complex plane on the left- and right-hand sides of the PPMP, respectively (see the Appendix at the end of this chapter, Fig. 2.11 of section 2.7). The general WKB solutions using the left-hand-side turning point z_1 as the phase reference level are written as

$$(z_{tp1}, z) \equiv Q^{-1/4}(z) \exp\left(i \int_{z_{tp1}}^{z} Q^{1/2}(z')dz'\right) \tag{2.8}$$

$$(z, z_{tp1}) \equiv Q^{-1/4}(z) \exp\left(i \int_{z}^{z_{tp1}} Q^{1/2}(z')dz'\right). \tag{2.9}$$

A linear combination of these two expressions define approximate solutions which are valid away from the turning points. The "complex WKB method" consists in finding the linear combination of the general solutions which satisfies the boundary conditions in a given region, and then in extending this solution to the entire complex plane by finding the coefficients which ensure continuity (asymptotically) between adjacent regions [29, 30, 31]. The details of the calculation are shown in the appendix (section 2.7); here we only state the result: the signal at the end of the grating z_L is

$$A_s(z_L) \approx \left[\frac{\gamma(z_L)}{\gamma(z_0)}\right]^{1/2} e^{i\phi/2} \left(C_+ - iC_-\right) i[z_{tp2}, z_{tp1}] \left[(z_L, b) - i(b, z_L)\right], \tag{2.10}$$

with

$$C_+ = \frac{1}{(a, z_0)} \left[\left(1 + \frac{\gamma^2(z_0)}{\kappa^2(z_0)}\right) A_{s0} - \frac{\gamma(z_0)}{\kappa(z_0)} A_{i0}^*\right] \tag{2.11}$$

$$C_- = \frac{1}{(z_0, a)} \left[-\frac{\gamma^2(z_0)}{\kappa^2(z_0)} A_{s0} + \frac{\gamma(z_0)}{\kappa(z_0)} A_{i0}^*\right] \tag{2.12}$$

and

$$[z_{tp2}, z_{tp1}] \equiv \exp\left(i \int_{z_{tp2}}^{z_{tp1}} Q^{1/2}(z) dz\right). \tag{2.13}$$

As mentioned before, z_0 is the position of the input plane and z_{tp1} and z_{tp2} are the turning points, such that $Q(z_{tp1,2}) = 0$.

The factor $C_+ - iC_-$ together with the phase term $e^{i\phi/2}$ represent the contribution of the portion of grating located before the amplification region, where the waves propagate, accumulate a relative delay and are combined before entering the amplification region. The factor $i[z_{tp2}, z_{tp1}]$ is the contribution from the amplification region, where the waves grow with negligible phase accumulation. Finally, after the amplification region the waves propagate essentially independently of each other.

2.2.2 Design Formulas for a Single PPMP

We can simplify Eq. (2.10) further by retaining only its most significant contributions. An adequate approximation (as shown in section 2.7) is given by

$$A_s \approx R\left(A_{s0} + iA_{i0}^* e^{i\varphi(z_0,\, z_{pm})}\right) e^{g(z_{tp1},\, z_{tp2})}, \tag{2.14}$$

with $R = [\gamma(z_L)/\gamma(z_0)]^{1/2}$. The phase integral is

$$\varphi(z_0,\, z_{pm}) \equiv \int_{z_0}^{z_{pm}} \kappa(z)\, dz \tag{2.15}$$

and the gain integral is

$$g(z_{tp1}, z_{tp2}) \equiv \int_{z_{tp1}}^{z_{tp2}} \left(\gamma^2 - \kappa^2/4\right)^{1/2} dz, \tag{2.16}$$

where the integration is carried out between the two turning points $z_{tp1,2}$.

The operational formula Eq. (2.14) is the central result of this chapter. It is the basis of the design procedure explained below. It will be used repeatedly in several examples.

In a majority of cases we can linearize the grating profile around the PPMP. The

amplification factor $G = e^g$ then becomes

$$G_{\text{linear}} = \exp\left(\frac{\pi\gamma^2(z_{pm})}{|\kappa'(z_{pm})|}\right), \tag{2.17}$$

where the chirp rate and the coupling coefficient are evaluated at the PPMP. This is the Rosenbluth amplification formula [32], an important result first obtained in the context of laser-plasma interactions. For polynomial profiles the gain is given in terms of beta functions [24]. In particular, a case that we will be using later is the cubic profile $\kappa = \kappa'''(z - z_{pm})^3$, for which

$$G_{\text{cubic}} = \exp\left[\left(\frac{2\gamma^4(z_{pm})}{|\kappa'''|}\right)^{1/3} \int_{-1}^{1} \sqrt{1-u^6}\, du\right], \tag{2.18}$$

with $\int_{-1}^{1}(1-u^6)^{1/2}du = \frac{1}{3}\beta(\frac{1}{6}, \frac{3}{2}) \approx 1.82$.

2.2.3 Design formulas for multiple PPMPs

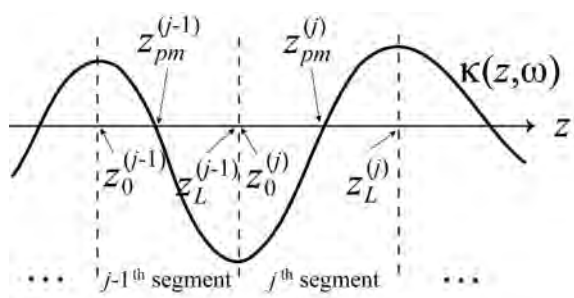

Figure 2.3: Grating profile with multiple PPMPs.

When a profile contains multiple PPMPs, the output of each monotonic segment becomes the input of the next. This situation is illustrated in Fig. 2.3.

A subtlety arises due to the fact that the phase mismatch at the input of a given segment is not zero, but results from the phase accumulation over the previous segments. This problem can be solved by absorbing the accumulated phase into the fields, i.e. letting $A_{s,i}^{(j)} = B_{s,i}^{(j)} e^{i\phi^{(j)}/2}$, where the superscripts refer to the segment

number and $\phi^{(j)} \equiv \int_{z_0^{(1)}}^{z_0^{(j)}} \kappa(z)dz$ is the phase mismatch accumulated before segment j. Then the new fields obey the coupled-mode equations (2.3) and (2.4) with initial conditions $B_{s,i0}^{(j)} = A_{s,i0}^{(j)} e^{-i\phi^{(j)}/2}$, and we can use the results derived above. Consequently, the contribution of a segment j can be written:

$$A_s^{(j)} = R^{(j)} \left[A_{s0}^{(j)} + i A_{i0}^{(j)*} e^{i\varphi\left(z_0^{(1)}, z_{pm}^{(j)}\right)} \right] e^{g\left(z_{tp1}^{(j)}, z_{tp2}^{(j)}\right)}, \tag{2.19}$$

$$A_i^{(j)} = R^{(j)} \left[A_{i0}^{(j)} + i A_{s0}^{(j)*} e^{i\varphi\left(z_0^{(1)}, z_{pm}^{(j)}\right)} \right] e^{g\left(z_{tp1}^{(j)}, z_{tp2}^{(j)}\right)}. \tag{2.20}$$

In the case of periodic profiles, $A_{s0}^{(j)} = A_s^{(j-1)}$, $A_{i0}^{(j)} = A_i^{(j-1)}$. However, when multiple gratings are used in a cascaded configuration this is not necessarily the case. A typical example is the tandem configuration discussed in the next section.

2.3 Analysis of Various Grating Profiles

This section illustrates the engineering of chirped gratings. We first review the well-known case of a uniform QPM grating. Then, we examine the linear profile, which yields essentially constant gain over a large bandwidth, and also examine ways of eliminating the ripple affecting the spectrum. Then as an example of non-uniform chirp rate we discuss a sinusoidal modulation superposed onto a linear ramp, providing enhanced amplification at select frequencies. Finally we examine a tandem design for simultaneous gain and group delay control.

2.3.1 Uniform Profile

In the case of a uniform QPM grating, there are no turning points since the wavevector mismatch κ is constant, and as a consequence the nature of the solutions (i.e. real or complex exponentials) remains unchanged throughout the medium. The WKB analysis developed above does not apply in this simple case.

When the wave vector mismatch κ and the coupling coefficient γ are constant,

the coupled equations (2.3) and (2.4) can be solved exactly [27, 28]:

$$A_s(z_L) = A_{s0}e^{i\kappa L/2}\left[\cosh gL - \frac{i\kappa}{2g}\sinh gL\right] + i\frac{\gamma}{g}A_{i0}^{*}e^{i\kappa L/2}\sinh gL, \quad (2.21)$$

$$A_i(z_L) = A_{i0}e^{i\kappa L/2}\left[\cosh gL - \frac{i\kappa}{2g}\sinh gL\right] + i\frac{\gamma}{g}A_{s0}^{*}e^{i\kappa L/2}\sinh gL, \quad (2.22)$$

where $L = z_L - z_0$ is the length of the grating and

$$g = \sqrt{\gamma^2 - \left(\frac{\kappa}{2}\right)^2} \quad (2.23)$$

is the growth rate in the presence of constant wave vector mismatch. With input at the signal wave only, and in the large-gain regime ($gL \gg 1$) the amplitudes of the waves are approximately

$$|A_{s,i}(z_L)| \approx A_{s0}\frac{\gamma}{2g}e^{gL}. \quad (2.24)$$

The peak gain, achieved when $\kappa = 0$, is

$$G_{\text{unif}} = \frac{1}{2}e^{\gamma L}. \quad (2.25)$$

The gain increases exponentially with the length of the device. The FWHM bandwidth is reached when the wave vector mismatch is equal to

$$\kappa_{FWMH} = \pm\frac{2}{L}\sqrt{\gamma^2 L^2 - (\ln 2)^2}. \quad (2.26)$$

The amplification bandwidth takes a simple form if we neglect group velocity dispersion at the signal and idler wavelengths. In this case, the intrinsic wave vector mismatch is

$$\begin{aligned}\Delta k(\delta\omega) &= k_p - k_s - k_i \\ &= k_p - k_{s0} - \left.\frac{\partial k}{\partial\omega}\right|_{\omega_s}\delta\omega - k_{i0} + \left.\frac{\partial k}{\partial\omega}\right|_{\omega_i}\delta\omega \\ &= k_p - k_{s0} - k_{i0} + \left(\frac{1}{v_s} - \frac{1}{v_i}\right)\delta\omega, \end{aligned} \quad (2.27)$$

where k_{s0} and k_{i0} are the signal and idler wave vectors at the nominal frequencies, and $v_{s,i} = \partial\omega/\partial k|_{\omega_{s,i}}$ are the group velocities. The grating wavevector is equal to $K_g = k_p - k_{s0} - k_{i0}$ (by definition of the nominal frequencies), so that the overall mismatch, given by Eq. (2.1), is simply

$$\kappa(\delta\omega) = \left(\frac{1}{v_s} - \frac{1}{v_i}\right)\delta\omega. \tag{2.28}$$

We define the group velocity mismatch parameter, δv, as

$$\frac{1}{\delta v} = \frac{1}{v_s} - \frac{1}{v_i}. \tag{2.29}$$

Substituting into Eq. (2.26), we find the following expression for the bandwidth:

$$\Delta\omega_{BW,\,unif} = \frac{4|\delta v|}{L}\sqrt{\gamma^2 L^2 - (\ln 2)^2} \approx 4|\delta v|\,\gamma, \tag{2.30}$$

where the approximation is valid in the large-gain regime. Therefore the bandwidth of a uniform QPM grating is essentially independent of the grating length; it depends only on the strength of the coupling coefficient and on the dispersive properties of the material.

2.3.2 Linear Profile for Broadband Amplification

Application of the Design Formula

The most basic chirped QPM grating profile is the linear chirp. We consider an input signal wave only, as this is the most common situation in practice, and let the idler develop from the interaction. For simplicity, we neglect group-velocity dispersion at the signal and idler wavelengths, so that the phase mismatch varies linearly with frequency. (The extension to higher-order dispersion is straightforward if somewhat more tedious.) The total wave vector mismatch, Eq. (2.1), is given by

$$\kappa(z, \delta\omega) = \kappa'(z - z_{pm0}) - \frac{\delta\omega}{\delta v}, \tag{2.31}$$

where κ' is the constant chirp rate and z_{pm0} is the position of the PPMP at the nominal frequency. As the input frequency is varied, the PPMP is shifted linearly with frequency according to

$$z_{pm} = z_{pm0} + \frac{\delta\omega}{\kappa'\,\delta v}. \tag{2.32}$$

The mismatch then takes the simple form

$$\kappa = \kappa'(z - z_{pm}). \tag{2.33}$$

The two turning points are located at a distance given by $2\gamma/|\kappa'|$ on each side of the PPMP; therefore the length of the amplification region is

$$L_g = \frac{4\gamma}{|\kappa'|}. \tag{2.34}$$

The present approximate treatment is valid for gratings for which $L \gg L_g$. If this condition is satisfied, then the dephasing effects due to the chirp of the grating dominate the behavior of the device. Conversely, if $L \ll L_g$, then the grating is essentially uniform.

The limits of the amplification spectrum are reached when the frequency shift results in one of the turning points being at the edge of the grating. Therefore the amplification bandwidth is

$$\Delta\omega_{BW} = |\kappa'\,\delta v\,(L - L_g)|\,. \tag{2.35}$$

As expected, the bandwidth is proportional to the product of chirp rate and grating length, i.e. to the range of grating k-vectors in the device. The bandwidth takes this simple form when the group velocity dispersion of the material can be neglected. Otherwise, higher dispersive orders have to be included in Eq. (2.31) and the bandwidth may have to be calculated directly from the dispersion relation.

Application of formula (2.14) for each wave gives

$$A_s \;=\; A_{s0}e^{\pi\gamma^2/|\kappa'|}, \tag{2.36}$$

$$A_i = iA_{s0}^* e^{\pi\gamma^2/|\kappa'|} e^{-i\kappa'(z_{pm}-z_0)^2/2}. \tag{2.37}$$

Both waves experience the constant *amplitude* gain given by the Rosenbluth gain formula,

$$G_R = e^{\pi\gamma^2(\delta\omega)/|\kappa'|}. \tag{2.38}$$

However, they differ in their phases. While the signal experiences negligible phase shift, the idler accumulates a quadratic phase, corresponding to a time delay (with respect to a reference traveling at the idler velocity) of

$$\tau_i = \frac{z_{pm} - z_0}{\delta v}. \tag{2.39}$$

Since this delay is itself linear in the input frequency (through its dependence on $z_{pm}(\delta\omega)$), the idler experiences group delay dispersion, the magnitude of which depends on the chirp rate. Alternatively, the idler group delay with respect to the *signal* wave is

$$\tau_{i-s} = -\frac{z_L - z_{pm}}{\delta v}. \tag{2.40}$$

It is important to keep in mind that these phases represent the contribution from the grating only; the dispersive properties of the material must be considered separately. They are accounted for by the carrier phase $k_{s,i}z - \omega_{s,i}t$ which must be added to the envelopes in order to recover the fields. The reason for this is that the material dispersion is buried in the wavevectors $k_{s,i} = \omega_{s,i}n(\omega_{s,i})/c$.

Comparison with WKB Solution

The approximate design formulas lead to simple expressions for the gain, bandwidth and phase. It is natural to expect that this simplicity comes at the price of a loss of accuracy. How accurate our expressions are can be verified by comparing with the fuller WKB and numerical solutions.

The WKB solution, Eq (2.10), is valid for general grating profiles. In the appendix (section 2.7) we obtain an explicit expression in the special case of a linear profile [see Eq. (2.89)]. The spatial evolution of the waves is plotted in Fig. 2.12 of section 2.7,

along with the numerical solution. The underlying assumptions behind the WKB solution are also discussed there.

Fig. 2.4 compares the gain spectra obtained from the explicit WKB solution, Eq. (2.89), with the numerical solution, together with the simplified result obtained in this section, Eqs. (2.36) and (2.37). Fig. 2.5 shows the phase spectra. The signal has a small phase drift which is not captured by the simplified expressions. However, the idler has a large quadratic spectral phase predicted by Eq. (2.37). Finally, Fig. 2.6 shows the relative group delay, τ, with respect to the accumulated delay between the waves, $L/|\delta v|$. As expected, the idler experiences a linear group delay.

A striking feature of those plots is the significant ripple affecting the gain, phase and group delay spectra. While the WKB solutions recover this ripple correctly, the simplified expressions presented in this section do not capture the small-scale features of the amplification. The origins of the ripple and ways to reduce it will be discussed in the next section.

Fig. 2.6 indicates that the magnitude of the group delay ripple is typically of the order of 10 % of the delay accumulated between signal and idler, and that it decreases with increasing chirp rate or increasing length. For femtosecond pulse amplification, this group delay ripple is often unacceptable as it causes pulse distortion.

Comparison with Uniform Gratings

From the point of view of applications, the clear advantage of linearly chirped QPM gratings lies in their arbitrarily wide amplification bandwidth. For a fixed grating length, the bandwidth is essentially proportional to the chirp rate κ'. Naturally, an increase of bandwidth comes at the expense of a reduction of gain, since the Rosenbluth factor is proportional to $1/\kappa'$. The trade-off between gain and bandwidth is expressed by the fact that the logarithmic-gain-bandwidth product is a quantity independent of the chirp rate:

$$\ln G_R \times \Delta\omega_{BW} \approx \pi|\delta v|\,\gamma^2 L. \tag{2.41}$$

In the case of a uniform grating, the peak gain and the amplification bandwidth

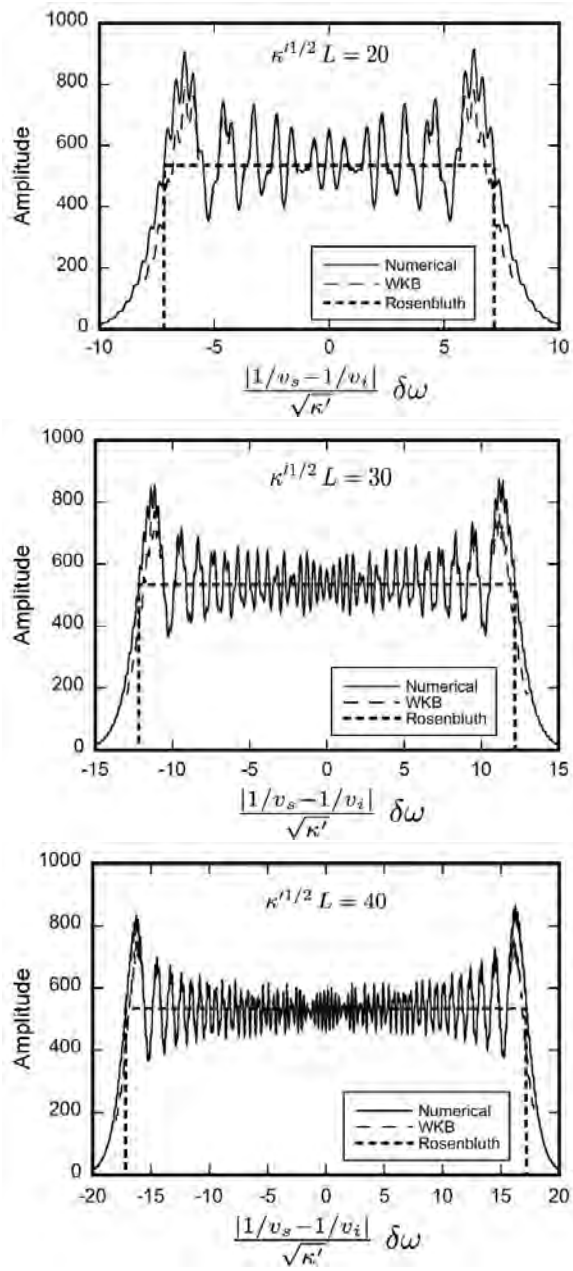

Figure 2.4: Gain spectrum of a linear profile, comparing the numerical solution with the WKB solution and the Rosenbluth gain factor, for various grating lengths. The numerical values used are $\gamma^2/\kappa' = 2$ and $\kappa'^{1/2}L = 20$ (top), $\kappa'^{1/2}L = 30$ (middle) and $\kappa'^{1/2}L = 40$ (bottom).

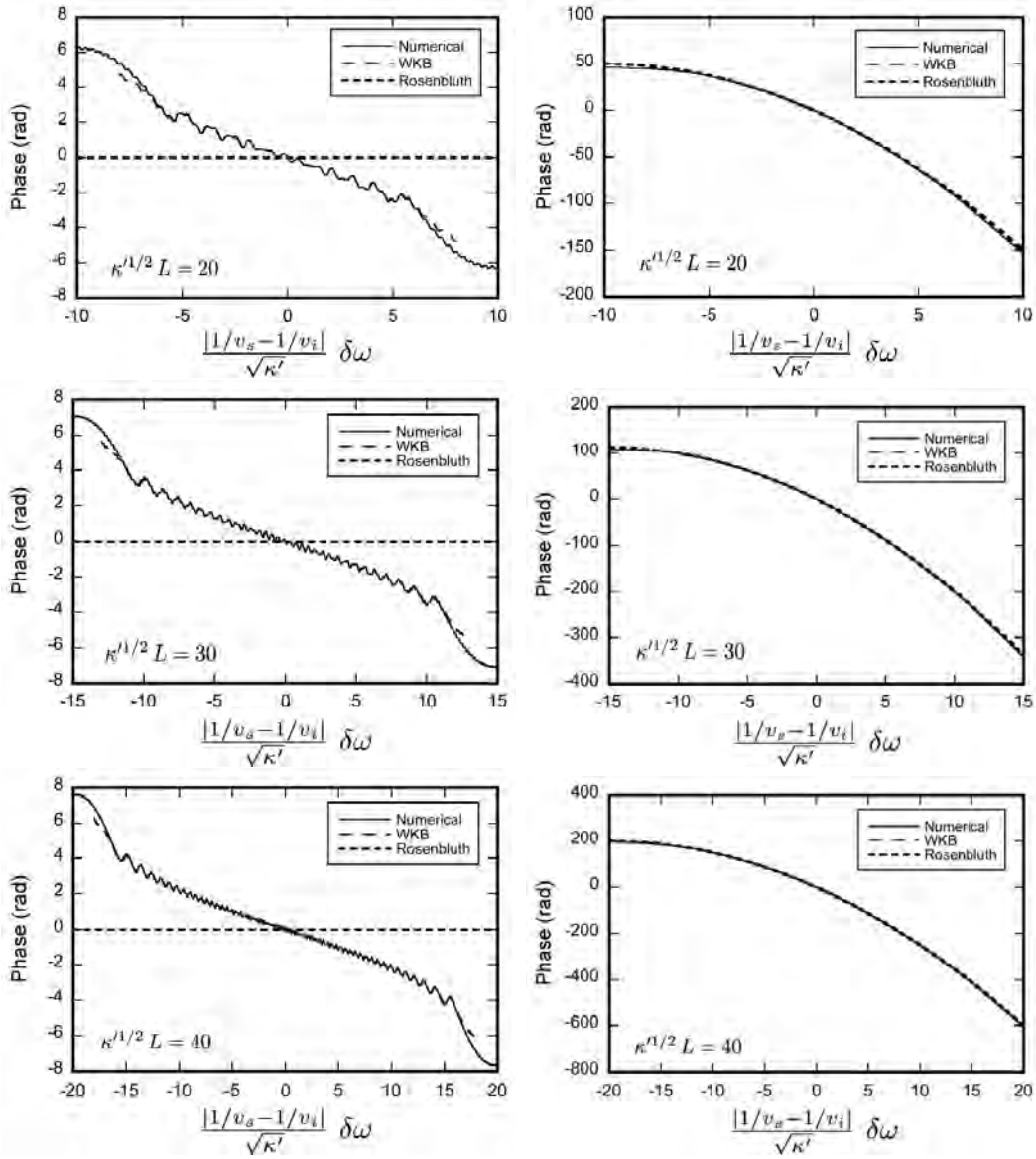

Figure 2.5: Phase spectrum of a linear profile, comparing the numerical solution with the WKB solution and the simplified expressions, Eq. (2.36) and (2.37), for various grating lengths. The left column corresponds to the signal; the right column, the idler. The numerical values used are $\gamma^2/\kappa' = 2$ and $\kappa'^{1/2}L = 20$ (top), $\kappa'^{1/2}L = 30$ (middle), $\kappa'^{1/2}L = 40$ (bottom).

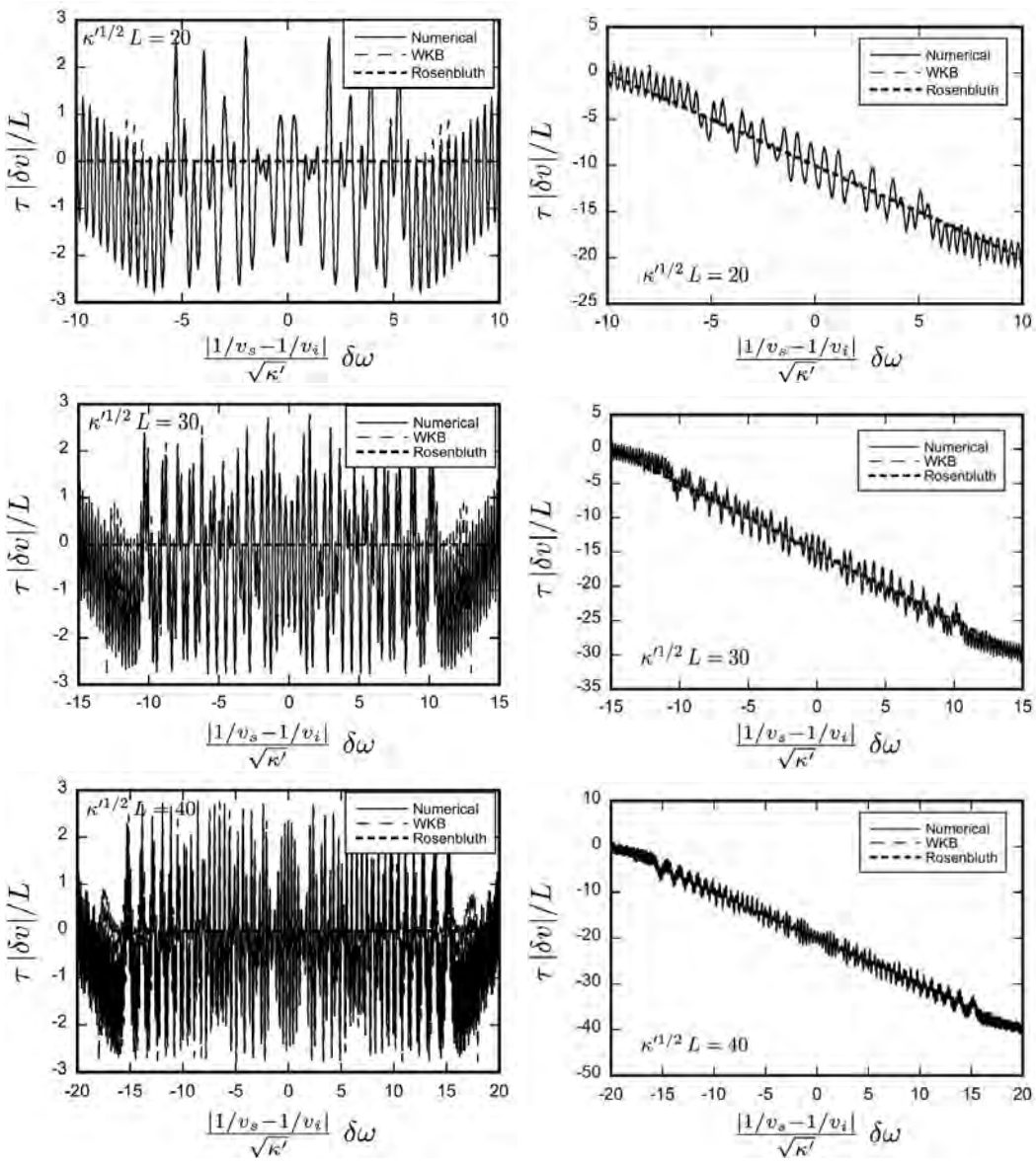

Figure 2.6: Relative group delay spectrum of a linear profile, $\tau/|1/v_s - 1/v_i|L = \tau|\delta v|/L$, comparing the numerical solution with the WKB solution and the simplified expressions, Eq. (2.36) and (2.37), for various grating lengths. The left column corresponds to the signal; the right column, the idler. The numerical values used are $\gamma^2/\kappa' = 2$ and $\kappa'^{1/2}L = 20$ (top), $\kappa'^{1/2}L = 30$ (middle), $\kappa'^{1/2}L = 40$ (bottom).

are given by Eqs. (2.25) and (2.30), respectively. The logarithmic-gain-bandwidth product in this case is approximately

$$\ln G_{unif} \times \Delta\omega_{BW,\,unif} \approx 4|\delta v|\,\gamma^2 L. \tag{2.42}$$

The logarithmic gain-bandwidth products of uniform and chirped gratings are essentially the same (except for a factor of 4 instead of π).

The advantage of chirped gratings over uniform gratings is to enable (in principle) arbitrarily large bandwidths. However, this increase of bandwidth is accompanied by a reduction of the gain, according to formula (2.42).

2.3.3 Tapered Profiles for Ripple Reduction

The gain, phase and group delay ripple affecting the amplification spectrum of chirped gratings can be relatively large. This section explores ways of reducing the ripple by tapering the magnitude of the coupling coefficient or the grating profile.

The ripple is due to the fact that some amount of idler wave is generated before reaching the gain region. When they reach the phase-matching region, the signal and idler interfere and their relative phase affects the magnitude of the gain.

This phenomenon can be understood using the WKB description. The solution is constructed by the superposition of the two elementary WKB solutions given by Eqs. (2.8) and (2.9). These positive and negative complex exponentials interfere, causing small oscillations in the signal and idler amplitudes.

Mathematically, reducing the ripple amounts to reducing the amplitude of one of the positive and negative complex exponentials. As pointed out in section 2.7, this can be accomplished by decreasing the coupling coefficient or increasing the wavevector mismatch at the ends of the grating.

From a physical point of view, the ripple is caused by the "hard" edges of the grating, where the interaction is turned on and off abruptly. Therefore ripple reduction schemes should aim at making the transition into and out of the interaction region as smooth as possible. There are two ways of accomplishing this. One way is to turn on the coupling coefficient adiabatically; the other consists in starting from a completely

mismatched interaction which is then brought progressively into phase-matching.

Tapering of the coupling coefficient $\gamma(z)$ can be accomplished, for example, by varying the duty cycle of the QPM gratings [33]. For instance, let us consider the profile

$$\frac{\gamma(z)}{\gamma_{max}} = a + b \times \tanh\left(\frac{z - z_0 - l_1}{w_1}\right) \times \tanh\left(\frac{L - z + z_0 - l_2}{w_2}\right). \tag{2.43}$$

The various constants can be chosen to achieve satisfactory ripple reduction. The Rosenbluth gain factor is now frequency-dependent, with $\gamma = \gamma[z_{pm}(\delta\omega)]$ and $z_{pm}(\delta\omega)$ given by Eq. (2.32). The reduction of the gain at the edges of the spectrum causes a narrowing of the amplification bandwidth. Fig. 2.7 shows the tapering function and the corresponding amplification and group delay spectra. For this particular bandwidth and gain, the amplitude of the gain ripple could be reduced from about 100% of the average gain (peak-to-peak variation) to 2% with the parameters $l_1 = l_2 = w_1 = w_2 = 0.04 \times L$ and a and b chosen so that $\gamma(z_0) = \gamma(z_L) = 0$ and $\max \gamma(z) = \gamma_{max}$.

Let us now turn our attention to the tapering of the phase profile of the grating, $\kappa(z)$. As an example, we consider a profil‘e which is linear for most of the grating, but becomes large at the ends. This is accomplished for instance by adding a large, odd power to the linear grating profile:

$$\kappa = \kappa_0'(z - z_{pm0}) + \mu\left(\frac{z - z_{pm0}}{L/2}\right)^{\nu} - (1/v_s - 1/v_i)\,\delta\omega, \tag{2.44}$$

where μ is the amplitude of the departure from linearity and ν is a large, odd integer. The Rosenbluth amplification factor is now dependent on frequency through the non-uniform chirp rate $\kappa' = \kappa'[z_{pm}(\delta\omega)]$. The gain is reduced at the edges of the spectrum, corresponding to regions of large chirp rate.

Fig. (2.8) shows the grating profile and the corresponding amplification and group delay spectra. The amplitude of the ripple could be kept below 5 % of the average gain using the parameters $\mu/\kappa_0'^{1/2} = 100$ and $\nu = 21$. These numerical results show that tapering of the coupling coefficient seems more effective at eliminating the group

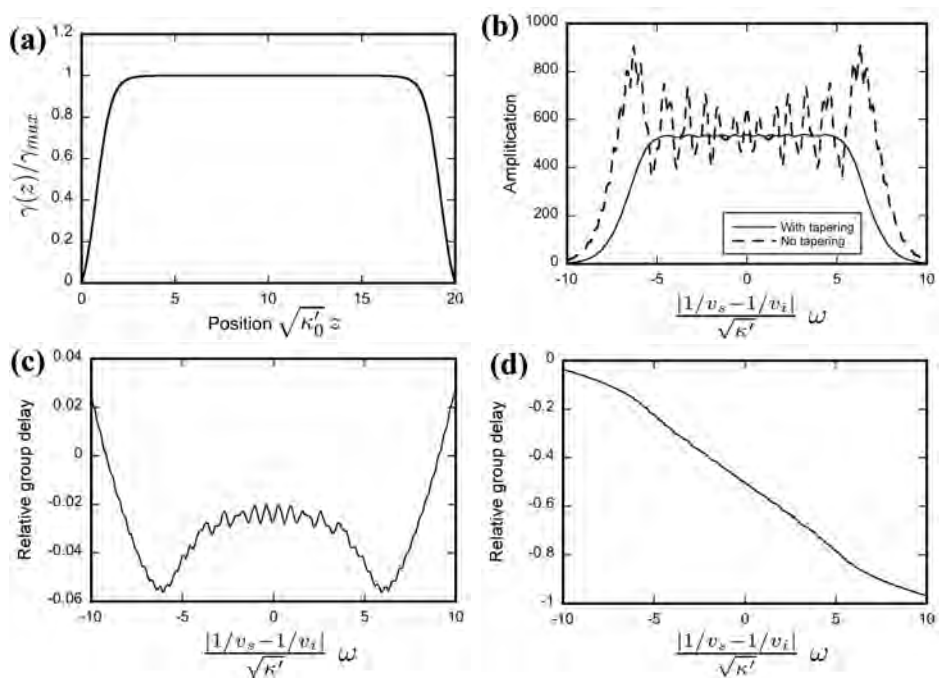

Figure 2.7: Ripple reduction using tapering of the coupling coefficient: (a) coupling coefficient profile, (b) gain spectrum, (c) signal group delay spectrum and (d) idler group delay spectrum. The tapering profile is given by Eq. (2.43) with $l_1 = l_2 = w_1 = w_2 = 0.04 \times L$. The gain parameter is $\gamma^2/\kappa' = 2$ and the length is $\kappa'^{1/2}L = 20$. The gain and group delay spectra *without* apodization were shown in Figs. 2.4 and 2.6, top case.

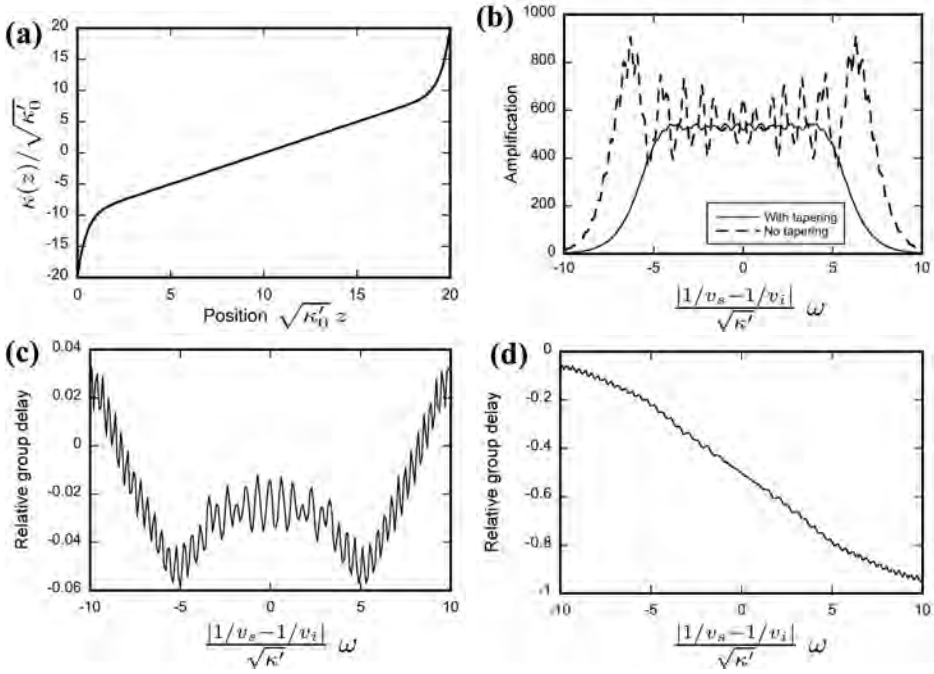

Figure 2.8: Ripple reduction using tapering of the QPM profile: (a) grating profile, (b) gain spectrum, (c) signal group delay spectrum and (d) idler group delay spectrum. The grating profile is given by Eq. (2.44) with $\mu/\kappa_0'^{1/2} = 100$ and $\nu = 21$. The gain parameter is $\gamma^2/\kappa_0' = 2$ and the length is $\kappa'^{1/2}L = 20$.

delay ripple than is tapering of the phase profile of the grating.

2.3.4 Sinusoidal Profile for Selective Frequency Amplification

According to the design formulas, the amplification in the case of a monotonic profile with no input idler is simply e^g, where g is the gain integral given in Eq. (2.16). Thus the amplification depends predominantly on the local properties of the grating in the vicinity of the PPMP. This opens the possibility of engineering the amplification spectrum through careful design of the grating profile.

By way of illustration, we consider a sinusoidal modulation superposed onto a linear profile, and show that it gives rise to an amplification spectrum with enhanced

gain around certain frequencies only. Such a profile is described by

$$\kappa = \kappa_0'(z - z_{pm0}) - \mu \sin\left[k_\mu(z - z_{pm0})\right] - (1/v_s - 1/v_i)\,\delta\omega, \tag{2.45}$$

where μ and k_μ are the amplitude and spatial frequency of the modulation, respectively. If the amplitude of the modulation is small (i.e. $\mu k_\mu \ll \kappa_0'$), then the linearization of the profile is valid everywhere and the gain is obtained from the Rosenbluth formula, using the frequency-dependent chirp rate $\kappa' = \kappa_0' - \mu k_\mu \cos k_\mu(z_{pm} - z_{pm_0})$, where z_{pm} is now the solution of the transcendental equation $\kappa(z_{pm}) = 0$. However, as the amplitude of the modulation increases the chirp rate becomes close to zero at certain locations inside the grating. When $\mu k_\mu = \kappa_0'$ the profile can be approximated by a cubic at those locations where κ' vanishes, and in these cases we can use the gain formula Eq. (2.18), which in our particular case becomes

$$G = \exp\left[4.17\left(\frac{\gamma^4}{\kappa_0' k_\mu^2}\right)^{1/3}\right]. \tag{2.46}$$

The amplification spectrum of this sinusoidal profile is shown in Fig. (2.9) for parameters $\gamma^2/\kappa_0' = 2$, ${\kappa_0'}^{1/2}L = 40$, $k_\mu = 2\pi/(L/3)$ and $\mu = \kappa_0'/k_\mu$.

2.3.5 Tandem Gratings for Simultaneously Flat Gain and Group-delay Spectra

The examples presented above illustrate how one can tailor the amplification spectrum through careful engineering of the grating profile. Little has been said about designing the phase response. Nevertheless, control of the phase spectrum is often critical, especially for applications in ultrafast optics.

Recently, we proposed the use of a pair of gratings in a tandem configuration in order to achieve simultaneous control of the gain and group-delay spectra [26]. Here is an analysis of this design using the simple design expressions. We will see that the equations governing the design procedure follow in a straightforward manner.

The tandem configuration is shown in Fig. 2.10. Its principle of operation is the

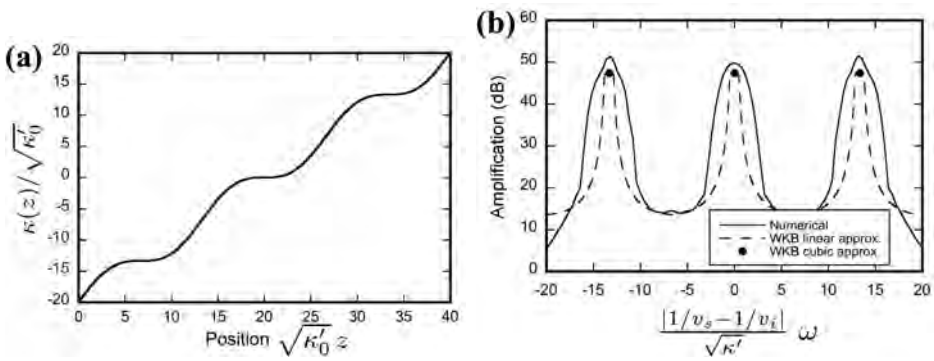

Figure 2.9: Sinusoidal profile for selective frequency amplification: (a) QPM grating profile and (b) amplification spectrum, comparing the numerical values with the Rosenbluth amplification formula. The cubic approximation to the grating profile gives the peak amplification (marked by the dots on the plot), while the linear approximation (dashed line) is valid away from the peaks but breaks down in the vicinity of the maxima. The numerical parameters in this example are $\gamma^2/\kappa_0' = 2$, ${\kappa_0'}^{1/2}L = 40$, $k_\mu = 2\pi/(L/3)$ and $\mu = \kappa_0'/k_\mu$.

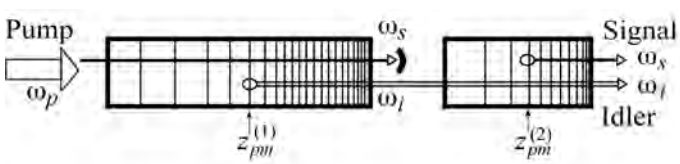

Figure 2.10: Tandem configuration.

following. The signal to be amplified is incident on the first grating. After the first grating, we block the signal wave, so that only the pump and the idler are incident on the second grating. The output idler of the first grating is used as the input signal of the second. The "idler" generated by the second grating then has the same frequency as the original signal. By choosing the position of the PPMPs in the two gratings and their local chirp rates, we can control at the same time the gain and group delay spectra.

This idea of using the idler wave in a cascaded geometry has also been used to reduce the amplified spontaneous emission and improve the pulse contrast in high-gain OPAs [10].

Let us now describe the output of the tandem-grating design. We use the expressions describing the amplification in the presence of multiple PPMPs, Eqs. (2.19) and (2.20), with $A_{i0} = 0$. The output of the first grating is

$$A_s^{(1)} = R^{(1)} A_{s0} e^{g^{(1)}} \tag{2.47}$$

$$A_i^{(1)} = i R^{(1)} A_{s0}^* e^{g^{(1)}} e^{i\varphi\left(z_0^{(1)}, z_{pm}^{(1)}\right)}, \tag{2.48}$$

where $g^{(1)}$ denotes the gain integral around the PPMP of the first grating. Before entering the second grating, the signal is filtered out. The inputs to the second gratings are therefore $A_{s0}^{(2)} = 0$, $A_{i0}^{(2)} = A_i^{(1)}$. A second application of Eq. (2.19) then gives

$$A_s^{(2)} = A_{s0}^* R^{(1)} R^{(2)} e^{g^{(1)}+g^{(2)}} e^{i\varphi\left(z_{pm}^{(1)}, z_{pm}^{(2)}\right)}. \tag{2.49}$$

This expression contains all the information needed to design grating profiles with the desired gain and phase spectra. First, the total logarithmic gain is equal to the sum of the individual gains; using the Rosenbluth factors, we obtain the total logarithmic gain in terms of the chirp rates:

$$\ln G(\delta\omega) = \frac{\pi\gamma^2\left(z_{pm}^{(1)}\right)}{\left|\kappa'\left(z_{pm}^{(1)}\right)\right|} + \frac{\pi\gamma^2\left(z_{pm}^{(2)}\right)}{\left|\kappa'\left(z_{pm}^{(2)}\right)\right|}. \tag{2.50}$$

Second, the accumulated phase corresponds to the delay accumulated by propagation

at the idler velocity between the two PPMPs. Differentiating the total phase with respect to frequency, we can express the total group delay in terms of the positions of the PPMPs:

$$\begin{aligned}\tau(\delta\omega) &= \frac{z_{pm}^{(1)} - z_0^{(1)}}{v_s} + \frac{z_L^{(1)} - z_{pm}^{(1)}}{v_i} \\ &\quad + \frac{z_{pm}^{(2)} - z_0^{(2)}}{v_i} + \frac{z_L^{(2)} - z_{pm}^{(2)}}{v_s}\end{aligned} \tag{2.51}$$

These two equations can then be solved to obtain the desired gain and group delay spectra are specified. This was done in Ref. [26] in order to obtain constant gain and constant group delay across a specified bandwidth.

2.4 Concrete Design Example

In order to give an idea of typical experimental values, let us consider an OPA consisting of a chirped QPM grating designed to offer a (power) gain of 50 dB over a bandwidth of 100 nm around 1550 nm. The nonlinear crystal is made of periodically-poled lithium niobate (PPLN) and has a length of 5 cm. We assume that the OPA is pumped by a Nd:YAG laser (1064 nm). The numerical values of the various experimental parameters involved are listed in Table 2.2. The chirp rate required is $\kappa' = 4.13 \times 10^5 \ \ \mathrm{m}^{-2}$. In order to obtain the desired gain, the coupling coefficient must be $\gamma = 870 \ \mathrm{m}^{-1}$. The required pump intensity to achieve this is 438 MW/cm^2. In terms of normalized quantities, the gain parameter is $\gamma^2/\kappa' = 1.8$ and the length is $\kappa'^{1/2}L = 32$. This situation is very similar to the one illustrated in Fig. 2.4-(b).

By comparison, the pump intensity required to achieve the same gain in a uniform grating of equal length is 7.6 MW/cm^2. However, in this case the bandwidth is around 6 nm only.

The 1-D model studied here assumes that the pump, signal and idler are plane waves. In a free-space experiment, however, the light pulses are localized in space and time. A reasonable approximation (neglecting diffraction and dispersion) is to

Specifications	
Material	$LiNbO_3$
Center signal wavelength	1550 nm
Bandwidth	100 nm
Pump wavelength	1064 nm
Grating length, L	5 cm
Power gain	50 dB
Operating temperature	150 ^{O}C
QPM grating	
QPM grating period range	28.3 - 31.2 μm
Chirp rate, κ'	4.13×10^5 m^{-2}
Normalized length, $\sqrt{\kappa'}L$	32
Pump intensity	
Effective nonlinear coefficient, d_{eff}	$2/\pi \times 27$ pm/V
Coupling coefficient, γ	870 m^{-1}
Gain parameter, γ^2/κ'	1.83
Gain length, L_g	8.4 mm
Pump intensity	438 MW/cm^2

Table 2.2: Numerical values for the OPA design.

average the gain over the entire pulse:

$$G_{\mathrm{3D}} = \int\int\int \exp\left(\frac{\pi\gamma^2(x,y,t)}{\kappa'}\right) dxdydt, \tag{2.52}$$

where now the coupling coefficient has a transverse and temporal profile related to the intensity of the pump pulse, $\gamma^2(x,y,t) \propto I_p(x,y,t)$.

If we assume that the pump pulses are gaussian in space and time, with a spot size of 300 μm (1/e^2 intensity diameter) and a duration of 1 ns (1/e^2 intensity full duration) but the same peak intensity, then the gain of the OPA is 35 dB instead of 50 dB. Diffraction, inevitable when gain narrowing occurs, will decrease this value even further.

2.5 OPA in the Low-Gain Limit

When the gain is low, we can assume that the signal wave remains unamplified and that only the idler grows. This process is called difference-frequency generation (DFG). DFG and SHG (second-harmonic generation) in chirped QPM gratings have been studied in detail by Imeshev *et al* [22, 23]. They have shown that the spectrum of the generated wave is related to the spectrum of the input by a transfer function which is given by the Fourier transform of the grating profile. In the case of linearly-chirped gratings, this transfer function can be expressed in terms of Fresnel integrals. Its spectrum is broad and flat, with rapid oscillations, similar to the gain spectrum of chirped-grating OPAs.

We can recover these results by considering parametric amplification, Eqs. (2.3) and (2.4), in the low-gain limit. In this case, the signal amplitude is constant and the evolution of the idler is described by a single first-order differential equation which can be integrated in a straightforward manner:

$$A_i(z) = i\gamma A_s^* \int_{z_0}^{z} e^{i\phi(z')} dz'. \tag{2.53}$$

In the case of linearly chirped gratings, $\phi(z)$ is quadratic and the solution can be expressed in terms of error functions or Fresnel integrals [22, 23]. Alternatively, the integral can be evaluated approximately using the stationary phase method [34]:

$$A_i(z) \approx i e^{i\pi/4} \gamma \sqrt{\frac{2\pi}{\kappa'}} A_s^* e^{-\frac{i}{2}\kappa'(z_0 - z_{pm})^2}. \tag{2.54}$$

The gain, which was given by the Rosenbluth gain factor in the case of parametric amplification, is now equal to $\gamma\sqrt{2\pi/\kappa'} \ll 1$. Nevertheless, both regimes are similar in two aspects: their gain is essentially constant over a wide bandwidth, and the idler wave experiences group velocity dispersion through the frequency dependence of the PPMP. Although their mathematical descriptions differ, the physics of OPA and DFG is very similar.

2.6 Conclusion

In this chapter, we presented a general procedure for the design of OPAs using non-uniform QPM gratings.

The model used was one-dimensional and assumed an undepleted, time-independent pump wave. We considered slowly-varying, but otherwise general profiles for the coupling coefficient and the wave vector mismatch. We treated the problem in the frequency domain.

We solved for the wave evolution using the complex WKB method. These expressions were then simplified to reveal the main features of the amplification process.

We illustrated the use of the design formula by studying a variety of QPM grating profiles. We considered the canonical linear profile, which provides gain over wide bandwidths; tapered profiles for ripple reduction; sinusoidal profiles for selective frequency amplification; and finally a tandem grating design for engineered gain and group-delay spectra (such as flat profiles for both).

We also discussed the similarities existing between parametric amplification in chirped QPM gratings and its low-gain limit, difference-frequency generation.

The analysis presented here dealt exclusively with the spectral properties of the amplifiers. In chapter 3, we present the time-domain analysis, which will lead to a discussion of the temporal properties of the amplified pulses.

The 1-D model presented here ignored transverse effects such as diffraction and non-collinear interactions. A 2-D model including those effects will be described in the last chapters of this dissertation.

2.7 Appendix

This appendix contains the derivation of the WKB solutions, Eqs. (2.10), and of the design formula, Eq. (2.14).

2.7.1 General WKB solutions

We consider profiles for which $\kappa(z)$ is a smooth, monotonic function of position. The smoothness condition is required for the validity of the WKB method. Monotonicity is also important because it ensures that there exists only one PPMP at any given input frequency. We can define a characteristic chirp rate, κ_0' which sets the scale of $\kappa(z)$. (In other words, we decompose the wavenumber mismatch into a linear part, $\kappa_0'(z - z_{pm0})$, and another function which represents the departure from linearity.) We assume that this chirp rate is positive. The solution for negative chirp rate can then be obtained using the substitutions $\kappa' \to -\kappa'$, $A_s \to A_s^*$ and $A_i \to -A_i^*$.

We normalize the position axis using the characteristic chirp rate κ_0':

$$\zeta = \sqrt{\kappa_0'}(z - z_{pm}), \tag{2.55}$$

where z_{pm} is the perfect phase-matching point (PPMP). Then Eq. (2.6) becomes

$$\frac{d^2 a_s}{d\zeta^2} + \bar{Q}(\zeta) a_s = 0, \tag{2.56}$$

where

$$\bar{Q}(\zeta) = \left(\frac{\bar{\kappa}}{2} - \frac{i}{4}\frac{\lambda'}{\lambda}\right)^2 - \lambda + \frac{i\bar{\kappa}'}{2} + \frac{1}{4}\left(\frac{\lambda'}{\lambda}\right)'. \tag{2.57}$$

In this expression, $\bar{\kappa} = \kappa/{\kappa_0'}^{1/2}$ is the normalized wavenumber mismatch, $\lambda = \gamma^2/\kappa_0'$ is the Rosenbluth gain exponent and the primes denote differentiation with respect to ζ. Since the profiles κ and γ are, by assumption, smooth functions of position, we neglect small terms such as λ'' or $(\lambda')^2$ from now on. The solution is also subject to the boundary conditions

$$a_s(\zeta_0) = \gamma^{-1/2}(\zeta_0) A_{s0} \tag{2.58}$$

$$\frac{da_s(\zeta_0)}{d\zeta} = \gamma^{-1/2}(\zeta_0)\left[i\lambda^{1/2}(\zeta_0)A_{i0}^* - \frac{i}{2}\bar{\kappa}(\zeta_0)A_{s0} - \frac{1}{4}\frac{\lambda'(\zeta_0)}{\lambda(\zeta_0)}A_{s0}\right]. \tag{2.59}$$

These come from the input conditions $A_s(z_0) = A_{s0}$, $A_i(z_0) = A_{i0}$, where z_0 is the position of the input plane in real units.

Eq. (2.56) is in a form suitable for WKB analysis; its two linearly independent WKB solutions are [29, 30, 31, 34]

$$\bar{Q}^{-1/4} \exp\left(\pm i \int^{\zeta} \left[\bar{Q}(\zeta')\right]^{1/2} d\zeta'\right). \tag{2.60}$$

The conditions of validity of the WKB approximation will be discussed below. As observed in section 2.1 and illustrated in Fig. 2.2, the solutions are of exponential type between the turning points, were $\mathrm{Re}(\bar{Q}) < 0$ (region II), and of oscillatory type outside the interaction region, where $\mathrm{Re}(\bar{Q}) > 0$ (regions I and III).

Approximations to the signal and idler waves can be written as linear combinations of these elementary WKB solutions. As we will see, different linear combinations are required in each of the regions I, II and III. One way of calculating the correct coefficients is to use connection formulae to match the WKB solutions on either sides of each turning point [34]. Another, possibly more elegant approach is to employ the complex WKB method [31, 29], which consists in extending the solution to the entire complex plane and enforcing continuity asymptotically far from the turning points. In this paper we will take the second approach; the procedure for doing so is detailed in the next section.

2.7.2 Application of the Complex WKB Method

In this section we apply the complex WKB method to extend each elementary solution to the entire complex plane. We establish the Stokes diagram corresponding to the function Q and use of the usual rules for crossing Stokes and anti-Stokes lines. (Complete accounts of these procedures are given by Budden [31], Heading [29] and White [35].)

In order to define the WKB solutions uniquely we have to specify the lower bound of integration. It is typical to take one of the two complex turning points ζ_1 and ζ_2, which are the values of ζ for which $\bar{Q} = 0$. Following Heading [29], we represent the

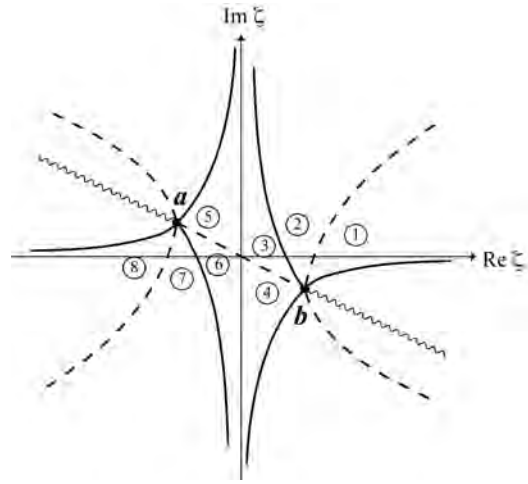

Figure 2.11: Stokes diagram of the function $\bar{Q}$ defined by Eq. (2.57). Solid line: anti-Stokes lines; dashed lines: Stokes lines; zig-zag: branch cut.

WKB solutions by the notation

$$(\zeta_1, \zeta) \equiv \bar{Q}^{-1/4} \exp\left(i \int_{\zeta_1}^{\zeta} \left[\bar{Q}(\zeta')\right]^{1/2} d\zeta' \right) \tag{2.61}$$

$$(\zeta, \zeta_1) \equiv \bar{Q}^{-1/4} \exp\left(i \int_{\zeta}^{\zeta_1} \left[\bar{Q}(\zeta')\right]^{1/2} d\zeta' \right) \tag{2.62}$$

Moreover, and still following Heading, we will use the subscripts d or s according to whether a solution is asymptotically dominant (exponentially growing) or subdominant (exponentially decaying) as $|\zeta| \to \infty$.

The Stokes diagram of the function $\bar{Q}$ is shown in Fig. 2.11. We assume that the turning points are well separated. From each turning point emerges a branch cut, which we specify to be away from the real axis; three Stokes lines, on which $\mathrm{Re}(\bar{Q}^{1/2} d\zeta) = 0$, where the magnitude of the two WKB solutions are most different; and three anti-Stokes lines on which $\mathrm{Im}(\bar{Q}^{1/2} d\zeta) = 0$, where the two solutions have equal magnitude. We number the various regions from 1 through 8 as shown in Fig. 2.11. Our goal is to determine how each global WKB solution becomes a different linear combination of (ζ_1, ζ) and (ζ, ζ_1), or (ζ_2, ζ) and (ζ, ζ_2), when ζ moves from a region to another in the complex plane.

Let us start from (ζ_1, ζ) in region 8 ($\mathrm{Re}\zeta \to -\infty$). This solution being dominant in this sector, we write

$$\text{Region 8:} \quad (\zeta_1, \zeta)_d. \tag{2.63}$$

To go to region 7 we cross a Stokes line in the counter-clockwise direction, so we must add the subdominant solution multiplied by the Stokes coefficient i:

$$\text{Region 7:} \quad (\zeta_1, \zeta)_d + i(\zeta, \zeta_1)_s. \tag{2.64}$$

To get to region 6, we cross an anti-Stokes line and the roles of dominance and sub-dominance are interchanged:

$$\text{Region 6:} \quad (\zeta_1, \zeta)_s + i(\zeta, \zeta_1)_d. \tag{2.65}$$

Again, as we cross the Stokes line to go to region 5, we must add the sub-dominant solution:

$$\text{Region 5:} \quad (\zeta_1, \zeta)_s + i\left\{(\zeta, \zeta_1)_d + i(\zeta_1, \zeta)_s\right\} = i(\zeta, \zeta_1)_d. \tag{2.66}$$

We can match region 5 and 3 by connecting turning points ζ_1 and ζ_2:

$$\text{Region 3:} \quad i[\zeta_2, \zeta_1](\zeta, \zeta_2)_s, \tag{2.67}$$

where we have introduced the coefficient

$$[\zeta_2, \zeta_1] \equiv \exp\left(i \int_{\zeta_2}^{\zeta_1} [Q(\zeta')]^{1/2} d\zeta'\right). \tag{2.68}$$

In region 2, this solution becomes dominant:

$$\text{Region 2:} \quad i[\zeta_2, \zeta_1](\zeta, \zeta_2)_d. \tag{2.69}$$

Finally, as we cross the Stokes line between regions 2 and 1 in the clockwise direction, we add the subdominant solution multiplied by $-i$:

$$\text{Region 1:} \quad i[\zeta_2, \zeta_1]\left\{(\zeta, \zeta_2)_d - i(\zeta_2, \zeta)_s\right\}. \tag{2.70}$$

Thus we obtain the continuation in the complex plane. In particular, we have a representation of the asymptotic behavior of this solution over the entire real axis.

Now let us consider the second solution. We start from (ζ, ζ_1) in region 8. Proceeding as before, we have the following connections:

$$\text{Region 8:} \quad (\zeta, \zeta_1)_s \tag{2.71}$$

$$\text{Region 7:} \quad (\zeta, \zeta_1)_s \tag{2.72}$$

$$\text{Region 6:} \quad (\zeta, \zeta_1)_d \tag{2.73}$$

$$\text{Region 5:} \quad (\zeta, \zeta_1)_d + i(\zeta_1, \zeta)_s \tag{2.74}$$

$$\text{Region 3:} \quad [\zeta_2, \zeta_1](\zeta, \zeta_2)_s + i[\zeta_1, \zeta_2](\zeta_2, \zeta)_d \approx [\zeta_2, \zeta_1](\zeta, \zeta_2)_s \tag{2.75}$$

$$\text{Region 2:} \quad [\zeta_2, \zeta_1](\zeta, \zeta_2)_d \tag{2.76}$$

$$\text{Region 1:} \quad [\zeta_2, \zeta_1]\left\{(\zeta, \zeta_2)_d - i(\zeta_2, \zeta)_s\right\} \tag{2.77}$$

In going from regions 5 to 3, we have dropped the term with the coefficient $[\zeta_1, \zeta_2]$ because it is exponentially small compared to $[\zeta_2, \zeta_1]$ (this follows from the assumption that the turning points are well separated). We note that the two global solutions, which can be represented in region 8 by (ζ_1, ζ) and (ζ, ζ_1), only differ in region 1 by a factor of i.

2.7.3 WKB Solutions for the Signal and Idler Waves

In the previous section we have given the proper asymptotic representations for two global, linearly independent solutions. Now we are left with the task of determining the linear combinations which satisfy the boundary conditions, Eqs. (2.58)-(2.59). Then each solution can be continued over the entire real axis using the results from the previous section. We obtain the following solutions in each region:

$$a_s^I \approx C_s^+(\zeta_1, \zeta) + C_s^-(\zeta, \zeta_1), \quad \zeta \ll -\zeta_{tp} \tag{2.78}$$

$$a_s^{II} \approx (iC_s^+ + C_s^-)(\zeta, \zeta_1), \quad -\zeta_{tp} \ll \zeta \ll \zeta_{tp} \tag{2.79}$$

$$a_s^{III} \approx (iC_s^+ + C_s^-)[\zeta_2, \zeta_1](\zeta, \zeta_2)\left\{1 - i\frac{(\zeta_2, \zeta)}{(\zeta, \zeta_2)}\right\}, \quad \zeta \gg \zeta_{tp}. \tag{2.80}$$

The coefficients $C_s^{\pm}$ are given approximately (provided $\zeta_0 \ll -\zeta_{tp}$) by

$$C_s^+ \approx \frac{1}{(\zeta_1,\zeta_0)\gamma^{1/2}(\zeta_0)}\left[\left(1+\frac{\lambda(\zeta_0)}{\bar{\kappa}(\zeta_0)^2}\right)A_{s0}-\frac{\lambda^{1/2}(\zeta_0)}{\bar{\kappa}(\zeta_0)}A_{i0}^*\right] \tag{2.81}$$

$$C_s^- \approx \frac{1}{(\zeta_0,\zeta_1)\gamma^{1/2}(\zeta_0)}\left(-\frac{\lambda(\zeta_0)}{\bar{\kappa}^2(\zeta_0)}A_{s0}+\frac{\lambda^{1/2}(\zeta_0)}{\bar{\kappa}(\zeta_0)}A_{i0}^*\right) \tag{2.82}$$

The corresponding coefficients for the idler wave are obtained by interchanging the role of signal and idler.

We recover the wave envelope functions by multiplying by $\gamma^{1/2}\exp(i\phi/2)$, resulting in the expression given in the text, Eq. (2.10).

Even when only one wave is present initially (e.g. $A_{i0}=0$), the coefficients $C_s^{\pm}$ are in general both non-zero. The solution is then the superposition of a positive and a negative complex exponential, which interfere and cause the ripple observed on the amplification spectrum (as discussed in section 2.3.3). These oscillations can be suppressed by letting either $\lambda(\zeta_0)\to 0$, $\lambda(\zeta_L)\to 0$ or $\bar{\kappa}(\zeta_0)\to\infty$, $\bar{\kappa}(\zeta_L)\to\infty$ (where ζ_L refers to the output plane). This is accomplished by the ripple-reduction techniques presented in section 2.3.3.

2.7.4 Validity of the WKB Solutions

A few key assumptions have been made to obtain Eqs. (2.78)-(2.80); they will be examined in this section.

We have assumed, when obtaining the continuation of the solution in the complex plane, that the turning points are well separated. This requirement is necessary for the WKB solutions to be valid between the turning points. It also allowed us to drop the exponentially decaying solution when connecting between the turning points. In the case of a linear grating, for which the magnitude of the amplification factor is $|[\zeta_2,\zeta_1]| = \exp(\pi\lambda)$, neglecting the decaying exponential is valid provided $\lambda \gg 1/\pi$. This value can be considered as the threshold of significant gain.

Second, we have assumed that neither turning point is close to the edges of the grating. This allowed us to define unambiguously the three regions I, II and III. The assumption that $\zeta_0 \ll -\zeta_{tp}$ was used to obtain the coefficients C^+ and C^-. Similarly,

when obtaining expressions involving the position of the output of the grating, ζ_L, we assume that $\zeta_L \gg \zeta_{tp}$. Consequently, the description given here ceases to be valid at the edges of the spectrum, because our results cannot be applied if the gain region reaches the edges of the grating.

To summarize, the WKB formalism developed here is best suited when (i) the gain is large, (ii) the gain region is short compared to the grating length and (iii) the PPMPs are far from the edges of the grating. In the case of the linear profile described in section 2.3.2, these conditions are satisfied when $\lambda = \gamma^2/|\kappa'| \gg 1/\pi$, $L_g = 4\gamma/|\kappa'| \ll L$ and $\delta\omega \ll \Delta\omega_{BW}$.

2.7.5 Explicit Expressions for the Linear Profile

Linear grating profiles are given simply by $\bar{\kappa} = \zeta$. Therefore, assuming a constant coupling coefficient, we have $\bar{Q} = \zeta^2/4 - \lambda + i/2$. The complex turning points are then given by $\zeta_1, \zeta_2 = \mp 2(\lambda - i/2)^{1/2}$.

In this case the integrals appearing in the WKB expressions can be evaluated exactly; approximate and simpler expressions are useful however. First, for $\zeta_0 \ll -\zeta_{tp}$:

$$\begin{aligned}\int_a^{\zeta_0} Q^{1/2} d\zeta' &= (\lambda - i/2)\left\{\frac{\zeta_0}{2\sqrt{\lambda - i/2}}\sqrt{\frac{\zeta_0^2}{4(\lambda - i/2)} - 1}\right. \\ &\quad \left. + \ln\left[\frac{|\zeta_0|}{2\sqrt{\lambda - i/2}} + \sqrt{\frac{\zeta_0^2}{4(\lambda - i/2)} - 1}\right]\right\} \\ &\approx -\frac{\zeta_0^2}{4} + (\lambda - i/2)\ln\left(\frac{|\zeta_0|}{\lambda^{1/2}}\right) + \frac{\lambda}{2}. \end{aligned} \tag{2.83}$$

For $-\zeta_{tp} \ll \zeta \ll \zeta_{tp}$:

$$\int_a^{\zeta} Q^{1/2} d\zeta' \approx i\sqrt{\lambda}\left(1 - \frac{i}{4\lambda}\right)\zeta + \frac{i\pi\lambda}{2} + \frac{\pi}{4}. \tag{2.84}$$

Similarly, for $\zeta_L \gg \zeta_{tp}$:

$$\int_b^{\zeta_L} Q^{1/2} d\zeta' \approx \frac{\zeta_L^2}{4} - (\lambda - i/2)\ln\left(\frac{\zeta_L}{\lambda^{1/2}}\right) - \frac{\lambda}{2}. \tag{2.85}$$

Finally, the integral between the two turning points is simply

$$\int_a^b Q^{1/2} d\zeta' = i\pi(\lambda - i/2). \tag{2.86}$$

The solutions *for the linear profile* can then be written approximately as

$$\begin{aligned}
A_s^I(\zeta) &\approx \left[\left(1+\epsilon^2(\zeta_0)\right) A_{s0} + \epsilon(\zeta_0) A_{i0}^*\right] \exp\left(i\lambda \ln\left|\frac{\zeta}{\zeta_0}\right|\right) \\
&\quad \times \left[1 - \epsilon(\zeta)\left(\frac{A_{i0}^* + \epsilon(\zeta_0)A_{s0}}{A_{s0} + \epsilon(\zeta_0)A_{i0}^*}\right) \exp\left(\frac{i}{2}(\zeta^2 - \zeta_0^2) - 2i\lambda \ln\left|\frac{\zeta}{\zeta_0}\right|\right)\right], \qquad (2.87) \\
A_s^{II}(\zeta) &\approx \frac{1}{\sqrt{2}} \exp\left[\frac{\pi\lambda}{2} + \lambda^{1/2}\zeta - i\left(\frac{\zeta}{4\lambda^{1/2}} + \frac{\zeta^2}{4} + \lambda \ln \epsilon(\zeta_0) - \frac{\lambda}{2}\right)\right] \\
&\quad \times \left[\left(1+\epsilon^2(\zeta_0)\right) A_{s0} - \epsilon(\zeta_0) A_{i0}^* - (A_{i0}^* - \epsilon(\zeta_0) A_{s0}) \exp\left(-i\Phi(\zeta_0)\right)\right], \qquad (2.88) \\
A_s^{III}(\zeta) &\approx \exp\left(\pi\lambda + i\lambda \ln\left|\frac{\zeta}{\zeta_0}\right|\right) F(\zeta) \left[F^*(\zeta_0) A_{s0} - F(\zeta_0) e^{-i\Phi(\zeta_0)} A_{i0}^*\right], \qquad (2.89)
\end{aligned}$$

with

$$\begin{aligned}
F(\zeta) &= 1 - \epsilon(\zeta) \exp(i\Phi(\zeta)), && (2.90) \\
\Phi(\zeta) &= \frac{\zeta^2}{2} + 2\lambda \ln \epsilon(\zeta) - \lambda + \frac{\pi}{2}, && (2.91) \\
\epsilon(\zeta) &= \frac{\lambda^{1/2}}{|\zeta|}. && (2.92)
\end{aligned}$$

The expressions for the signal wave are obtained, as usual, by interchanging the signal and idler subscripts.

The spatial evolution of the signal and idler magnitudes for typical parameter values is plotted in Fig. 2.12 along with the numerical solution. The solutions are oscillatory before and after the gain region, where the interaction is phase-mismatched, while they grow exponentially in the phase-matched region. As expected, the WKB solution is not a very good approximation in the vicinity of the turning points.

Finally, it is interesting to point out that the ripple-reduction schemes described in section 2.3.3 (namely, reduction of γ or increase of κ at the ends of the grating) amount to reducing the values of $\epsilon(\zeta_0)$ and $\epsilon(\zeta_L)$. Setting $\epsilon(\zeta_0) = \epsilon(\zeta_L) = 0$ into

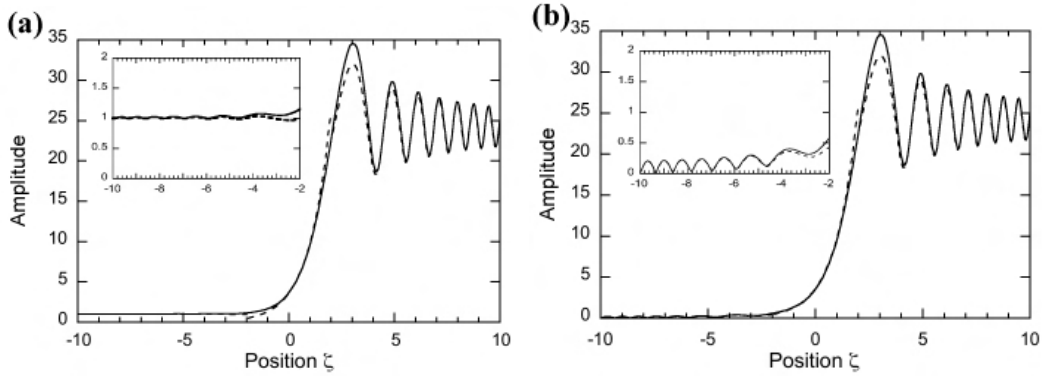

Figure 2.12: Comparison between the WKB solution and the numerical solution for $\lambda = 1$, $A_{s0} = 1$, $A_{i0} = 0$, $\bar{L} = 20$ and ζ_{pm} located at the center of the grating: (a) signal; (b) idler.

Eqs. (2.87)-(2.89) leads to major simplifications:

$$A_s^I(\zeta) \approx A_{s0} e^{i\lambda \ln|\zeta/\zeta_0|}, \tag{2.93}$$

$$A_s^{II}(\zeta) \approx \frac{1}{\sqrt{2}} \left[A_{s0} + i A_{i0}^* e^{-i\left(\zeta_0^2/2-\lambda\right)} \right] \times \exp\left[\frac{\pi\lambda}{2} + \lambda^{1/2}\zeta - i\left(\frac{\zeta}{4\lambda^{1/2}} + \frac{\zeta^2}{4} - \frac{\lambda}{2} \right) \right], \tag{2.94}$$

$$A_s^{III}(\zeta) \approx e^{\pi\lambda} \left[A_{s0} + i A_{i0}^* e^{-i\left(\zeta_0^2/2-\lambda\right)} \right] e^{i\lambda \ln|\zeta/\zeta_0|}. \tag{2.95}$$

2.7.6 Derivation of the Simplified Design formula

The WKB solutions, Eqs. (2.78)-(2.80), are quite complicated as they involve several integrals of the function $\bar{Q}^{1/2}$. To simplify these expressions, the integrals can be evaluated approximately for general (smooth) grating profiles.

Let us outline the evaluation procedure using as an example $\int_{\zeta_2}^{\zeta_L} \bar{Q}^{1/2} d\zeta$. We neglect the variation of coupling coefficient; therefore we can write $\bar{Q} \approx \bar{\kappa}^2/4 - \lambda + i\bar{\kappa}'/2$. The integral can be separated into two parts. The first one corresponds to the vicinity of the turning point, where $\bar{\kappa}(z)$ is approximately linear; the second one corresponds to the portion away from the turning point, where $\bar{\kappa}$ is large. Thus the two integration ranges are from ζ_2 to $\widetilde{\zeta}$, and from $\widetilde{\zeta}$ to ζ_L, respectively, with $\widetilde{\zeta}$ located

on the real axis somewhere between $\mathrm{Re}(\zeta_2)$ and ζ_L, close enough to ζ_2 so that $\bar{\kappa}$ is linear but far enough so that the behavior of $\bar{Q}$ is dominated by $\bar{\kappa}^2/4$. The integral over the linear range is given by Eq. (2.85); retaining the most significant real and imaginary contributions, we have

$$\int_{\zeta_2}^{\widetilde{\zeta}} \bar{Q}^{1/2} d\zeta \approx \frac{\bar{\kappa}^2}{4} + \frac{i}{2} \ln\left(\frac{\widetilde{\zeta}}{\lambda^{1/2}}\right). \tag{2.96}$$

The second integral can be approximated by

$$\int_{\widetilde{\zeta}}^{\zeta_L} \bar{Q}^{1/2} d\zeta \approx \frac{1}{2}\int_{\widetilde{\zeta}}^{\zeta_L} \bar{\kappa}\, d\zeta + \frac{i}{2} \ln\left(\frac{\bar{\kappa}(\zeta_L)}{\widetilde{\zeta}}\right). \tag{2.97}$$

Adding both contributions gives

$$\int_{\zeta_2}^{\zeta_L} \bar{Q}^{1/2} d\zeta \approx \frac{1}{2}\int_{0}^{\zeta_L} \bar{\kappa}\, d\zeta + \frac{i}{2} \ln\left(\frac{\bar{\kappa}(\zeta_L)}{\lambda^{1/2}}\right). \tag{2.98}$$

The integral $\int_{\zeta_1}^{\zeta_0} \bar{Q}^{1/2} d\zeta$ can be evaluated in a similar manner. Using these approximations, the elementary WKB solutions can be written as

$$(\zeta_1, \zeta_0) \approx 2^{1/2}\lambda^{-1/4}(\zeta_0)\, e^{\frac{i}{2}\int_{\zeta_0}^{0} \kappa(\zeta)\, d\zeta} \tag{2.99}$$

$$(\zeta_0, \zeta_1) \approx \frac{2^{1/2}\lambda^{1/4}(\zeta_0)}{|\kappa(\zeta_0)|}\, e^{-\frac{i}{2}\int_{\zeta_0}^{0} \kappa(\zeta)\, d\zeta} \tag{2.100}$$

$$(\zeta_2, \zeta_L) \approx \frac{2^{1/2}\lambda^{1/4}(\zeta_0)}{\kappa(\zeta_L)}\, e^{\frac{i}{2}\int_{0}^{\zeta_L} \kappa(\zeta)\, d\zeta} \tag{2.101}$$

$$(\zeta_L, \zeta_2) \approx 2^{1/2}\lambda^{-1/4}(\zeta_0)\, e^{-\frac{i}{2}\int_{0}^{\zeta_L} \kappa(\zeta)\, d\zeta}. \tag{2.102}$$

Similarly, the amplification factor can be approximated by

$$\begin{aligned} [\zeta_2, \zeta_1] &= e^{i\int_{\zeta_2}^{\zeta_1} \bar{Q}^{1/2}\, d\zeta} \\ &\approx -ie^{\int_{\zeta_1^*}^{\zeta_2^*} \left(\lambda - \bar{\kappa}^2/4\right)^{1/2} d\zeta}, \end{aligned} \tag{2.103}$$

where $\zeta_{1,2}^*$ are the real-valued turning points of $\lambda - \bar{\kappa}^2(\zeta)/4$. These approximations

can then be substituted into the expressions for signal and idler, (2.80), to yield the following formula, valid for general smooth grating profiles:

$$\begin{aligned} A_s^{III} \approx & \left[\left(1 - \frac{i\lambda^{1/2}(\zeta_0)}{\kappa(\zeta_0)} e^{i\int_{\zeta_0}^{0}\kappa(\zeta)d\zeta}\right) A_{s0} \right. \\ & \left. + i\, e^{i\int_{\zeta_0}^{0}\kappa(\zeta)d\zeta}\left(1 + \frac{i\lambda^{1/2}(\zeta_0)}{\kappa(\zeta_0)} e^{-i\int_{\zeta_0}^{0}\kappa(\zeta)d\zeta}\right) A_{i0}^*\right] \\ & \times\, e^{\int_{\zeta_1^*}^{\zeta_2^*}\left(\lambda-\bar{\kappa}^2/4\right)^{1/2}d\zeta}\left(1 - \frac{i\lambda^{1/2}(\zeta_L)}{\kappa(\zeta_L)} e^{i\int_{0}^{\zeta_L}\kappa(\zeta)d\zeta}\right) \end{aligned} \tag{2.104}$$

In order to simplify the formulas further, we neglect the oscillatory terms. This step yields

$$A_s \approx \left[A_{s0} + iA_{i0}^* e^{i\int_{\zeta_0}^{0}\bar{\kappa}\,d\zeta}\right] e^{\int_{\zeta_1^*}^{\zeta_2^*}\left(\lambda-\bar{\kappa}^2/4\right)^{1/2}d\zeta}, \tag{2.105}$$

which is the design formula, Eq. (2.14).

Chapter 3

Space-time Problem

3.1 Introduction

Chapter 2 treated the problem in the frequency domain, relying heavily on the WKB technique. In this chapter we present the time-domain analysis. This analysis provides insight into the shape of the amplified pulse. Chapters 4 and beyond return to a frequency domain analysis.

This problem is in fact similar to models found in other fields of physics. For instance, in atomic physics the non-adiabatic crossing of energy levels is modeled by coupled oscillators with linearly-varying phase mismatch. That problem was solved in terms of parabolic cylinder functions independently by Landau, Zener and Stuckelberg in 1932 [36, 37, 38]. The entire field was revived in the early 1970s by the pioneering work of Rosenbluth and coworkers, in the study of parametric instabilities driven by lasers in inhomogeneous plasma. The Rosenbluth model is equivalent to the Landau-Zener-Stuckelberg model except for a sign change in the exponent: an exponentially small probability of diabatic atomic transition now becomes an exponentially growing amplified wave in the case of a parametric instability. The Green's function of the space-time Rosenbluth problem is also known [39, 40]. More recently, Short and Simon studied the shape of the amplified pulses [41], emphasizing the important differences existing between the impulse response and an amplified pulse.

The Rosenbluth model assumes a time-independent pump wave. A completely

different situation, that of a uniform medium with a time-dependent pump wave, has been presented by Afeyan and Fejer [42]. The case where both the medium and the pump wave are variable will be the subject of future research.

The goal of this chapter is to obtain the shape and phase of the amplified signal and idler optical pulses. Because of their large amplification bandwidth, chirped QPM gratings are potential candidates for short-pulse OPAs. It is therefore important to understand the behavior of the amplified pulses. For several high-peak-power applications, effects such as pre-pulsing are undesired, and a precise knowledge of the pulse shape is required.

This chapter is divided into three main sections. The first one is a review of the uniform medium. We derive the Green's functions for the amplified waves, following the work of Bobroff and Haus [43]. We also discuss the nature of the instability in the co- and counter-propagating situations. This overview serves as a preparation to the study of the non-uniform medium, which comes next. We derive the Green's functions for a linear non-uniform phase-matching profile, show how to recover the uniform-medium limit and discuss the nature of the instability. The last third of this chapter is dedicated to obtaining the pulse shape. We consider two regimes, that of long and short pulses.

3.2 Uniform Medium

3.2.1 Propagation Equations in the Frequency Domain

The physics of optical parametric amplification in non-uniform phase-matched media is described in Part 1. Two co-propagating plane waves, the signal and the idler, satisfying the frequency-matching condition, are coupled through their interaction with the pump wave. The equations describing the evolution of the envelopes A_s and A_i are [44, 45]

$$\frac{\partial A_s}{\partial z} + \frac{1}{v_s}\frac{\partial A_s}{\partial t} = i\gamma A_i^* \tag{3.1}$$

$$\frac{\partial A_i^*}{\partial z} + \frac{1}{v_i}\frac{\partial A_i^*}{\partial t} = -i\gamma A_s. \tag{3.2}$$

These envelopes have been obtained from the electric field $\widetilde{E}_{s,i}$ by extracting the fast carrier phase according to $\widetilde{E}_s = E_s \exp\{i[k_{s0}(\omega_{s0})z - \omega_{s0}t]\}$. The normalized envelope functions are then obtained from $A_{s,i} = (n_{s,i}/\omega_{s,i})^{1/2}E_{s,i}$. Note the slight difference between this time-domain definition (which extracts only the center carrier phase $k_{s,i0}z - \omega_{s,i0}t$) and the one used in the frequency-domain description, chapter 2 (which extracts the phase $k_{s,i}z - \omega_{s,i}t$ at each frequency under consideration).

We take Laplace transforms in time, assuming input at the signal wave only. Using $-i\omega$ as the transform variable, we obtain

$$\frac{\partial \widetilde{A_s}}{\partial z} - i\frac{\omega}{v_s}\widetilde{A_s} = i\gamma\widetilde{A_i^*} + \frac{1}{v_s}A_s(z,0) \tag{3.3}$$

$$\frac{\partial \widetilde{A_i^*}}{\partial z} - i\frac{\omega}{v_i}\widetilde{A_i^*} = -i\gamma\widetilde{A_s}, \tag{3.4}$$

where $A_s(z,0)$ denotes the initial signal distribution, and the tilde indicates a Laplace transform in time. Before reaching the nonlinear medium (i.e. for $t < 0$), an impulse is given by $\delta[t - (z - z_0)/v_s]$. Therefore the initial impulse is given by $A_s(z,0) = v_s\delta(z - z_0)$.

The two coupled equations can then be combined to eliminate one of the two waves, and simplified using

$$\widetilde{A_s} = y_s \exp\left[\frac{i}{2}\left(\frac{1}{v_s} + \frac{1}{v_i}\right)\omega(z - z_0)\right] \tag{3.5}$$

$$\widetilde{A_i^*} = y_i^* \exp\left[\frac{i}{2}\left(\frac{1}{v_s} + \frac{1}{v_i}\right)\omega(z - z_0)\right]. \tag{3.6}$$

The evolution of the signal wave is given by

$$\begin{aligned}\frac{d^2y_s}{dz^2} &+ \left\{\left[\frac{1}{2}\left(\frac{1}{v_s} - \frac{1}{v_i}\right)\omega\right]^2 - \gamma^2\right\}y_s \\ &= \frac{1}{v_s}\left[-i\frac{\omega}{v_i}A_s(z,0) + \frac{d}{dz}A_s(z,0)\right]e^{-i(1/v_s+1/v_i)\omega(z-z_0)/2}.\end{aligned} \tag{3.7}$$

Similarly, the idler wave obeys

$$\begin{aligned} \frac{d^2 y_i}{dz^2} &+ \left\{ \left[\frac{1}{2} \left(\frac{1}{v_s} - \frac{1}{v_i} \right) \omega \right]^2 - \gamma^2 \right\} y_i \\ &= i \frac{\gamma}{v_s} A_s^*(z,0) e^{i(1/v_s + 1/v_i)\omega(z-z_0)/2}. \end{aligned} \tag{3.8}$$

The homogeneous parts of these equations are identical; the signal and idler waves differ by their driving terms and initial conditions.

3.2.2 Green's Functions

The homogeneous solutions of Eqs. (3.7) and (3.8) are

$$\Psi_{1,2} = e^{\pm iz\sqrt{\left[\frac{1}{2}\left(\frac{1}{v_s} - \frac{1}{v_i}\right)\omega\right]^2 - \gamma^2}}. \tag{3.9}$$

The particular solutions can be constructed using a linear combination of Ψ_1 and Ψ_2 satisfying the boundary conditions at the input plane z_0.

Alternatively, we can obtain the solution of Eqs. (3.7) and (3.8) by taking Fourier transforms in z. The Fourier-domain representation of the impulse response is

$$\widehat{y}_s(k,\omega) = \frac{i\left[\frac{1}{2}\left(\frac{1}{v_s} - \frac{1}{v_i}\right)\omega - k\right] e^{kz_0}}{\left[\frac{1}{2}\left(\frac{1}{v_s} - \frac{1}{v_i}\right)\omega\right]^2 - \gamma^2 - k^2} \tag{3.10}$$

$$\widehat{y}_i(k,\omega) = \frac{i\gamma e^{kz_0}}{\left[\frac{1}{2}\left(\frac{1}{v_s} - \frac{1}{v_i}\right)\omega\right]^2 - \gamma^2 - k^2}. \tag{3.11}$$

The hats indicate spatial Fourier transforms, and k is the transform variable.

The Green's functions are obtained by inverting the transforms in k and ω. In the case of the signal, we must evaluate

$$G_s(z,t) = \frac{1}{4\pi^2} \int_{-\infty+i\epsilon}^{\infty+i\epsilon} d\omega \int_{-\infty}^{\infty} dk\ \widehat{y}_s e^{-ik(z-z_0) - i\left[t - \frac{1}{2}(1/v_s - 1/v_i)(z-z_0)\right]\omega}\ . \tag{3.12}$$

In order to insure that $G_s = 0$ for $z - z_0 < 0$, the k-contour must be taken above all

the singularities. For $z - z_0 > 0$, it can be closed in the lower half-plane. This yields two contributions, one for each of the two poles $k_\pm = \pm\{[\frac{1}{2}(1/v_s - 1/v_i)\omega]^2 - \gamma^2\}^{1/2}$:

$$\begin{aligned} G_s &= \frac{1}{4\pi i}\left(\frac{\partial}{\partial z} + \frac{1}{v_i}\frac{\partial}{\partial t}\right) \\ &\left\{\int_{-\infty+i\epsilon}^{\infty+i\epsilon} \frac{e^{i\sqrt{(\omega/\delta v)^2-\gamma^2}\,(z-z_0)-i[t-(z-z_0)/\bar{v}]\omega}}{\sqrt{\left(\frac{\omega}{\delta v}\right)^2-\gamma^2}}\,d\omega \right. \\ &\left. - \int_{-\infty+i\epsilon}^{\infty+i\epsilon} \frac{e^{-i\sqrt{(\omega/\delta v)^2-\gamma^2}\,(z-z_0)-i[t-(z-z_0)/\bar{v}]\omega}}{\sqrt{\left(\frac{\omega}{\delta v}\right)^2-\gamma^2}}\,d\omega \right\}, \end{aligned} \tag{3.13}$$

where $1/\delta v = \frac{1}{2}(1/v_s - 1/v_i)$ and $1/\bar{v} = \frac{1}{2}(1/v_s + 1/v_i)$. Note that in order to simplify the notation, the definition of $1/\delta v$ used in this chapter contains a factor of 1/2.

The two integrands in Eq. (3.13) have a branch cut along the real axis ranging from $\omega = -|\delta v|\gamma$ to $\omega = +|\delta v|\gamma$. When $|\omega|$ is large, the exponent in the first integral becomes $-i(t - t_s)\omega$, where $t_s = (z - z_0)/v_s$ is the signal wave front. If $t < t_s$, the ω-contour can be closed in the upper half-plane, which contains no singularities, and therefore the first integral is zero. Conversely, if $t > t_s$, the ω-contour can be closed in the lower half-plane, around the branch cut. By a similar argument, we find that the second integral is zero if $t < t_i$, where $t_i = (z - z_0)/v_i$ is the idler wave front, and non-zero otherwise.

It is useful to introduce the delays with respect to the wavefronts, V_s and V_i, as follows:

$$V_s = \begin{cases} t_s - t, & \text{if } v_s < v_i \\ t - t_s, & \text{if } v_s > v_i \end{cases} \tag{3.14}$$

$$V_i = \begin{cases} t - t_i, & \text{if } v_s < v_i \\ t_i - t, & \text{if } v_s > v_i \end{cases} . \tag{3.15}$$

With these definitions, V_s and V_i are both positive between the wave fronts (i.e. for $t_s < t < t_i$ if $v_s > v_i$ or $t_i < t < t_s$ if $v_s < v_i$). We will see that t_s and t_i define the

edges of the causal region, outside of which the amplitude of the impulse response is zero.

Next, we perform the change of variables $\omega = \frac{1}{2}|\delta v|\gamma\sqrt{V_s/V_i}\,u + |\delta v|\gamma\sqrt{V_i/V_s}/2u$. We find that the two integrals are in fact equal. Their sum is non-zero only in the causal region, $V_sV_i > 0$. Outside of the causal region, the two integrals are either both zero or they cancel because they have opposite signs. After the change of variables, Eq. (3.13) becomes

$$\begin{aligned} G_s &= \frac{|\delta v|}{4\pi i}\left(\frac{\partial}{\partial z} + \frac{1}{v_i}\frac{\partial}{\partial t}\right)\theta(V_sV_i) \\ &\quad \times \oint e^{\frac{i}{2}|\delta v|\gamma\sqrt{V_sV_i}(u-1/u)}\frac{du}{u}. \end{aligned} \tag{3.16}$$

We recognize an integral representation for the modified Bessel function I_0. Finally, carrying out the differentiation, we obtain the result

$$G_s = \delta(t-t_s) + \frac{1}{2}|\delta v|\gamma\sqrt{\frac{V_i}{V_s}}\theta(V_sV_i)I_1\left(|\delta v|\gamma\sqrt{V_sV_i}\right). \tag{3.17}$$

The idler Green's function can be calculated by repeating this calculation. An alternative approach is to rewrite Eq. (3.20) in terms of the delays V_s and V_i:

$$A_i^* = \frac{1}{i\gamma}\frac{\partial A_s}{\partial V_i}. \tag{3.18}$$

Carrying out the differentiation, we find

$$G_i = i\frac{|\delta v|}{2}\gamma\theta(V_sV_i)I_0\left(|\delta v|\gamma\sqrt{V_sV_i}\right). \tag{3.19}$$

These expressions are identical to those given by Bobroff and Haus (Eqs. (23) and (24) of Ref. [43]).

The point of maximum amplification, $z^* = \bar{v}t$, travels at velocity $\bar{v} = 1/[\frac{1}{2}(1/v_s + 1/v_i)$. At that location, the waves grow as $e^{\gamma(z^*-z_0)}$. The shape of the Green's functions are shown in Fig. 3.1

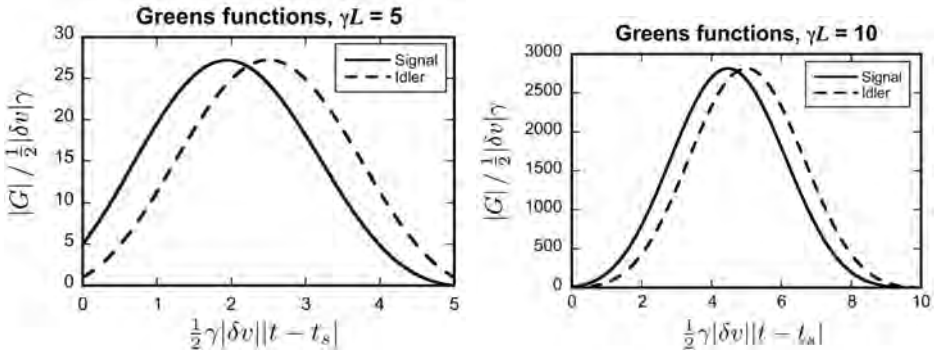

Figure 3.1: Green's functions of the uniform medium, Eqs. (3.17) and (3.19), for different values of $\gamma(z - z_0) \equiv \gamma L$.

3.2.3 Counter-Propagating Waves

In the derivation above we were concerned with the case of co-propagating waves, typical in nonlinear optics. However, in plasma physics the case commonly studied is that of counter-propagating waves. Here, we point out the differences between the two situations.

The coupled-mode equations describing the interaction of counter-propagating waves in uniform media are [43]

$$\frac{\partial A_s}{\partial z} + \frac{1}{v_s}\frac{\partial A_s}{\partial t} = i\gamma A_i^* \tag{3.20}$$

$$\frac{\partial A_i^*}{\partial z} - \frac{1}{v_i}\frac{\partial A_i^*}{\partial t} = i\gamma A_s. \tag{3.21}$$

In other words, inverting the direction of one of the waves (here, the idler) amounts to flipping the sign of its velocity and of its coupling coefficient. Therefore, the expressions for the Green's functions obtained in the co-propagating case can also be applied to the counter-propagating case provided $v_i \to -v_i$, $V_i \to -V_i$ and $\gamma^2 \to -\gamma^2$ (or $\gamma \to i\gamma$). These transformations leave the expression of the Green's functions unchanged as the various sign changes cancel each other. Nevertheless, the relative direction of propagation has a profound implication as it determines the absolute or convective nature of the instability. This distinction will be discussed in the next section.

3.2.4 Character of the Instability

An instability is absolute when a perturbation increases without limit at any fixed position in space as $t \to \infty$. An instability is convective when it tends to zero at any fixed point as $t \to \infty$ [46, 47]. In this section we examine how the relative propagation directions of the waves determines the nature of the instability.

The distinction between the co- and counter-propagating cases can be examined using the representation of the solution in (k, ω)-space, Eq. (3.10) and (3.11). Both $\widehat{y_s}$ and $\widehat{y_i}$ are of the form $g(k, \omega)/\Delta(k, \omega)$. The singularities are given by $\Delta(k, \omega) = 0$, the dispersion relation of the system. In the case of co-propagating waves, $\Delta(k, \omega) = (\omega/\delta v)^2 - k^2 - \gamma^2$. In the case of counter-propagating waves, γ^2 changes sign, and so $\Delta(k, \omega) = (\omega/\delta v)^2 - k^2 + \gamma^2$.

To determine the nature of the instability, we use the usual "pole-pinching" argument [46, 47]. Let us first consider the case of counter-propagating waves. The poles are given by the roots of the dispersion relation, $\Delta(k, \omega) = 0$; they are

$$k_\pm = \pm\sqrt{(\omega/\delta v)^2 + \gamma^2}. \tag{3.22}$$

The contour of integration of the ω-integral must be above all singularities. Initially, when $\mathrm{Im}(\omega)$ is large, the two poles are located on either side of the real axis, that is, on either side of the contour of the k-integral. As $\mathrm{Im}(\omega)$ is reduced, the poles come closer to the real axis. When $\omega = \omega_c \equiv i|\delta v|\gamma$ the two poles merge at the origin. Since the k-contour is pinched between the two poles, it cannot be deformed to avoid the singularities. Therefore the smallest value that $\mathrm{Im}(\omega)$ can take is $\mathrm{Im}(\omega_c) = |\delta v|\gamma$. Since this value is positive, the time-asymptotic behavior of the integral, dominated by $\exp[-i\mathrm{Im}(\omega)t]$, becomes exponentially large as $t \to \infty$. The instability is therefore absolute.

In the case of co-propagating waves, the poles are given by

$$k_\pm = \pm\sqrt{(\omega/\delta v)^2 - \gamma^2}. \tag{3.23}$$

The ω-contour can be lowered until it reaches the real axis. Pole pinching occurs

when $\omega = \pm\omega_c \equiv \pm|\delta v|\gamma$. However, in this case $\mathrm{Im}(\omega_c) = 0$. The solution does not diverge as $t \to \infty$; the instability is convective.

3.3 Non-Uniform Medium

In the previous section we derived the Green's functions in the case of a uniform medium. In this section, we repeat the calculation for the more general case of a linear non-uniform medium. This problem was studied by Chambers [39], Rosenbluth, White and Liu [40] and Short and Simon [41] in the context of laser-plasma interactions.

3.3.1 Propagation Equations in the Frequency Domain

In the presence of a spatially-varying phase mismatch, the coupled-mode equations are [45]

$$\frac{\partial A_s}{\partial z} + \frac{1}{v_s}\frac{\partial A_s}{\partial t} = i\gamma A_i^* e^{i\varphi(z)} \tag{3.24}$$

$$\frac{\partial A_i^*}{\partial z} + \frac{1}{v_i}\frac{\partial A_i^*}{\partial t} = -i\gamma A_s e^{-i\varphi(z)} \tag{3.25}$$

where

$$\varphi(z) = \int_{z_0}^{z} \kappa(z')dz' \tag{3.26}$$

is the accumulated phase mismatch.

We first eliminate the exponential factor in the driving terms by substituting

$$A_s = a_s e^{i\varphi(z)/2} \tag{3.27}$$

$$A_i^* = a_i^* e^{-i\varphi(z)/2}. \tag{3.28}$$

After taking Laplace transforms in time, and using $-i\omega$ as the transform variable, we obtain

$$\frac{\partial \widetilde{a}_s}{\partial z} + i\left[\frac{1}{2}\kappa(z) - \frac{\omega}{v_s}\right]\widetilde{a}_s = i\gamma\widetilde{a}_i^* + \frac{1}{v_s}a_s(z,0) \tag{3.29}$$

$$\frac{\partial \widetilde{a}_i^*}{\partial z} - i\left[\frac{1}{2}\kappa(z) + \frac{\omega}{v_i}\right]\widetilde{a}_i^* = -i\gamma\widetilde{a}_s, \tag{3.30}$$

where $a_s(z,0)$ denotes once again the initial signal distribution. As before, we combine the two equations and introduce

$$\widetilde{a}_s = y_s \exp\left[\frac{i}{2}\left(\frac{1}{v_s} + \frac{1}{v_i}\right)\omega(z - z_0)\right] \tag{3.31}$$

$$\widetilde{a}_i^* = y_i^* \exp\left[\frac{i}{2}\left(\frac{1}{v_s} + \frac{1}{v_i}\right)\omega(z - z_0)\right]. \tag{3.32}$$

The equations describing the evolution of the waves are

$$\begin{aligned}\frac{d^2 y_s}{dz^2} &+ \left\{\frac{1}{4}\left[\kappa - \left(\frac{1}{v_s} - \frac{1}{v_i}\right)\omega\right]^2 + \frac{i}{2}\frac{d\kappa}{dz} - \gamma^2\right\} y_s \\ &= \frac{1}{v_s}\left[-i\left(\frac{1}{2}\kappa(z) + \frac{\omega}{v_i}\right)a_s(z,0) + \frac{d}{dz}a_s(z,0)\right] e^{-i(1/v_s + 1/v_i)\omega(z-z_0)/2}\end{aligned} \tag{3.33}$$

and

$$\begin{aligned}\frac{d^2 y_i}{dz^2} &+ \left\{\frac{1}{4}\left[\kappa - \left(\frac{1}{v_s} - \frac{1}{v_i}\right)\omega\right]^2 + \frac{i}{2}\frac{d\kappa}{dz} - \gamma^2\right\} y_i \\ &= i\frac{\gamma}{v_s}a_s^*(z,0)e^{i(1/v_s + 1/v_i)\omega(z-z_0)/2}.\end{aligned} \tag{3.34}$$

3.3.2 Homogeneous Solutions for the Linear Profile

In order to proceed with the calculation of the spatial evolution of the Fourier components, we need to assume a certain functional form for the wavenumber mismatch, $\kappa(z)$. In this chapter we consider linear phase-matched media, described by the profile

$$\kappa(z) = \kappa'(z - z_{pm0}). \tag{3.35}$$

In this expression, κ' is the dephasing rate (or chirp rate in the context of QPM technology), and z_{pm0} is the perfect phase-matching point at zero frequency detuning. Unless specified otherwise, we will assume that $\kappa' > 0$.

In the case of a uniform medium, the homogeneous solutions were exponentials. In a linear non-uniform medium, the homogeneous solutions of Eqs. (3.33) and (3.34) can be expressed in terms of parabolic cylinder functions. To see this, and to proceed with the calculation, it is convenient to introduce the normalized position, frequency and time, as follows:

$$\bar{z} = \sqrt{\kappa'}\,(z - z_{pm0}) \tag{3.36}$$

$$\bar{\omega} = \frac{|1/v_s - 1/v_i|\,\omega}{\sqrt{\kappa'}} \tag{3.37}$$

$$\bar{t} = \frac{\sqrt{\kappa'}\,t}{|1/v_s - 1/v_i|}. \tag{3.38}$$

In these coordinates, space is defined with respect to the phase-matching point z_{pm0}. The wavenumber mismatch takes the simple form $\kappa/\sqrt{\kappa'} = \bar{z}$, and the phase mismatch becomes $\varphi(\zeta) = \frac{1}{2}(\bar{z}^2 - \bar{z}_0^2)$. We also introduce the gain parameter,

$$\lambda = \frac{\gamma^2}{\kappa'}. \tag{3.39}$$

Finally, we define the shifted position,

$$\zeta = \bar{z} - \sigma\bar{\omega} \tag{3.40}$$

where $\sigma = 1$ if $1/v_s - 1/v_i > 0$ and -1 if $1/v_s - 1/v_i < 0$.

With these definitions, the homogeneous parts of Eqs. (3.33) and (3.34) can be written as

$$\frac{d^2y}{d\zeta^2} + \left(\frac{i}{2} - \lambda + \frac{1}{4}\zeta^2\right) y = 0, \tag{3.41}$$

the solutions of which are the parabolic cylinder functions $D_{i\lambda}(\pm\zeta e^{i\pi/4})$ and $D_{-1-i\lambda}(\pm\zeta e^{-i\pi/4})$. Since we are considering the co-propagating case, we must choose a pair of solutions which behave like two different waves as $\zeta \to +\infty$. Possible pairs are either one of $D_{i\lambda}(\pm\zeta e^{i\pi/4})$ with either one of $D_{-1-i\lambda}(\pm\zeta e^{-i\pi/4})$.

It is important to realize that the frequency does not appear explicitly in the solution, but only through the new space variable ζ. A shift in frequency amounts to

a displacement of the perfect phase-matching (PPMP) point from its initial position $\bar{z}_{pm0} = 0$ to $\bar{z}_{pm} = \sigma\bar{\omega}$.

3.3.3 Green's Functions in the Frequency Domain

As before, we consider the initial impulse $a_s(z, 0) = v_s\delta(z - z_0)$. Substitution into the right-hand-side term Eq. (3.33) gives the impulse driving the signal wave. Integrating twice over an infinitesimal region around the input position $\zeta = \zeta_0$ (and using the boundary condition $y_s \equiv 0$ for $\zeta < \zeta_0$) gives the initial values of y_s and its derivative:

$$y_s'(\zeta_0^+) = -i\zeta_0/2 \tag{3.42}$$

$$y_s(\zeta_0^+) = 1. \tag{3.43}$$

We choose the two homogeneous solutions

$$\Psi_1 = D_{i\lambda}(\zeta e^{i\pi/4}) \tag{3.44}$$

and

$$\Psi_2 = D_{-1-i\lambda}(-\zeta e^{-i\pi/4}), \tag{3.45}$$

which behave as forward- and backwards-propagating waves at $\zeta \to +\infty$. Their Wronskian is $W\{\Psi_1, \Psi_2\} = e^{-i\pi/4}e^{\pi\lambda/2}$. The linear combination of Ψ_1 and Ψ_2 satisfying the boundary conditions gives the frequency-domain representation of the Green's function:

$$\begin{aligned}\widetilde{G_s}(\bar{z}, \bar{\omega}) &= \frac{e^{-i\pi/4}}{W}\theta(\bar{z} - \bar{z}_0)\exp\left\{i\left[\frac{1}{4}\left(\bar{z}^2 - \bar{z}_0^2\right) + \frac{1}{2}\left|\frac{v_s + v_i}{v_s - v_i}\right|\sigma\bar{\omega}(\bar{z} - \bar{z}_0)\right]\right\} \\ &\quad \times \left[D_{-i\lambda}\left(-\zeta_0 e^{-i\pi/4}\right) D_{i\lambda}\left(\zeta e^{i\pi/4}\right)\right. \\ &\quad \left. + \lambda D_{i\lambda-1}\left(\zeta_0 e^{i\pi/4}\right) D_{-i\lambda-1}\left(-\zeta e^{-i\pi/4}\right)\right]. \end{aligned} \tag{3.46}$$

Similarly, the impulse response of the idler wave in the frequency domain is

$$\widetilde{G_i}(\bar{z}, -\bar{\omega}) = \frac{-i\lambda^{1/2}}{W}\theta(\bar{z} - \bar{z}_0)\exp\left\{i\left[\frac{1}{4}\left(\bar{z}^2 - \bar{z}_0^2\right) - \frac{1}{2}\left|\frac{v_s + v_i}{v_s - v_i}\right|\sigma\bar{\omega}(\bar{z} - \bar{z}_0)\right]\right\}$$

$$\times \left[D_{-i\lambda-1}\left(-\zeta_0 e^{-i\pi/4}\right) D_{i\lambda}\left(\zeta e^{i\pi/4}\right) \right.$$
$$\left. -D_{i\lambda}\left(\zeta_0 e^{i\pi/4}\right) D_{-i\lambda-1}\left(-\zeta e^{-i\pi/4}\right) \right]. \tag{3.47}$$

The spatial evolution of each Fourier component can be better understood by looking at the asymptotic behavior of the parabolic cylinder functions [34], assuming a large gain $\lambda \gg 1$. *Before* the PPMP, namely for $\zeta_0 < \zeta \ll 0$, we have

$$\begin{aligned} \widetilde{G_s} &\sim e^{i\frac{\bar{\omega}}{|1/v_s - 1/v_i|}\left(\frac{\zeta-\zeta_0}{v_s}\right)} e^{i\lambda \ln|\zeta/\zeta_0|} \\ &\quad \times \left[1 - \frac{\lambda}{|\zeta_0 \zeta|} e^{-2i\lambda \ln|\zeta/\zeta_0|} e^{i\left(\zeta^2-\zeta_0^2\right)/2} \right] \end{aligned} \tag{3.48}$$

$$\begin{aligned} \widetilde{G_i} &\sim \lambda^{1/2} e^{i\left(\bar{z}^2-\bar{z}_0^2\right)/2} e^{-i\frac{\bar{\omega}}{|1/v_s - 1/v_i|}\left(\frac{\zeta-\zeta_0}{v_s}\right)} \\ &\quad \times \left[\frac{1}{|\zeta|}\left|\frac{\zeta}{\zeta_0}\right|^{-i\lambda} - \frac{1}{|\zeta_0|}\left|\frac{\zeta}{\zeta_0}\right|^{-\lambda} e^{-i\left(\zeta^2-\zeta_0^2\right)/2} \right] \end{aligned} \tag{3.49}$$

In other words, before the PPMP the signal is essentially a plane wave propagating at phase velocity v_s, affected by a modulation of small amplitude $\lambda/|\zeta_0\zeta|$ oscillating rapidly at the rate of the phase mismatch $\varphi = \frac{1}{2}(\zeta^2 - \zeta_0^2)$. The idler remains small, of the order of $\lambda^{1/2}/|\zeta|$. As it propagates towards the PPMP (i.e. when $1/|\zeta| \gg 1/|\zeta_0|$), it behaves like a plane-wave propagating at the *signal* velocity v_s.

After the PPMP, i.e. for $\zeta_0 \ll 0$ and $\zeta \gg 0$, the waves behave as follows:

$$\begin{aligned} \widetilde{G_s} &\sim e^{\pi\lambda} e^{i\frac{\bar{\omega}}{|1/v_s - 1/v_i|}\left(\frac{\zeta-\zeta_0}{v_s}\right)} e^{i\lambda \ln|\zeta/\zeta_0|} \\ &\quad \times \left[1 + i\frac{\lambda^{1/2}}{|\zeta_0|} e^{-i\lambda\left[\ln\left(\lambda/\zeta_0^2\right)-1\right]} e^{-i\zeta_0^2/2} \right] \\ &\quad \times \left[1 - i\frac{\lambda^{1/2}}{|\zeta|} e^{i\lambda\left[\ln\left(\lambda/\zeta^2\right)-1\right]} e^{i\zeta^2/2} \right] \end{aligned} \tag{3.50}$$

$$\begin{aligned} \widetilde{G_i} &\sim i e^{\pi\lambda} e^{i\bar{\omega}^2/2} e^{-i\frac{\bar{\omega}}{|1/v_s - 1/v_i|}(\zeta/v_i - \zeta_0/v_s)} e^{-i\zeta_0^2/2} e^{i\lambda \ln(|\zeta/\zeta_0|/\lambda)} \\ &\quad \times \left[1 - i\frac{\lambda^{1/2}}{|\zeta_0|} e^{i\lambda\left[\ln\left(\lambda/\zeta_0^2\right)-1\right]} e^{i\zeta_0^2/2} \right] \\ &\quad \times \left[1 - i\frac{\lambda^{1/2}}{|\zeta|} e^{i\lambda\left[\ln\left(\lambda/\zeta^2\right)-1\right]} e^{i\zeta^2/2} \right] \end{aligned} \tag{3.51}$$

The key point is that both waves are amplified by $e^{\pi\lambda}$, the Rosenbluth gain factor

[32]. The factors in square brackets are small modulations, of the order of $\lambda^{1/2}/|\zeta|$ and $\lambda^{1/2}/|\zeta_0|$, which depend on the position of the PPMP with respect to the edges of the medium. Those oscillations are due to the finite length of the system; they vanish in the limit of an infinitely long medium. The idler wave experiences dispersion, through the quadratic phase term $-\frac{1}{2}\bar{\omega}^2 = -\frac{1}{2}\left(1/v_s - 1/v_i\right)^2 \omega/\kappa'$. The physical origin of this dispersion is that the idler wave effectively travels at the *signal* velocity before the PPMP and at the *idler* velocity thereafter. This results in frequency dispersion because the position of the PPMP is itself frequency-dependent.

3.3.4 Green's function in the Time Domain

In the previous section we have obtained the representation of the Green's functions in the frequency domain. In this section we derive its time-domain representation. In other words, we evaluate

$$G_s(\bar{z},\bar{t}) = \frac{1}{2\pi}\frac{\sqrt{\kappa'}}{|1/v_s - 1/v_i|}\int_{-\infty+i\epsilon}^{+\infty+i\epsilon} \widetilde{G_s}(\bar{z},\bar{\omega})e^{-i\bar{\omega}\bar{t}}d\bar{\omega} \tag{3.52}$$

where $\widetilde{G_s}$ is given by Eq. (3.46) and the contour is taken above the real axis.

We use the following integral representation for the parabolic cylinder function [34, 48]:

$$D_\nu(x) = \frac{1}{i\sqrt{2\pi}}e^{x^2/4}\int_{-i\infty}^{i\infty} e^{-xp+p^2/2}p^\nu dp, \tag{3.53}$$

with the contour taken to the right of the imaginary axis. This representation has the advantage of being valid for all values of the parameter ν. The remainder of the derivation can be found in Refs. [39, 40]. We substitute these integrals into the expression for $\widetilde{G}_s$, Eq. (3.46), labeling the integration variables by p and q, then substitute into (3.52) and exchange the order of integration. The expression now consists of two terms (corresponding to the two terms in the curly brackets of Eq. (3.46)), each involving a triple integral in $\bar{\omega}$, p, and q.

This is the point in the calculation where the positions with respect to the wave fronts intervene. To this end, we introduce the normalized travel times of the signal

and idler wave fronts:

$$\bar{t}_s = \frac{\sqrt{\kappa'}}{|1/v_s - 1/v_i|}\left(\frac{z - z_0}{v_s}\right) \tag{3.54}$$

$$\bar{t}_i = \frac{\sqrt{\kappa'}}{|1/v_s - 1/v_i|}\left(\frac{z - z_0}{v_i}\right). \tag{3.55}$$

We also define the delays with respect to the wave fronts:

$$U_s = \begin{cases} \bar{t}_s - \bar{t}, & \text{if } v_s < v_i \\ \bar{t} - \bar{t}_s, & \text{if } v_s > v_i \end{cases} \tag{3.56}$$

$$U_i = \begin{cases} \bar{t} - \bar{t}_i, & \text{if } v_s < v_i \\ \bar{t}_i - \bar{t}, & \text{if } v_s > v_i \end{cases}. \tag{3.57}$$

These delays correspond to V_s and V_i, defined in our discussion of the uniform medium, Eqs. (3.14) and (3.15). As before, U_s and U_i are both positive between the wave fronts (i.e. for $\bar{t}_s < \bar{t} < \bar{t}_i$ if $v_s > v_i$ or $\bar{t}_i < \bar{t} < \bar{t}_s$ if $v_s < v_i$).

Armed with these definitions, we can evaluate the integrals in $\bar{\omega}$. The first one yields $2\pi\delta(q + p - U_i)$, the second one $2\pi\delta(q + p + U_s)$. These delta functions render straightforward the subsequent evaluation of the integrals in q.

At this point we are left with two integrals in p. The rest of the calculation is similar to that of the uniform medium. Closing the contours, we find the values of $\bar{t}$ for which these integrals are non-zero. Ultimately we obtain the following expression for the signal Green's function:

$$\begin{aligned} G_s(\bar{z}, \bar{t}) = \frac{\sqrt{\kappa'}}{|1/v_s - 1/v_i|}\Bigg[&\delta(U_s) - \frac{\lambda}{2\pi}\frac{\theta(U_s U_i)}{U_s} e^{iU_s(\bar{z}+\bar{z}_0)/2} \\ &\times \oint e^{iU_s U_i p}\left(\frac{p - 1/2}{p + 1/2}\right)^{i\lambda} \frac{dp}{(p - 1/2)(p + 1/2)}\Bigg], \end{aligned} \tag{3.58}$$

where the closed contour is taken around the branch cut going from $-1/2$ to $1/2$. An equivalent expression, sometimes more convenient because it does not involve the

singularity at $U_s = 0$, can be obtained by integration by parts:

$$\begin{aligned} G_s(\bar{z},\bar{t}) &= \frac{\sqrt{\kappa'}}{|1/v_s - 1/v_i|}\left[\delta(U_s) + \frac{1}{2\pi}\theta(U_s U_i)\, U_i\, e^{iU_s(\bar{z}+\bar{z}_0)/2}\right. \\ &\quad \left. \times \oint e^{iU_s U_i p}\left(\frac{p-1/2}{p+1/2}\right)^{i\lambda} dp\right]. \end{aligned} \tag{3.59}$$

The Green's function for the idler wave can be obtained in a similar manner:

$$\begin{aligned} G_i(\bar{z},\bar{t}) &= \frac{\sqrt{\kappa'}}{|1/v_s - 1/v_i|}\frac{\sqrt{\lambda}}{2\pi}\,\theta(U_s U_i)\, e^{iU_i(\bar{z}+\bar{z}_0)/2} \\ &\quad \times \oint e^{iU_s U_i p}\left(\frac{p-1/2}{p+1/2}\right)^{i\lambda}\frac{dp}{p+1/2}. \end{aligned} \tag{3.60}$$

These integral representations of the Green's functions involve the time delays with respect to the wave fronts $\bar{t}_s$ and $\bar{t}_s$, the gain parameter λ but also the position with respect to the PPMP. The appearance of the term $\bar{z} + \bar{z}_0$ in the phase factor underlines the fact that the medium is non-uniform (if it were uniform, then space would enter only through functions of $\bar{z} - \bar{z}_0$).

The result being expressed in terms of an integral over the complex plane, additional work is required to understand its behavior and extract its physical meaning. One can rewrite it in terms of special functions, calculate it numerically or evaluate it asymptotically in various regimes. Each one of these approaches will be taken in the following sections.

3.3.5 Transition to the Uniform-Medium Limit

The transition to the two regimes must be treated carefully because the uniform medium is a singular limit of the linear profile. (We cannot simply substitute $\kappa' = 0$ in the expressions, for in this case $\lambda = \infty$ and $U_s = U_i = 0$.)

We first make the dependence on the dephasing rate explicit by extracting κ' from the normalizations; we make use of the delays $V_{s,i} = U_{s,i}|\delta v|/2\sqrt{\kappa'}$ defined in the context of the uniform medium. Starting from the integral representation (3.58), we make the substitution $p = p'/\kappa'$. With this transformation, we can write

$[(p-1/2)/(p+1/2)]^{i\lambda} = \exp\{i(\gamma^2/\kappa')\ln[1-\kappa'/p' + O(\kappa'^2)]\}$. We can expand the logarithm in powers of κ', and then take the limit $\kappa' \to 0$. Using the substitution $p' = -i|\delta v|\gamma u/2\sqrt{V_s V_i}$ gives rise to the integral

$$\oint e^{\frac{1}{2}|\delta v|\gamma\sqrt{V_s V_i}(u+1/u)}\frac{du}{u^2}, \tag{3.61}$$

which is nothing but an integral representation for the modified Bessel function I_1. Thus we recover the Green's function for the signal wave in the case of a uniform medium, Eqs (3.17) and (3.19).

3.3.6 Counter-Propagating Waves

In our discussion of the uniform medium, we saw that the counter-propagating case can be recovered by inverting the sign of one of the velocities and of γ^2 (or, in this case, λ). Therefore, upon inversion of the direction of the idler wave, the Green's functions are

$$\begin{aligned} G_s(\bar{z},\bar{t}) &= \frac{\sqrt{\kappa'}}{|1/v_s - 1/v_i|}\left[\delta(U_s) + \frac{1}{2\pi}\theta(U_s U_i)\, U_i\, e^{iU_s(\bar{z}+\bar{z}_0)/2}\right. \\ &\quad \left. \times \oint e^{iU_s U_i p}\left(\frac{p-1/2}{p+1/2}\right)^{i\lambda} dp\right]. \end{aligned} \tag{3.62}$$

$$\begin{aligned} G_i(\bar{z},\bar{t}) &= \frac{\sqrt{\kappa'}}{|1/v_s - 1/v_i|}\frac{\sqrt{\lambda}}{2\pi}\,\theta(U_s U_i)\, e^{-iU_i(\bar{z}+\bar{z}_0)/2} \\ &\quad \times \oint e^{iU_s U_i p}\left(\frac{p-1/2}{p+1/2}\right)^{i\lambda}\frac{dp}{p-1/2}, \end{aligned} \tag{3.63}$$

where the delay relative to the wave fronts are now defined as

$$U_s = \bar{t} - \bar{t}_s, \tag{3.64}$$

$$U_i = \bar{t} - \bar{t}_i, \tag{3.65}$$

with

$$\bar{t}_i = -\frac{\sqrt{\kappa'}}{|1/v_s - 1/v_i|}\left(\frac{z-z_0}{v_i}\right). \tag{3.66}$$

Except for the location of the wave fronts, the behavior of the Green's functions in the co- and counter-propagating situations is essentially the same. The character of the instability will be examined in the following section.

3.3.7 Character of the Instability

The nature of the instability can be determined by considering the Fourier representation of the Green's functions, $\widetilde{G_s}$ and $\widetilde{G_i}$, Eqs. (3.46) and (3.47). The parabolic cylinder functions yield integrals of the form

$$\int_{-i\infty}^{i\infty} e^{(\bar{z}_0-\sigma\bar{\omega})e^{-i\pi/4}p+p^2/2}p^{-i\lambda}dp. \tag{3.67}$$

In the case of counter-propagating waves, the sign of λ must be inverted.

Let us recall our discussion of the uniform medium. In that case, the value of the k-integral was determined by the poles in the integrand. In the present case, there are no poles; instead, the behavior of the p-integral is determined by the saddle points, located at

$$p_\pm = \frac{1}{2}\sigma\bar{\omega}e^{-i\pi/4} \pm \frac{e^{-i\pi/4}}{2}\sqrt{\bar{\omega}^2-4\lambda} \tag{3.68}$$

in the co-propagating case, and

$$p_\pm = \frac{1}{2}\sigma\bar{\omega}e^{-i\pi/4} \pm \frac{e^{-i\pi/4}}{2}\sqrt{\bar{\omega}^2+4\lambda} \tag{3.69}$$

in the counter-propagating case. When the $\bar{\omega}$-contour is taken far above the real axis, the trajectories of the saddle points are well separated. As the $\bar{\omega}$-contour is lowered towards the real axis, the saddle points come closer to each other. They merge when $\bar{\omega} = \pm 2\sqrt{\lambda}$ in the co-propagating case, and $\bar{\omega} = i2\sqrt{\lambda}$ in the counter-propagating case. Those are precisely the values for which pole pinching occurs in the case of a uniform medium. The difference is that the crossing of saddle points does not lead to a singularity; it does not impose a limit to the value of $\mathrm{Im}(\bar{\omega})$. The $\bar{\omega}$-contour can be lowered all the way down to the real axis. Therefore, regardless of the relative propagation directions, the perturbation remains bounded since $\mathrm{Im}(\bar{\omega}) = 0$;

the instability is convective.

The transition to the uniform medium is a singular limit. As long as $\kappa' > 0$, the integrand contains saddle points which can merge without imposing a limit to $\mathrm{Im}(\bar{\omega})$: the instability is convective. However, as κ' is reduced (λ is increased), the saddle points become more strongly peaked. When $\kappa' = 0$, the saddle points become singularities; they cannot cross. This imposes a limit to the value of $\mathrm{Im}(\bar{\omega})$. In the case of counter-propagating waves, $\mathrm{Im}(\omega) > 0$ and the instability is absolute. In the case of co-propagating waves, $\mathrm{Im}(\omega) = 0$ and the instability is convective.

The fact that the character of the instability changes abruptly from absolute to convective as soon as $\kappa' > 0$ is introduced is counterintuitive. In fact, the linear profile is an exceptional case; in general, the instability is absolute in a counter-propagating geometry [49]. For instance, the absolute character of the instability is recovered when a quadratic [32] or random [50] perturbation is superposed to a linear profile, or when the pump wave is spatially localized [51].

3.3.8 Alternative Representations for the Green's Functions

We expressed the Green's functions in terms of integrals over a closed contour in the complex plane. These forms present the advantage that the contour of integration can be adapted to a particular method of evaluation, for example to facilitate numerical integration or make possible asymptotic evaluation. Alternative representations have been proposed in the literature and are reviewed here.

Rosenbluth, White and Liu [40] gave their solutions in terms of an integral over the real axis. This form can be obtained by collapsing the contour along the branch cut ranging from $-1/2$ to $1/2$. On the segments above and below the cut, the integrand gives rise to factors of $e^{\mp\pi\lambda}$, respectively. Redefining the integration variable, we can write the Green's functions in terms of integrals ranging from 0 to 1:

$$\begin{aligned} G_s &= \frac{\sqrt{\kappa'}}{|1/v_s - 1/v_i|}\left[\delta(U_s) + \frac{\sinh \pi\lambda}{\pi}\theta(U_s U_i)\, U_i\, e^{iU_s(\bar{z}+\bar{z}_0)/2} e^{-iU_s U_i/2}\right. \\ &\quad \left. \times \int_0^1 e^{iU_s U_i p}\left(\frac{1-p}{p}\right)^{i\lambda} dp\right], \end{aligned} \tag{3.70}$$

$$G_i = \frac{\sqrt{\kappa'}}{|1/v_s - 1/v_i|}\sqrt{\lambda}\,\frac{\sinh \pi\lambda}{\pi}\,\theta(U_sU_i)\,e^{iU_i(\bar{z}+\bar{z}_0)/2}e^{-iU_sU_i/2} \times \int_0^1 e^{iU_sU_ip}\left(\frac{1-p}{p}\right)^{i\lambda}\frac{dp}{p}. \tag{3.71}$$

This is the form given in Eq. (8) of Ref. [40].

Short and Simon [41] pointed out that the integral appearing in Eqs. (3.70) and (3.71) are in fact confluent hypergeometric functions, an integral representation of which is [48]

$$\Phi(\beta,\gamma,x) = \frac{\Gamma(\gamma)}{\Gamma(\beta)\Gamma(\gamma-\beta)}\int_0^1 (1-s)^{\gamma-\beta-1}s^{\beta-1}e^{sx}ds. \tag{3.72}$$

Using this definition, we can rewrite the Green's functions as

$$G_s = \frac{\sqrt{\kappa'}}{|1/v_s - 1/v_i|}\left[\delta(U_s) + \lambda\theta(U_sU_i)\,U_i\,e^{iU_s(\bar{z}+\bar{z}_0)/2}e^{-iU_sU_i/2}\,\Phi(1-i\lambda,2,iU_sU_i)\right] \tag{3.73}$$

$$G_i = \frac{\sqrt{\kappa'}}{|1/v_s - 1/v_i|}\,i\sqrt{\lambda}\,\theta(U_sU_i)\,e^{iU_i(\bar{z}+\bar{z}_0)/2}e^{-iU_sU_i/2}\,\Phi(-i\lambda,1,iU_sU_i). \tag{3.74}$$

Alternatively, we can express the solutions in terms of generalized Laguerre functions:

$$G_s = \frac{\sqrt{\kappa'}}{|1/v_s - 1/v_i|}\left[\delta(U_s) - i\theta(U_sU_i)\,U_i\,e^{iU_s(\bar{z}+\bar{z}_0)/2}e^{-iU_sU_i/2}\,L^1_{i\lambda-1}(iU_sU_i)\right] \tag{3.75}$$

$$G_i = \frac{\sqrt{\kappa'}}{|1/v_s - 1/v_i|}\,i\sqrt{\lambda}\,\theta(U_sU_i)\,e^{iU_i(\bar{z}+\bar{z}_0)/2}e^{-iU_sU_i/2}\,L_{i\lambda}(iU_sU_i). \tag{3.76}$$

3.3.9 Approximate Expressions for the Green's Functions

In section 3.3.4 we obtained the exact solutions for the Green's functions. However the integral representation does not lend itself to an immediate interpretation. We need to examine the behavior of the integral in various regimes in order to understand the solution.

We distinguish three cases, depending on the relative magnitude of the product U_sU_i and the gain parameter λ. Note that the quantity U_sU_i represents the position

inside the pulse. Using the definitions (3.56) and (3.57), it can be written as $(\bar{t}_s - \bar{t})(\bar{t} - \bar{t}_i)$, which is a parabola in time centered at the mean position $(\bar{t}_s + \bar{t}_i)/2$ and reaching zero at the wave fronts $\bar{t}_s$ and $\bar{t}_i$, as shown in Fig. 3.3.

Whether we are interested in investigating the behavior of G_s or G_i using expressions (3.58), (3.59) or (3.60), we have to evaluate integrals of the form $\oint e^{\rho(p)} f(p) dp$, where

$$\rho(p) = iU_s U_i p + i\lambda \ln\left(\frac{p - 1/2}{p + 1/2}\right). \tag{3.77}$$

The three regimes examined below are distinguished by the location of the saddle points of $\rho(p)$, given by

$$p_\pm = \pm\frac{1}{2}\sqrt{1 - \frac{4\lambda}{U_s U_i}}. \tag{3.78}$$

Their trajectory is shown in Fig. 3.2. When $U_s U_i \ll 4\lambda$, the saddle points are purely imaginary and located far on either side of the real axis. As the value of $U_s U_i$ increases, they move towards the real axis, and they meet at the origin when $U_s U_i = 4\lambda$. As the value of $U_s U_i$ increases further, the saddle points become real and they move apart towards to the branch points $\pm 1/2$ as $U_s U_i \gg 4\lambda$.

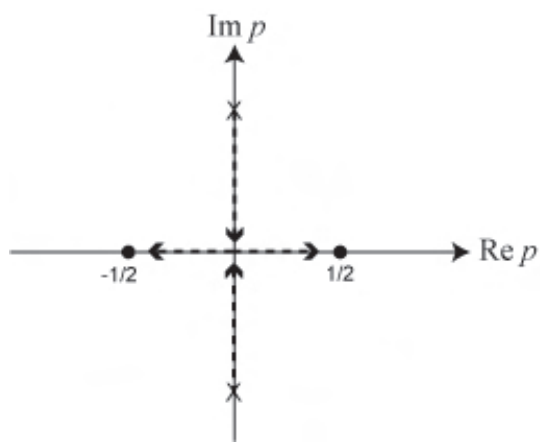

Figure 3.2: Trajectory of the saddle points in the complex plane as $U_s U_i$ goes from 0 to ∞.

The nature of the saddle points dictates the local behavior of the Green's functions. Close to the wave fronts ($U_s U_i \ll 4\lambda$), the saddle points are imaginary and the waves grow exponentially. Conversely, away from the wave fronts ($U_s U_i \gg 4\lambda$), the saddle

points are real and the amplification is saturated. This situation is depicted in Fig. 3.3.

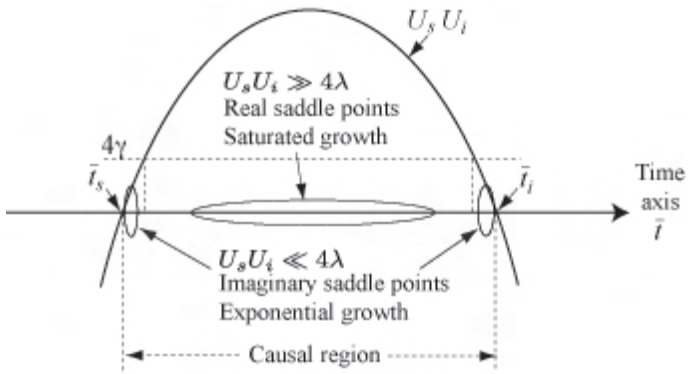

Figure 3.3: Nature of saddle points and local behavior of the Green's function as a function of position inside the causal region. $\bar{t}_s$ and $\bar{t}_i$ are the wave front arrival times, defined by Eqs. (3.54) and (3.55). U_s and U_i are the delays with respect to the wave fronts, defined by Eqs. (3.56) and (3.57).

Case 1: $U_s U_i \ll 4\lambda$

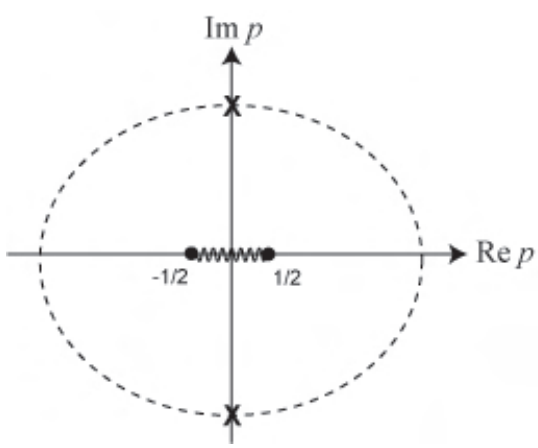

Figure 3.4: Steepest descent contour in the regime $U_s U_i \ll 4\lambda$.

As the value of $U_s U_i$ increases from zero, the saddle points move from $\pm i\infty$ towards the origin. The contour can be deformed in a loop passing through the saddle points, as shown in Fig. 3.4, and for $0 \ll U_s U_i \ll 4\lambda$ the integral can be evaluated using

the steepest descent method. We find the following approximations for the Green's functions:

$$G_s \approx \frac{\sqrt{\kappa'}}{|1/v_s - 1/v_i|}\frac{1}{2\sqrt{\pi}}\left(\frac{\lambda U_i}{U_s^3}\right)^{1/4} e^{iU_s(\bar{z}+\bar{z}_0)/2} e^{2\sqrt{\lambda U_s U_i}}, \qquad (0 \ll U_s U_i \ll 4\lambda) \tag{3.79}$$

$$G_i \approx \frac{\sqrt{\kappa'}}{|1/v_s - 1/v_i|}\frac{i}{2\sqrt{\pi}}\left(\frac{\lambda}{U_s U_i}\right)^{1/4} e^{iU_i(\bar{z}+\bar{z}_0)/2} e^{2\sqrt{\lambda U_s U_i}}, \qquad (0 \ll U_s U_i \ll 4\lambda) \tag{3.80}$$

Except for the phase factors, these expressions are identical to the asymptotic behavior of the Green's functions in uniform media, Eqs. (3.17) and (3.19), for $2\gamma\sqrt{V_s V_i}$ large. Thus in the regime $U_s U_i \ll 4\lambda$ the dephasing due to the non-uniformity of the medium is still unimportant and the wave amplitudes grow exponentially. However, when $U_s U_i \gtrsim 4\lambda$ the amplification saturates and the pulse enters a regime where the dephasing dominates.

Case 2: $U_s U_i \gg 4\lambda$

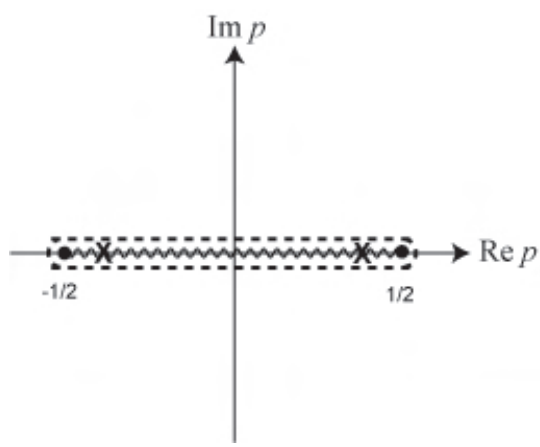

Figure 3.5: Stationary phase contour in the regime $U_s U_i \gg 4\lambda$.

In the middle of the pulse, where $U_s U_i \gg 4\lambda$, the saddle points are located on the real axis and tend towards the branch points at $\pm 1/2$. The contour can be collapsed around the cut as shown in Fig. 3.5 and the integrals can be evaluated asymptotically using the stationary phase method. The contributions from the lower side of the cut then dominate the value of the integral.

In the case of the signal wave, the two saddle points yield contributions which are complex conjugates; the signal Green's function is oscillatory:

$$\begin{aligned} G_s &\approx \frac{\sqrt{\kappa'}}{|1/v_s - 1/v_i|}\sqrt{\frac{2\lambda}{\pi}}\,\frac{1}{U_s}e^{\pi\lambda}e^{iU_s(\bar{z}+\bar{z}_0)/2} \\ &\quad \times \cos\left\{\frac{U_sU_i}{2} - \lambda\left[\ln\left(\frac{U_sU_i}{\lambda}\right)+1\right] - \frac{\pi}{4}\right\}, \qquad (U_sU_i \gg 4\lambda). \end{aligned} \tag{3.81}$$

Due to the factor $1/U_s$, the amplitude of G_s increases as $\bar{t} \to \bar{t}_s$ and reaches its maximum in the region where $U_sU_i \sim 4\lambda$. Therefore we also need to develop an approximation valid in the transition region.

In the case of the idler, the contribution from the saddle point p_- dominates. The idler Green's function has essentially constant magnitude with some modulation added to it:

$$\begin{aligned} G_i &\approx \frac{\sqrt{\kappa'}}{|1/v_s - 1/v_i|}\frac{1}{\sqrt{2\pi}}e^{\pi\lambda}e^{iU_i(\bar{z}+\bar{z}_0)/2} \\ &\quad \times \exp\left\{-i\frac{U_sU_i}{2} + i\lambda\left[\ln\left(\frac{U_sU_i}{\lambda}\right)+1\right] + i\frac{\pi}{4}\right\} \\ &\quad \times \left(1 - \frac{i\lambda}{U_sU_i}\exp\left\{iU_sU_i - 2i\lambda\left[\ln\left(\frac{U_sU_i}{\lambda}\right)+1\right]\right\}\right), \qquad (U_sU_i \gg 4\lambda). \end{aligned} \tag{3.82}$$

In this regime the signal and idler waves reach their maximum amplitudes, given by the Rosenbluth gain factor $e^{\pi\lambda}$. The amplification saturates because the non-uniformity of the medium brings the interaction out of phase-matching.

Case 3: $U_sU_i \sim 4\lambda$

As mentioned earlier, the signal Green's function reaches its maximum amplitude close to the signal wavefront, in a region where $U_sU_i \sim 4\lambda$. It is important to obtain an approximation valid in this transitional regime.

When $U_sU_i \to 4\lambda$, the two saddle points merge at the origin. The integrals cannot be evaluated asymptotically; we have to adopt a different strategy. Since the value of the integral is dominated by the behavior of the integrand around the origin we can expand $\rho(p)$ around $p = 0$ and collapse the contour around the branch cut. Then the

contribution from the bottom of the cut dominates and we obtain the integral

$$\int_{-\infty}^{\infty} \exp\left[i\left(U_s U_i - 4\lambda\right)p - \frac{16}{3}i\lambda p^3\right] dp, \tag{3.83}$$

which can be rewritten in terms of an Airy function using the substitution $p = (16\lambda)^{-1/3}u$. Thus the signal Green's function is approximately given by

$$G_s \approx \frac{\sqrt{\kappa'}}{|1/v_s - 1/v_i|}\frac{1}{2(2\lambda)^{1/3}}e^{\pi\lambda}U_i e^{iU_s(\bar{z}+\bar{z}_0)/2}\mathrm{Ai}\left[\frac{4\lambda - U_s U_i}{2(2\lambda)^{1/3}}\right], \qquad (U_s U_i \sim 4\lambda). \tag{3.84}$$

The Airy function ensures the transition between exponential to oscillatory behavior as $U_s U_i$ goes from $\ll 4\lambda$ to $\gg 4\lambda$.

3.3.10 Numerical Evaluation of the Green's Functions

Various means of approaching the integral representation of the Green's functions were outlined at the end of section 3.3.4. In section 3.3.8, the integrals were written in terms of known special functions; in section 3.3.9 they were evaluated approximately. In this section we calculate them numerically and show plots of their time evolution.

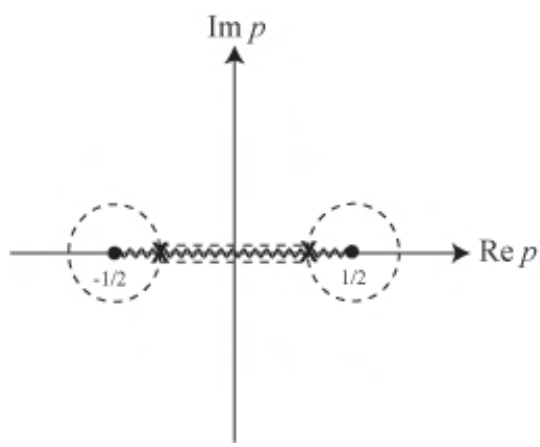

Figure 3.6: Contour for numerical integration.

The integrals in question here must be handled carefully since the integrand oscillates infinitely rapidly at the branch points. We can make use of the flexibility offered

by the integral representations (3.58), (3.59) and (3.60) to choose a contour which avoids this difficulty. An example of such contour is the dumbbell shape shown in Fig. 3.6. If $U_s U_i$ is large enough, the radius of the circles around the branch points can be chosen such that the contour goes through the saddle point. In any case it is possible to adjust the sampling along the path to resolve the oscillations of the integrand. One can also use the asymptotic representation for large values of $U_s U_i$.

Fig. 3.7 shows a numerical example with various input and output positions and compares it with the analytical approximations developed in section 3.3.9. As expected from the asymptotic analysis, the agreement becomes better as $\bar{z}_0 \to -\infty$ and $\bar{z} \to \infty$.

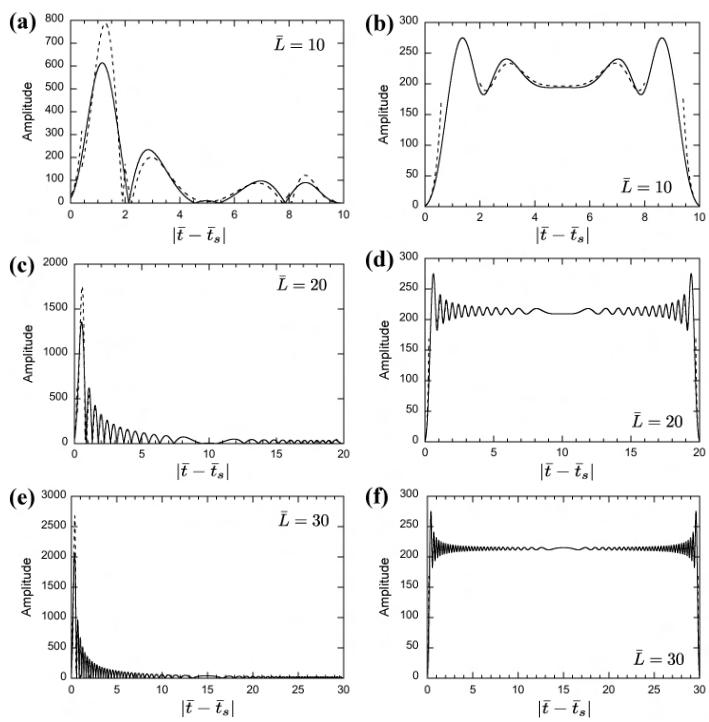

Figure 3.7: Signal (left) and idler (right) Green's functions calculated numerically (solid lines), and comparison with the asymptotic expressions developed in section 3.3.9 (dashed lines). The gain parameter is $\lambda = 2$. The input and output positions are (a,b) $z_0 = -5$, $z = 5$; (c,d) $z_0 = -10$, $z = 10$, (e,f) $z_0 = -15$, $z = 15$.

3.4 Amplified Pulses

The first half of this chapter was concerned with solving for and understanding the behavior of the Green's functions for the signal and idler waves. In this section we use them to calculate the amplified waves, given various initial pulse shapes.

The Laplace transform technique used to solve the space-time evolution equations is ideally suited for initial-value problems. However, in the case of optical parametric amplification we are in presence of a boundary-value problem since we have knowledge of the incident waves at the input facet of the nonlinear crystal at any given time. The solution procedure consists of decomposing the input pulse, $A(z_0, t) \equiv A_{s0}(t)$, into a continuous sum of impulses delayed in time, $\int A_{s0}(t')\delta(t-t')dt'$. The evolution of each impulse is given by the Green's functions. Thus we are left with summing up their contributions. In other words, our goal is to evaluate the following convolution integrals:

$$A_s(\bar{z}, \bar{t}) = \frac{|1/v_s - 1/v_i|}{\sqrt{\kappa'}} \int_{-\infty}^{\infty} A_{so}(\bar{t} - \bar{t}')G_s(\bar{z}, \bar{z}_0, \bar{t}')d\bar{t}' \tag{3.85}$$

$$A_i(\bar{z}, \bar{t}) = \frac{|1/v_s - 1/v_i|}{\sqrt{\kappa'}} \int_{-\infty}^{\infty} A^*_{so}(\bar{t} - \bar{t}')G_i(\bar{z}, \bar{z}_0, \bar{t}')d\bar{t}'. \tag{3.86}$$

We will consider the cases of long and short input pulses. The distinction between the two is defined with respect to the delay accumulated between the signal and idler wave fronts $|\bar{t}_s - \bar{t}_i| = \bar{z}_L - \bar{z}_0 \equiv \bar{L}$ (here $\bar{z}_L$ denotes the end position).

3.4.1 Long Pulses

We consider long initial signal pulses, and allow for a frequency shift $\delta\omega$ with respect to the carrier frequency. The input pulse can be written

$$A_{s0}(\bar{t}) = B_{s0}(\bar{t})e^{-i\delta\bar{\omega}\bar{t}}, \tag{3.87}$$

where the envelope B_{s0} is a smooth function which varies slowly compared to the group delay between the signal and idler wave fronts, $|\bar{t}_s - \bar{t}_i| = \bar{z}_L - \bar{z}_0 = \bar{L}$.

The details of the calculation are given in the Appendix at the end of this chapter,

section 3.6. The final expression shown in Eq. (3.102) in the case of the signal and Eq. (3.103) in the case of the idler. Except for correction terms which vanish in the infinite medium limit, the output pulse is essentially an amplified replica of the input, given by

$$A_s \approx A_{s0}(\bar{t} - \bar{t}_s)e^{\pi\lambda}e^{i\lambda \ln|\zeta/\zeta_0|}, \tag{3.88}$$

$$A_i \approx iA^*_{s0}(\bar{t} - \bar{t}_{si})e^{\pi\lambda}e^{i\lambda[\ln(|\zeta\zeta_0|/\lambda)+1]}e^{-i\zeta_0^2/2}. \tag{3.89}$$

Here, ζ and ζ_0 are the positions with respect to the frequency-dependent phase-matching point: $\zeta = \bar{z} - \delta\bar{\omega}$.

As expected, the waves are amplified by the Rosenbluth gain factor, $e^{\pi\lambda} = e^{\pi\gamma^2/|\kappa'|}$. The delay of the signal pulse is simply the travel time at the signal velocity, $t_s = L/v_s$. On the other hand, the delay of the idler pulse is the sum of the delays associated with propagation at the *signal* velocity *before* the prefect phase-matching point (PPMP) and at the *idler* velocity *after* the PPMP: $t_{si} = (z_{pm} - z_0)/v_s + (z_L - z_{pm})/v_i$.

The phase is the feature for which signal and idler are most different. The signal is amplified with very little phase accumulation: at the center of the passband (i.e. assuming $\bar{z} = -\bar{z}_0$ and small $\delta\bar{\omega}$), the phase of the signal wave is $\phi_s = \lambda \ln|\zeta/\zeta_0| \approx -4\delta\bar{\omega}/\bar{L}$, corresponding to a small linear phase with $d\phi_s/d\delta\omega = 4\lambda|1/v_s - 1/v_i|/\kappa' L$, which vanishes in the limit of a long medium. On the other hand, the phase of the idler is $\phi_i \approx -\zeta_0^2/2 = -(\bar{z}_0 - \delta\bar{\omega})^2/2$. This quadratic phase is associated with group delay dispersion, with a coefficient $d^2\phi_i/d\delta\omega^2 = -(1/v_s - 1/v_i)^2/\kappa'$. The idler suffers dispersion because its group delay t_{si} depends on the position of the PPMP, which is itself a function of frequency.

We can also calculate the bandwidth of the amplifier. Significant amplification is possible only if the PPMP remains inside the grating. This limits the maximum frequency shift allowed: $\zeta < \bar{L}$, $|\zeta_0| < \bar{L}$. Therefore the bandwidth is simply $\Delta\bar{\omega}_{BW} = \bar{L}$; in real units, with the definitions given in Eqs. (3.36) and (3.37), it is

$$\Delta\omega_{BW} = \frac{|\kappa'|L}{|1/v_s - 1/v_i|}, \tag{3.90}$$

in agreement with Eq. (2.35) of chapter 2. As expected, increasing the grating length or the chirp rate increases the amplification bandwidth.

This discussion has ignored the presence of small corrections, which are derived in detail in section 3.6. Those terms describe the effect of the finite length of the system and are due to the fact that the interaction is turned on and off abruptly at the edges of the medium. This causes a modulation of the gain as a function of frequency, or "gain ripple". (The gain ripple is treated in more details in chapter 2.) An upper bound for the magnitude of these oscillations is given by $\sqrt{\lambda}\,(|\zeta_0|^{-1} + \zeta^{-1})$; they vanish in the limit of an infinitely long grating. The ripple can be reduced by varying the strength of the interaction adiabatically at the edges of the medium.

3.4.2 Short Pulses

A short pulse is one whose duration is shorter than the delay accumulated between the signal and idler wave fronts. We consider a gaussian input pulse,

$$A_{s0}(\bar{t}) = e^{-(\bar{t}/\bar{\tau})^2}, \tag{3.91}$$

with $\Delta\bar{t} \equiv 2\bar{\tau} \ll \bar{L}$. In physical units, the condition defining a short pulse is equivalent to $\Delta t \ll |1/v_s - 1/v_i|L$.

When the duration of the input pulse is decreased, the output pulse is increasingly distorted. The main pulse is typically preceded or followed by smaller pulses. Naturally, the pulse shape tends to the impulse response in the limit of very short pulses.

Complete expressions for the amplified short pulses are given by Eqs. (3.109) and (3.111) of this chapter's appendix, section 3.6. Here we will only discuss the main features of the amplified waves.

Let us first consider the regime for which the duration is not too short: $4/\bar{L} \ll \bar{\tau} \ll \frac{1}{2}\bar{L}$. In the spectral domain, this corresponds to the case for which the spectral width of the pulse is well contained inside the bandwidth of the amplifier ($\Delta\bar{\omega} \ll$

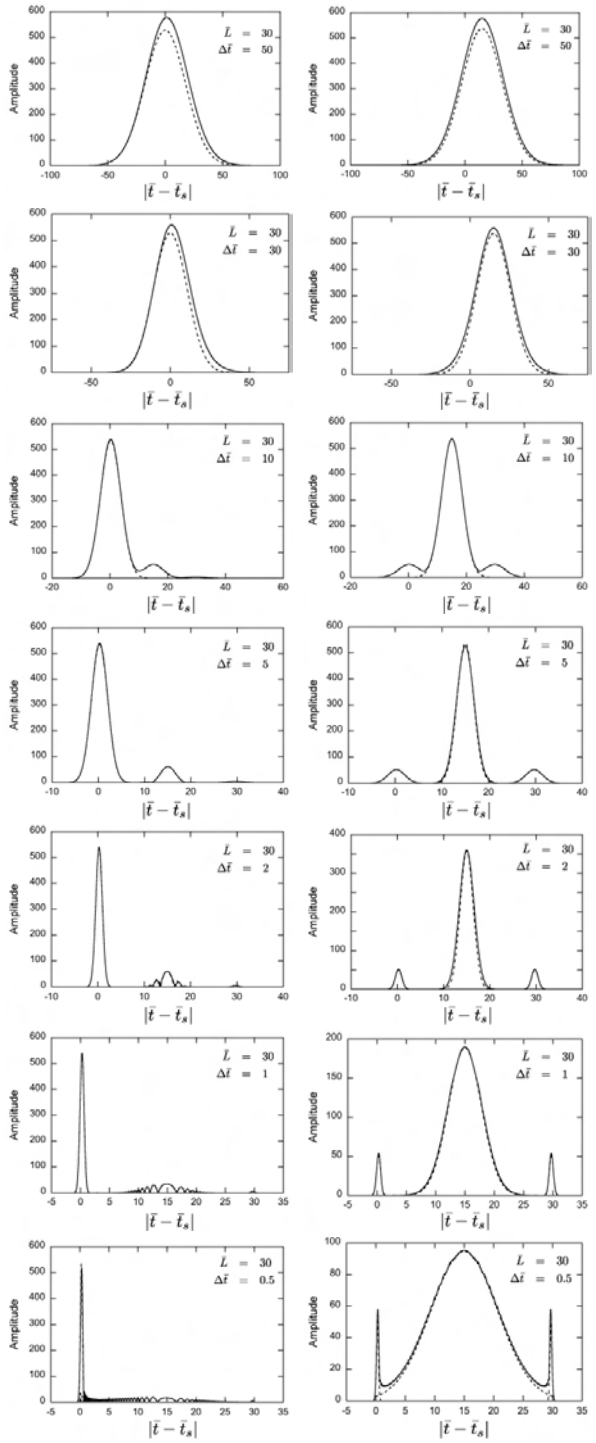

Figure 3.8: Amplified signal (left) and idler (right) pulses of various durations. The pulses are incident at $\bar{z}_0 = -15$, and observed at $\bar{z} = 15$, for a grating length of $\bar{L} = 30$. The gain parameter is $\lambda = 2$, corresponding to a Rosenbluth gain factor $e^{\pi\lambda} \approx 535$. The solid line is the numerical solution while the dashed line corresponds to the analytical expressions developed section 3.6.

$\Delta\bar{\omega}_{BW} = \bar{L}$). The main contribution to the signal wave is given by

$$A_s \approx e^{\pi\lambda} A_{s0} \left(\bar{t} - \bar{t}_s + 4\lambda/\bar{L}\right). \tag{3.92}$$

It is a pulse of the same width as the input pulse, amplified by the Rosenbluth gain factor $e^{\pi\lambda}$, located at the signal wave front (except for a small delay of $4\lambda/\bar{L}$ corresponding to the linear spectral phase described above).

The output signal contains another pulse of identical width located at the idler wave front, but of much small amplitude (by a factor of $4\lambda\bar{\tau}/\bar{L}^2 \ll 1$). In addition, there is a wide train of small-amplitude pulses located between the two wave fronts. This train becomes wider and wider as the duration of the input pulse is decreased.

When the input pulse is even shorter ($\bar{\tau} \ll 4/\bar{L}$, the "very-short-pulse" regime), the pulse train covers the entire range between the signal and idler wave fronts. In this limit, the output is essentially the same as the impulse response. In the spectral domain, the width of the input pulse is wider than the amplification bandwidth; in the temporal domain, the input pulse is so short that it can be regarded as an impulse.

The amplified idler is significantly different. In the short-pulse regime, it contains two small-amplitude replicas of the input pulse traveling at the signal and idler velocities. The main contribution to the idler wave is a large, wide pulse located between the two wave fronts, given by

$$A_i \approx \frac{\bar{\tau}}{\sqrt{2}} e^{\pi\lambda} e^{-[\bar{\tau}(\bar{t}-\bar{t}_{si})/2]^2} e^{i(\bar{t}-\bar{t}_{si})^2/2}. \tag{3.93}$$

The width of this pulse is $2/\bar{\tau}$, which when $\bar{\tau} \ll 1$ is much larger than the duration of the input pulse. In physical units, the duration of the amplified pulse is $\Delta t = 2(1/v_s - 1/v_i)^2/\kappa'\tau$. This broadening is due to the fact that the amplification of the idler wave is accompanied by group delay dispersion, as discussed in section 3.4.1. The pulse is also chirped, with a quadratic phase $-\frac{1}{2}\kappa' t^2/(1/v_s - 1/v_i)^2$, as a result of this dispersion. The arrival time is $t_{si} = (z_{pm} - z_0)/v_s + (z_L - z_{pm})/v_i$, which as discussed before is the time required to travel at the signal velocity up to the PPMP and at the idler velocity thereafter. As the duration of the input pulse is decreased,

the idler pulse becomes wider but is limited in duration by the delay between the wave fronts. In the very-short-pulse limit ($\bar{\tau} \ll 4/\bar{L}$), the pulse occupies the region between the wave fronts entirely, and resembles the impulse response.

Fig. 3.8 shows the evolution amplified pulse shapes as the input pulse duration is reduced. In this example the gain parameter is $\lambda = 2$; the corresponding Rosenbluth gain factor is $e^{\pi\lambda} \approx 535$. The input plane is located at $\bar{z}_0 = -15$ and the wave is observed at $\bar{z} = 15$, for a total length of $\bar{L} = 30$. The pulse durations range from $\Delta\bar{t} = 50$ (long-pulse regime) to $\Delta\bar{t} = 0.5$ (short-pulse regime). The corresponding impulse response (very-short-pulse limit) was shown in Figs. 3.7-(e), (f).

3.4.3 Pulse Distortion

In the short-pulse regime, the main pulse is followed or preceded by smaller pulses. These contributions represent distortions introduced by the amplifier. They are due to the abruptly terminated edges. They are the manifestation in the time domain of the ripple observed in the frequency domain. As a consequence, the techniques proposed to reduce the ripple, such as tapering the gain or the grating profile, will also reduce the pulse distortion.

Calculating the distortions correctly is one of the reasons why we used the exact expressions for the Green's functions as a starting point. Simplified approximations to the Green's functions may obtain the features of the main pulse correctly, but are likely to fail to capture the pulse distortion.

For instance, it may seem reasonable to approximate the amplification spectrum by a constant Rosenbluth gain over the entire bandwidth, with dispersion in the case of the idler wave:

$$\widetilde{G}_s \approx \begin{cases} e^{\pi\lambda}, & |\delta\omega| < \Delta\omega_{BW}/2 \\ 0, & |\delta\omega| > \Delta\omega_{BW}/2 \end{cases} \tag{3.94}$$

$$\widetilde{G}_i \approx \begin{cases} ie^{\pi\lambda}e^{-i\delta\bar{\omega}^2/2}, & |\delta\omega| < \Delta\omega_{BW}/2 \\ 0, & |\delta\omega| > \Delta\omega_{BW}/2 \end{cases} . \tag{3.95}$$

This approximation amounts to ignoring the gain and phase ripple affecting the amplification spectrum. Then one finds the correct behavior for the main amplified pulse (namely, amplification by the Rosenbluth gain factor and stretching in the case of the idler wave) but completely misses the pedestal and pulse trains. It was necessary to carry out the calculation in detail in order to be aware of the effects neglected by using simpler approximations.

3.5 Conclusion

In this chapter we investigated the temporal evolution of optical pulses in parametric amplifiers using linearly-chirped quasi-phase-matching gratings. For completeness, we began by a review of space-time parametric amplification in uniform media, including both co- and counter-propagating geometries and a discussion of the character of the instability in each case.

Then we considered the central topic of this chapter: the linearly non-uniform phase-matching profile. The Green's functions for the signal and idler waves were derived both in the frequency and time domains. We showed how to recover the uniform medium limit. We also showed that, exceptionally, counter-propagating waves interacting in non-uniform media do not constitute an absolute instability. Returning to the Green's functions, we gave equivalent representations found in the literature and explored their behavior in various regimes.

The final portion of this study was dedicated to the temporal shape of the amplified pulses. We examined the cases of long and short pulses. Long pulses emerge essentially undistorted and amplified by the Rosenbluth gain factor. The signal wave sees no significant phase shift. On the other hand, the idler wave accumulates frequency-dependent phase, indicative of group delay dispersion.

In the short-pulse regime, the amplified signal and idler pulses are considerably different. In the case of the signal, the major contribution is a replica of the input pulse, amplified by the Rosenbluth gain factor. In the case of the idler, the pulse is stretched because of dispersion. The distortions affecting short pulses (pulse train or pedestal in the case of the signal and pre- and post-pulses in the case of the idler) are

features caused by the abrupt medium edges; they can be mitigated by tapering the gain.

3.6 Appendix

In this Appendix we give the details of the calculation of the amplified pulse shapes in various regimes. For definiteness, we will assume that $v_i > v_s$, hence $\bar{t}_i < \bar{t}_s$, and according to Eqs. (3.56) and (3.57), the delays with respect to the wave fronts are defined as $U_s = \bar{t}_s - \bar{t}$ and $U_i = \bar{t} - \bar{t}_i$.

3.6.1 Long Pulses: $\Delta\bar{t} \gg \bar{L}$

We consider a long pulse with a frequency shift with respect to the reference frequency ω_0:

$$A_{s0}(\bar{t}) = B_{s0}(\bar{t})e^{-i\delta\bar{\omega}\bar{t}} \tag{3.96}$$

The duration $\Delta\bar{t}$ of the envelope $B_{s0}(\bar{t})$ is assumed to be long compared to the delay between signal and idler after propagation through the medium: $\Delta\bar{t} \gg \bar{t}_s - \bar{t}_i = \bar{L}$.

Signal

We use the signal Green's function (3.59) in the convolution integral (3.85). We ignore the delta-function term since we are interested in the amplified wave. After inverting the order of integration, we have to calculate

$$\begin{aligned} A_s &= -\frac{1}{2\pi}\oint\left(\frac{p+1/2}{p-1/2}\right)^{i\lambda}\int_{\bar{t}_i}^{\bar{t}_s} A_{s0}(\bar{t}-\bar{t}') \\ &\quad \times(\bar{t}'-\bar{t}_i)e^{-i(\bar{t}'-\bar{t}_s)(\bar{z}+\bar{z}_0)/2+i(\bar{t}'-\bar{t}_s)(\bar{t}'-\bar{t}_i)p}d\bar{t}'dp \end{aligned} \tag{3.97}$$

We evaluate the time integral using the stationary-phase method [34] in the limit $\bar{z}_0 \to -\infty$, $\bar{z} \to \infty$. It is easy to verify that the stationary point $\bar{t}_0$ is located inside the causal region ($\bar{t}_i < \bar{t}_0 < \bar{t}_s$) provided $\zeta_0 < 0$ and $\zeta > 0$. If those conditions are satisfied, the main contribution to the integral comes from the saddle point and the

following analysis is valid; if not, the integrand is oscillatory over the entire range of integration and the integral is small. In other words, amplification occurs only if the waves are launched *before* the perfect phase-matching point (PPMP) ($\bar{z}_0 < \delta\bar{\omega}$), and are observed *after* the PPMP ($\bar{z} > \delta\bar{\omega}$). Thus we have demonstrated mathematically a fact which is obvious physically, namely that the amplification region is located in the vicinity of the phase-matching point $\bar{z}_{pm} = \delta\bar{\omega}$.

After evaluation of the time integral, we are left with

$$\begin{aligned} A_s &\approx -\frac{e^{i\pi/4}}{2\pi^{1/2}} e^{i\left(\zeta^2-\zeta_0^2\right)/4} e^{-i\delta\bar{\omega}(\bar{t}-\bar{t}_s)} \\ &\quad \times \oint B_{s0}(\bar{t}-\bar{t}_0)(\bar{t}_0-\bar{t}_i)\left(\frac{p+1/2}{p-1/2}\right)^{i\lambda} \\ &\quad \times e^{-ip(\zeta-\zeta_0)^2/4-i(\zeta+\zeta_0)^2/16p}\frac{dp}{p^{1/2}}, \end{aligned} \tag{3.98}$$

with $\bar{t}_0 = \frac{1}{2}\left(\frac{1/v_s+1/v_i}{1/v_s-1/v_i}\right)(\zeta-\zeta_0) + (\zeta+\zeta_0)/4p$. The p-integral can once again be evaluated using the stationary phase method. It can be put in the form $\int e^{i\rho(p)} f(p)dp$ with

$$\rho(p) = -\frac{1}{4}p(\zeta-\zeta_0)^2 - \frac{1}{16p}(\zeta+\zeta_0)^2 + \lambda \ln\left(\frac{p+1/2}{p-1/2}\right) \tag{3.99}$$

There are four saddle points, two close to the origin and two close to the branch points:

$$p_{1,2} \approx \pm\frac{\zeta+\zeta_0}{2(\zeta-\zeta_0)} \tag{3.100}$$

$$p_{3,4} \approx \pm\frac{1}{2}\sqrt{1+\frac{4\lambda}{\zeta\zeta_0}} \tag{3.101}$$

The integration contour can be taken along the real axis, along the branch cut ranging from $-1/2$ to $+1/2$. The contribution from the saddle point p_1 is the leading asymptotic form; that from p_2 is negligible; those of p_3 and p_4 are the first terms of the asymptotic series $1 + 1/\zeta + 1/\zeta_0 + \ldots$. The final result is

$$A_s \approx A_{s0}(\bar{t}-\bar{t}_s)e^{\pi\lambda}e^{i\lambda\ln|\zeta/\zeta_0|}$$

$$\times \left\{ 1 + \frac{i\lambda^{1/2}}{|\zeta_0|} e^{-i\zeta_0^2/2 + i\lambda\left[\ln\left(\zeta_0^2/\lambda\right)+1\right]} \right.$$
$$\left. - \frac{i\lambda^{1/2}}{\zeta} e^{i\zeta^2/2 - i\lambda\left[\ln\left(\zeta^2/\lambda\right)+1\right]} \right\}. \tag{3.102}$$

The second and third terms inside the curly brackets represent oscillatory corrections due to the finite length of the medium; they vanish as $\zeta \to \infty$, $\zeta_0 \to -\infty$.

Idler

The idler pulse is calculated in a similar manner by substituting the Green's function (3.60) in the convolution integral (3.86). Both integrals are evaluated asymptotically as before. The saddle points in the p complex plane are again given by Eqs. (3.100) and (3.101) but they play different roles. The contributions of p_1 and p_2 correspond to the first terms of the asymptotic expansion, that of p_3 is the leading asymptotic form and that of p_4 is negligible. The result is

$$\begin{aligned} A_i \approx\ & iA_{s0}^*(\bar{t} - \bar{t}_{si}) e^{\pi\lambda} e^{i\lambda[\ln(|\zeta\zeta_0/\lambda)+1]} e^{-i\zeta_0^2/2} \\ & \times \left\{ 1 - \frac{i\lambda^{1/2}}{|\zeta_0|} e^{i\zeta_0^2/2 - i\lambda\left[\ln\left(\zeta_0^2/\lambda\right)+1\right]} \right. \\ & \left. - \frac{i\lambda^{1/2}}{\zeta} e^{i\zeta^2/2 - i\lambda\left[\ln\left(\zeta^2/\lambda\right)+1\right]} \right\} \end{aligned} \tag{3.103}$$

where $\bar{t}_{si} = |1/v_s - 1/v_i|^{-1} (\bar{z}/v_i - \bar{z}_0/v_s)$ is the time delay associated with propagation at the signal velocity before the phase-matching point and at the idler velocity after the phase-matching point.

3.6.2 Short Pulses: $\Delta\bar{t} \ll \bar{L}$

We consider a gaussian pulse,

$$A_{s0}(\bar{t}) = e^{-(\bar{t}/\bar{\tau})^2}, \tag{3.104}$$

short compared to the time delay accumulated between the signal and idler wave fronts: $\Delta\bar{t} = 2\bar{\tau} \ll \bar{t}_s - \bar{t}_i = \bar{L}$.

Signal

We use the Green's function Eq. (3.59) into the convolution integral and invert the order of integration. The expression to evaluate is

$$\begin{aligned} A_s &= -\frac{1}{2\pi}\oint\left(\frac{p+1/2}{p-1/2}\right)^{i\lambda}\int_{\bar{t}_i}^{\bar{t}_s} e^{-[(\bar{t}-\bar{t}')/\bar{\tau}]^2} \\ &\quad\times(\bar{t}'-\bar{t}_i)e^{-i(\bar{t}'-\bar{t}_s)(\bar{z}+\bar{z}_0)/2+i(\bar{t}'-\bar{t}_s)(\bar{t}'-\bar{t}_i)p}d\bar{t}'dp. \end{aligned} \tag{3.105}$$

We introduce

$$x = \sqrt{1/\bar{\tau}^2 - ip}\,(\bar{t}'-\bar{t}) + \frac{i\left[(U_s-U_i)p + (\bar{z}+\bar{z}_0)/2\right]}{2\sqrt{1/\bar{\tau}^2-ip}}. \tag{3.106}$$

Similarly, we define x_s and x_i by replacing $\bar{t}'$ by $\bar{t}_s$ and $\bar{t}_i$ in the expression above. Using this change of variables, we can evaluate the integral in $\bar{t}'$ approximately in terms of error functions; the result is

$$\begin{aligned} A_s &\approx \frac{1}{4\pi^{1/2}}e^{iU_s(\bar{z}+\bar{z}_0)/2}\oint\frac{x_i\left[\mathrm{erf}(x_s)-\mathrm{erf}(x_i)\right]}{\sqrt{1/\bar{\tau}^2-ip}} \\ &\quad\times\exp\left\{-\frac{\left[(U_s-U_i)p+(\bar{z}+\bar{z}_0)/2\right]^2}{4(1/\bar{\tau}^2-ip)}\right\} \\ &\quad\times e^{-iU_sU_ip}\left(\frac{p+1/2}{p-1/2}\right)^{i\lambda}dp. \end{aligned} \tag{3.107}$$

Again, the contour can be taken along the branch cut. The gaussian appearing in the integrand determines the range which contributes significantly to the value of the integral. Let $\Delta p = 2/(\bar{\tau}|U_s - U_i|)$ be the width of that gaussian.

If $\bar{\tau} \ll 4/\bar{L}$, then $\Delta p \gg 1/2$ and the gaussian is essentially flat over the range of integration $[-1/2, 1/2]$. In addition, the factor $[\mathrm{erf}(x_s) - \mathrm{erf}(x_i)] \approx \theta(U_sU_i)$. Then the integral in p is identical to the one appearing in the expression for the Green's

function and we find

$$A_s \approx \sqrt{\pi}\frac{\bar{\tau}|1/v_s - 1/v_i|}{\sqrt{\kappa'}}G_s. \tag{3.108}$$

As expected, in the very-short-pulse limit ($\bar{\tau} \ll 4/\bar{L}$) we recover the impulse response. The multiplicative factor is simply the area under the impulse (equal to $\pi^{1/2}\tau$ in physical units).

If $\bar{\tau} \gg 4/\bar{L}$, then the gaussian plays an important role. The location of the saddle points depends on the position inside the pulse. Let us first consider the regions close to the wave front (i.e. either $U_s \approx 0$ and $U_i \approx \bar{L}$ or $U_s \approx \bar{L}$ and $U_i \approx 0$). In this case there is a saddle point close to the origin which gives rise to shifted replicas of the input pulse located in the vicinity of each wave front. On the other hand, away from either wave fronts, the saddle points are located near the branch points at $\pm\frac{1}{2}$. They give rise to a train of pulses centered in the middle of the causal region. Gathering all these contributions, we find:

$$\begin{aligned}
A_s \approx\ & e^{\pi\lambda}\left\{A_{s0}\left(\bar{t} - \bar{t}_s + 4\lambda/\bar{L}\right)\right. \\
& \left. + \frac{4\lambda}{\bar{L}^2}A_{s0}\left(\bar{t} - \bar{t}_i - 4\lambda/\bar{L}\right)e^{i(\bar{z}-\bar{z}_0)^2/2}\right\} \\
& + \frac{1}{U_s}\sqrt{\frac{\lambda}{2}}\frac{\bar{\tau}}{\left(1+\bar{\tau}^4/4\right)^{1/4}}e^{\pi\lambda}e^{iU_s(\bar{z}+\bar{z}_0)/2} \\
& \left(\exp\left\{-\frac{\bar{\tau}^2}{4}\frac{(\bar{t}-\bar{t}_{is})^2}{(1+\bar{\tau}^4/4)} + \frac{i}{2}U_sU_i\right.\right. \\
& \left. -i\lambda\left[\ln\left(\frac{U_sU_i}{\lambda}\right)+1\right] - \frac{i\pi}{4} - \frac{i}{2}\arctan\left(\frac{\bar{\tau}^2}{2}\right)\right\} \\
& + \exp\left\{-\frac{\bar{\tau}^2}{4}\frac{(\bar{t}-\bar{t}_{si})^2}{(1+\bar{\tau}^4/4)} - \frac{i}{2}U_sU_i\right. \\
& \left.\left. +i\lambda\left[\ln\left(\frac{U_sU_i}{\lambda}\right)+1\right] + \frac{i\pi}{4} + \frac{i}{2}\arctan\left(\frac{\bar{\tau}^2}{2}\right)\right\}\right),
\end{aligned} \tag{3.109}$$

where $\bar{t}_{si} = |1/v_s - 1/v_i|^{-1}\left(\bar{z}/v_i - \bar{z}_0/v_s\right)$ and $\bar{t}_{is} = |1/v_s - 1/v_i|^{-1}\left(\bar{z}/v_s - \bar{z}_0/v_i\right)$ are the time delays associated with propagation at one velocity before the PPMP and at the other after the PPMP. (Note that this result is valid provided the PPMP is not too close to the edges of the medium, i.e. $\bar{z} + \bar{z}_0 \ll \bar{L}$).

If we ignore the distortion and keep only the main pulse, we get the rough approximation

$$A_s \approx e^{\pi\lambda} A_{s0}\left(\bar{t} - \bar{t}_s\right). \tag{3.110}$$

The output signal is an amplified replica of the original pulse, traveling with the signal wave front.

Idler

The calculation of the amplified idler pulse is very similar to that of the signal. The only difference is the role of the saddle points: the saddle point close to the origin leads to small pulses propagating at the wave-front velocities, while one of the saddle points close to the branch points is associated with the main idler pulse. The expression for the amplified idler pulses is the following:

$$\begin{aligned} A_i \approx\ & \sqrt{\frac{\lambda}{\bar{L}}} e^{\pi\lambda} \left[A_{s0}^* \left(\bar{t} - \bar{t}_i - 4\lambda/\bar{L}\right) \right. \\ & \left. + A_{s0}^* \left(\bar{t} - \bar{t}_s + 4\lambda/\bar{L}\right) e^{i(\bar{z}-\bar{z}_0)^2/2} \right] \\ & + \frac{\bar{\tau}}{\sqrt{2}(1+\bar{\tau}^4/4)^{1/4}} e^{\pi\lambda} e^{-[\bar{\tau}(\bar{t}-\bar{t}_{si})/2]^2} e^{iU_i(\bar{z}+\bar{z}_0)/2} \\ & \times \exp\left\{ i\left[-\frac{1}{2}U_s U_i + \lambda\left[\ln\left(\frac{U_s U_i}{\lambda}\right) + 1\right] + \frac{\pi}{4} + \frac{1}{2}\arctan\left(\frac{\bar{\tau}^2}{2}\right)\right]\right\} \end{aligned} \tag{3.111}$$

where $\bar{t}_{si} = |1/v_s - 1/v_i|^{-1}\left(\bar{z}/v_i - \bar{z}_0/v_s\right)$ is the time delay associated with propagation at the signal velocity before the phase-matching and at the idler velocity after the phase-matching point.

If we ignore pulse distortion, the main idler pulse is given by

$$A_i \approx \frac{\bar{\tau}}{\sqrt{2}} e^{\pi\lambda} e^{-[\bar{\tau}(\bar{t}-\bar{t}_{si})/2]^2} e^{i(\bar{t}-\bar{t}_{si})^2/2}. \tag{3.112}$$

It is stretched due to the dispersion seen by the idler wave.

It is important to keep in mind that the dispersion calculated here is the contribution of the QPM grating only. It does not account for material dispersion.

Chapter 4

Design of Experiment

The goal of the experiment is to see the extent to which the Rosenbluth model can explain a real OPA system's performance in the laboratory. In particular, we wanted to show that we could obtain essentially constant gain over a wide bandwidth, using chirped QPM gratings.

We use a periodically-poled lithium niobate (PPLN) crystal as the nonlinear material. We hold the crystal at a temperature of 150^oC to avoid photorefractive damage [52] and green-induced infrared absorption [53].

4.1 Dispersion Relation of Lithium Niobate

The extraordinary index of refraction of lithium niobate ($LiNbO_3$) is given by the following Sellmeier equation [54]:

$$n_e^2 = a_1 + b_1 f + \frac{a_2 + b_2 f}{\lambda^2 - (a_3 + b_3 f)^2} + \frac{a_4 + b_4 f}{\lambda^2 - a_5^2} - a_6 \lambda^2, \tag{4.1}$$

where the temperature dependence is given by

$$f = (T - 24.5^o\text{C})(T + 570.82). \tag{4.2}$$

Table 4.1: Coefficients of the Sellmeier equation (4.1) [54]

Coefficient	Value
a_1	5.35583
a_2	0.100473
a_3	0.20692
a_4	100
a_5	11.34927
a_6	1.5334×10^{-2}
b_1	4.629×10^{-7}
b_2	3.862×10^{-8}
b_3	-0.89×10^{-8}
b_4	2.657×10^{-5}

The wavelength is expressed in micrometers and the temperature in degrees Celcius. The numerical values of the coefficients appearing in the Sellmeier equation are given in Table 4.1.

The group velocity in dispersive media is given, in general, by

$$\frac{1}{v_g} = \frac{\partial k}{\partial \omega} = \frac{1}{c}\left(n - \lambda \frac{\partial n}{\partial \lambda}\right). \tag{4.3}$$

The rate of change of refractive index with wavelength, $\partial n/\partial \lambda$, can be obtained from the Sellmeier relation given above:

$$\frac{\partial n}{\partial \lambda} = -\frac{\lambda}{n_e}\left[\frac{a_2 + b_2 f}{\left(\lambda^2 - (a_3 + b_3 f)^2\right)^2} + \frac{a_4 + b_4 f}{\left(\lambda^2 - a_5^2\right)^2} + a_6\right]. \tag{4.4}$$

Plots of the refractive index and group velocities in $LiNbO_3$ are given in Fig. 4.1.

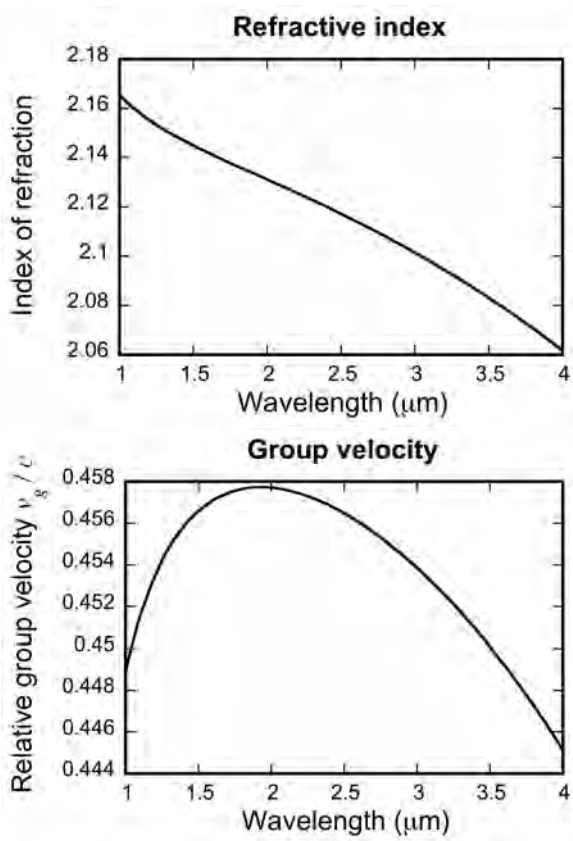

Figure 4.1: Index of refraction and group velocity of lithium niobate.

4.2 Phase Matching

The wavevector-matching condition can be written as $k_p - k_s - k_i - K_g = 0$, or

$$\frac{n_p}{\lambda_p} - \frac{n_s}{\lambda_s} - \frac{n_i}{\lambda_i} - \frac{1}{\Lambda_g} = 0. \tag{4.5}$$

Here, the subscripts p, n and i refer to the pump, signal and idler waves, respectively. The refractive index at wavelength λ_j is n_j. The period of the QPM grating is denoted by Λ_g. The wave-vector matching condition must be solved numerically, subject to the frequency matching condition $\omega_p = \omega_s + \omega_i$. The phase-matching curve is shown in Fig. 4.2 for a pump wavelength of $\lambda_p = 1064$ nm and a temperature of 150°C. A signal wavelength around 1.55 μm is phase-matched by a grating period of 29.6 μm; the corresponding idler wavelength is 3.38 μm.

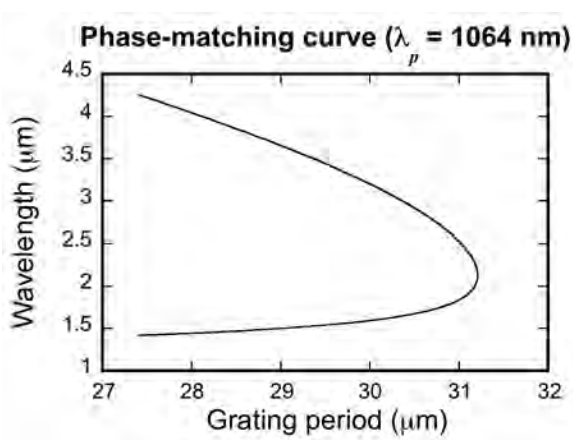

Figure 4.2: Phase-matching curve for a pump wave at 1064 nm.

4.3 PPLN Crystals

4.3.1 Fabrication Procedure

The fabrication process of PPLN is illustrated in Fig. 4.3. More details on the poling process can be found in Refs. [55, 56, 57, 58, 59, 60].

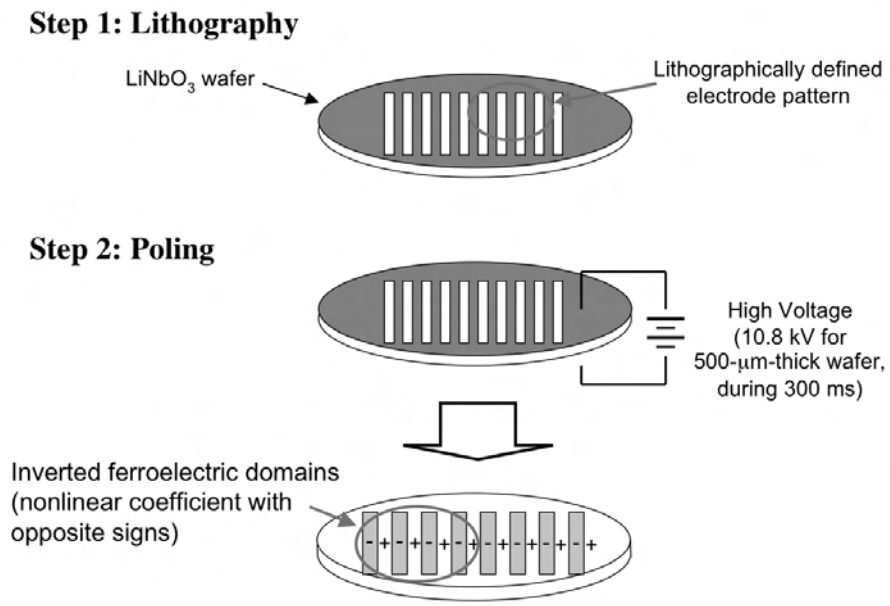

Figure 4.3: Fabrication procedure.

The first step of the process is the lithographic definition of the electrode pattern. A mask is made with the desired poling pattern. A layer of resist is spun on the $LiNbO_3$ wafer. The resist is then exposed, developed and baked. The electrode pattern corresponding to the desired QPM grating is now printed in the resist.

The second step is the poling. It consists of applying an electric field across the wafer in order to invert the ferroelectric domains. For the 0.5-mm-thick wafers used, the voltage was held at 10.8 kV for 300 ms.

The final step consists in etching the surface of the wafer with HF to reveal the poling pattern. Then the crystals are diced and the end surfaces are polished.

4.3.2 QPM Gratings

The resulting crystals are 5-cm long, 1-cm wide and 0.5-mm thick. Each crystal contains 9 gratings.

Many gratings with different chirp rates were fabricated. However, for many of them the chirp rate was too large to give significant gain. The experimental results

described in the next chapter were obtained with gratings offering bandwidths of 50, 120 and 190 nm around 1550 nm, corresponding to chirp rates of 7.8×10^4, 1.6×10^5 and 2.3×10^5 m^{-1}, respectively.

Pictures of the gratings are shown in Fig. 4.4.

Figure 4.4: Pictures of QPM gratings.

4.4 Experimental Setup

A diagram of the experimental setup is presented in Fig. 4.5.

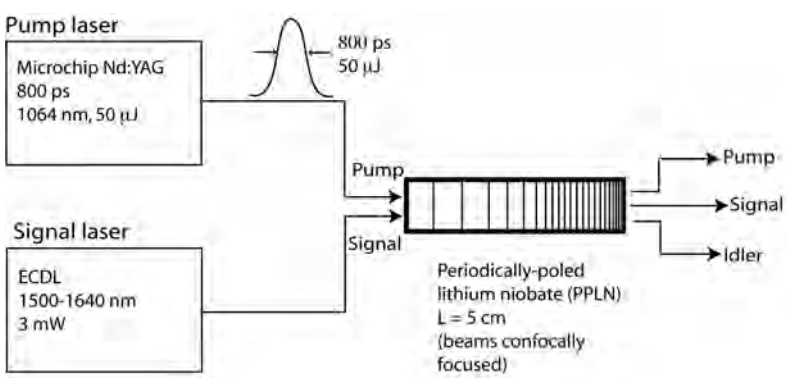

Figure 4.5: Experimental setup.

The pump laser was a Q-switched Nd:YAG laser, from JDS-Uniphase, model "Power Chip Nanolaser". Its features are listed in table 4.2. The signal laser was a

tunable external-cavity diode laser (ECDL), fabricated by New Focus, model "Vidia-Swept".

Table 4.2: Specifications for the pump and signal lasers

Pump laser	
Type	Pulsed
Wavelength	1064 nm
Repetition rate	1 kHz
Pulse duration	0.8 ns
Pulse energy	30 μJ
Signal laser	
Type	CW
Wavelength	1520 - 1570 nm
Power	1 mW

The beams go through some conditioning optics (isolator, attenuators, polarizers, spatial filter). Then they are combined and focused inside the nonlinear crystal. The mode beam waist of both the pump and the signal was 115 μm ($1/e^2$ intensity radius), which corresponds to slightly looser than confocal focusing.

After the nonlinear crystal, the pump light is filtered out using a dichroic mirror. Cameras are used to monitor the beam profiles. A slab of silicon is used to eliminate wavelengths below 1.1 μm (such as the green light resulting from the parasitic second-harmonic generation of the pump). The output beam (now containing signal and idler) is sent through a monochromator. The monochromator is used to filter out the parametric fluorescence light. The output, consisting of light at the signal wavelength only, is then detected using a Thorlabs InGaAs photodiode, model PDA400 (response time around 30 ns).

There is a difficulty associated with the measurement of the gain, due to the fact that the average power increase is very small, because the pump duty cycle is very low, of the order of 10^{-6} (pump pulses have a duration of roughly 1 ns, and are emitted every millisecond). The average power increase due to parametric amplification is therefore 10^6 times lower than the actual gain. To solve this problem, we used a box-car integrator in order to integrate the electrical signal over the duration of the electrical pulse (around 200 ns). The average power increase over that duration is

then lower than the parametric gain by a factor of 200 only.

We found large pulse-to-pulse variations in the measured gain. In order to obtain a statistical description of the amplification, the electrical signal coming from the box-car was acquired by a computer. The value quoted for the gain is the mode of a distribution of 10^4 pulses.

Chapter 5

Experimental Results

The original purpose of this experiment was to validate the 1-D Rosenbluth model. However, as we will see in this chapter, the experiment revealed two unexpected facts. First, the gain spectrum and its magnitude were very different depending on the sign of the chirp rate. Second, the level of parametric fluorescence was much higher than expected. These observations cannot be explained by the Rosenbluth model. They will force us to revise our understanding of parametric amplification in the presence of finite-sized beams (as opposed to ideal beams with plane parallel wave fronts).

Throughout this chapter, we adopt the following definition of gain:

$$\text{“Gain”} = \frac{\text{Output energy}}{\text{Input energy}}. \tag{5.1}$$

It is understood that these energies refer to the signal wavelength (since other wavelengths are filtered out), and that they are measured over the duration of the pump pulse (since the signal laser is CW). The problem with this definition is that the output is composed of amplified signal and parametric fluorescence:

$$\text{“Gain”} = \frac{\text{Amplified signal} + \text{Parametric fluorescence}}{\text{Input signal}}. \tag{5.2}$$

The parametric fluorescence is independent of the input signal level (provided the

amplifier is not saturated). (As explained below, the fluorescence is due to the spontaneous generation of signal photons; it does not require external input signal photons.) If the parametric fluorescence is negligible, then the definition of gain given above is adequate. However, if it is large, then this definition is invalid because it does not correspond to the amount of amplification experienced by the signal.

In summary, the ratio of output to input, which we call "gain" in this chapter, is meaningful when the fluorescence emission is negligible. Measurements where this is not the case will be pointed out and different experimental measurements will be necessary.

5.1 Positive Chirp Rate

5.1.1 Gain Spectrum

The gain spectra of three chirped gratings designed to phase-match bandwidths of 50, 120 and 190 nm are shown in Fig. 5.1. They were obtained for a pump pulse energy of 25 μJ per pulse. The solid lines show the square bandwidths expected from the Rosenbluth model while the dots represent experimental data. The measured gain behaves as predicted over the short-wavelength side portion of the spectrum but is completely dominated by parametric fluorescence over the long-wavelength side portion of the spectrum (and as such it is not a meaningful value of the gain).

Parametric fluorescence is the spontaneous decay of a pump photon into of a pair of signal and idler photons. Like other spontaneous emission phenomena, its origin is purely quantum mechanical (i.e. its explanation requires quantization of the electromagnetic field [28, 61, 62, 63, 64]). It is caused by the interaction of the pump photons with the zero-point energy fluctuations. It can be regarded as parametric amplification seeded by a fictitious signal consisting of one photon per mode [64, 44]. As we will see in chapter 11, for a uniform grating used in this experiment, this corresponds to an input power of the order of 10 nW over the gain bandwidth of the OPA. However, we seeded the amplifier with a power around 1 mW, much larger than the "parametric noise" level. According to the Rosenbluth model, the parametric

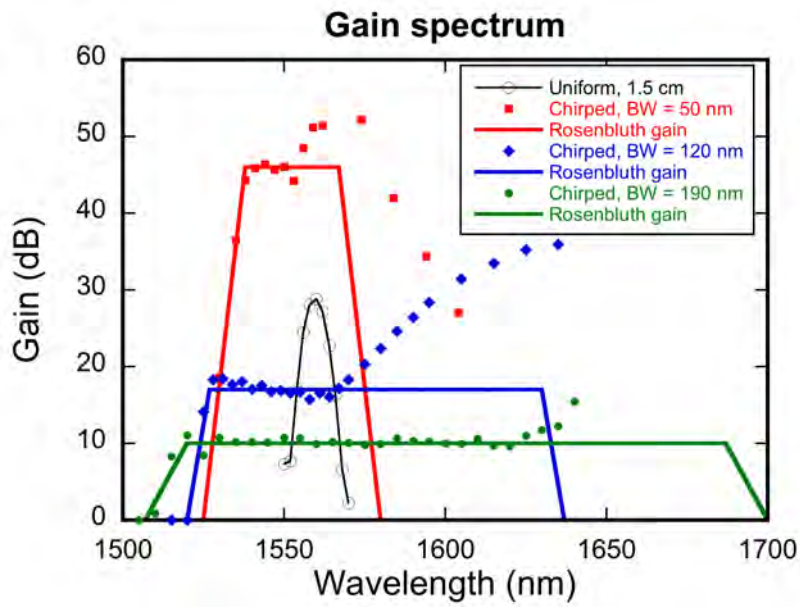

Figure 5.1: Measured gain spectrum of gratings with positive chirp rate, compared to that of a uniform grating.

fluorescence should not dominate the output of the device. Other processes have to exist to explain this result.

It is possible to dominate the parametric fluorescence by using a more intense signal beam. We showed this by using an erbium-doped fiber amplifier (EDFA) in order to raise the power of the input signal from around 1 mW up to 1 W. In this case, the amplified light was sufficiently intense and we could observe the long-wavelength side portion of the Rosenbluth gain spectrum, as shown in Fig. 5.2.

The fluorescence could also be reduced by lowering the pump intensity. Naturally, this also causes a reduction of the Rosenbluth gain. Fig. 5.3 shows the broad and relatively flat gain spectrum of a chirped grating. Its gain, however, had to be kept very low (slightly more than 5 dB) otherwise the parametric fluorescence would have become too large. The gain spectrum of a 1.5-cm-long uniform grating is shown to illustrate the bandwidth increase provided by the chirped grating (100 nm for the chirped grating compared to slightly more than 5 nm in the case of the uniform grating).

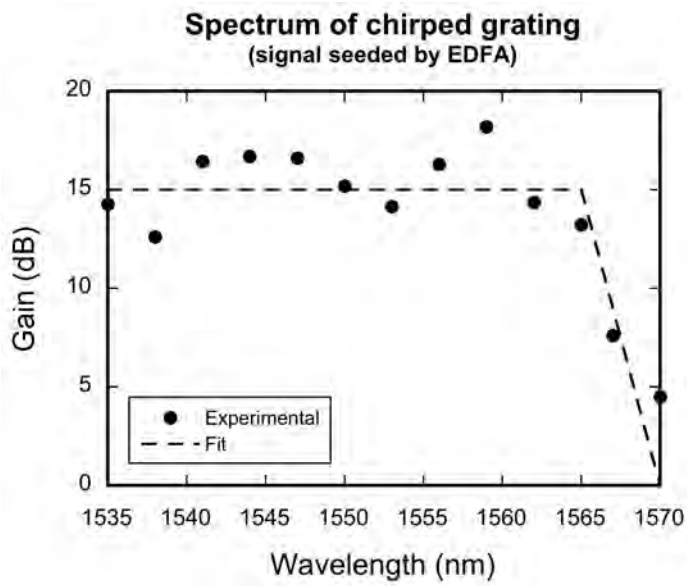

Figure 5.2: Long-wavelength side portion of the gain spectrum of a positively chirped grating seeded with an EDFA in order to dominate the fluorescence.

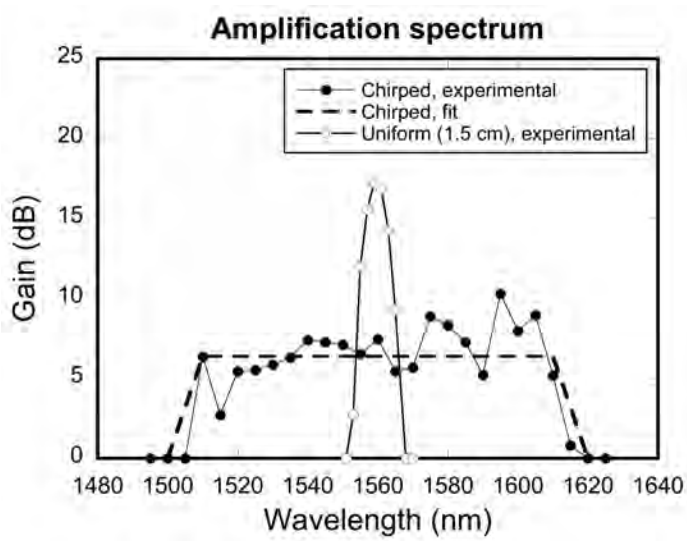

Figure 5.3: Gain spectrum of a chirped grating, with a pump intensity sufficiently low (15 μJ per pulse) to cause negligible parametric fluorescence. The gain spectrum of a uniform grating is shown for comparison to illustrate the bandwidth increase due to the chirped QPM grating.

5.1.2 Confirmation of the Scaling Predicted by the Rosenbluth Model

Except for the intense parametric fluorescence, the amplification spectrum of chirped gratings with positive chirp rate behaves as predicted by the Rosenbluth model: the gain is essentially flat over a wide bandwidth.

According to the Rosenbluth gain formula, $G = \exp(2\pi\gamma^2/\kappa')$, the logarithmic gain is proportional to the *intensity* of the pump (rather than to its amplitude) and inversely proportional to the chirp rate. These basic scaling laws were confirmed experimentally.

We operated at a signal of 1540 nm, in the left-hand-side portion of the spectrum where there was no significant parametric fluorescence. Fig. 5.4 shows the gain as a function of pump-pulse energy, for two gratings of different chirp rates. The logarithmic gain increases linearly with pulse energy (and therefore with pump intensity), as predicted by the Rosenbluth model.

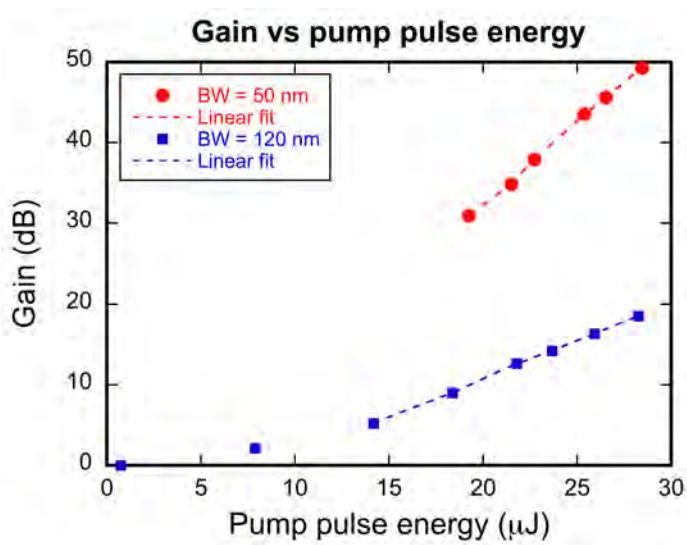

Figure 5.4: Gain vs pump pulse energy for two chirped gratings, measured at a signal wavelength of 1540 nm.

Fig. 5.5 shows the gain obtained with three gratings of different chirp rates, at

constant pump pulse energy. The linear dependence on a logarithmic scale is consistent with the fact that the Rosenbluth gain is inversely proportional to the chirp rate.

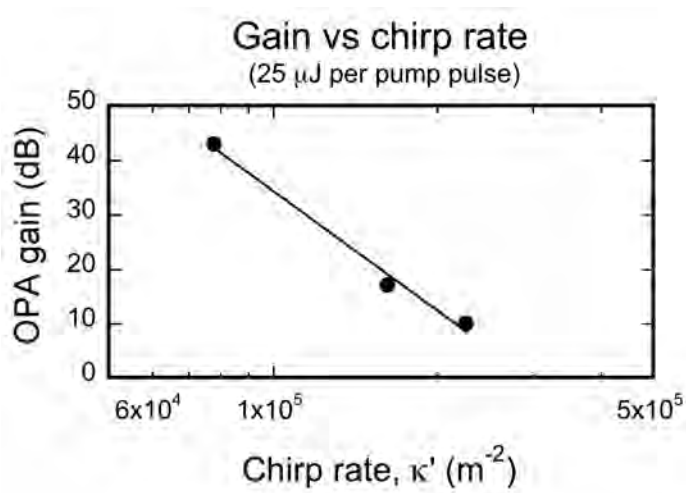

Figure 5.5: Gain vs chirp rate, measured at a signal wavelength of 1540 nm and a pump pulse energy of 25 μJ.

5.1.3 Comparison with Theory

The previous section confirmed the basic trends predicted by the Rosenbluth model. However, as shown in Fig. 5.6, numerically the Rosenbluth gain formula grossly overestimates the experimental result.

A more realistic estimate of the gain can be obtained by averaging the Rosenbluth gain over the radial and temporal profile of the pulse:

$$G_{average} = \frac{\int I_s(x,y,t) \exp\left[2\pi\gamma^2(x,y,t)/\kappa'\right] \, dxdydt}{\int I_s(x,y,t) \, dxdydt} \tag{5.3}$$

where in general $I_s(x,y,t)$ is the input signal pulse and the coupling coefficient $\gamma^2(x,y,t) \propto I_p(x,y,t)$ is proportional to the intensity of the pump pulse. In our experiment the input signal was CW (constant in time), so all the time dependence came from $\gamma(x,y,t)$. The time average was taken over the duration of the electrical

signal corresponding to an amplified pulse; this step was carried out by the box-car integrator (see section 4.4). As seen in Fig. 5.6, the averaged Rosenbluth formula also overestimates the gain.

A much better agreement is obtained by including diffraction into the model. In this case the coupled-mode equations must be solved numerically. We used a finite-difference beam propagator written by Andrew M. Schober [65]. This program includes a chirped QPM grating and diffraction, assuming radial symmetry. As shown in Fig. 5.6, the numerical results agree with the experimental data relatively well.

5.2 Negative Chirp Rate

The gain spectrum of a grating with negative chirp rate is shown in Fig. 5.7. Far from being flat, the gain varies from 15 to 40 dB across the 100-nm bandwidth. (In this measurement, the amplified signal dominated the parametric fluorescence, so Fig. 5.7 is a plot of the actual gain spectrum.)

The parametric fluorescence in the case of negative chirp rates was even more intense than in the case of positive chirp rates. Fig. 5.8 compares the fluorescence spectrum obtained with chirp rates of opposite signs but same magnitude. This grating was designed to phase-match wavelengths ranging from 1520 to 1570 nm. The measurement was taken by collecting all the emitted light (i.e. over all solid angles of significant emission). The pump energy was 25 μJ per pulse. Regardless of the sign of the chirp, the fluorescence spectrum reaches a maximum around the upper passband limit ($\sim$1570 nm).

As mentioned previously, the differences between positive and negative chirp rates are not explained by the Rosenbluth model.

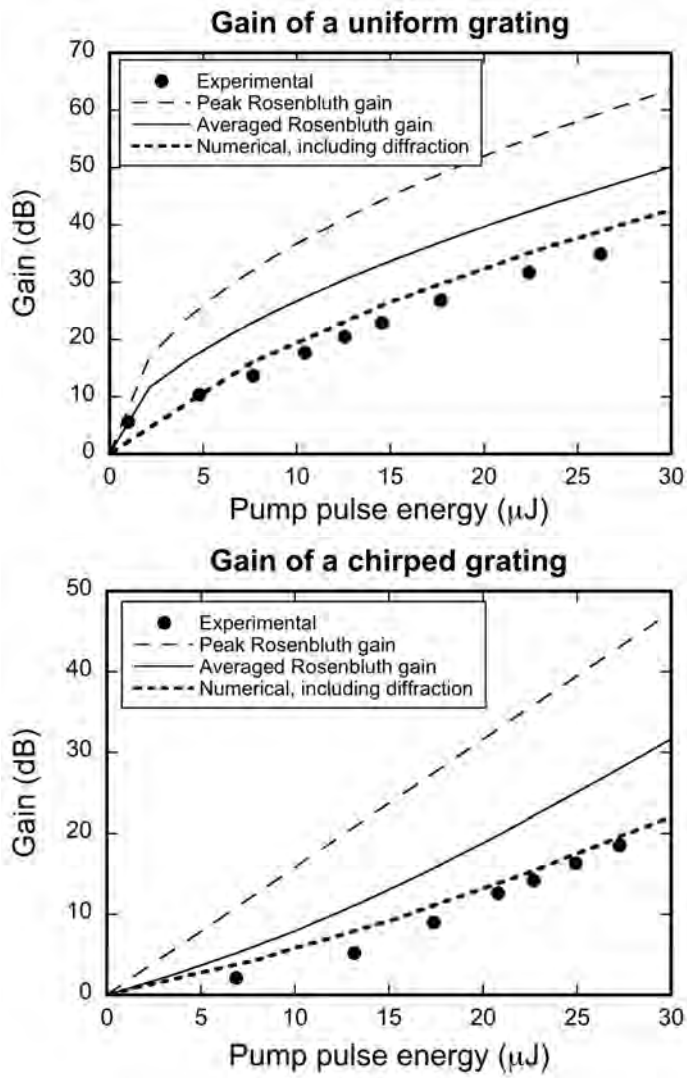

Figure 5.6: Comparison of experimentally observed parametric gain with a pulses gaussian in space and time, with theoretical expressions for peak and average Rosenbluth gain, as well as numerical simulations including gain-induced diffraction effects.

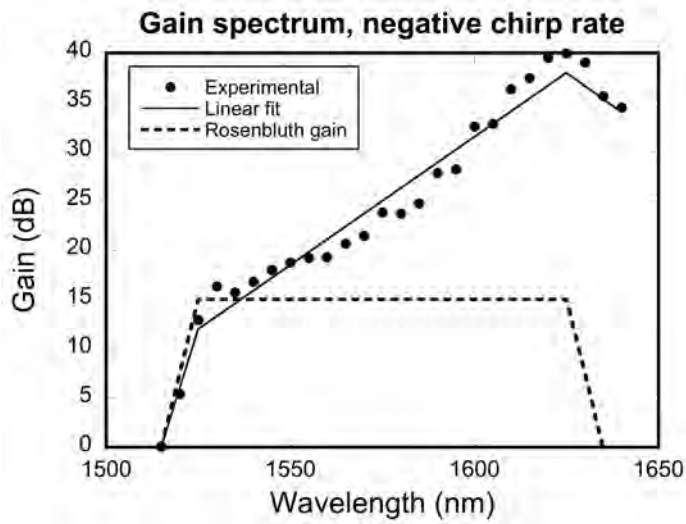

Figure 5.7: Measured gain spectrum of a grating with negative chirp rate.

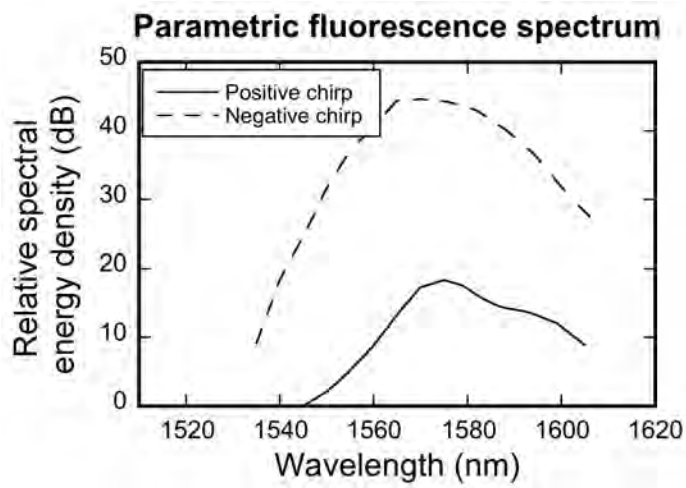

Figure 5.8: Parametric fluorescence spectrum of gratings with chirp rate of equal magnitude but opposite signs. The gratings were design to phase match wavelengths ranging from 1520 to 1570 nm. The reference level for the spectral energy density was 0.2 pJ/nm.

5.3 Parametric Fluorescence: Far-Field Pattern

The far-field patterns of the parametric fluorescence are shown in Fig. 5.9. The typical angular diameter of those patterns is from 1 to 2 degrees. The fluorescence patterns associated with a positive chirp rate consist of two symmetric lobes, in no particular relationship with the plane of the nonlinear crystal. This pattern seems to be related to the asymmetric profile of the pump beam (see section 9.7). The pattern corresponding to a negative chirp rate has the shape of a ring. Clearly, in order to explain such characteristic patterns we must revise our physical model to include transverse effects.

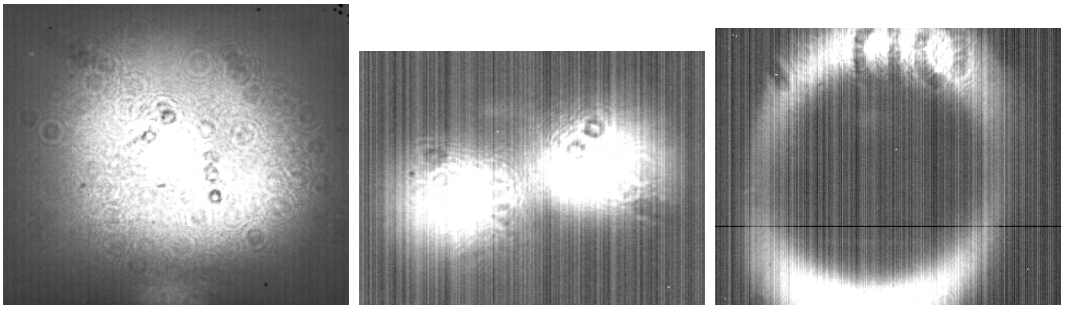

Figure 5.9: Far-field parametric fluorescence patterns: uniform grating (top), positive chirp (middle), negative chirp (bottom).

Chapter 6

Towards a 2-D Model

The goal of the experiment was to see to what extent a physically realizable system would reproduce results obtained by the 1-D Rosenbluth model equations. There was little doubt that the physical picture behind the Rosenbluth model was valid; the experiment was simply supposed to tell on a quantitative level how accurate the agreement was. Whether nonlinear effects, saturation, 2-D effects, diffraction or unanticipated coupling channels would result, only actual experiments could tell.

The outcome of the experiment was indeed interesting: the parametric fluorescence was so intense that it dominated the output spectrum, and, as a second surprise, chirp rates of different signs behaved drastically differently. We tried unsuccessfully to find experimental artifacts or systematic errors that could explain these problems. Finally, we started to look for other effects not included in the 1-D linear model which could explain the experimental results. It was a long, frustrating process. Several times, we thought about a possible explanation, became excited at the prospect of finally finding the solution to the problem, only to realize later that the effect in question could not provide a valid explanation.

Several hypotheses were explored. It was suspected that random perturbations to the QPM grating profile could suppress dephasing and restore the growth outside the phase-matched region. The idea of a parametric oscillator caused by Fresnel reflections at the surfaces of the crystal was considered. Nonlinear effects such as

self-focusing were examined. It was even thought that the interaction could be continuously seeded for instance by noncollinear emission reflected towards the pump beam by total internal reflection off the sides of the crystal. Finally, the possibility of phase-matched cascaded processes, or processes phase-matched at a higher order, were explored. All these hypotheses lead to contradictions and were eventually rejected.

There was another type of explanation that had not been explored yet: those pertaining to transverse effects. This hypothesis was motivated by the far-field fluorescence pattern, which required emission of light at a small angle with respect to the axis of the pump beam. We decided to build a numerical model to investigate transverse effects systematically.

Obviously, the idealized 1-D model was inadequate, so our stragegy was to make the numerical simulations as realistic as possible in 2-D without nonlinearity at first – and if that failed, start exploring nonlinear regimes. We wanted to include effects such as diffraction, noncollinearity, focused beams, temporal effects, cascaded processes, etc, until an explanation to the results observed in the lab was found. We built our first model using Femlab, a user-friendly finite-element PDE solver [66]. This way, our attention could be concentrated on the modeling effort because we did not have to stall in the physics exploration while writing our own numerical beam propagation code. We started with a simple model consisting of the two coupled equations in two dimensions, in the presence of a linear phase-matching profile and a plane-wave pump. We included diffraction at the signal and idler waves and allowed for noncollinear propagation. The amplification remained confined to the vicinity of the phase-matched point, as predicted by the Rosenbluth model.

Next, we gave the pump wave the shape of an actual beam, i.e. localized in the lateral dimension. Suddenly the amplification ceased to be limited to the phase-matched region. Instead, the waves grew as if there were no dephasing at all! *Noncollinear laterally-localized gain-guided modes* had been discovered.

With this insight provided by the numerical simulations, we returned to the lab. We seeded the amplifier at a small noncollinear angle and observed an increase in the parametric gain.

This marked the starting point of our investigation of transverse effects. The following chapters describe our efforts via numerical, experimental and analytical means.

Chapter 7

2-D Model

7.1 Coupled-Mode Equations

The derivation of the equations including noncollinear propagation and diffraction is very similar to that of the coupled-mode equations in one dimension (chapter 2) [27, 28]. In this derivation we simply highlight the differences related to the transverse dimension.

We use as a starting point the wave equation:

$$\nabla^2 \widetilde{E} - \frac{1}{c^2}\frac{\partial^2 \widetilde{E}}{\partial t^2} = \mu_0 \frac{\partial^2 \widetilde{P}_{NL}}{\partial t^2}. \tag{7.1}$$

Here, $\widetilde{E}$ and $\widetilde{P}_{NL}$ represent the physical electric field and nonlinear polarization, respectively. We extract the fast phase associated to a noncollinear wave of frequency ω and wave vector $\mathbf{k}$:

$$\widetilde{E} = E e^{i(\mathbf{k}\cdot\mathbf{r}-\omega t)}, \tag{7.2}$$

$$\widetilde{P}_{NL} = P_{NL} e^{i(\mathbf{k}\cdot\mathbf{r}-\omega t)}, \tag{7.3}$$

where $E(\mathbf{r})$ and $P(\mathbf{r})$ are the field envelopes. Substituting into the wave equation, and using the dispersion relation $\omega = ck/n$ (assuming a scalar wave vector and neglecting

birefringence), we obtain

$$\nabla^2 E + 2i\mathbf{k}\cdot\nabla E = -\mu_0\omega^2 P_{NL}. \tag{7.4}$$

We assume that the wave vector $\mathbf{k}$ forms a small angle with respect to the axis of propagation (z-axis). Then we make the slowly-varying envelope approximation (SVEA), dropping the second derivative of the envelope with respect to z. Considering only one transverse dimension, x, the wave equation describing noncollinear propagation in the presence of diffraction is

$$\frac{\partial E}{\partial z} + \frac{k_x}{k_z}\frac{\partial E}{\partial x} - \frac{i}{2k_z}\frac{\partial^2 E}{\partial x^2} = i\frac{\mu_0\omega^2}{2k_z}P_{NL}. \tag{7.5}$$

The remainder of the derivation is identical to that of the 1-D coupled-mode equations: we decompose the electric field into three waves, the pump, signal and idler. Each one is driven by the product of the two others through the nonlinear polarization. Assuming that the pump wave remains undepleted, we obtain the following coupled equations:

$$\frac{\partial E_1}{\partial z} + \tan\theta_1\frac{\partial E_1}{\partial x} - \frac{i}{2k_1\cos\theta_1}\frac{\partial^2 E_1}{\partial x^2} = i\frac{\omega_1}{n_1\cos\theta_1}\frac{d_{eff}}{c}E_0E_2^*e^{i\Delta kz} \tag{7.6}$$

$$\frac{\partial E_2}{\partial z} + \tan\theta_2\frac{\partial E_2}{\partial x} - \frac{i}{2k_2\cos\theta_2}\frac{\partial^2 E_2}{\partial x^2} = i\frac{\omega_2}{n_2\cos\theta_2}\frac{d_{eff}}{c}E_0E_1^*e^{i\Delta kz}, \tag{7.7}$$

where θ_1 and θ_2 are the signal and idler noncollinear angles (i.e. with respect to the pump beam, which is assumed to propagate along the z-axis), defined by $\tan\theta_1 = k_{1x}/k_{1z}$ and $\tan\theta_2 = k_{2x}/k_{2z}$. The angles θ_1 and θ_2 define the directions of the plane-wave carriers about which the spatial envelopes are defined. They are related to each other by the requirement of noncollinear phase-matching, developed in the next section.

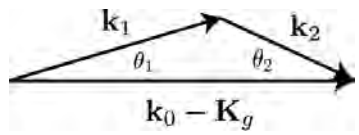

Figure 7.1: Vector diagram for noncollinear phase matching.

7.2 Noncollinear Phase Matching

A diagram of noncollinear phase-matching is displayed in Fig. 7.1. We assume that the pump and grating wave vectors, $\mathbf{k}_0$ and $\mathbf{K}_g$, are collinear. The vectorial phase-matching condition is satisfied when $\mathbf{k}_0 - \mathbf{k}_1 - \mathbf{k}_2 - \mathbf{K}_g = 0$. The equivalent scalar equations are

$$k_1 \sin\theta_1 + k_2 \sin\theta_2 = 0 \tag{7.8}$$

$$k_1 \cos\theta_1 + k_2 \cos\theta_2 = k_0 - K_g. \tag{7.9}$$

We define the nominal wavelengths, λ_{s0} and λ_{i0}, which phase match the interaction collinearly (for $\theta_1 = \theta_2 = 0$). They satisfy $k_{s0} + k_{i0} = k_0 - K_g$. Substitution into (7.9) gives

$$k_1 \cos\theta_1 + k_2 \cos\theta_2 = k_{s0} + k_{i0}. \tag{7.10}$$

The phase-matching angle obtained numerically using the dispersion relation of $LiNbO_3$ is plotted in Fig. 7.2 vs wavelength for different nominal wavelengths.

An approximation for the phase-matching angle can be obtained assuming small angles, which is typically the case. Then Eqs. (7.8) and (7.10) become

$$k_1\theta_1 + k_2\theta_2 = 0 \tag{7.11}$$

$$k_1\left(1 - \theta_1^2/2\right) + k_2\left(1 - \theta_2^2/2\right) = k_{s0} + k_{i0} \tag{7.12}$$

Assuming a linear dispersion relation, we can write the wave vectors in terms of the frequency shift:

$$k_1 = k_{s0} + \left(\frac{\partial k}{\partial \omega}\right)\bigg|_{k_{s0}} \delta\omega$$

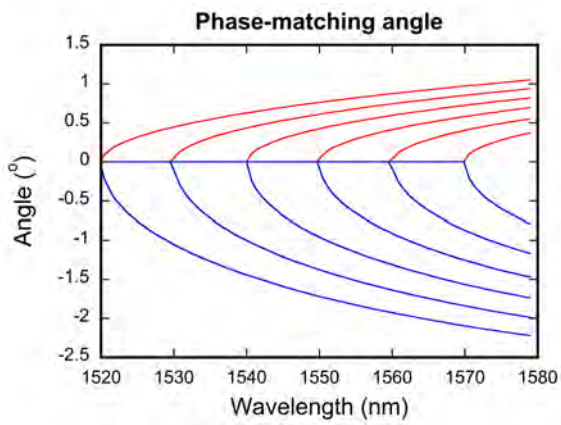

Figure 7.2: Phase-matching angle as a function of wavelength, at different locations inside a grating designed to phase-match (collinearly) a wavelength range from 1520 to 1570 nm. The signal angle is shown in red (positive angles) while the idler angle is shown in blue (negative angles).

$$= \quad k_{s0} + \frac{\delta\omega}{v_s}, \tag{7.13}$$

and

$$\begin{aligned} k_2 &= k_{i0} - \left(\frac{\partial k}{\partial \omega}\right)\bigg|_{k_{i0}} \delta\omega \\ &= k_{i0} - \frac{\delta\omega}{v_i}, \end{aligned} \tag{7.14}$$

where v_s and v_i are the signal and idler group velocities. Using $\delta\omega = -2\pi c\,\delta\lambda/\lambda_{s0}^2$ in Eqs. (7.13) and (7.14), we can express the noncollinear angle as a function of wavelength shift using Eqs. (7.11) and (7.12):

$$\theta_s \equiv \theta_1 = \pm\sqrt{\frac{2c}{n_{s0}\lambda_{s0}}\,\frac{\delta\lambda}{\delta v}}. \tag{7.15}$$

The angle of the idler is then given by

$$\theta_i \equiv \theta_2 = -(k_{s0}/k_{i0})\theta_1. \tag{7.16}$$

Conversely, the wavelength shift required to phase match the interaction at an angle

θ_s is

$$\delta\lambda = \frac{n_{s0}\,\delta v}{2c}\lambda_{s0}\theta_s^2. \tag{7.17}$$

The sign of the wavelength shift is determined by the relative magnitude of v_s and v_i. If $v_s > v_i$, then the phase-matching wavelength is shifted towards longer wavelengths; if $v_s < v_i$, then the phase-matching wavelength is shifted towards shorter wavelengths.

In the case of our experiment, ($\lambda_s \approx 1.5$ μm and $\lambda_i \approx 3.4$ μm), $v_s > v_i$ (the dispersion relation of $LiNbO_3$ is plotted in Fig. 4.1). Therefore the wavelength shift associated with noncollinear interactions is positive, as shown in Fig. 7.2.

7.3 Normalized Equations

7.3.1 Noncollinear Propagation

We assume that the pump beam is longitudinally invariant. We introduce the pump profile, $A_0(x)$, given by

$$E_0(x) = \bar{E}_0 A_0(x), \tag{7.18}$$

where $\bar{E}_0$ is the peak electric field amplitude of the pump beam. The signal and idler waves are normalized with respect to their photon numbers:

$$E_{1,2}(z,x) = \sqrt{\frac{\omega_{1,2}}{n_{1,2}\cos\theta_{1,2}}}\,A_{1,2}(z,x). \tag{7.19}$$

With these definitions, the coupling coefficient becomes

$$\gamma_0 = \sqrt{\frac{\omega_1\omega_2}{n_1 n_2 \cos\theta_1 \cos\theta_2}}\frac{d_{eff}}{c}\bar{E}_0. \tag{7.20}$$

It is natural to use the half-width of the pump beam, w_0, to normalize the transverse dimension:

$$\bar{x} = \frac{x}{w_0}. \tag{7.21}$$

Each of the waves overlaps with the pump over a length $w_0/\tan\theta_{1,2}$. Their geometric mean gives the characteristic noncollinear length:

$$L_{NC} = \frac{w_0}{\sqrt{\tan\theta_1 \tan\theta_2}}. \tag{7.22}$$

In the case of noncollinear propagation ($\theta_1 \neq 0$, $\theta_2 \neq 0$), we use this noncollinear length to normalize the longitudinal position:

$$\bar{z} = \frac{z}{L_{NC}}. \tag{7.23}$$

The normalized coupled-mode equations are

$$\frac{\partial A_1}{\partial \bar{z}} + \alpha_1 \frac{\partial A_1}{\partial \bar{x}} - i\beta_1 \frac{\partial^2 A_1}{\partial \bar{x}^2} = i\lambda^{1/2} A_0(\bar{x}) A_2^* e^{i\phi(\bar{z})} \tag{7.24}$$

$$\frac{\partial A_2}{\partial \bar{z}} + \alpha_2 \frac{\partial A_2}{\partial \bar{x}} - i\beta_2 \frac{\partial^2 A_2}{\partial \bar{x}^2} = i\lambda^{1/2} A_0(\bar{x}) A_1^* e^{i\phi(\bar{z})}, \tag{7.25}$$

with

$$\alpha_{1,2} = \mathrm{sgn}\,(\tan\theta_{1,2}) \sqrt{\left|\frac{\tan\theta_{1,2}}{\tan\theta_{2,1}}\right|} \tag{7.26}$$

$$\beta_{1,2} = \frac{1}{2k_{1,2}\cos\theta_{1,2} w_0 \sqrt{|\tan\theta_1 \tan\theta_2|}} \tag{7.27}$$

$$\lambda = (\gamma_0 L_{NC})^2. \tag{7.28}$$

Note that, since phase matching is possible only if the angles θ_1 and θ_2 have opposite signs, we have the relation

$$\alpha_1 \alpha_2 = -1. \tag{7.29}$$

From the discussion of noncollinear phase-matching, section 7.2, Eq. (7.16), we know that the angles are related by $\theta_2 = -(k_{s0}/k_{i0})\theta_1$. Therefore, in the limit of small angles, the non-degeneracy parameters $\alpha_{1,2}$ can be written

$$\alpha_1 = 1/\sqrt{r} \tag{7.30}$$

$$\alpha_2 = -\sqrt{r}, \tag{7.31}$$

where

$$r = \frac{k_{s0}}{k_{i0}} = \frac{n_{s0}\lambda_{i0}}{n_{i0}\lambda_{s0}}. \tag{7.32}$$

The normalized parameters can be related in a simple manner to the ratio of the wavelengths.

In normalized units, a linearly chirped grating profile is given by

$$\bar{\kappa}(\bar{z}) = \bar{\kappa}'(\bar{z} - \bar{z}_{pm}), \tag{7.33}$$

where

$$\bar{\kappa}' = \kappa' L_{NC}^2 \tag{7.34}$$

is the normalized chirp rate and $\bar{z}_{pm}$ is the perfect phase-matched point. The dephasing is then

$$\phi(\bar{z}) = \frac{\bar{\kappa}'}{2}\left[(\bar{z} - \bar{z}_{pm})^2 - (\bar{z}_0 - \bar{z}_{pm})^2\right]. \tag{7.35}$$

The normalization introduced in this section is very convenient to study noncollinear interactions. However there is a difficulty associated with the fact that the angle is built into the normalized parameters. In practice, it is useful to plot the growth rate, K, as a function of angle. In normalized units the growth rate is $\bar{K} = L_{NC}K$. The physical growth rate can be extracted, and its intrinsic dependence on angle eliminated, by plotting $\bar{K}/\sqrt{\lambda} = K/\gamma_0$, as a function of $1/\sqrt{\lambda} = 1/\gamma_0 L_{NC} = |\tan\theta_1 \tan\theta_2|^{1/2}/\gamma_0 w_0$, which, for small angles, is proportional to the geometric mean of the noncollinear angles, $|\theta_1\theta_2|^{1/2}$.

7.3.2 Collinear Propagation with Diffraction

The normalization discussed above is well suited for the study of a noncollinear situation. However it is inadequate in a collinear geometry because in this case $L_{NC} = \infty$.

When $\theta_1 = \theta_2 = 0$, it is best to normalize the longitudinal position using the chirp rate:

$$\bar{z} = {\kappa_0'}^{1/2} z, \tag{7.36}$$

where κ_0' is a reference value for the chirp rate. This is in fact the normalization we used in our study of the Rosenbluth model in chapter 2. The normalization of the x-axis remains the same. The coupled equations can be written as

$$\frac{\partial A_1}{\partial \bar{z}} - i\beta_1 \frac{\partial^2 A_1}{\partial \bar{x}^2} = i\lambda_R^{1/2} A_0(\bar{x}) A_2^* e^{i\phi(\bar{z})} \tag{7.37}$$

$$\frac{\partial A_2}{\partial \bar{z}} - i\beta_2 \frac{\partial^2 A_2}{\partial \bar{x}^2} = i\lambda_R^{1/2} A_0(\bar{x}) A_1^* e^{i\phi(\bar{z})}, \tag{7.38}$$

where now

$$\beta_{1,2} = \frac{1}{2k_{1,2} w_0^2 {\kappa_0'}^{1/2}}, \tag{7.39}$$

and where the coupling coefficient is that of the Rosenbluth model,

$$\lambda_R = \frac{\gamma_0^2}{\kappa_0'}. \tag{7.40}$$

(We use the subscript R to distinguish the gain parameter associated with the Rosenbluth model.) In those units, the dephasing associated with a linearly chirped QPM grating is

$$\phi(\bar{z}) = \frac{1}{2}\frac{\kappa'}{\kappa_0'}\left[(\bar{z} - \bar{z}_{pm})^2 - (\bar{z}_0 - \bar{z}_{pm})^2\right]. \tag{7.41}$$

7.4 Two Known Limits

The novelty of the model presented here lies in the fact that it combines at the same time a *laterally localized pump* and a *non-uniform phase-matching profile*.

Pump localization and dephasing are well known limits which have been studied separately. The case where none are present has been solved by Bobroff and Haus [43]. In the presence of dephasing but no pump localization, we recover the time-dependent Rosenbluth model [40]. The opposite limit, that of a localized pump with no dephasing, has been studied by Sushchik [67], who showed that gain-guided modes can exist when the noncollinear angles have opposite signs (i.e. $\alpha_1\alpha_2 < 0$).

A special case of the Sushchik modes is obtained when the two waves are counter-propagating ($\theta_1 = 90^{\mathrm{O}}$, $\theta_2 = -90^{\mathrm{O}}$). This is the typical case encountered in laser-plasma interactions (discussed in chapter 3), the field in which the Rosenbluth and Sushchik analyses were performed. An example in optics is that of a backwards wave oscillator [68].

The Suschik modes are in fact a case of absolute instability [46]. The case $\alpha_1\alpha_2 < 0$ corresponds to counter-propagating waves in the transverse dimension. It is a necessary condition for the existence of an absolute instability. If $\alpha_1\alpha_2 > 0$, then the waves are co-propagating and the instability is convective (i.e. the amplification is finite). This situation was studied by Afeyan and Fejer [42], who calculated the gain and shape of pulses generated by a short pump pulse in the presence of group-velocity walk-off.

What will be the outcome when pump localization *and* dephasing are both present? Will the instability remain absolute like the Suschik modes, or will it become convective like the Rosenbluth model? Preliminary numerical simulations suggest that the absolute instability can be restored when the pump is localized. The following chapters explore this in great detail.

Chapter 8

2-D Model: Numerical Simulations

8.1 Numerical Method

We solve the propagation equations numerically using the operator splitting method [69].

The mesh size used depends on the type of problem. Non-uniform phase-matching profiles cause rapid phase accumulation and require a finer resolution. Table 8.1 lists typical values for $\Delta\bar{z}$ and $\Delta\bar{x}$ in the three cases explored. In certain cases, it was necessary to use a finer mesh (for example in the case of particularly large chirp rates or propagation over very large distances).

Table 8.1: Typical mesh size for numerical simulations.

Equations modeled	Δz	Δx
Noncollinear, uniform	0.05	0.05
Noncollinear, non-uniform	0.025	0.05
Collinear, negative dephasing rate, diffraction	0.02	0.02

8.2 Noncollinear Interactions in Uniform Medium

The model for beams interacting at noncollinear phase-matching angles in uniform media is the following:

$$\left(\frac{\partial}{\partial z} + \alpha_1 \frac{\partial}{\partial x}\right) A_1 = i\lambda^{1/2} A_0(x) A_2^* \tag{8.1}$$

$$\left(\frac{\partial}{\partial z} + \alpha_2 \frac{\partial}{\partial x}\right) A_2 = i\lambda^{1/2} A_0(x) A_1^* \tag{8.2}$$

In this chapter we investigate this model in its own right: we drop the bars denoting normalized x and z variables and simply study the effect of the parameters (α_1, α_2 and λ in this case) on the evolution of the waves.

We require that α_1 and α_2 have opposite signs (this follows from the requirement of noncollinear phase-matching) and that $\alpha_1\alpha_2 = -1$ (as follows from the normalization introduced in chapter 7). We will consider a gaussian pump profile:

$$|A_0(x)|^2 = e^{-x^2}. \tag{8.3}$$

Therefore the only two parameters in this model are the "angle" α_1 and the gain parameter λ.

The interaction is seeded by the signal wave only. At the input we use a smoothed step function that covers entirely the pump beam. More precisely, the initial conditions at $z = 0$ are

$$A_1(0,x) = \frac{1}{4}\left[\tanh\left(\frac{x - w_1/2}{\Delta w}\right) + 1\right]\left[\tanh\left(\frac{x + w_1/2}{\Delta w}\right) + 1\right] \tag{8.4}$$

$$A_2(0,x) = 0, \tag{8.5}$$

with $w_1 = 4$ and $\Delta w = 0.5$.

The strength of the coupling is turned on adiabatically along the propagation direction in order to avoid undesired effects related to hard edges (see chapter 2). We use a profile for the gain parameter λ which is zero initially and approaches the

target value λ^* progressively:

$$\lambda(z) = \frac{\lambda^*}{2}\left[h \tanh\left(\frac{z - z_\lambda}{\Delta z_\lambda}\right) + 1 + \epsilon\right] \tag{8.6}$$

with $z_\lambda = 4$, $\Delta z_\lambda = 0.1$, and where h and ϵ are two constants chosen so that $\lambda = 0$ at $z = 0$ and $\lambda = \lambda^*$ when $z \gg z_\lambda$. This profile is shown in Fig. 8.1. From now on, however, we will drop the asterisk and use the symbol "λ" to represent its target value λ^*.

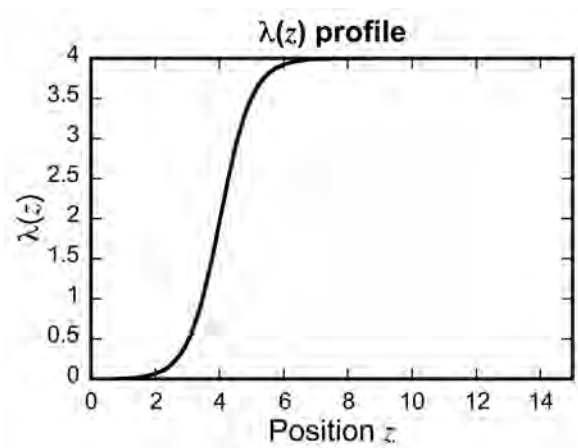

Figure 8.1: Adiabatic turn-on of the gain parameter λ.

8.2.1 Detailed Example: $\lambda = 4$, $\alpha_1 = 1$

Here we present in detail the numerical results for the case $\lambda = 4$, $\alpha_1 = 1$ (and, therefore, $\alpha_2 = -1$).

Fig. 8.2 shows 2-D plots of the amplitude of the beams. On a logarithmic scale, we see the input signal beam which propagates at the noncollinear angle. The signal and idler waves are then amplified along the direction of the pump beam.

Fig. 8.3 shows the peak amplitude along the propagation direction. The waves grow exponentially (increasing linearly on a logarithmic scale). The signal and idler see the same growth rate.

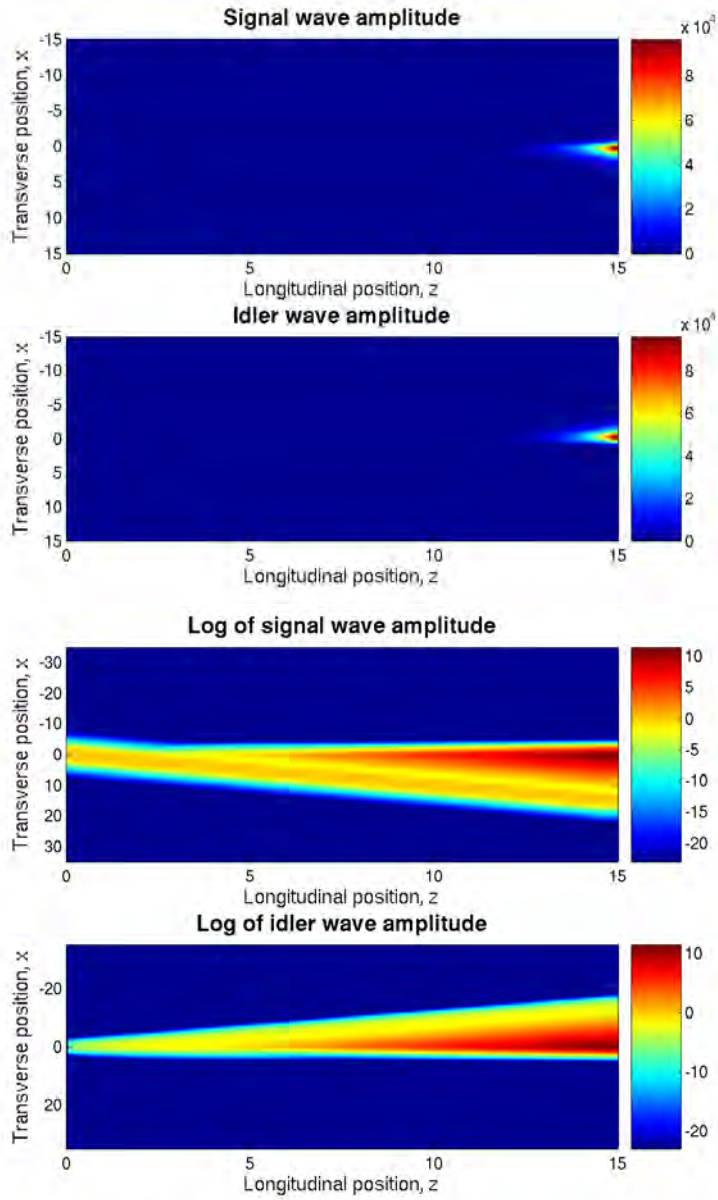

Figure 8.2: 2-D plots of the amplitude of the beams, in linear scale (top) and logarithmic scale (bottom).

The transverse beam profiles at the end of the simulation ($z = 15$) are shown in Fig. 8.4. The signal wave is purely real, while the idler wave is purely imaginary.

In order to examine the beam shape in more details, we take transverse cuts

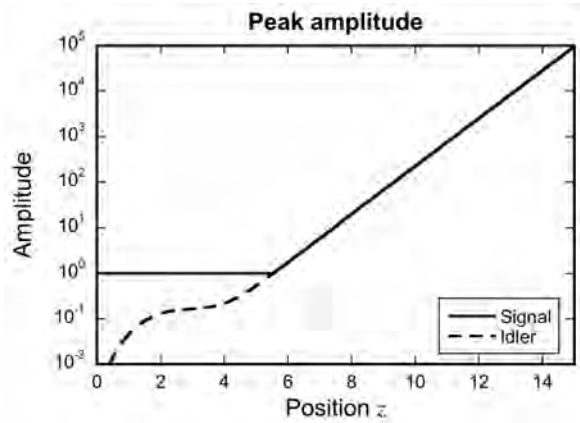

Figure 8.3: Peak amplitude.

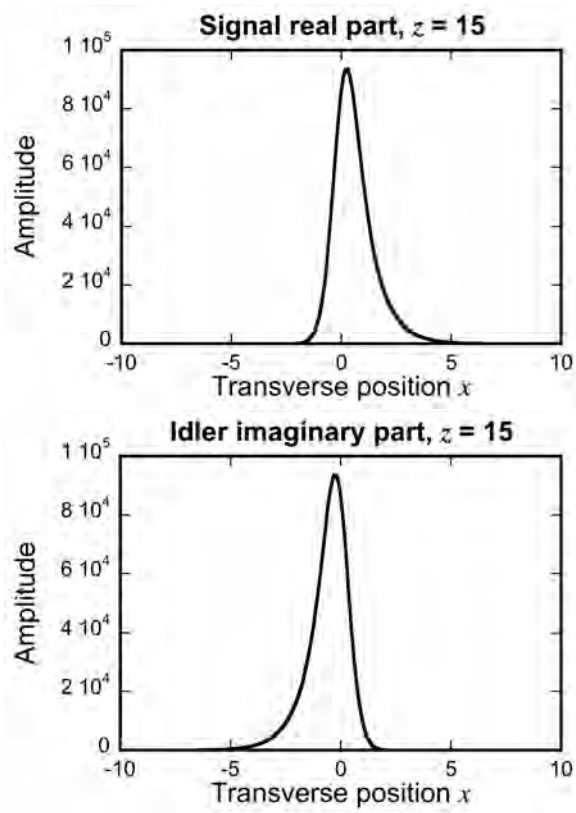

Figure 8.4: Transverse profile of the signal (top) and idler (bottom) beams.

at various positions along the propagation direction. These are shown in Fig. 8.5.

Clearly, after some distance, the shape of the amplified wave is independent of position. The amplified waves behave as modes localized inside the pump beam. In the present case, the signal and idler modes are symmetric, as expected from the symmetry of the original equations (recall that we are considering here the case of $\alpha_2 = -1/\alpha_1 = -1$). The asymmetry arising from $|\alpha_2| \neq \alpha_1$ will be explored later.

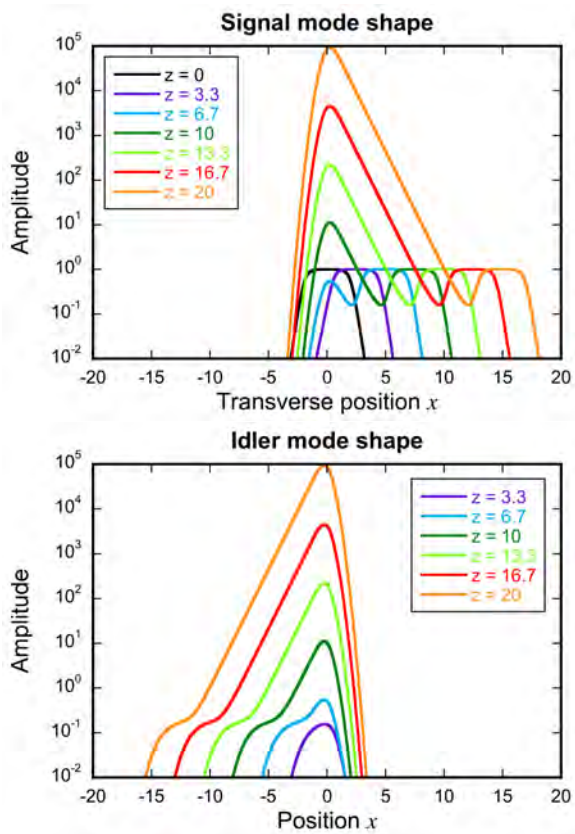

Figure 8.5: Mode shape at various positions along the direction of propagation.

We now examine the behavior of the waves in the Fourier domain. The 2-D plot of the Fourier transforms in x is shown in Fig. 8.6. Transverse cuts of the Fourier transforms of the final beam shapes are shown in Fig. 8.7.

Finally, the 2-D plot resulting from taking Fourier transforms in x and z is shown in Fig. 8.8. On a linear scale, the only visible feature is a dot located at the origin (the horizontal trace is due to the abrupt truncation of the beam in z). However, on a logarithmic scale the line corresponding to the dispersion relation of the wave is visible

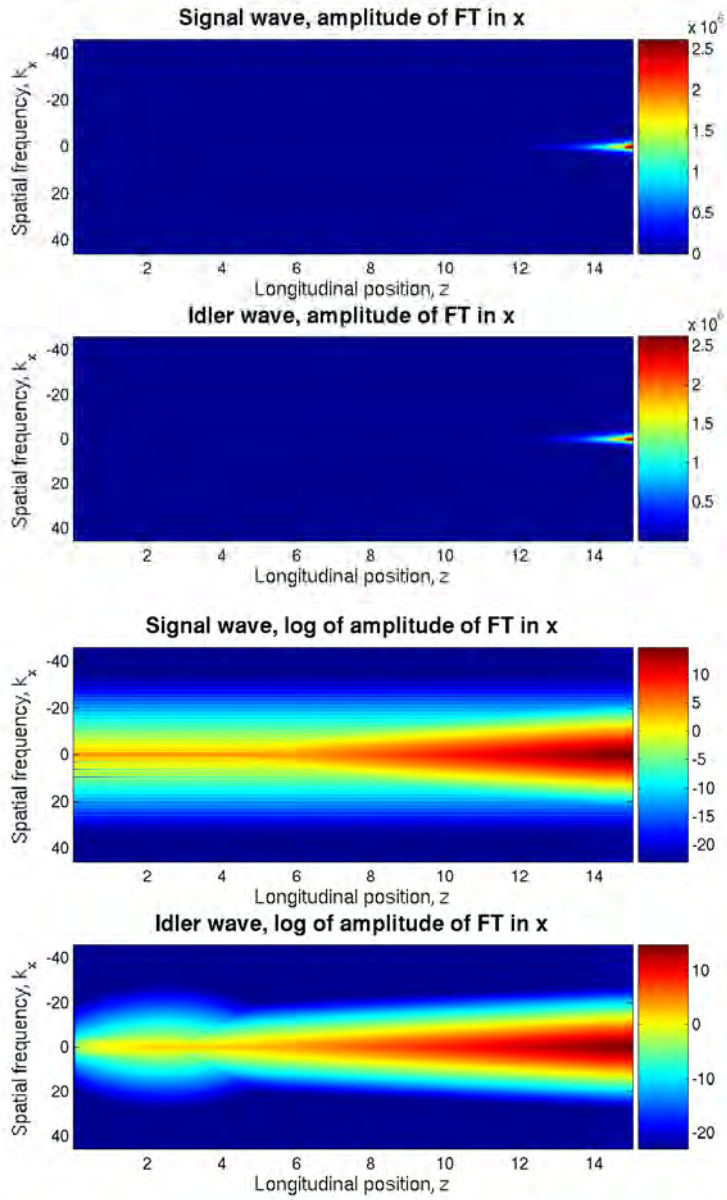

Figure 8.6: 2-D plots of the Fourier transforms in x of the beam profiles, on a linear (top) and logarithmic scale (bottom).

(faint diagonal line). (Recall that the Fourier-space equivalent of the differential operator in the left-hand-side of Eq. (8.1) is $-ik_z - i\alpha_1 k_x$; equating this quantity to zero gives the dispersion relation $k_x = -k_z/\alpha_1$.)

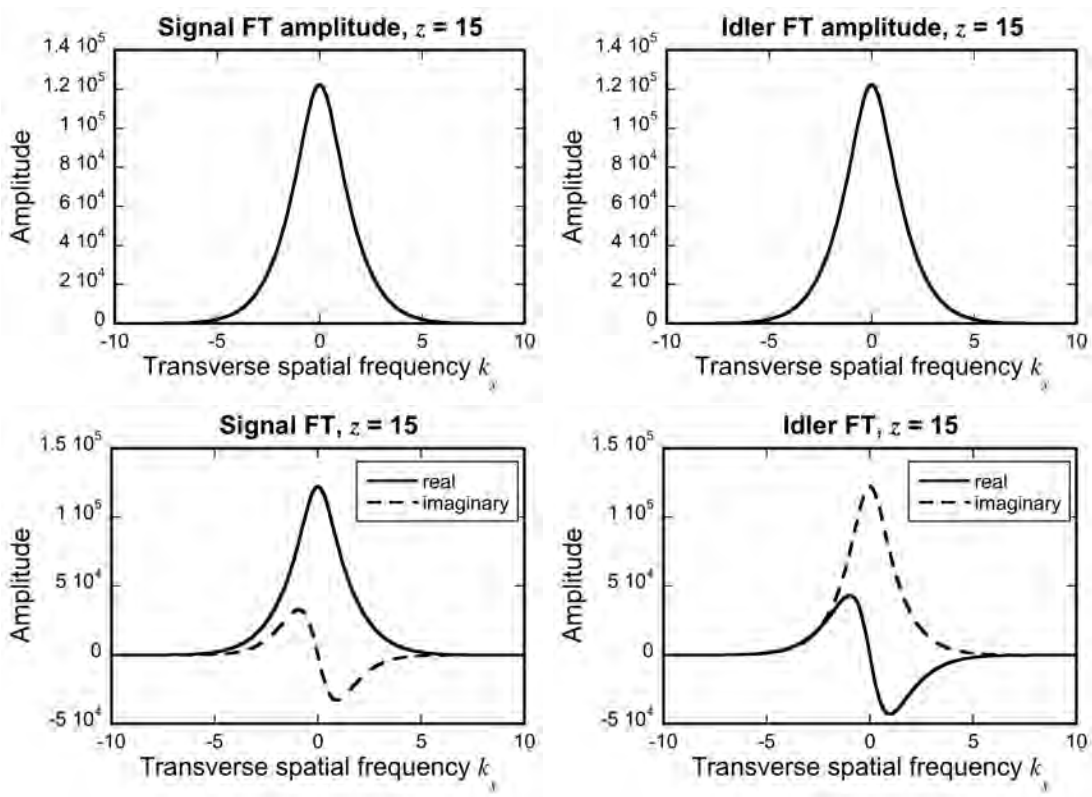

Figure 8.7: Transverse cuts of the Fourier transforms in x of the beam profiles.

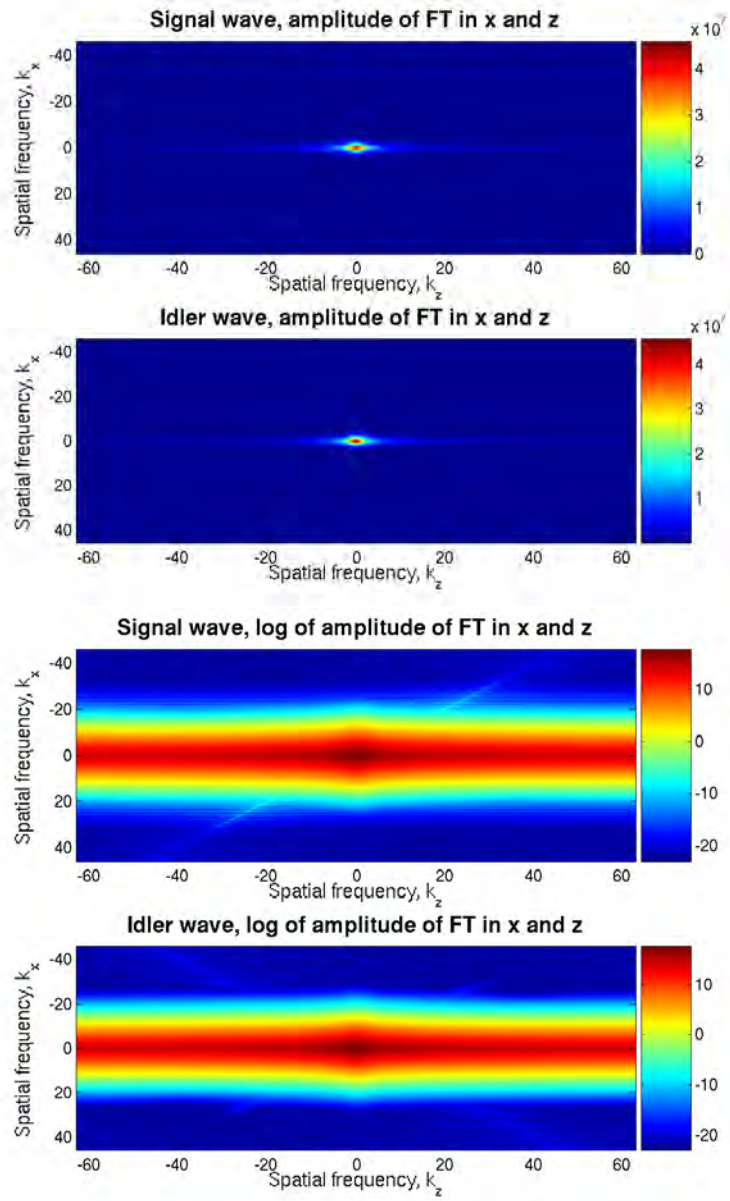

Figure 8.8: 2-D plots of the Fourier transforms in x and z, on a linear (top) and logarithmic scale(bottom).

8.2.2 Growth Rate

In the example shown above we saw that the signal and idler modes grow exponentially at the same rate. In this section we study how the growth rate depends on λ and α_1.

The (normalized) growth rate measured numerically is defined using the peak amplitude:

$$\bar{K} = \frac{d}{dz} \ln |A_{1,peak}|. \tag{8.7}$$

Here, $A_{1,peak}$ is the signal wave $A_1(z, x)$ evaluated at the transverse position x of maximum amplitude. (However, since the shape of the mode remains fixed, calculating the growth rate at a different lateral position would give the same value.) The growth rate is calculated at the end of the simulation ($z = 15$ in our case), in the regime where it is a constant.

Fig. 8.9 shows how the growth rate depends on the gain parameter λ, with $\alpha_1 = 1$ fixed. There is a threshold below which localized growing modes do not exist. This threshold depends on the pump profile. Although very interesting, the behavior close to threshold will not be explored in this thesis.

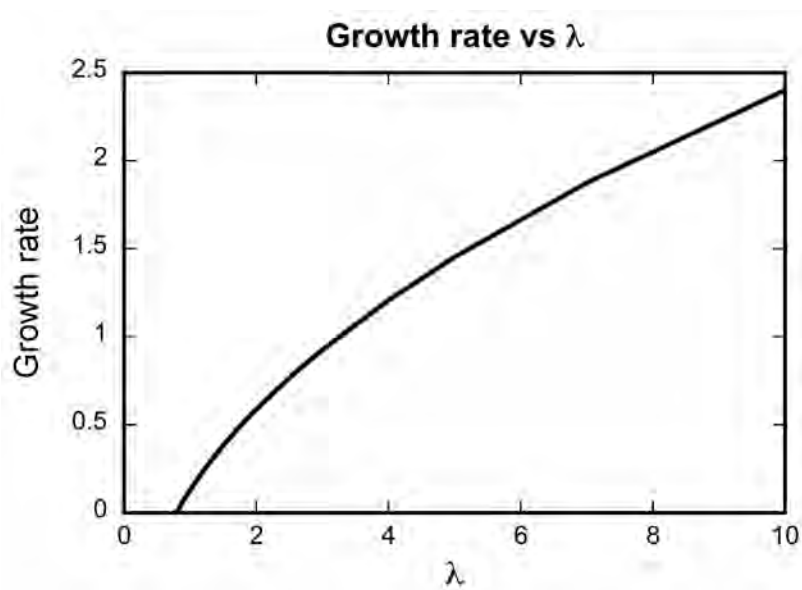

Figure 8.9: Growth rate, $\bar{K}$, as a function of the gain parameter λ, for $\alpha_1 = 1$.

The effect of the "angle" parameter α_1 is shown in Fig. 8.10. Recall that $\alpha_2 =$

$-1/\alpha_1$ is fixed once α_1 is determined. The growth is maximum in the symmetric case $\alpha_1 = -\alpha_2 = 1$ (i.e. when the signal and idler wavelengths are degenerate) and decreases when the symmetry is broken.

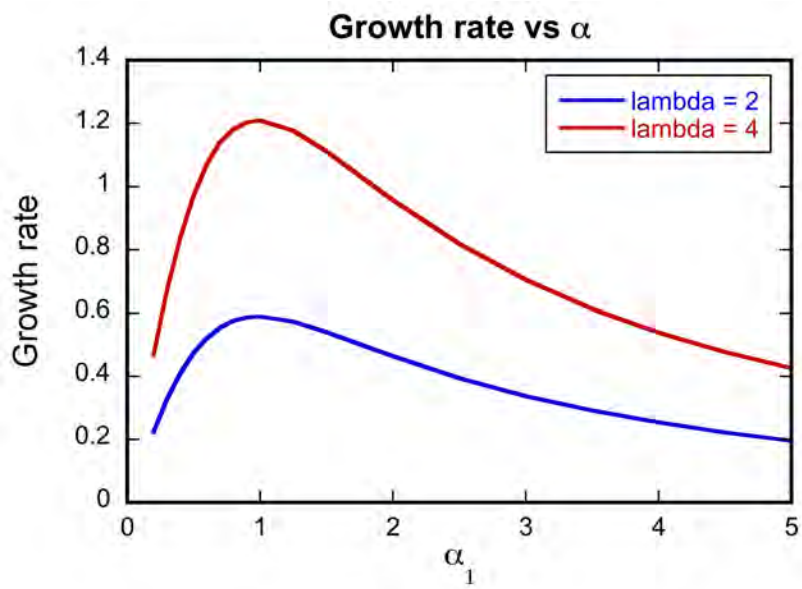

Figure 8.10: Growth rate, $\bar{K}$, as a function of the asymmetry parameter α_1.

8.2.3 Mode Shape

In the example shown above, we saw that the beam shapes are invariant in z. The signal and idler waves can be described as

$$A_{1,2} = e^{\bar{K}z}\Psi_{1,2}(x), \tag{8.8}$$

where $\Psi_{1,2}(x)$ is the mode shape.

Fig. 8.11 illustrates the mode shape for different values of α_1. The higher the α_1, the wider is the mode; however its shape remains similar. As expected, the signal and idler modes of same $|\alpha|$ are symmetric (in other words, the idler mode corresponding to $\alpha_2 = -2$ is symmetric with respect to the signal mode corresponding to $\alpha_1 = 2$).

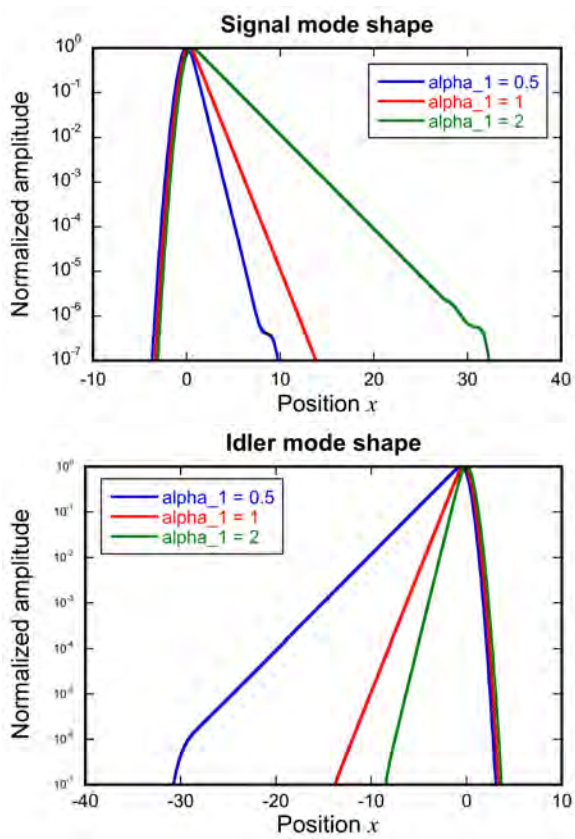

Figure 8.11: Mode shapes for various values of α_1, at fixed $\lambda = 4$.

8.3 Noncollinear Interactions in Non-Uniform Medium

The non-uniformity is modeled by introducing dephasing in the coupled equations:

$$\left(\frac{\partial}{\partial z} + \alpha_1 \frac{\partial}{\partial x}\right) A_1 = i\lambda^{1/2} A_0(x) A_2^* e^{i\phi(z)} \tag{8.9}$$

$$\left(\frac{\partial}{\partial z} + \alpha_2 \frac{\partial}{\partial x}\right) A_2 = i\lambda^{1/2} A_0(x) A_1^* e^{i\phi(z)}, \tag{8.10}$$

with

$$\phi(z) = \int_0^z \kappa(z')\, dz. \tag{8.11}$$

The phase-matching profile $\kappa(z)$ is characterized by its slope, κ'. In the simulation, the non-uniformity is turned on adiabatically once the growing modes are established in a short uniform section at the beginning of the medium. We use the following $\kappa(z)$ profile:

$$\kappa(z) = \begin{cases} \exp\left(\frac{z - z_\kappa}{\Delta z_\kappa}\right) - \epsilon, & z < z_\kappa \\ \kappa' z - C, & z > z_\kappa \end{cases}, \tag{8.12}$$

where ϵ and C are constants chosen to ensure that $\kappa = 0$ at $z = 0$ and that its derivative is continuous at z_κ. We use $z_\kappa = 8$ and $\Delta z_\kappa = 2$. The adiabatic λ and κ profiles are shown in Fig. 8.12.

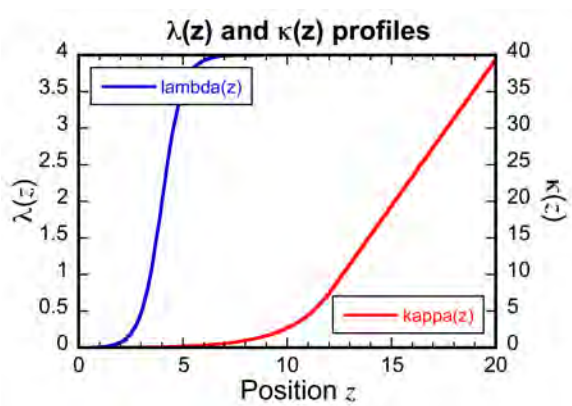

Figure 8.12: Profiles $\lambda(z)$ and $\kappa(z)$.

Again, we will assume the degenerate case (i.e. $\alpha_1\alpha_2 = -1$). There are now three

independent parameters: α_1, λ and κ'.

8.3.1 Detailed Example: $\alpha_1 = 1$, $\lambda = 4$, $\kappa' = 4$

Fig. 8.13 shows the 2-D plots of the amplitude of the beams. Their phase is shown in Fig. 8.14. These plots indicate that the phase and the logarithm of the amplitude are constant along the noncollinear direction of propagation (i.e. along the characteristics defined by the straight lines $\bar{z} - \bar{x}/\alpha_1$ in the case of the signal and $\bar{z} - \bar{x}/\alpha_2$ in the case of the idler).

Those plots reveal a most surprising result: the waves grow along z even in the presence of dephasing. According to the 1-D Rosenbluth model, we expect the growth to be limited to the phase-matched region. But these numerical results show that, in a noncollinear configuration, and in the presence of a laterally localized pump, exponentially growing modes can exist.

Fig. 8.15 shows the peak amplitude along the direction of propagation. The reduction in the growth rate (around $z = 11$) corresponds to the position where the non-uniformity is turned on (see the κ-profile shown in Fig. 8.12). It illustrates the reduction of growth rate caused by the non-uniformity.

Fig. 8.16 shows the phase accumulation caused by the non-uniformity. The signal and idler phases at peak amplitude are precisely equal to $\phi/2$.

The following transverse cuts illustrate the details of the amplification process. The location of these cuts is illustrated in Fig. 8.17. The first of these cuts, at $z = 6.7$, shows the modes as they grow before reaching the non-uniform region. (The signal wave contains a small imaginary component (and vice-versa for the idler) due to the tail of the κ-profile.) The second cut, at $z = 13.3$, illustrates the accumulation of transverse phase caused by the dephasing. The two other cuts, at $z = 16.7$ and $z = 20$, illustrate the transverse profile further along the propagation direction.

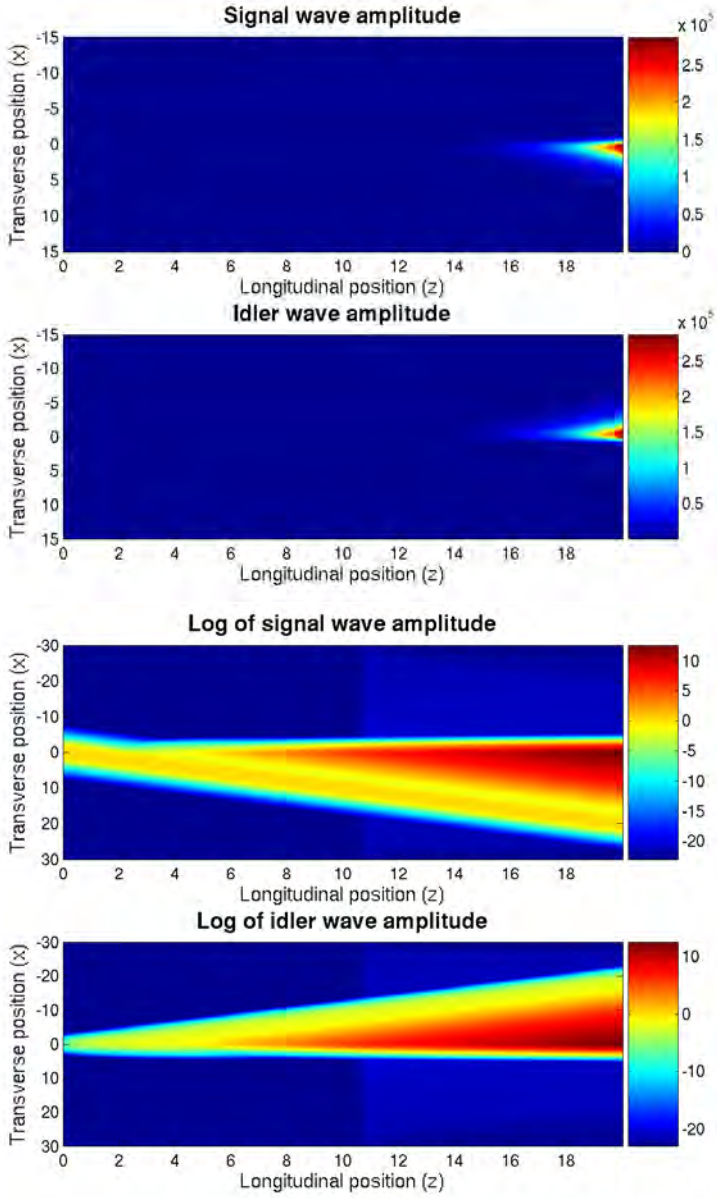

Figure 8.13: 2-D plots of the amplitude of the beams, in linear scale (top) and logarithmic scale (bottom).

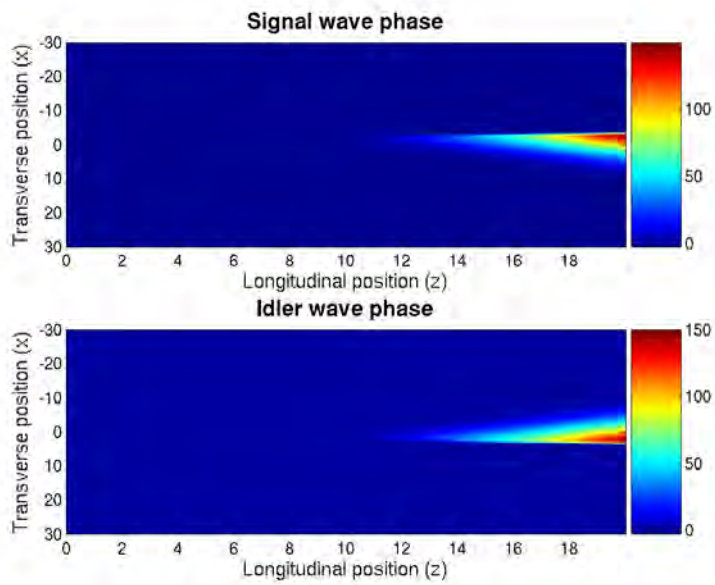

Figure 8.14: 2-D plots of the phase of the beams.

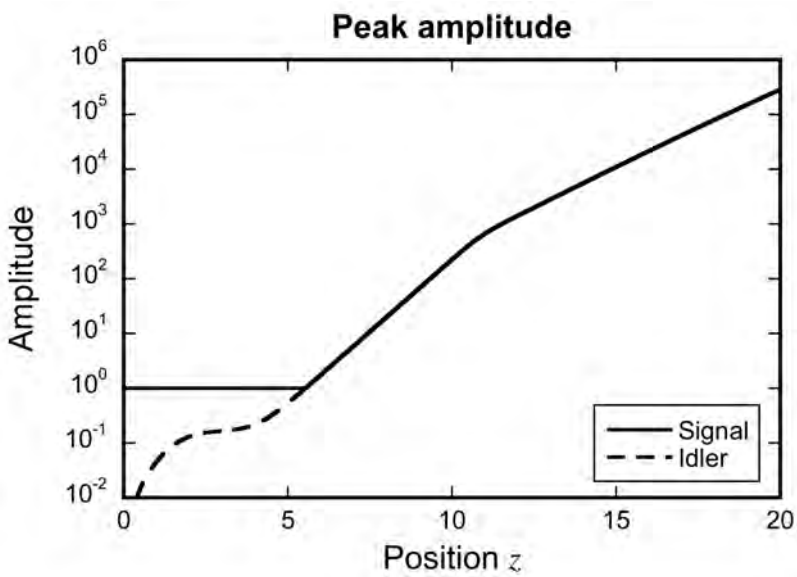

Figure 8.15: Peak amplitude.

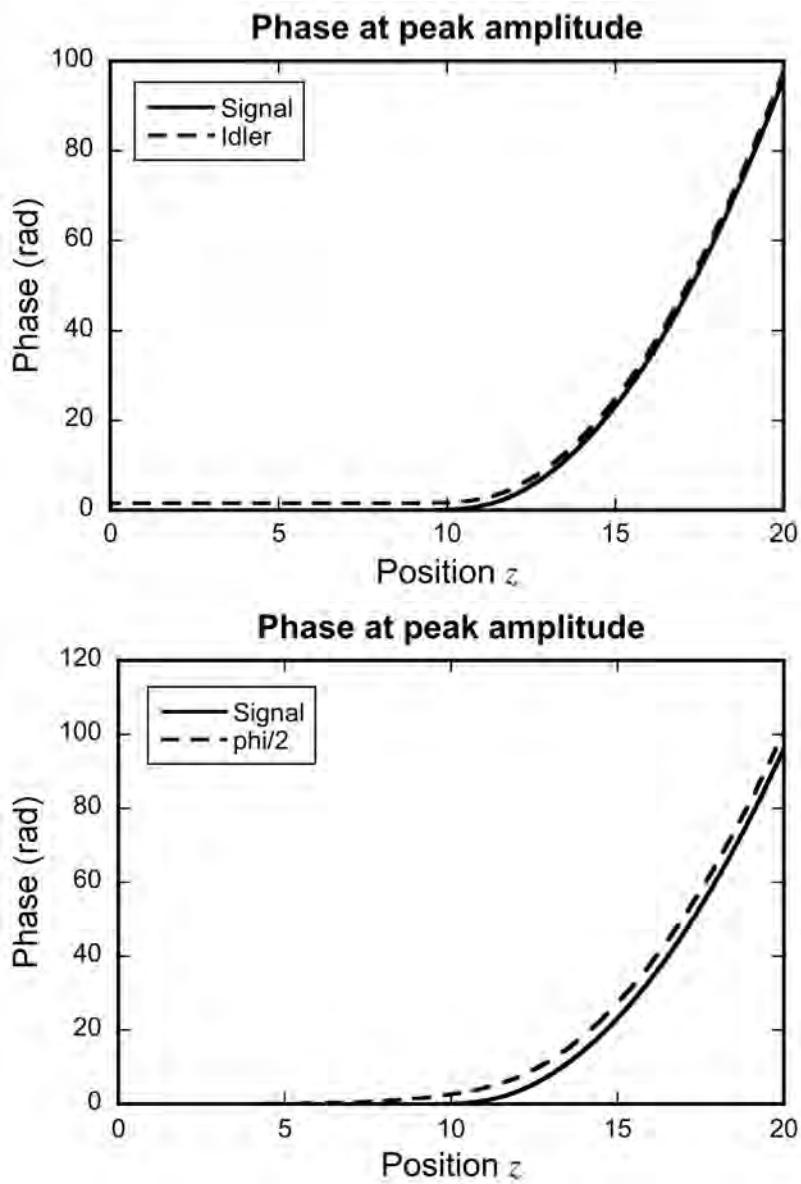

Figure 8.16: Phase at peak amplitude (top) and comparison with $\phi/2$ (bottom).

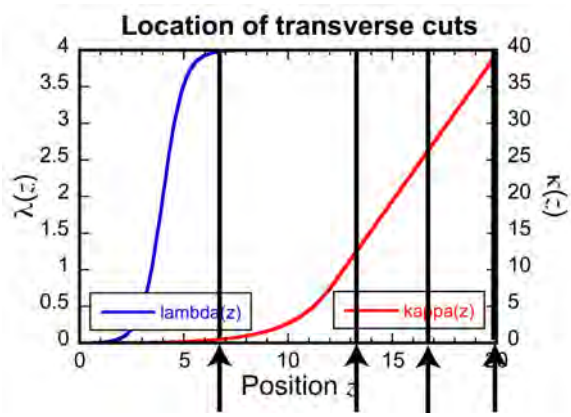

Figure 8.17: Location of the transverse cuts in Fig 8.18 - 8.21 compared with the λ and κ profiles.

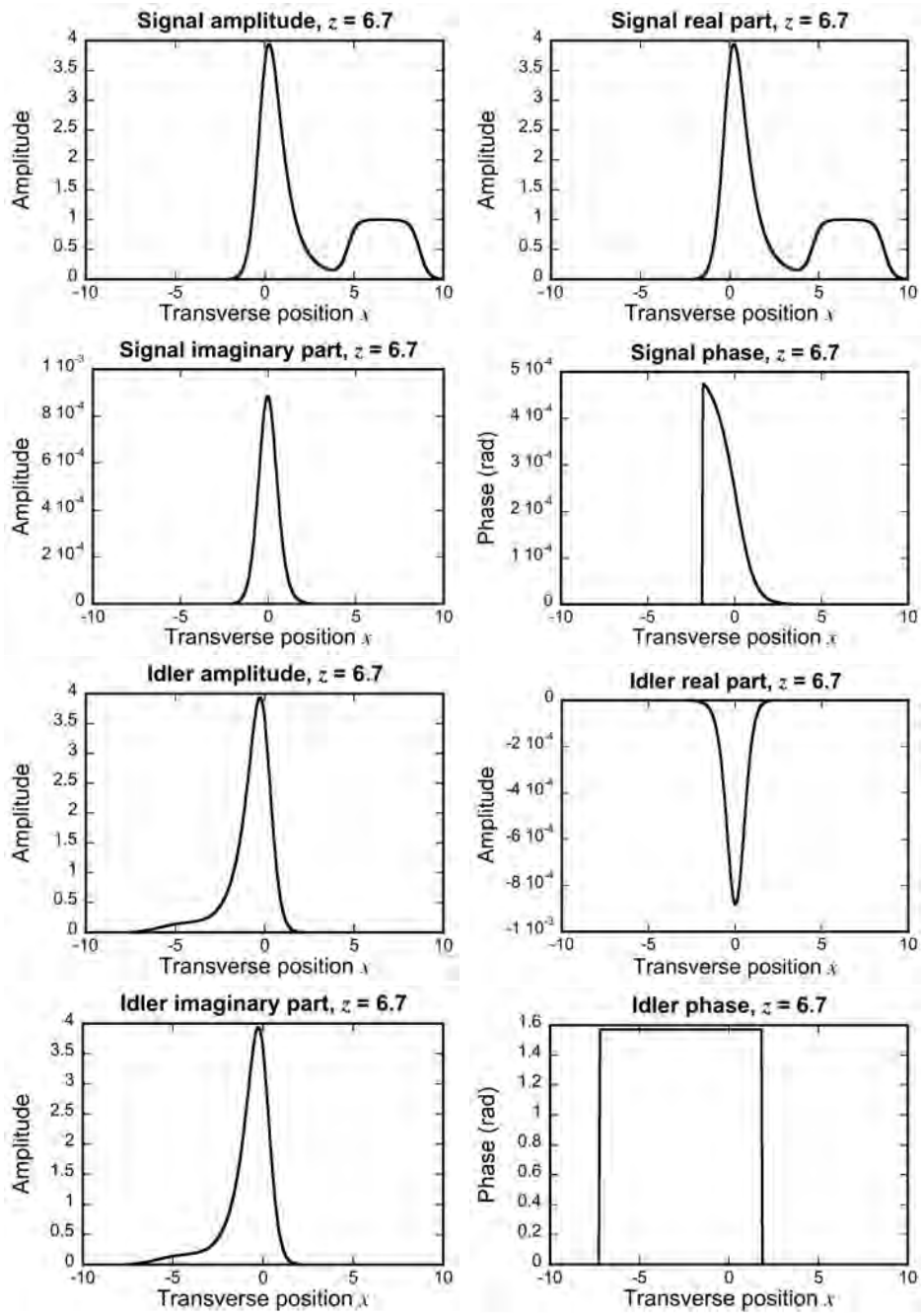

Figure 8.18: Transverse cuts before reaching the non-uniform region ($z = 6.7$).

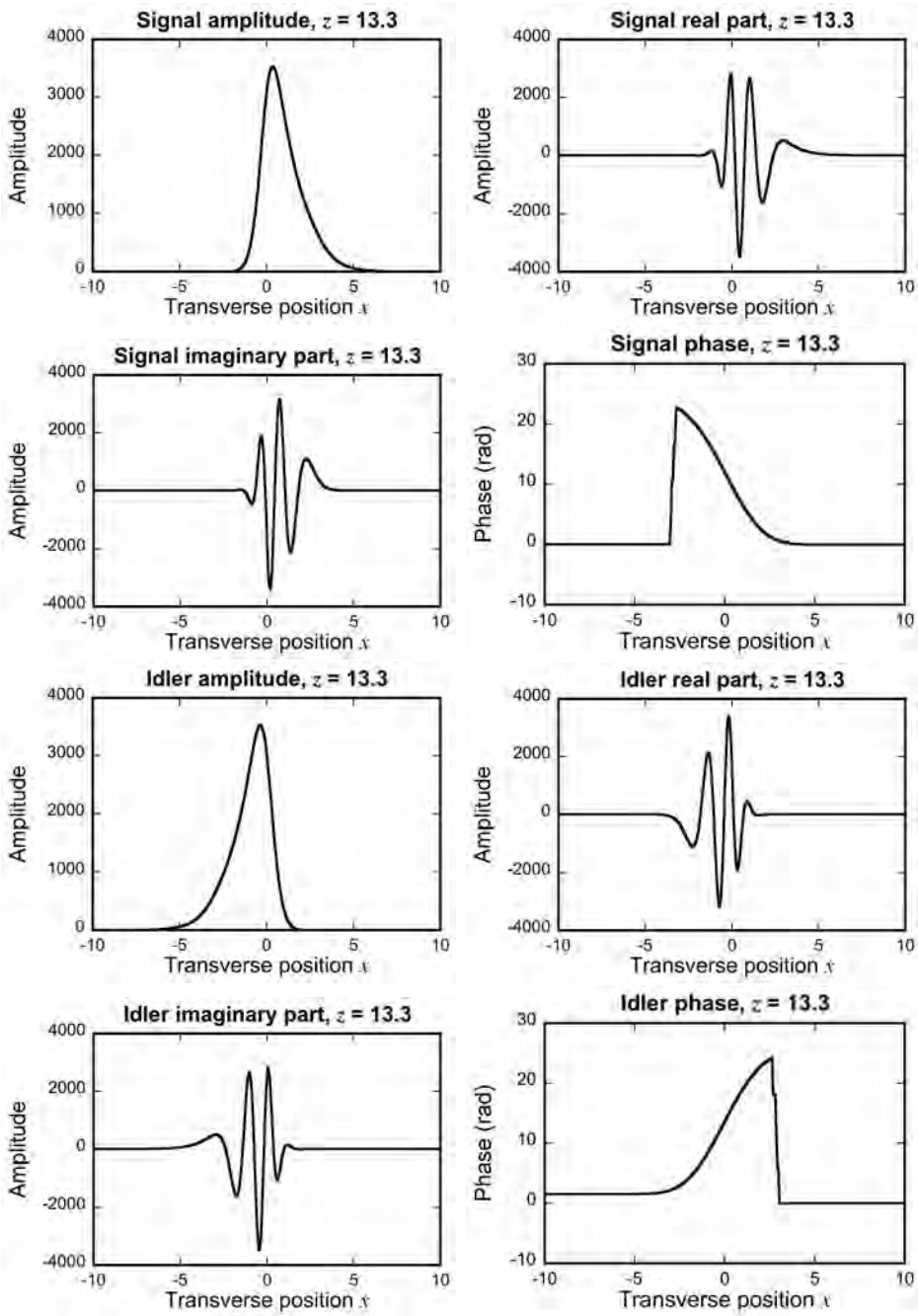

Figure 8.19: Transverse cuts after encountering the non-uniform region ($z = 13.3$).

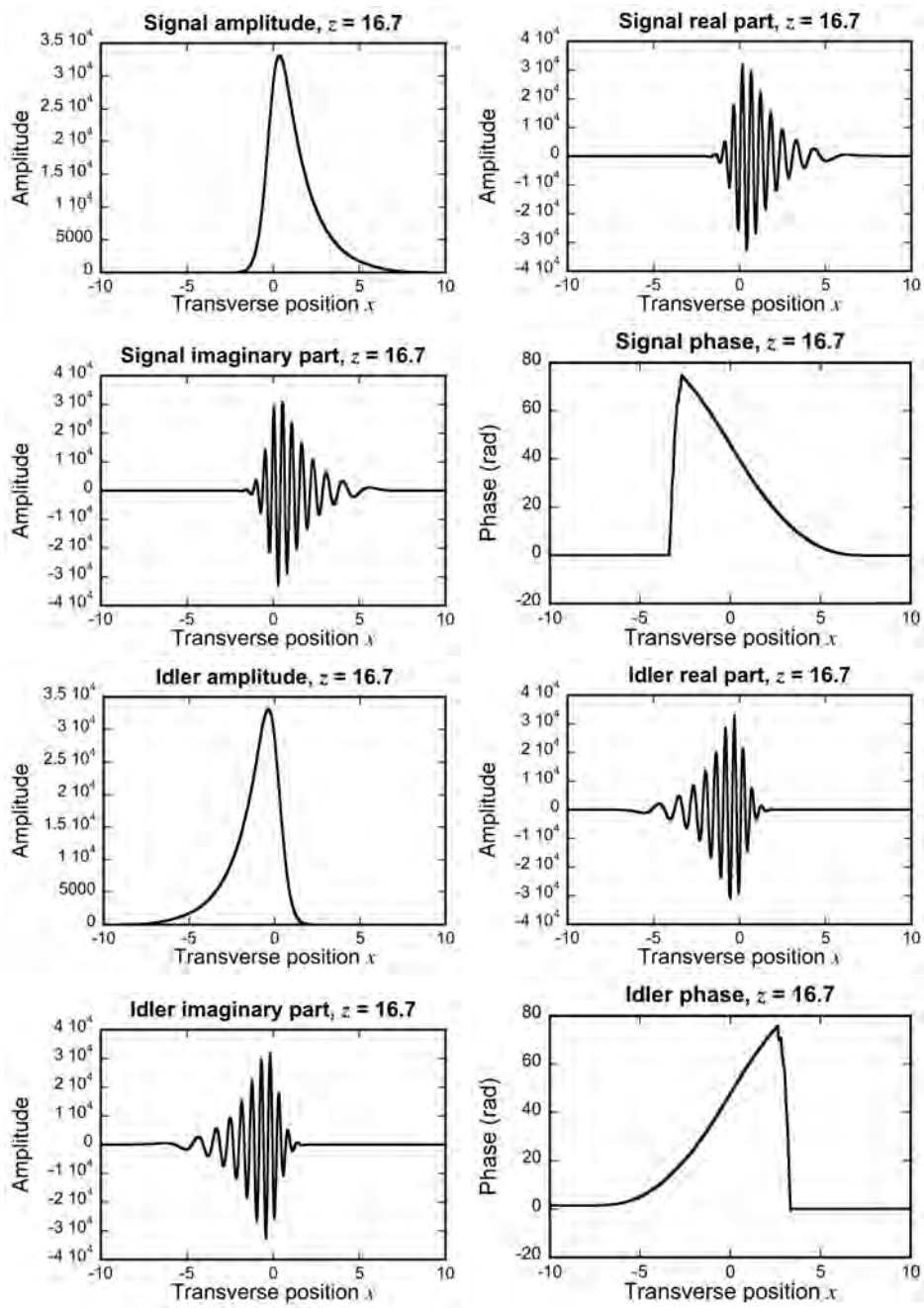

Figure 8.20: Transverse cuts further into the non-uniform region ($z = 16.7$).

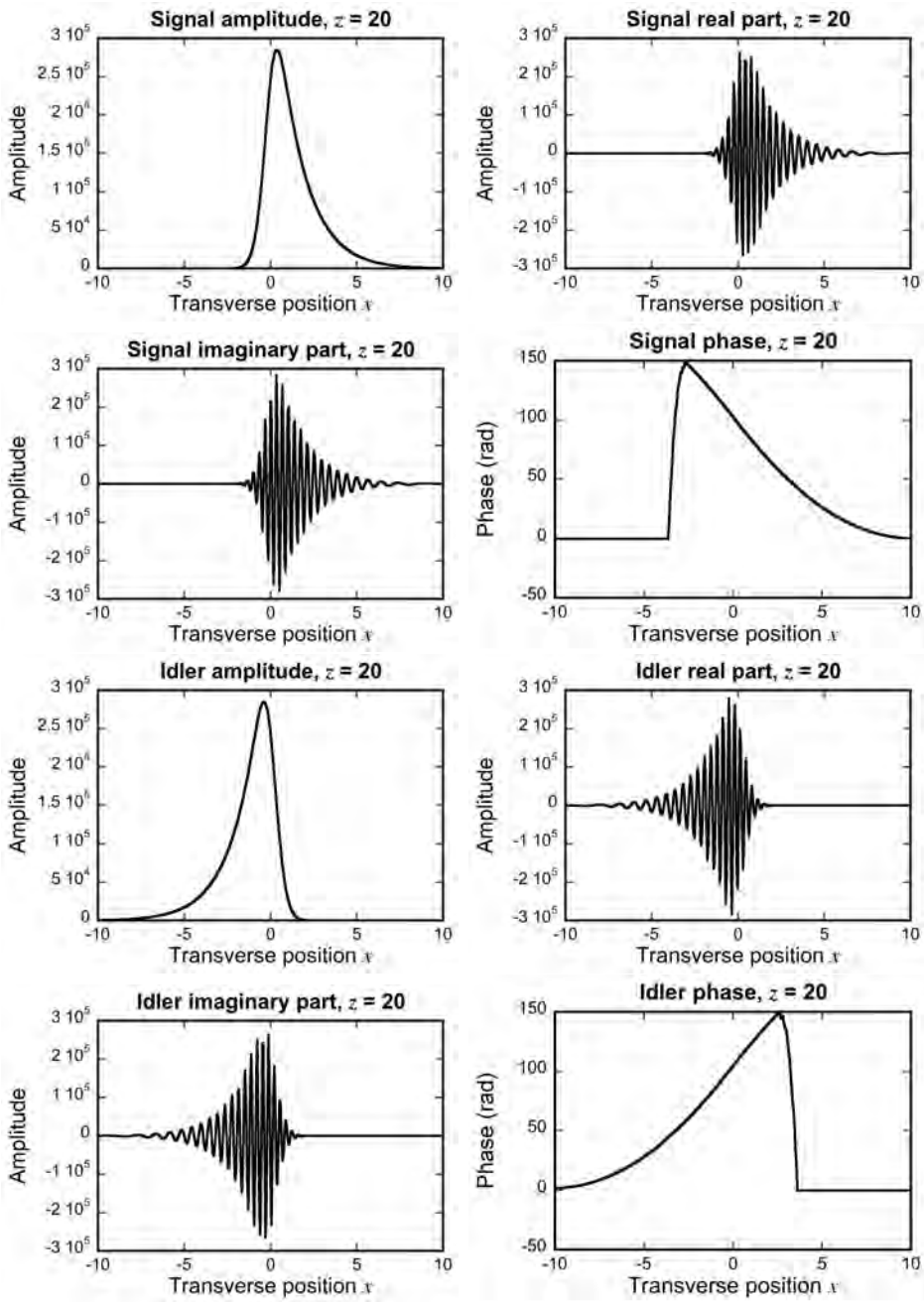

Figure 8.21: Transverse cuts at the end of the simulation ($z = 20$).

The 2-D plots of the Fourier transform in x are shown in Fig. 8.22. The field is shifted in k_x-space, consistent with a phase accumulation in x which increases along z.

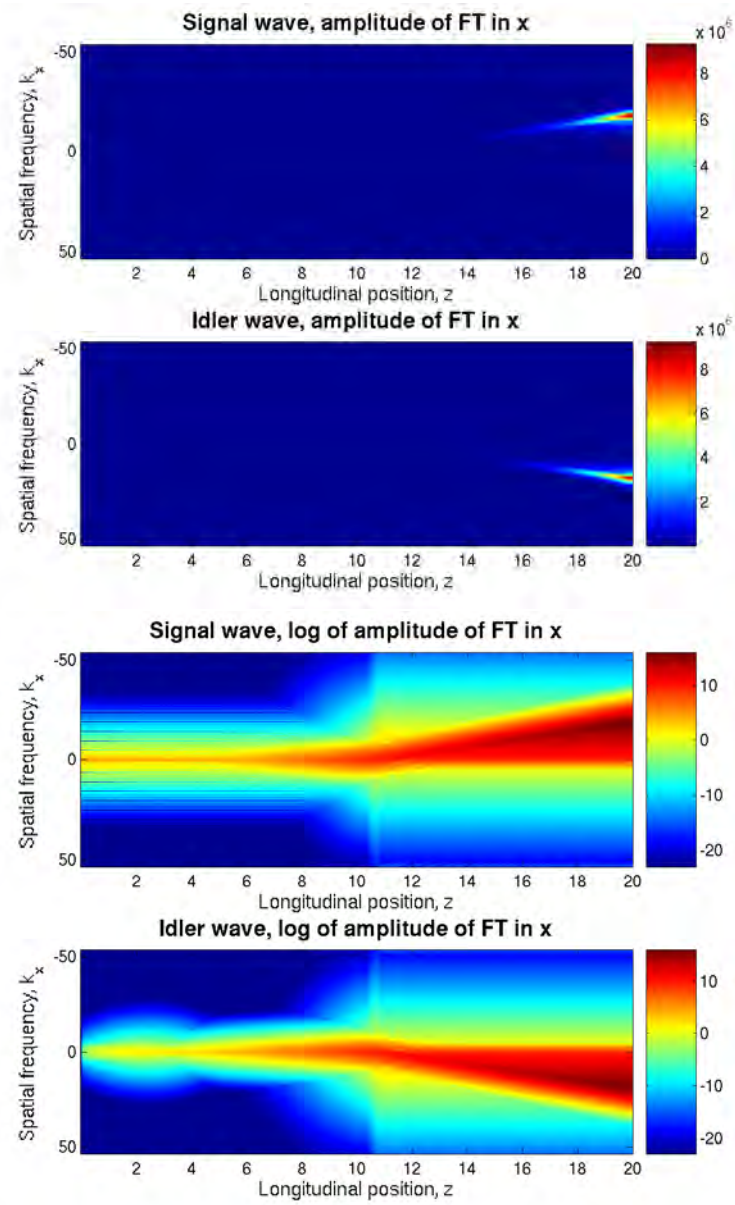

Figure 8.22: 2-D plots of the Fourier transforms in x, on a linear (top) and logarithmic scale(bottom).

Fig. 8.23 shows a transverse cut of the Fourier transform in x at the end of the simulation.

Fig. 8.24 shows 2-D plots of the Fourier transform in both x and z. The largest frequency components are shifted in k_x and k_z from the origin, a manifestation of the phase accumulated in those two directions. The dispersion relations $k_z + k_x/\alpha_{1,2} = 0$ are clearly visible on a logarithmic scale.

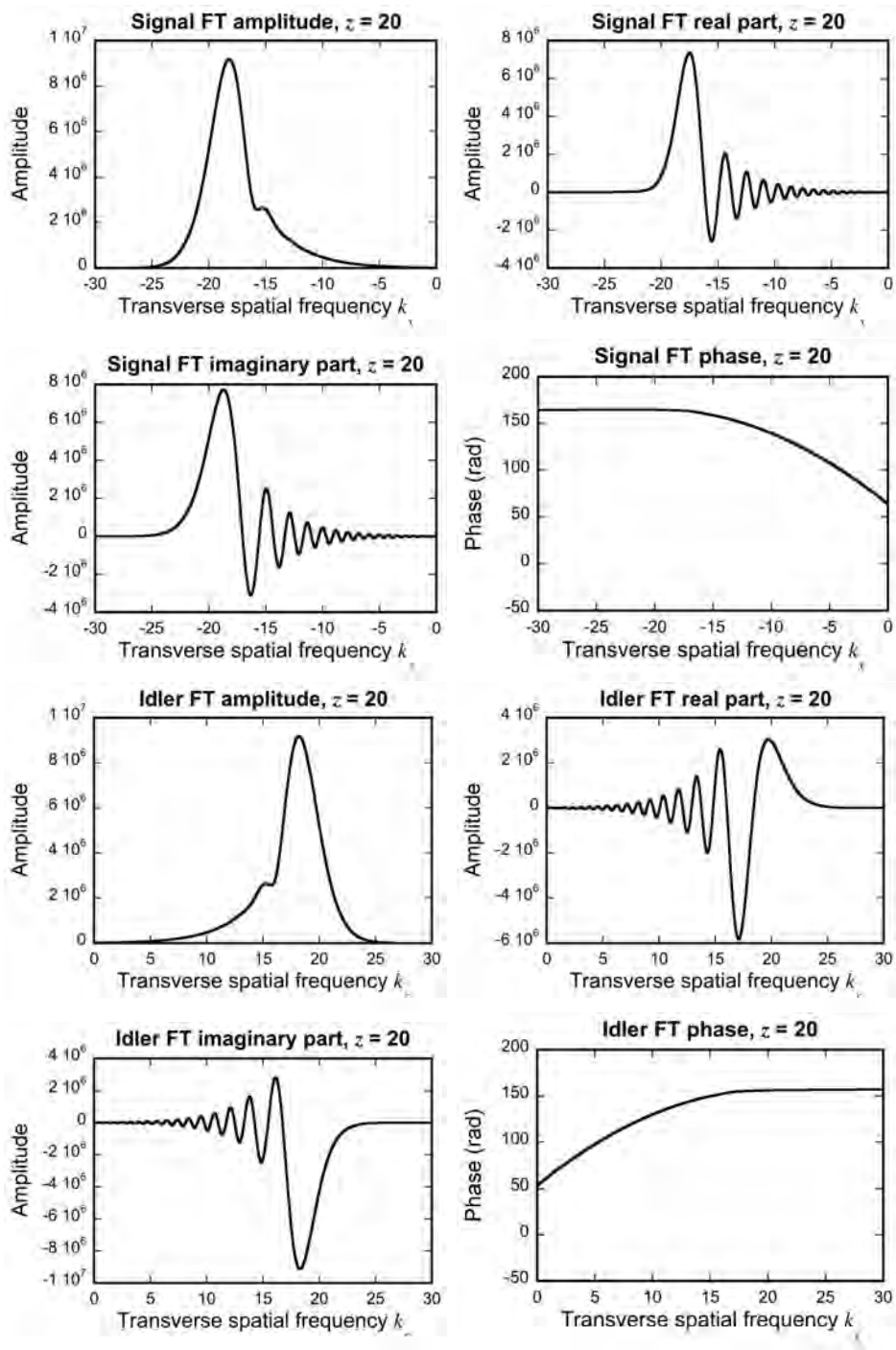

Figure 8.23: Transverse cuts of the Fourier transform in x at the end of the simulation ($z = 20$).

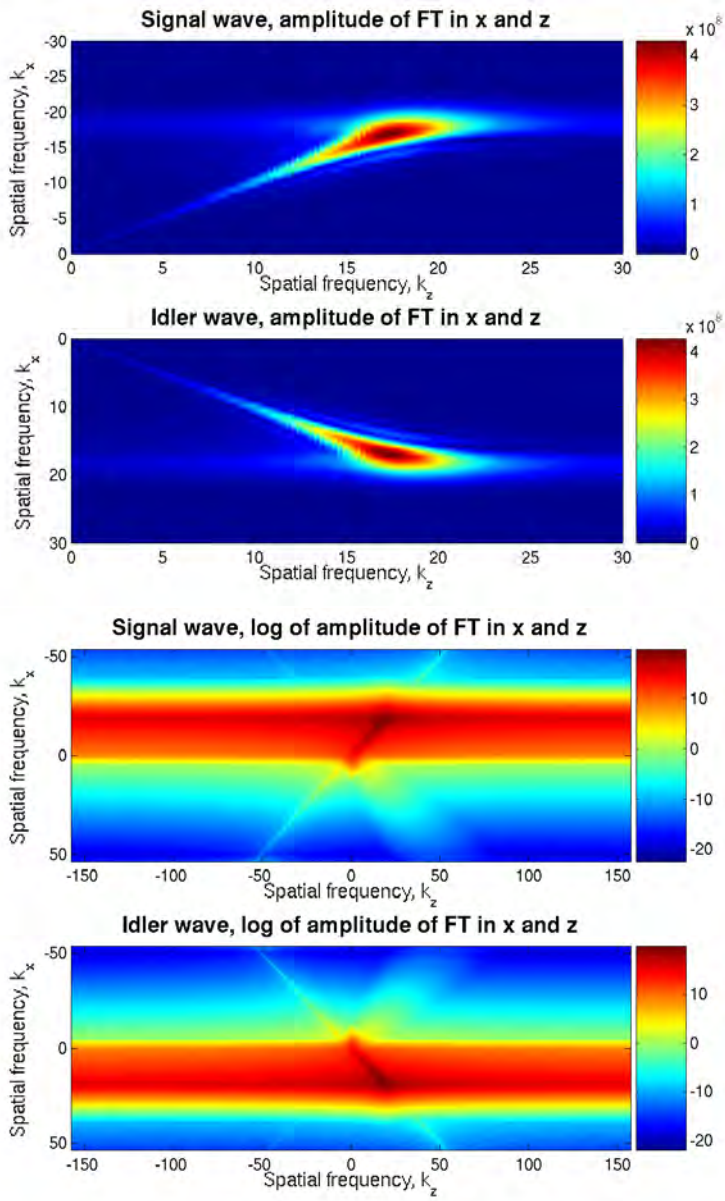

Figure 8.24: 2-D plots of the Fourier transforms in x and z, on a linear (top) and logarithmic scale(bottom).

8.3.2 Growth Rate

We calculate the normalized growth rate, $\bar{K}$, of the noncollinear modes suffficiently far in the non-uniform region.

Fig. 8.25 shows the growth rate as a function of the gain parameter λ, for various values of the dephasing rate. An increasing dephasing rate translates to a higher λ-threshold and a lower growth rate.

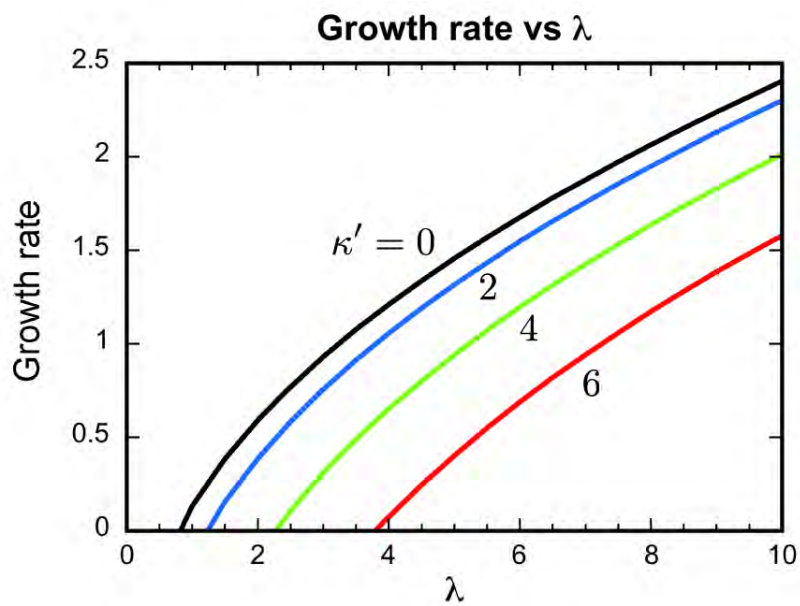

Figure 8.25: Growth rate $\bar{K}$ as a function of the gain parameter λ, for the degenerate case $\alpha_1 = 1$ and various values of the chirp rate κ'.

Fig. 8.26 shows the growth rate as a function of the dephasing rate κ', for different values of λ.

We saw in chapter 7) that the dependence of growth rate on angle is best understood by plotting $\bar{K}/\sqrt{\lambda} = K/\gamma_0$ (where K is the growth rate in physical units) as a function of $1/\sqrt{\lambda} = (\tan\theta_1 \tan\theta_2)^{1/2}/w_0\gamma_0$. This is done in Fig. 8.27 for various values of the ratio $\kappa'/\lambda = 1/\lambda_R$. From this plot, it is easy to extract the range of angles (i.e. $1/\sqrt{\lambda} = (\tan\theta_1 \tan\theta_2)^{1/2}/w_0\gamma_0$) for which confined growing modes are possible (Fig. 8.28).

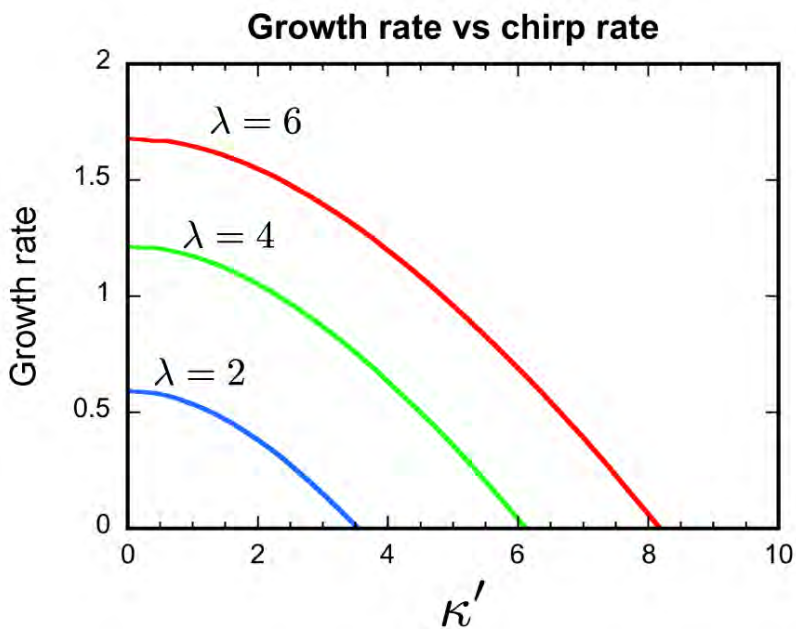

Figure 8.26: Growth rate $\bar{K}$ as a function of the chirp rate κ', for the degenerate case $\alpha_1 = 1$ and various values of the gain parameter λ.

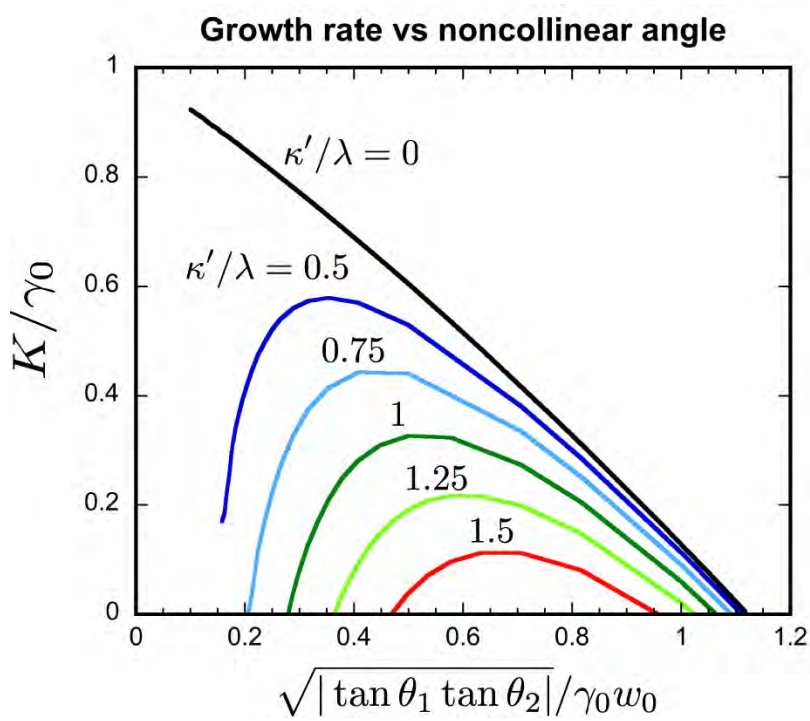

Figure 8.27: Normalized growth rate, $\bar{K}/\sqrt{\lambda} = K/\gamma_0$, as a function of normalized angle, $1/\sqrt{\lambda} = \sqrt{\tan\theta_1 \tan\theta_2}/\gamma_0 w_0$, for the degenerate case $\alpha_1 = 1$ and various values of the Rosenbluth gain parameter $1/\lambda_R = \kappa'/\lambda$. Following the discussion at the end of section 7.3 this plot illustrates more clearly the dependence on non-collinear angle than do the normalized coordinates.

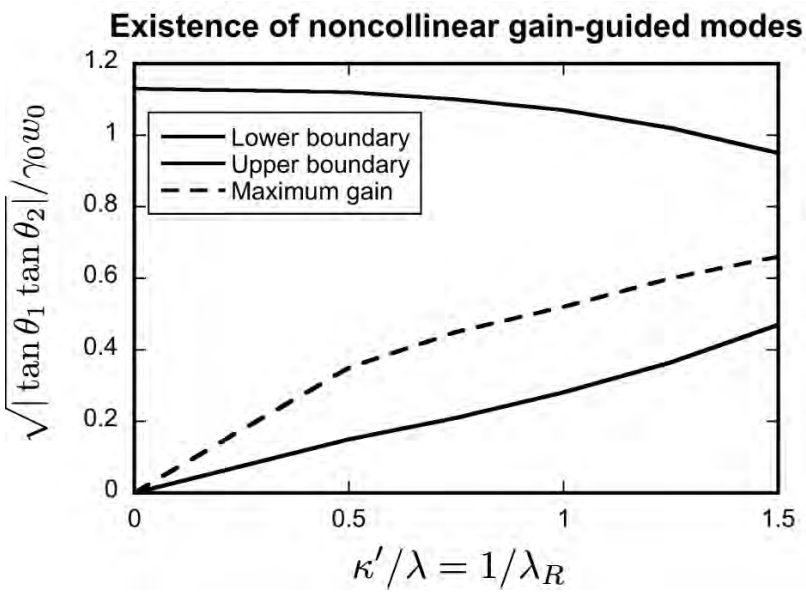

Figure 8.28: Angle range for which noncollinear gain-guided modes exist, as a function of $\kappa'/\lambda = 1/\lambda_R$, where λ_R is the Rosenbluth gain parameter, and for the degenerate case $\alpha_1 = -1/\alpha_2 = 1$. The solid lines show the maximum and minimum boundaries of this region, and the dashed line shows the location of maximum growth rate.

8.3.3 Conclusions

These numerical results indicate that, even in the presence of linearly increasing phase mismatch, exponentially growing modes are possible. The modes accumulate a phase which is quadratic in z (and in fact equal to $\phi/2$ when $\alpha_1 = 1$). Moreover, this phase is constant along the characteristics (i.e. along the straight lines defined by $z - x/\alpha_1$ in the case of the signal and $z - x/\alpha_2$ in the case of the idler). Therefore we can formulate the following "educated guess" about the form of the noncollinear growing modes:

$$A_{1,2} = e^{\bar{K}z} \exp\left[\frac{i}{2}C\phi\left(z - \frac{x}{\alpha_{1,2}}\right)\right]\Psi_{1,2}(x), \tag{8.13}$$

where $\bar{K}$ is the growth rate, C is a constant and $\Psi_{1,2}$ is the mode shape.

8.4 Collinear Interactions with Diffraction

When the noncollinear angles are small, the dominant transverse effect is diffraction. The equations describing collinear waves interacting in the presence of diffraction and dephasing are

$$\left(\frac{\partial}{\partial z} - i\beta_1\frac{\partial^2}{\partial x^2}\right)A_1 = i\lambda^{1/2}A_0(x)A_2^* e^{i\phi(z)} \tag{8.14}$$

$$\left(\frac{\partial}{\partial z} - i\beta_2\frac{\partial^2}{\partial x^2}\right)A_2 = i\lambda^{1/2}A_0(x)A_1^* e^{i\phi(z)}. \tag{8.15}$$

A normalization leading to this form of the equations was described in section 7.3.2. In this chapter we study this model by itself, so we are interested in the effect of the diffraction parameters β_1 and β_2, the coupling coefficient λ and the chirp rate κ'. We limit our investigation to the regime in which β_1 and β_2 are small. We again drop the symbols distinguishing the normalized coordinates from the physical coordinates.

As before, in the numerical simulations we turn on the coupling coefficient and the chirp rate progressively, in a manner similar to that shown in Fig. 8.12.

8.4.1 Positive dephasing rate: $\kappa' > 0$

When $\kappa' > 0$, the amplification process is accurately described by the Rosenbluth model. Fig. 8.29 shows the 2-D plots of the beam amplitude. Fig. 8.30 shows the peak amplitude and phase.

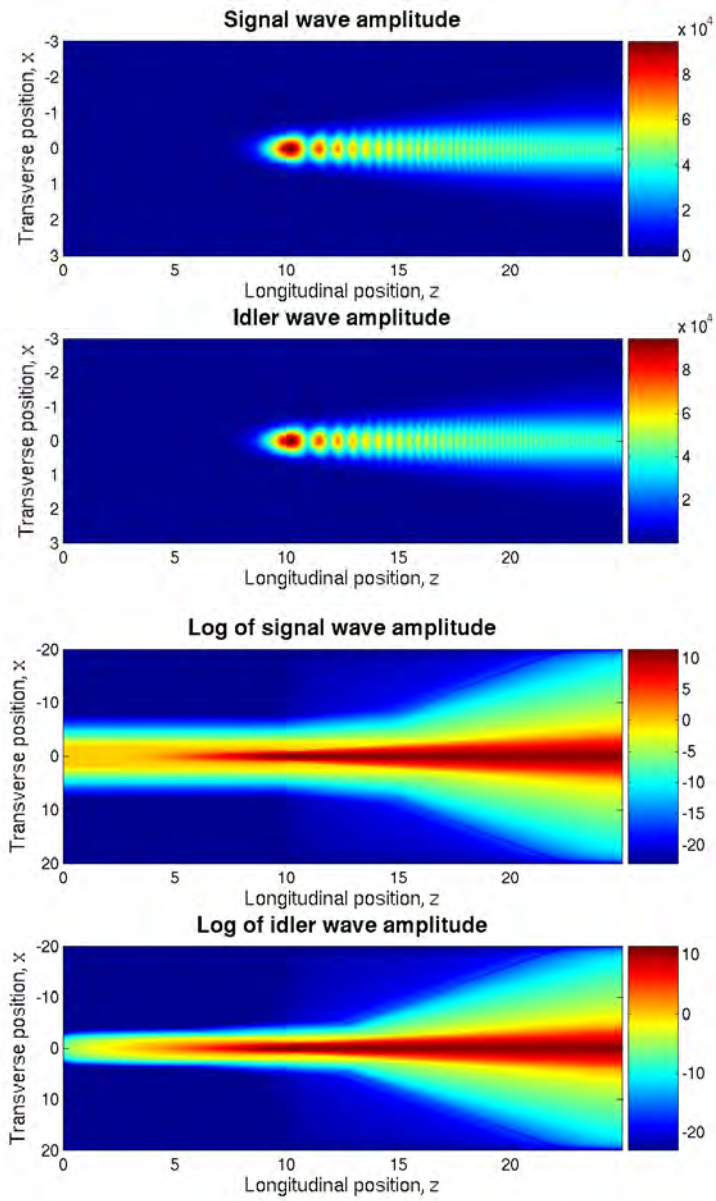

Figure 8.29: 2-D plots of the amplitude of the beams, in linear scale (top) and logarithmic scale (bottom), for $\lambda = 4$, $\kappa' = 4$, $\beta_1 = \beta_2 = 0.01$.

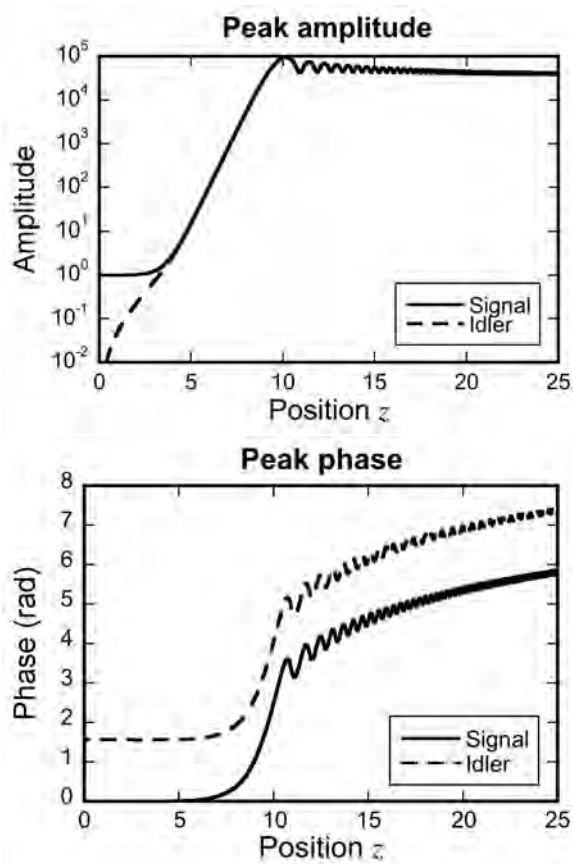

Figure 8.30: Peak amplitude (top) and phase at peak amplitude (bottom) for $\lambda = 4$, $\kappa' = 2$, $\beta_1 = \beta_2 = 0.01$.

8.4.2 Negative dephasing rate: $\kappa' < 0$

We use the same parameters as for the $\kappa' > 0$ case in section 8.4.1, except that we invert the sign of κ'. The resulting beam amplitudes are shown in Fig. 8.31, and the peak amplitude and phase is shown in Fig. 8.32. The amplification ceases for a short distance, as predicted by the Rosenbluth model, but quickly resumes, although at a growth rate inferior to that of the phase-matching region. The phase more or less follows the dephasing $\phi/2$, but with some delay.

Fig. 8.33 shows transverse cuts at the end of the simulation ($z = 25$). The amplitude is characterized by rapid oscillations in the transverse direction. The discontinuities in the phase are simply numerical artefacts caused by the phase unwrapping algorithm.

The Fourier space description is remarkably insightful. The 2-D plots of the Fourier transform in x is shown in Fig. 8.34. In k_x-space, the field is composed of two components located on either side of the origin. The superposition of these two frequency components explains the fact that the mode shape is highly oscillatory in x-space. Fig. 8.35 shows the trajectory along z of these frequency components. The two branches separate at the beginning of the non-uniform region. We will show later that these values of k_x are precisely those which ensure phase matching in a noncollinear configuration. The physical picture emerging is that of two superposed plane waves propagating at an angle with respect to the z-axis and with equal but opposite transverse wave vectors, thereby establishing a standing wave pattern in the x-direction.

Finally, the 2-D plots of the Fourier transforms in both x and z is shown in Fig. 8.36. The spectral content of the beams is dominated by two Fourier components located on either side of the k_z-axis. Their k_z values are nonzero, consistent with phase accumulation along z. Interestingly, the parabolic dispersion relation $k_z - \beta_{1,2}k_x^2 = 0$ is visible on a logarithmic scale.

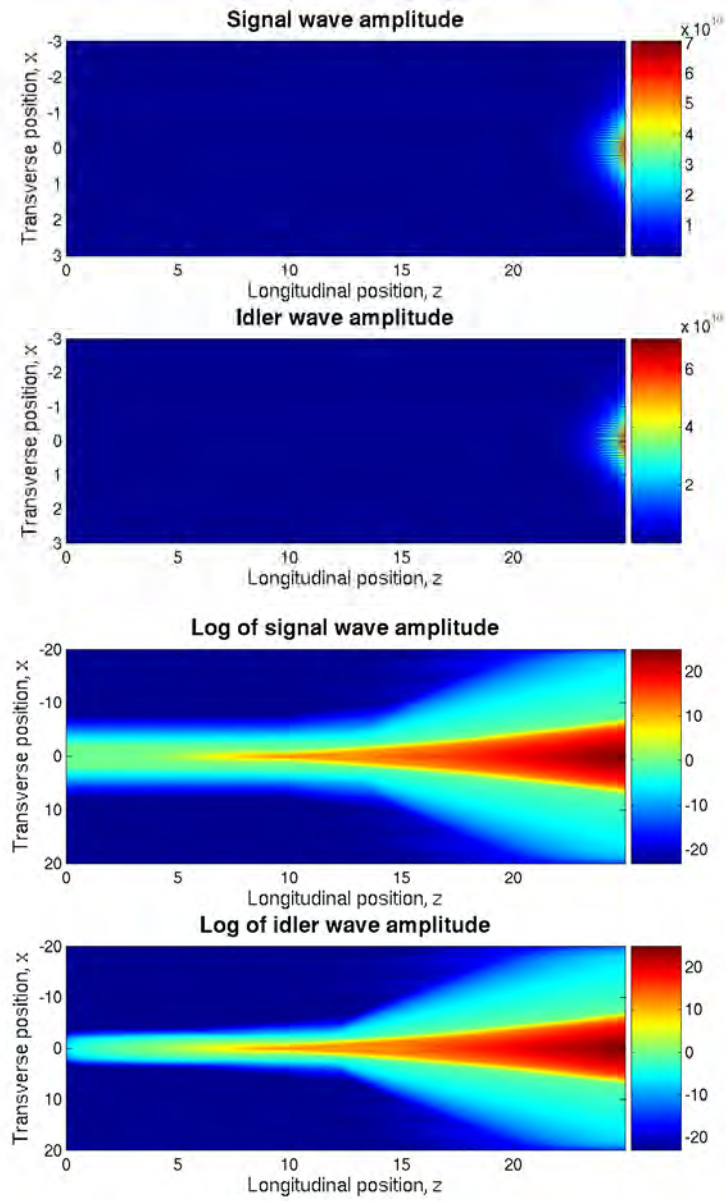

Figure 8.31: 2-D plots of the amplitude of the beams, in linear scale (top) and logarithmic scale (bottom), for $\lambda = 4$, $\kappa' = 4$, $\beta_1 = \beta_2 = 0.01$.

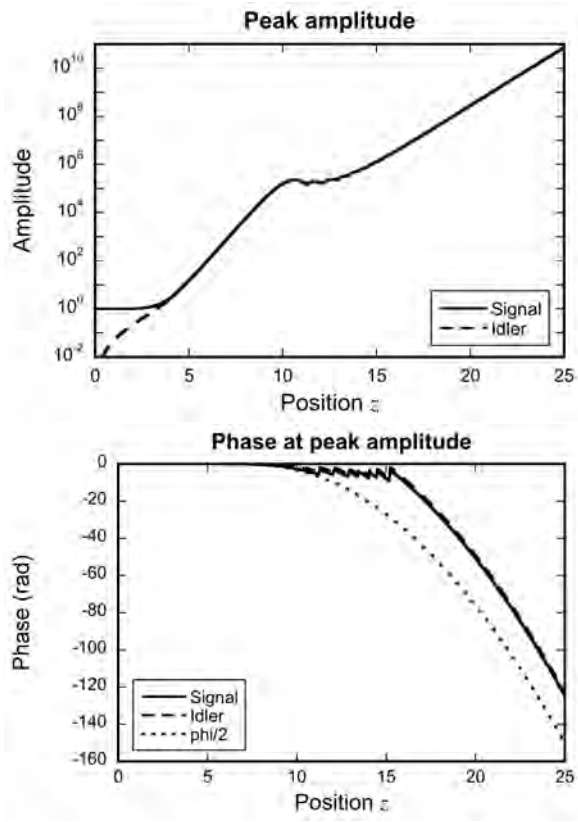

Figure 8.32: Peak amplitude (top) and phase at peak amplitude (bottom) for $\lambda = 4$, $\kappa' = -2$, $\beta_1 = \beta_2 = 0.01$.

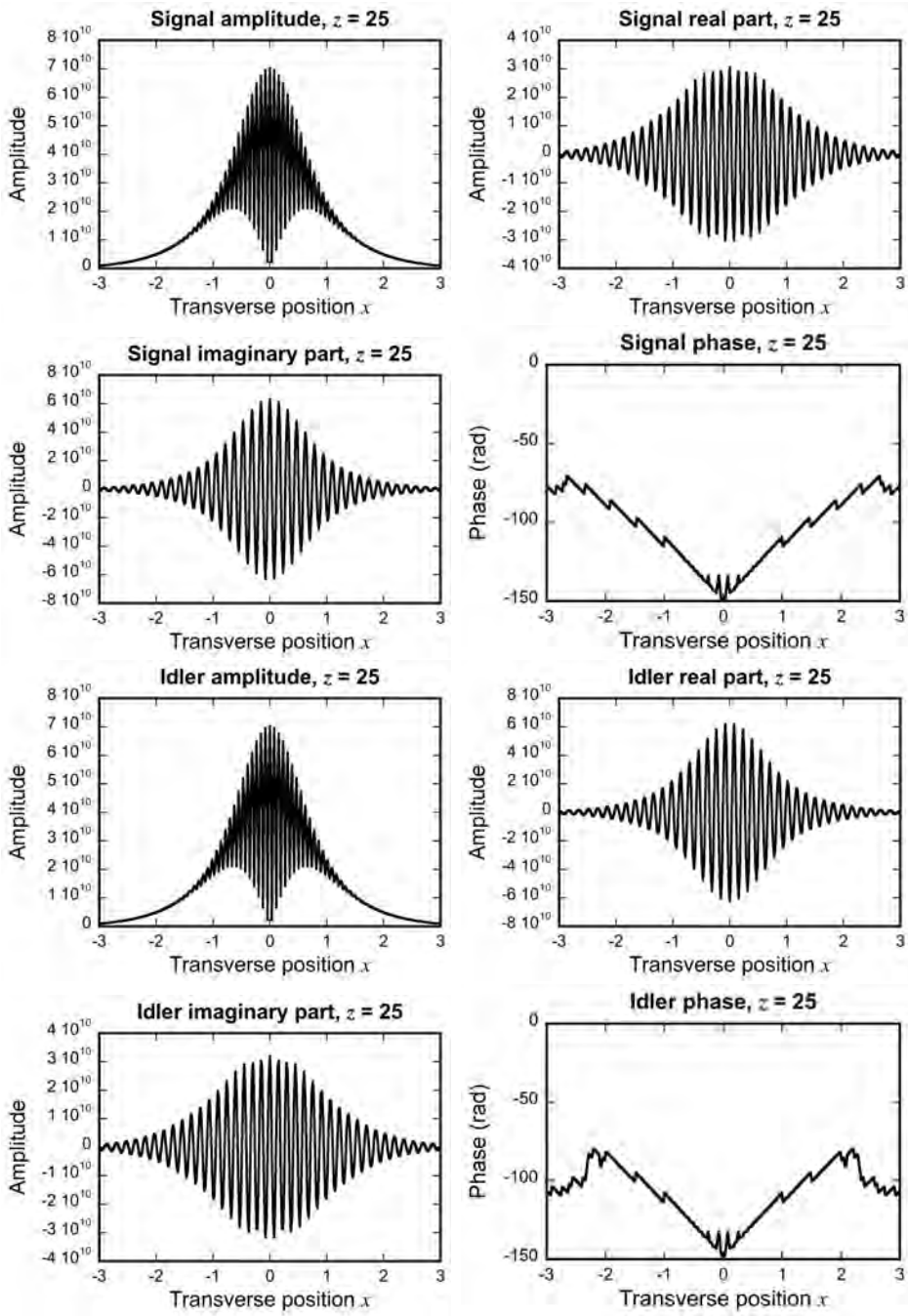

Figure 8.33: Transverse cuts at the end of the simulation ($z = 25$). The parameters used are $\lambda = 4$, $\kappa' = -2$, $\beta_1 = \beta_2 = 0.01$.

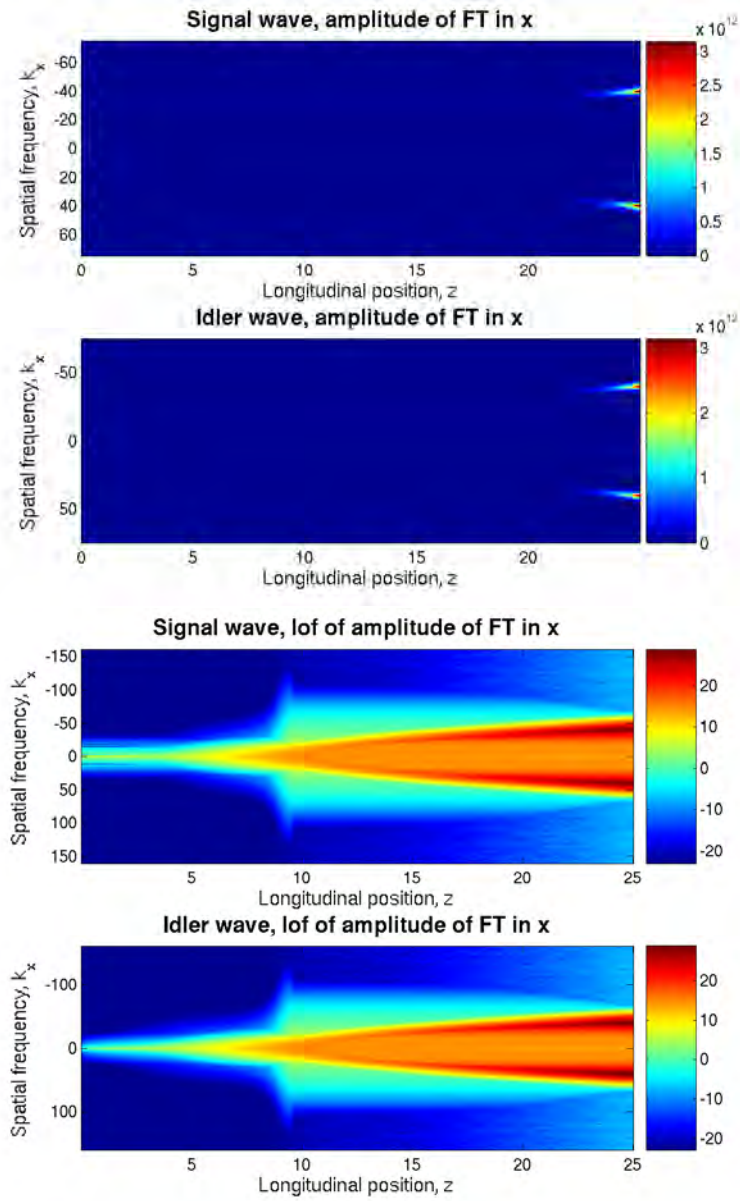

Figure 8.34: 2-D plots of the amplitude of the Fourier transform in x, on a linear (top) and logarithmic scale (bottom), for $\lambda = 4$, $\kappa' = -2$, $\beta_1 = \beta_2 = 0.01$.

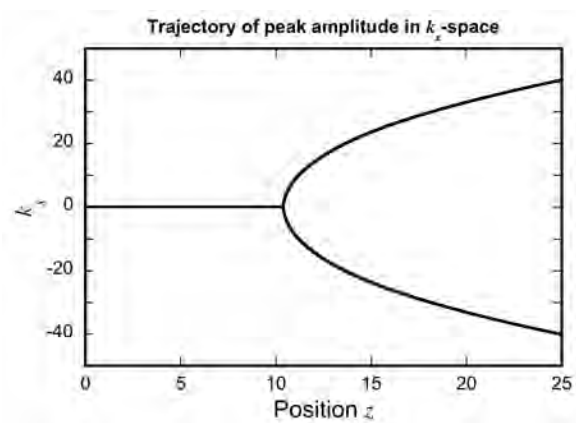

Figure 8.35: Trajectory of the peak amplitude points in k_x space. The parameters used here are $\lambda = 4$, $\kappa' = -2$, $\beta_1 = \beta_2 = 0.01$.

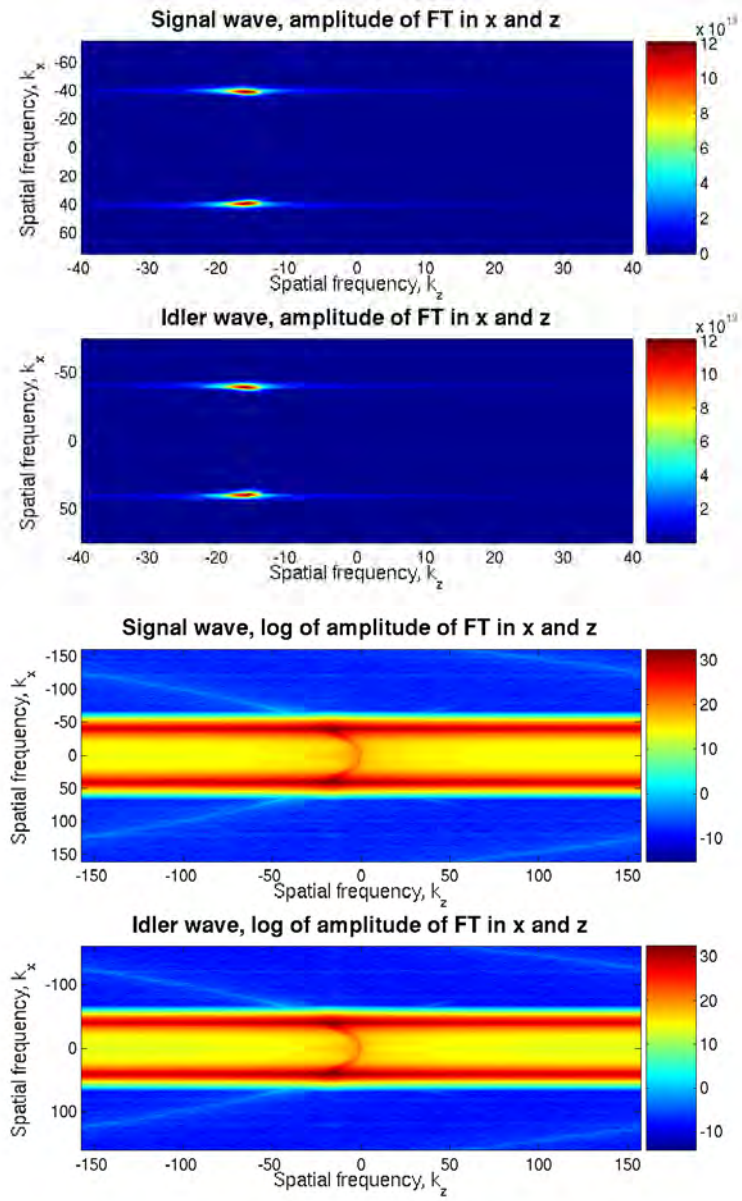

Figure 8.36: 2-D plots of the amplitude of the Fourier transforms in x and z, on a linear (top) and logarithmic scale (bottom), for $\lambda = 4$, $\kappa' = -2$, $\beta_1 = \beta_2 = 0.01$.

8.4.3 Growth Rate with $\kappa' < 0$

Let us consider the example with $\kappa' < 0$ given in the previous section. In the phase-mismatched region, the amplification stops for a certain distance before it grows again. We call *threshold length* the distance required for the growing modes to emerge. The threshold length is the distance over which the wave amplitudes are more or less constant.

Fig. 8.37 shows shows a plot of the threshold length multiplied by $\beta \equiv \beta_1 = \beta_2$, as a function of the dephasing rate. The curves corresponding to different values of β coincide, more or less. Fig 8.38 shows the dependence of the threshold length on λ for κ' and β fixed. From the numerical results, we find that the threshold length L_{th} is well approximated by

$$L_{th} \approx \frac{1}{8\beta}\left(\frac{\kappa'}{\lambda}\right)^2, \tag{8.16}$$

where $\beta = \beta_1 = \beta_2$. As $\beta \to 0$, $L_{th} \to \infty$, and growing modes do not appear, and the result corresponds to the simple Rosenbluth model.

The threshold length given in Eq. (8.16) is expressed in terms of the dimensionless parameters of the model. Using the normalized variables defined in section 7.3.2, the threshold length in physical units is

$$L_{th,physical} = \frac{k_1 w_0^2}{4\lambda_R^2}, \tag{8.17}$$

where as usual $\lambda_R = \gamma_0^2/\kappa'$ is the Rosenbluth gain parameter. This expression, developed numerically, is valid at degeneracy (i.e. $\beta_1 = \beta_2$).

After a distance greater than the threshold length, the waves grow exponentially. The growth rate is plotted in Fig. 8.39 against the dephasing rate for several values of β. Some of the curves are short because their threshold lengths were longer than the length of the simulation.

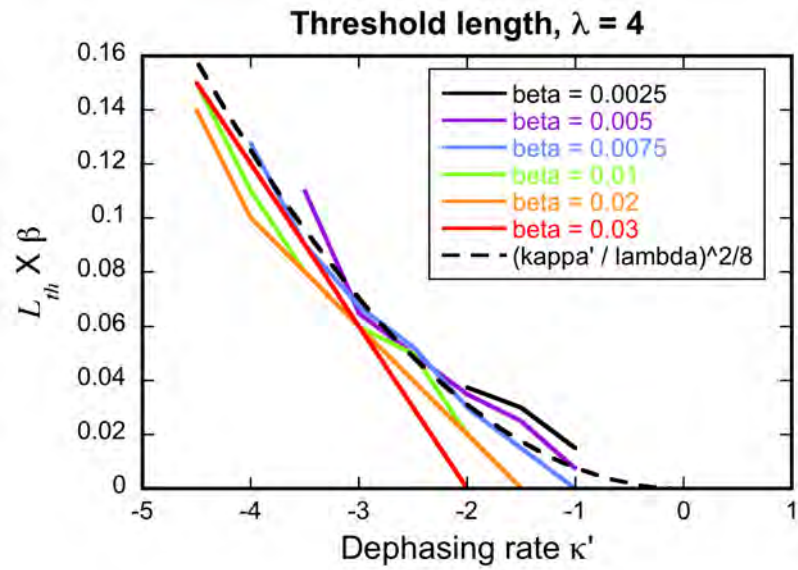

Figure 8.37: Product of threshold length and diffraction parameter, $\beta = \beta_1 = \beta_2$, as a function of the dephasing rate, for $\lambda = 4$.

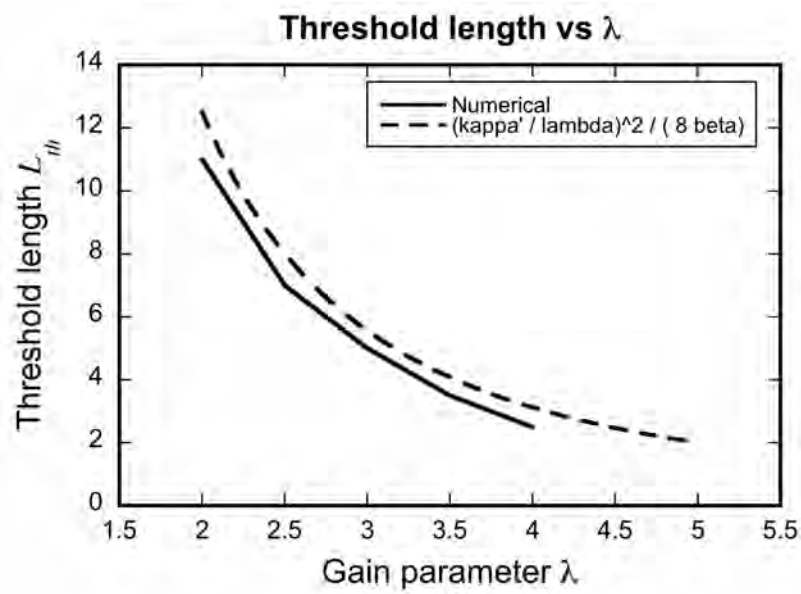

Figure 8.38: Threshold length vs λ, for fixed $\beta = \beta_1 = \beta_2 = 0.01$ and $\kappa' = -2$.

8.4.4 Conclusions

In this section we explored numerically the regime of collinear propagation in the presence of diffraction. If the chirp rate is positive, then the situation is identical to

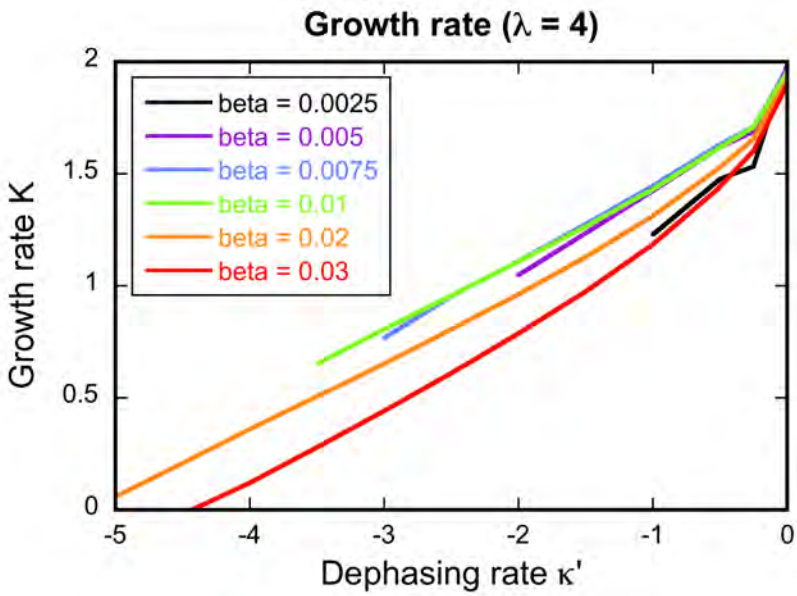

Figure 8.39: Growth rate as a function of the dephasing rate for different values of the diffraction parameter $\beta = \beta_1 = \beta_2$ with fixed coupling coefficient $\lambda = 4$.

the Rosenbluth model studied in chapter 2: the growth is limited to the vicinity of the phase-matched point and the amplification reaches a maximum. However, if the chirp rate is negative, the amplification stops temporarily after the phase-matched region, but resumes after a certain distance called the threshold length. This threshold length increases with the width of the pump beam and the magnitude of the chirp rate, but decreases with the strength of the coupling coefficient. Past the threshold length, amplification is possible in spite of the dephasing introduced by the chirped QPM grating. The larger the magnitude of the chirp rate, the lower the growth rate in the phase-mismatched region.

This effect is present in a collinear geometry even when diffraction is weak. The main impact of diffraction is to determine the threshold length. Provided the nonlinear crystal is long enough, the waves will resume their growth after a certain distance, regardless of how weak diffraction is.

In summary, the major implication of this investigation is that negatively-chirped QPM gratings offer a collinear gain which can be much larger than predicted by the 1-D Rosenbluth model. Design criteria to suppress this effect will be given in

chapter 11.

Chapter 9

Measurement of Noncollinear Interactions

The goal of this experiment is to measure the growth rate of noncollinear interactions in chirped QPM gratings, and to explore the discrepancy between positive and negative chirp rates.

9.1 Experimental Setup

The experimental setup is essentially the same as the one described in chapter 4.

Noncollinear incidence angles were introduced using a 1-cm-thick parallel glass plate placed on the path of the signal beam. The beam deflection d associated with a rotation of the plate by angle φ with respect to normal incidence is

$$d = D \sin\varphi \left(1 - \sqrt{\frac{1-\sin^2\varphi}{n^2-\sin^2\varphi}}\right), \tag{9.1}$$

where D is the thickness of the plate and n is the index of refraction of the plate. This deflection is mapped to a noncollinear incidence θ_{inc} angle by the focusing lens:

$$\theta_{inc} = \arctan\left(\frac{d}{f}\right), \tag{9.2}$$

where f is the focal length of the lens.

Instead of using a monochromator to isolate a particular wavelength, we used erbium-doped fiber amplifiers (EDFAs) to raise the signal power level in order to dominate the fluorescence.

Two signal lasers were available for this experiment. They were both tunable external-cavity diode lasers (ECDLs), New Focus model "Vidia-Swept". Their tunable ranges were 1520-1570 nm and 1560-1625 nm, respectively.

9.2 QPM gratings

The QPM grating profiles used in this experiment are illustrated in Fig. 9.1. They consist of two segments. The first segment is a 1-cm-long uniform grating. Its goal is to set up a noncollinear growing mode. The second segment is a 4-cm-long chirped grating. By measuring the total amplification, we can calculate the amount of gain provided by the chirped segment.

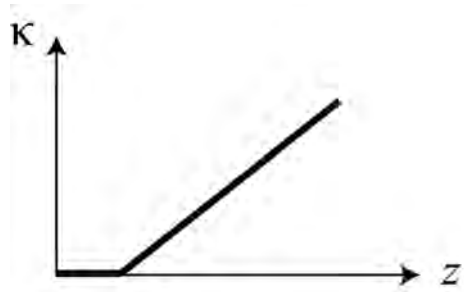

Figure 9.1: QPM grating profiles used in this experiment. The uniform segment is used to set up a noncollinear growing mode. The amplification due to the chirped segment is the quantity which we want to measure.

We designed QPM gratings with various chirp rates, corresponding to phase-matching bandwidths of 20, 30, 40, 50 and 60 nm. (Gratings with larger chirp rates were fabricated but they produced negligible gains with the available pump power.) The chirp rate corresponding to these bandwidths is plotted in Fig. 9.2.

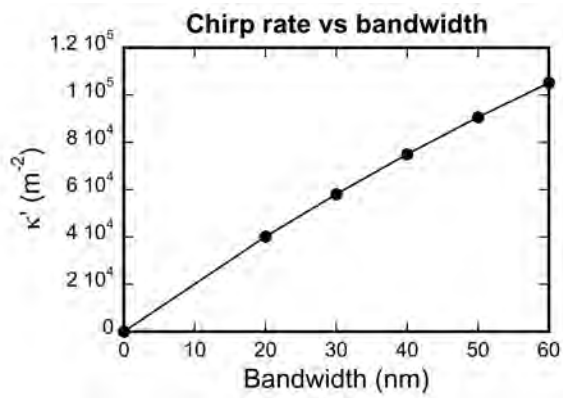

Figure 9.2: Chirp rate as a function of the collinear phase-matching bandwidth.

9.3 Parameter Space

In our discussion of noncollinear phase matching (section 7.2), we found that the angle of the idler wave is related to that of the signal by $\theta_i \approx -(k_s/k_i)\theta_s \approx -(k_{s0}/k_{i0})\theta_s$. In our experiment, the ratio of wave vectors is

$$r = \frac{k_{s0}}{k_{i0}} = \frac{n_{s0}}{n_{i0}}\frac{\lambda_{i0}}{\lambda_{s0}} \approx 2.1. \tag{9.3}$$

The ratio of angles is fixed: $\theta_i = -r\theta_s$. The values of the parameters $\alpha_{1,2}$, defined by Eq. (7.26) are therefore determined:

$$\alpha_1 = \frac{1}{\sqrt{r}} \approx 0.70 \tag{9.4}$$

$$\alpha_2 = -\sqrt{r} \approx -1.4. \tag{9.5}$$

The diffraction parameters, given by Eq. (7.27) are small: $\beta_1 \approx 0.02$, $\beta_2 \approx 0.04$. In the case of positive chirp rate, diffraction can be ignored. In the case of negative chirp rate *and* collinear geometry, diffraction could be responsible for amplification beyond the phase-matched point, which is why the measurement of noncollinear growth rate will be performed with positively-chirped QPM gratings.

There are two parameters which can be varied experimentally: λ and $\bar{\kappa}'$.

We recall that our pump laser has a duration of 0.8 ns and a spot size of 230 μm

($1/e^2$ intensity diameter). Pump pulse energies of up to 15 μJ per pulse gave sufficiently large gains. The pump intensities, coupling coefficient γ_0 and associated gain length, $1/\gamma_0$, used in this experiment are shown in Fig. 9.3.

The noncollinear gain length, L_{NC}, and normalized chirp rates, $\bar{\kappa}' = \kappa'/\kappa_0^2$, are shown as function of the incidence angle in Fig. 9.4.

Finally, the Rosenbluth gain parameter, $\lambda_R = \gamma_0^2/\kappa'$, and corresponding Rosenbluth gain, $\exp \pi\lambda_R$, associated with each grating are shown in Fig. 9.5. At the power level used, the Rosenbluth gain remains much smaller than the gain of uniform gratings of the same length. This is desirable since the goal of this experiment is to explore noncollinear growing modes.

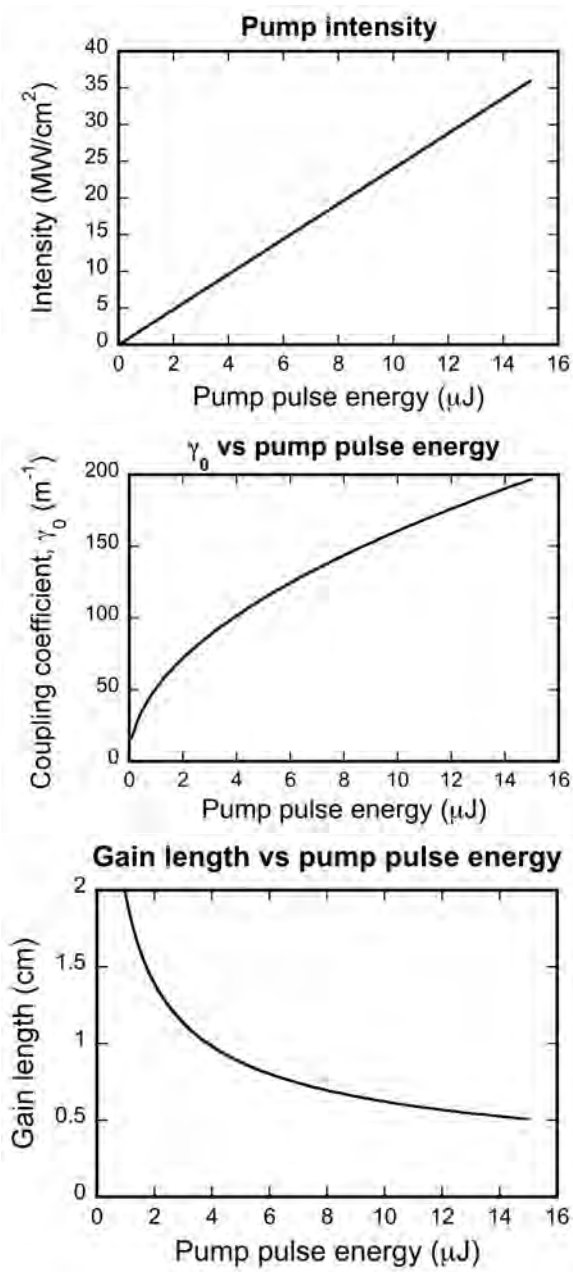

Figure 9.3: Parameter space explored in this experiment: Peak intensity (top), coupling coefficient, γ_0, (middle) and gain length, $1/\gamma_0$, (bottom) as a function of pump pulse energy.

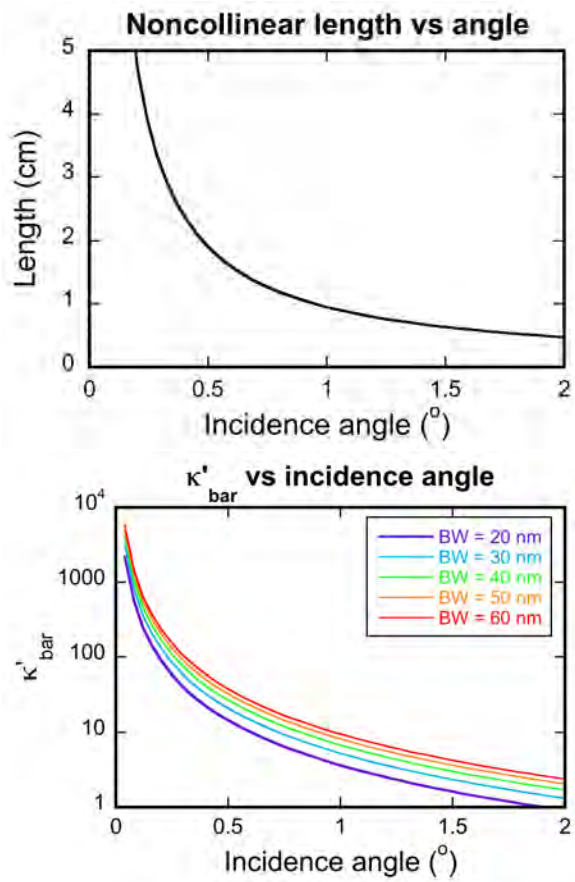

Figure 9.4: Parameter space explored in this experiment: Noncollinear length, $L_{NC} = w_0/(\sqrt{r}\tan\theta_1)$ (top), and normalized chirp rate, $\bar{\kappa}' = \kappa'/\kappa_0^2$ (bottom).

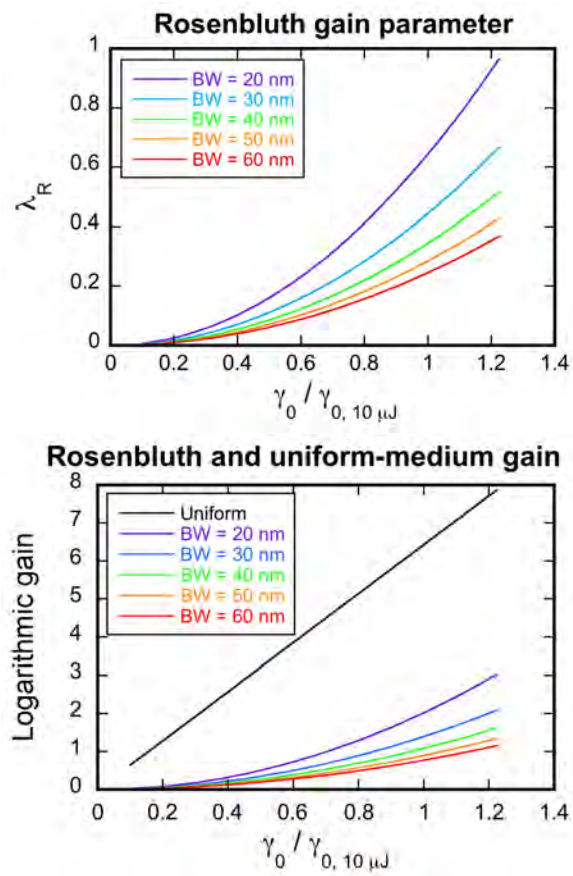

Figure 9.5: Rosenbluth gain parameter, $\lambda_R = \gamma_0^2/\kappa'$ (top) and Rosenbluth gain, $\exp(\pi\lambda_R)$ compared with the gain of a uniform grating, $\exp(\gamma_0 L)$ (bottom).

9.4 Noncollinear Gain vs Angle

The gain as a function of incidence angle is plotted in Fig. 9.6 for a number of uniform and chirped gratings. In the case of uniform gratings, the gain is largest at normal incidence and decreases as the angle increases. The gain in dB decreases linearly with the angle. A linear fit to the uniform grating data was used to remove the contribution of the linear segment in each of the chirped gratings (shown by the dashed line).

The noncollinear gain obtained in this manner was plotted on a normalized plot, as discussed in the previous chapter. This plot of the normalized growth rate, $\bar{K}/\sqrt{\lambda} = K/\gamma_0$, vs normalized angle, $1/\sqrt{\lambda} \approx \sqrt{r}\theta_1/\gamma_0 w_0$, where $r = k_{s0}/k_{i0}$ and w_0 is the half-width of the pump beam, is shown in Fig. 9.7 for fixed $\bar{\kappa}'/\lambda = \kappa'/\gamma_0^2$ ratios. This plot should be compared to that obtained numerically, Fig. 8.27. The numerical data was obtained for the degenerate case ($\alpha_1 = 1$, $\alpha_2 = -1$) while the experiment is non-degenerate ($\alpha_1 \approx 0.7$, $\alpha_2 \approx -1.4$), and therefore we don't expect perfect numerical agreement. Nevertheless the trends revealed by the experimental data agree with the numerical simulations. The important fact is that this experiment demonstrates the existence of noncollinear gain-guided modes in chirped QPM gratings.

9.5 Positive vs Negative Chirp Rate

In order to explore the difference between positive and negative chirp rate, we use a linearly chirped QPM grating (i.e. not one containing a uniform segment). By reversing the crystal, we measured the gain spectra associated with positive and negative chirp rate. The results are shown in Fig. 9.8. In the case of positive chirp, the gain is relatively flat over the bandwidth. However, in the case of negative chirp rate the logarithmic gain varies essentially linearly across the passband. (Note that the parametric fluorescence observed in Fig. 5.1 is not apparent here because of the higher signal input power level.)

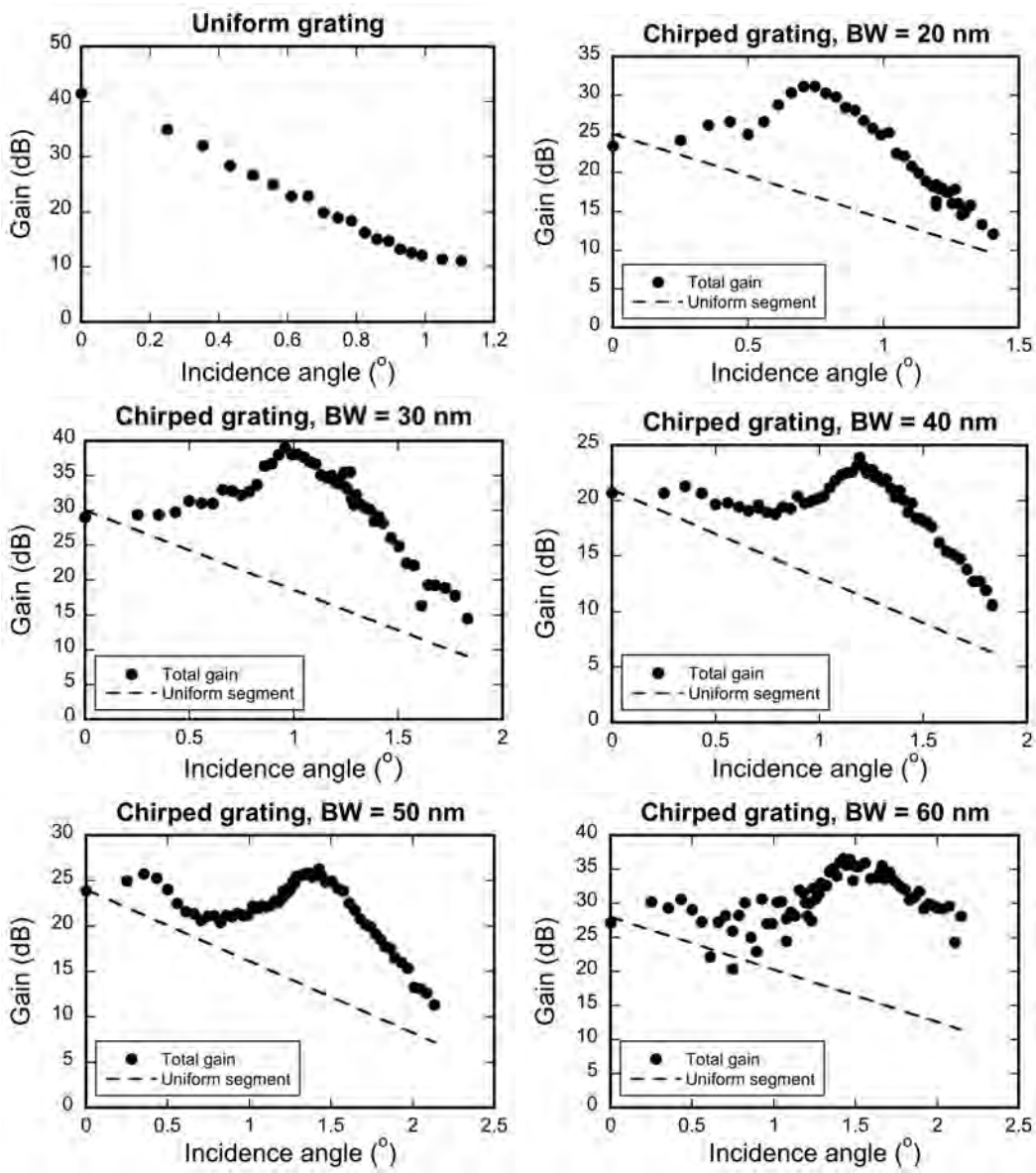

Figure 9.6: Noncollinear gain of uniform and chirped gratings. The dashed line represents the contribution from the uniform grating segment.

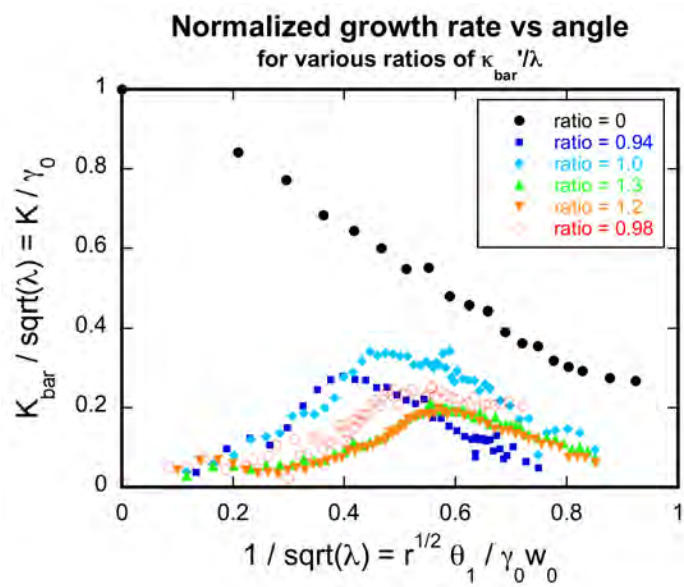

Figure 9.7: Normalized growth rate, K/γ_0 vs normalized angle, $\sqrt{r}\theta_1/\gamma_0 w_0$, for various ratios of $\kappa'/\gamma_0^2 = 1/\lambda_R$. Here, $r = k_{s0}/k_{i0} \approx 2.1$ and λ_R is the Rosenbluth gain parameter. Data are replotted from Fig. 9.6.

9.6 Parametric Fluorescence

Fig. 9.9 shows the energy of parametric fluorescence pulses. On a logarithmic scale, it is proportional to the square root of pump pulse energy. Saturation is visible at high pump intensity, when the energy of the fluorescence becomes comparable to that of the pump (in the order of microjoules per pulse).

Parametric fluorescence will be discussed in chapter 11. In the case of a uniform grating, the logarithm of the fluorescence energy is proportional to $2\gamma_0 L$, where L is the length of the QPM grating. The experimental value of the coupling coefficient, γ_0, can be inferred from the measurement of the parametric fluorescence. Fig. 9.10 shows the linear extrapolation to the experimental data, given by

$$\log U_{\text{fluorescence}} = 6.99\sqrt{U_p} + 3.9 \times 10^{-12}, \tag{9.6}$$

where the fluorescence and pump pulse energies are measured in microjoules. The intercept indicates that the fluorescence behaves as if it was seeded by 3.9×10^{-18} J

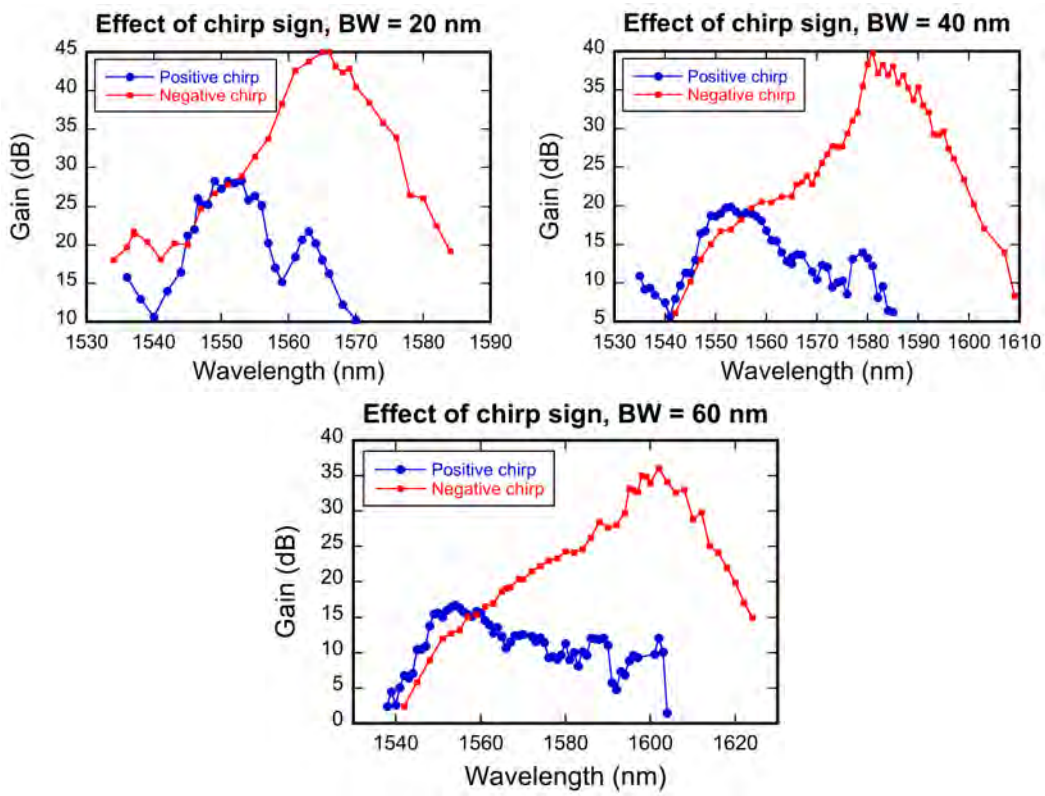

Figure 9.8: Collinear gain spectrum of linearly chirped gratings with positive and negative chirp rate.

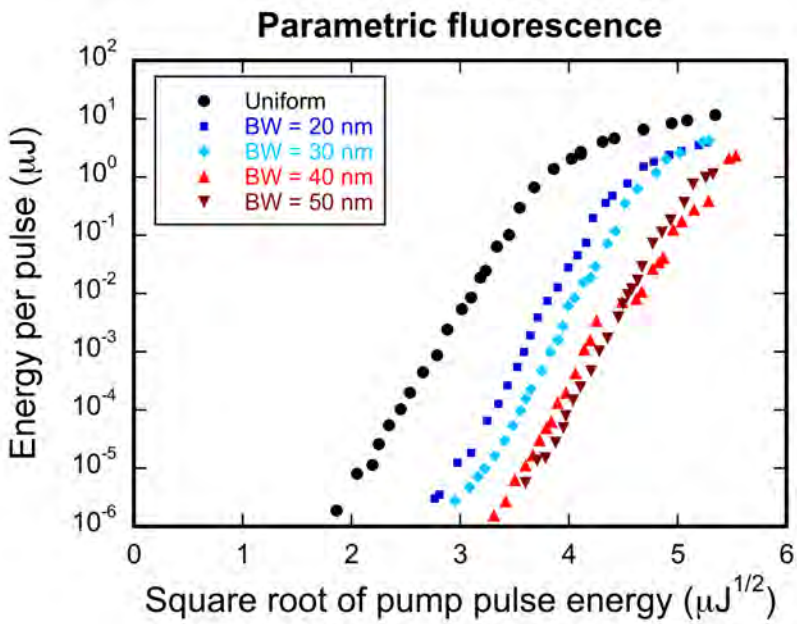

Figure 9.9: Energy of parametric fluorescence pulses, for uniform and chirped QPM gratings.

of energy. This is in good agreement with the expected theoretical value (chapter 11), which is 6.0×10^{-18} J. From the slope of this graph, and given that $L = 5$ cm, we calculate that

$$\gamma_0 = 69.9\sqrt{U_p}, \tag{9.7}$$

where U_p is the pump pulse energy in microjoules. We recall that the theoretical expression for the coupling coefficient is

$$\gamma_0 = \sqrt{\frac{\omega_s \omega_i}{n_s n_i}} \frac{d_{eff}}{c} |E_p| \tag{9.8}$$

where the amplitude of the electric field of the pump beam is

$$|E_p| = \sqrt{\frac{2\eta}{n_p} I_p}. \tag{9.9}$$

In this expression, $\eta = (\mu_0/\epsilon_0)^{1/2} \approx 377\ \Omega$ is the vacuum impedance. The pump

intensity is related to the beam radius w_0 and 1/e full pulse duration τ_0 by

$$I_p = \frac{U_p}{\pi w_0^2 \times \sqrt{\pi}\tau_0/2}. \tag{9.10}$$

According to the theoretical formula,

$$\gamma_0 = 75.6\sqrt{U_p}, \tag{9.11}$$

where again the pulse energy is measured in microjoules. As shown in Fig. 9.10, the experimental and theoretical values of γ_0 show good agreement.

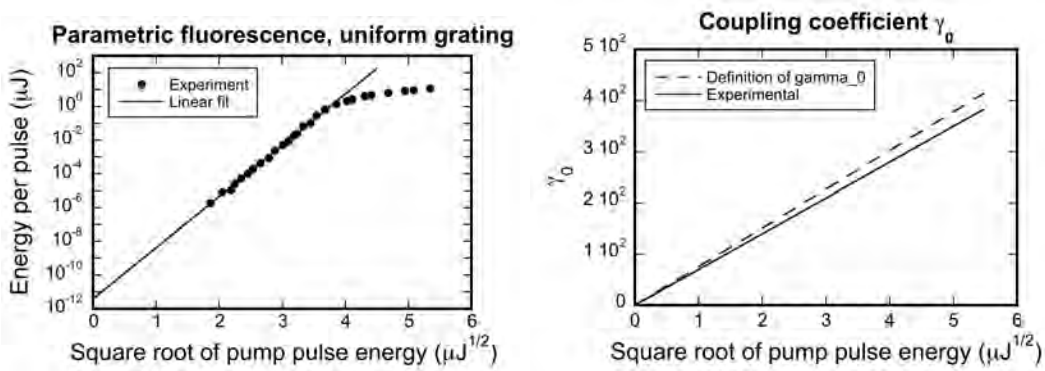

Figure 9.10: Experimental measurement of the coupling coefficient using the parametric fluorescence pulse energy. The slope of the plot of γ_0 vs $\sqrt{U_p}$ is 69.9 experimentally, compared to 75.6 theoretically.

9.7 Far-Field Beam Profiles

Additional insight about the behavior in the case of a negative chirp is provided by the far-field pattern of the amplified signal beam. As seen in Fig. 9.11, the output has the shape of a ring, and its size and intensity increase with wavelength. The bright inner ring is the amplified signal while the faint outer ring is the parametric fluorescence.

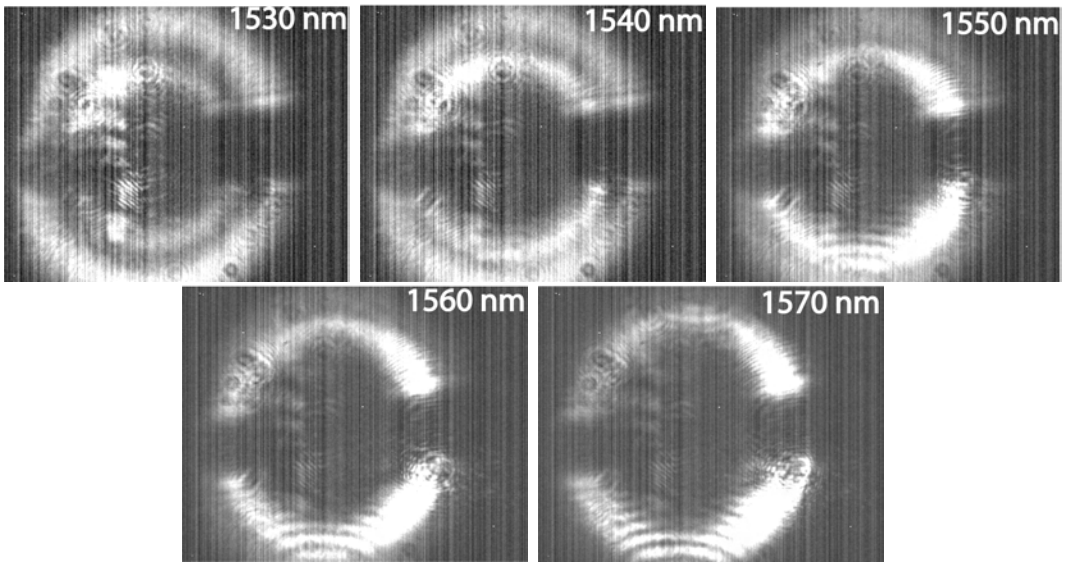

Figure 9.11: Far-field pattern of the amplified signal in the presence of a negative chirp rate. The dark line is the shadow of a wedge used to block the CW seed. The wavelength of the seed is indicated on the figure.

In the case of positive chirp rate, the asymmetry of the parametric fluorescence pattern seems to be related to that of the pump beam inside the crystal, as seen in Fig. 9.12. It remains unclear however why the far-field pattern should have the observed shape.

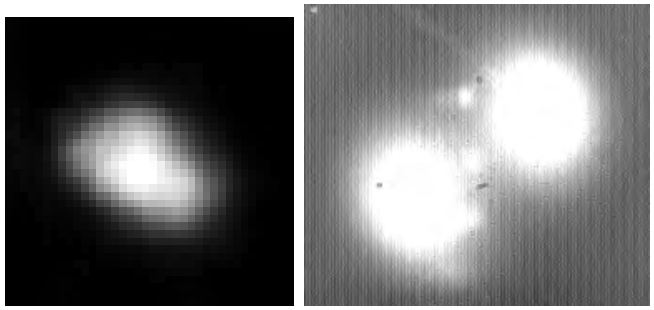

Figure 9.12: Pump beam profile inside the crystal (left) and far-field fluorescence profile with positive chirp rate (right). The fluorescence pattern appears to be related to the lack of cylindrical symmetry in the pump beam.

Chapter 10

Analysis of 2-D Model

In this chapter, we develop an analytical description of the transverse effects observed numerically and experimentally in the previous two chapters.

10.1 Derivation of the Equations

We begin by casting the equations (7.24) and (7.25) for the noncollinear optical parametric amplifier in a more convenient form:

$$\mathcal{L}_1 A_1 = i\lambda^{1/2}\mathcal{M}_{12}A_2^* \tag{10.1}$$

$$\mathcal{L}_2 A_2^* = -i\lambda^{1/2}\mathcal{M}_{21}A_1. \tag{10.2}$$

The operators are given by

$$\mathcal{L}_1 \equiv \frac{\partial}{\partial z} + \alpha_1\frac{\partial}{\partial x} - i\beta_1\frac{\partial^2}{\partial z^2} \tag{10.3}$$

$$\mathcal{L}_2 \equiv \frac{\partial}{\partial z} + \alpha_2\frac{\partial}{\partial x} + i\beta_2\frac{\partial^2}{\partial z^2} \tag{10.4}$$

$$\mathcal{M}_{12} \equiv A_0(x)e^{i\phi(z)} \tag{10.5}$$

$$\mathcal{M}_{21} \equiv A_0^*(x)e^{-i\phi(z)} \tag{10.6}$$

Note that $\mathcal{M}_{21} = \mathcal{M}_{12}^* \equiv \mathcal{M}$. In this calculation we will drop the "bars" denoting normalized variables.

We combine Eqs. (10.1) and (10.2):

$$\mathcal{L}_2\mathcal{L}_1 A_1 = [\mathcal{L}_2, \mathcal{M}]\, \mathcal{M}^{-1}\mathcal{L}_1 A_1 + \lambda|\mathcal{M}|^2 A_1. \tag{10.7}$$

The commutator between $\mathcal{L}_2$ and $\mathcal{M}$ is

$$[\mathcal{L}_2, \mathcal{M}] = \mathcal{L}_2\mathcal{M} + 2i\beta_2 \left(\frac{\partial \mathcal{M}}{\partial x}\right) \frac{\partial}{\partial x}. \tag{10.8}$$

Using the fact that $\partial\mathcal{M}^{-1}/\partial x = -\mathcal{M}^{-2}\partial\mathcal{M}/\partial x$; this yields

$$\begin{aligned} \mathcal{L}_1\mathcal{L}_2 A_1 - \lambda|\mathcal{M}|^2 A_1 - \mathcal{M}^{-1}\mathcal{L}_2\mathcal{M}\mathcal{L}_1 A_1 \\ -2i\beta_2 \left[\mathcal{M}^{-1}\left(\frac{\partial\mathcal{M}}{\partial x}\right)\frac{\partial}{\partial x} - \left(\mathcal{M}^{-1}\frac{\partial\mathcal{M}}{\partial x}\right)^2\right]\mathcal{L}_1 A_1 &= 0. \end{aligned} \tag{10.9}$$

Eq. (10.9) describes the wave in the most general way: it includes noncollinear propagation, diffraction, pump localization and a general phase-matching profile.

10.2 Noncollinear Interactions in a Uniform Medium

10.2.1 Equation for Bound States

We first consider a uniform medium in a collinear configuration with negligible diffraction. In this case, $\beta_1 = \beta_2 = 0$, $\phi = 0$, $\mathcal{M} = A_0(x)$, and Eq. (10.9) describing the amplified wave reduces to

$$\mathcal{L}_1\mathcal{L}_2 A_1 - \lambda|A_0(x)|^2 A_1 - \alpha_2 \frac{d\ln A_0}{dx}\mathcal{L}_1 A_1 = 0, \tag{10.10}$$

with $\mathcal{L}_{1,2} = \partial/\partial z + \alpha_{1,2}\partial/\partial z$. For now we will not specify the shape of the pump beam. The only requirement is that is be of half-width 1 (by definition of the normalization of x). We also recall that $\alpha_1\alpha_2 = -1$; this is due to the definitions of the normalized variables, as given in chapter 7.

We make the assumption that the solution $A_1(z,x)$ *is separable* in z and x. This assumption is motivated by the numerical simulations, which indicated that the beam profile is invariant along the direction of propagation (see chapter 8).

Taking the Fourier transform in z of Eq. (10.10) (or, equivalently, assuming exponential solutions in z) gives

$$\begin{aligned} \frac{d^2\widetilde{A}_1}{dx^2} - \left[\frac{d\ln A_0}{dx} - i(\alpha_1+\alpha_2)k_z\right]\frac{d\widetilde{A}_1}{dx} \\ + \left[k_z^2 + \lambda|A_0(x)|^2 - i\alpha_2 k_z \frac{d\ln A_0}{dx}\right]\widetilde{A}_1 &= 0, \end{aligned} \tag{10.11}$$

where k_z is the transform variable. The mode shape $\widetilde{A}_1$ is now function of x only. We eliminate the first-order derivative by the substitution

$$\widetilde{A}_1(x) = A_0^{1/2}(x)e^{-\frac{i}{2}(\alpha_1+\alpha_2)k_z x}\, a_1(x). \tag{10.12}$$

The mode profile $a_1(x)$ obeys

$$\frac{d^2 a_1}{dx^2} + Q(x)a_1 = 0 \tag{10.13}$$

with

$$Q(x) = \lambda|A_0(x)|^2 - \frac{1}{4}\left[\frac{d\ln A_0}{dx} - i(\alpha_1-\alpha_2)k_z\right]^2 + \frac{1}{2}\frac{d^2\ln A_0}{dx^2}. \tag{10.14}$$

Eq. (10.13) has the familiar form of the Schroedinger's equation describing the wave function in a potential well. In our case, the "well" is defined by the pump beam profile and the eigenvalue is k_z.

In the case of a top-hat pump profile, Eq. (10.13) can be solved exactly: the solutions are exponentials and the bound states can be found by matching the solution and its derivative at the edges of the pump. More generally, the bound states can be found using WKB analysis. Enforcing decay of the solution as $x \to \pm\infty$ leads to a quantization condition which determines the eigenvalue. This calculation is done in detail below.

The laterally localized gain-guided modes found this way have first been studied by Sushchik [70, 71, 67]. Ref. [67], in particular, investigates the growth rate and shape of the Sushchik modes in great detail.

10.2.2 Growth Rate for a Top-Hat Pump Profile

Let us consider a top-hat pump profile:

$$|A_0|^2 = \begin{cases} 1, & |x| \leq 1 \\ 0, & |x| > 1. \end{cases} \tag{10.15}$$

We introduce the growth rate $\bar{K} = -ik_z$, and define $\widetilde{K} = (\alpha_1 - \alpha_2)\bar{K}$ in order to simplify the notation. The boundary conditions are $\widetilde{A}_1 = 0$ at $x = -1$ (since the signal wave propagates towards positive x) and at $x = +\infty$. The solutions satisfying these conditions are

$$\widetilde{A}_1(x) \propto \begin{cases} 0 & x < -1 \\ \sin\left[\sqrt{\lambda - (\widetilde{K}/2)^2}\,(x+1)\right], & -1 < x < 1 \\ e^{-\widetilde{K}x/2}, & x > 1. \end{cases} \tag{10.16}$$

Enforcing continuity of the solution and its derivative at $x = 1$ determines the growth rate $\bar{K}$, which satisfies the following transcendental equation:

$$\cot 2\sqrt{\lambda - (\widetilde{K}/2)^2} = -\frac{(\widetilde{K}/2)^2}{\sqrt{\lambda - (\widetilde{K}/2)^2}}. \tag{10.17}$$

We introduce

$$u = 2\sqrt{\lambda - (\widetilde{K}/2)^2}. \tag{10.18}$$

Then the quantization condition becomes

$$\tan\left(u - \frac{\pi}{2}\right) = \frac{2\sqrt{\lambda - (u/2)^2}}{u}. \tag{10.19}$$

The graphical solution of this equation is shown in Fig. 10.1. A new mode appears every time $u = (n + 1/2)\pi$, for $n = 0, 1, 2, \ldots$. Therefore the threshold of mode n is

$$\lambda_{th,n} = \left[\left(n + \frac{1}{2}\right)\frac{\pi}{2}\right]^2. \tag{10.20}$$

In the infinite pump-strength limit, i.e. $\lambda \to \infty$, the solutions are $u_n = (n + 1)\pi$, or

$$\widetilde{K}_n = 2\sqrt{\lambda - (n+1)^2(\pi/2)^2}. \tag{10.21}$$

In this case, all modes grow at a rate asymptotic to $2\sqrt{\lambda}$.

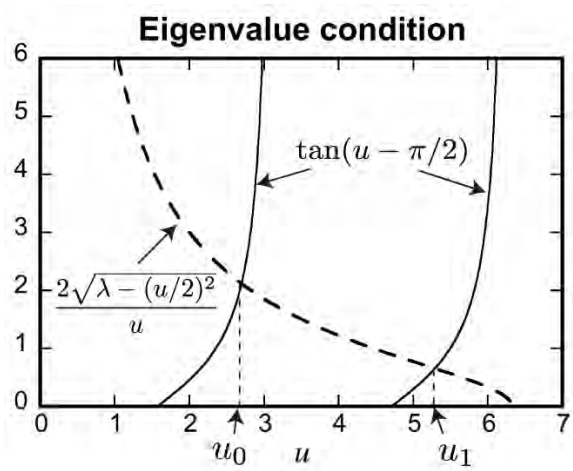

Figure 10.1: Graphical solution of the eigenvalue condition $\tan(u - \pi/2) = 2\sqrt{\lambda - (u/2)^2}/u$, Eq. (10.19), for $\lambda = 10$.

Let us convert these results into physical units. The threshold condition for the fundamental mode ($n = 0$) is $\lambda_{th,0} = (\pi/4)^2$. We recall that $\lambda = (\gamma_0 L_{NC})^2$, with $L_{NC} = w_0/|\tan\theta_1 \tan\theta_2|^{1/2}$. The threshold condition can be written

$$\frac{\gamma_0}{\sqrt{|\tan\theta_1 \tan\theta_2|}} \times 2w_0 = \frac{\pi}{2}. \tag{10.22}$$

The term $\gamma_0/|\tan\theta_1 \tan\theta_2|^{1/2} \equiv \gamma_\perp$ is the projection of the coupling coefficient on the x direction. The term $2w_0 \equiv L_\perp$ is the full width of the pump beam. Therefore, the

threshold condition simply states that $\gamma_\perp L_\perp = \pi/2$; in other words, the transverse gain must be larger than $\pi/2$. This is analogous to the instability threshold of a backward wave oscillator [68].

The growth rate in physical units is given by $K = \bar{K}/L_{NC}$. In the strong pump limit, the growth rate of mode n is

$$K_n = \frac{2\gamma_0}{\alpha_1 - \alpha_2}\sqrt{1 - \frac{(n+1)^2\pi^2}{4\lambda}}. \tag{10.23}$$

The quantization condition and growth rate for a flat pump profile developed in this section are identical to those found by Sushchik in Refs. [70, 71].

10.2.3 Growth Rate for More General Pump Profiles

For more general pump profiles, the mode shape and the associated growth rate can be found using WKB analysis. This method is described for instance in Bender and Orzsag [34] in the context of the bound states of a potential well.

Inside the pump (i.e. between the turning points), the WKB solutions of Eq. 10.13 are

$$a_1 \sim \exp \pm i \int^x \sqrt{Q}\, dx. \tag{10.24}$$

Imposing the boundary conditions $a_1 \to 0$ at $x \to \pm\infty$ leads to the Bohr-Sommerfeld quantization condition [34, 72]:

$$\int_{x_1}^{x_2} \sqrt{Q}\, dx = \left(n + \frac{1}{2}\right)\pi, \tag{10.25}$$

where x_1 and x_2 are the turning points (zeros of $Q(x)$). This condition determines the eigenvalues k_z.

The quantization condition obtained from WKB analysis can be compared to the exact calculation in the case of a top-hat pump profile. In this case, the turning points are located at the edges of the pump beam ($x_1 = -1$, $x_2 = 1$) and $Q =$

$\lambda + (\alpha_1 - \alpha_2)^2 k_z^2/4$. The quantization condition (10.25) gives the growth rate

$$\bar{K}_n = \frac{2}{\alpha_1 - \alpha_2}\sqrt{\lambda - \left(n + \frac{1}{2}\right)^2 \left(\frac{\pi}{2}\right)^2}. \tag{10.26}$$

This value tends to the exact solution, Eq. (10.21), in the infinite pump strength limit.

Let us now return to the evaluation of the quantization condition. In order to proceed further analytically, we assume a *parabolic pump profile*. Therefore we write

$$|A_0|^2 \approx 1 - x^2. \tag{10.27}$$

We also use the approximation $(d/dx)\ln A_0 = -x$. Then the "potential" takes the form

$$\begin{aligned} Q(x) &= \lambda(1 - x^2) - \frac{1}{4}\left[x + i(\alpha_1 - \alpha_2)k_z\right]^2 - \frac{1}{2} \\ &= -\left(\lambda + \frac{1}{4}\right)x^2 - \frac{i}{2}(\alpha_1 - \alpha_2)k_z x + \lambda + \frac{1}{4}(\alpha_1 - \alpha_2)^2 k_z^2 - \frac{1}{2} \end{aligned} \tag{10.28}$$

Since the evaluation of the quantization condition with a parabolic profile will be used repeatedly in this chapter, we present the details of the calculation. The turning points, x_1 and x_2, are solutions of $Q(x) = 0$. Eq. (10.25) can be written as

$$\sqrt{\lambda + \frac{1}{4}}\int_{x_1}^{x_2}\sqrt{-(x - x_1)(x - x_2)}\,dx = \left(n + \frac{1}{2}\right)\pi. \tag{10.29}$$

Let $y = 2(x - x_0)/\Delta$, where $x_0 = (x_1 + x_2)/2$ is located mid-way between the turning points and $\Delta = |x_1 - x_2|$ is the distance between them. We get

$$\sqrt{\lambda + \frac{1}{4}}\left(\frac{\Delta}{2}\right)^2\int_{-1}^{1}\sqrt{1 - y^2}\,dy = \left(n + \frac{1}{2}\right)\pi. \tag{10.30}$$

The integral is equal to $\pi/2$. In the present case, the turning points are separated by

$$\Delta = \frac{1}{\lambda + 1/4}\sqrt{\lambda(\alpha_1 - \alpha_2)^2 k_z^2 + 4(\lambda + 1/4)(\lambda - 1/2)}. \tag{10.31}$$

Substitution into the quantization condition leads to the determination of the eigenvalues

$$k_z = \pm\frac{2i}{\alpha_1 - \alpha_2}\sqrt{1 + \frac{1}{4\lambda}}\sqrt{\lambda - \frac{1}{2} - \sqrt{\lambda + \frac{1}{4}}(2n+1)}. \tag{10.32}$$

The growth rate of these modes is given by

$$\bar{K}_n = \frac{2}{\alpha_1 - \alpha_2}\sqrt{1 + \frac{1}{4\lambda}}\sqrt{\lambda - \frac{1}{2} - (2n+1)\sqrt{\lambda + \frac{1}{4}}}. \tag{10.33}$$

As mentioned above, the calculation of the growth rate using WKB analysis is valid in the infinite pump-strength ($\lambda \to \infty$) limit. In this case, the growth rate from Eq. (10.33) becomes

$$\bar{K}_n \approx \frac{2}{\alpha_1 - \alpha_2}\sqrt{\lambda - (2n+1)\sqrt{\lambda}}. \tag{10.34}$$

and the threshold is

$$\lambda_{th,n} = (1 + 2n)^2. \tag{10.35}$$

Fig. 10.2 compares these two expressions for the growth rate with the values obtained from the numerical simulations. The infinite-pump expression is the one which captures best the behavior close to threshold. We note that the infinite pump strength approximation corresponds to dropping the terms involving $(d/dx)\ln A_0$ in Eq. (10.10).

Fig. 10.3 shows plots of the growth rate as a function of α_1. Except for a constant offset, Eq. (10.34) captures the dependence on α_1 accurately.

The growth rate given above was expressed in normalized units. In physical units, $K = \bar{K}/L_{NC}$, and we have

$$K_n \approx \frac{2\gamma_0}{\alpha_1 - \alpha_2}\sqrt{1 - \frac{2n+1}{\sqrt{\lambda}}}. \tag{10.36}$$

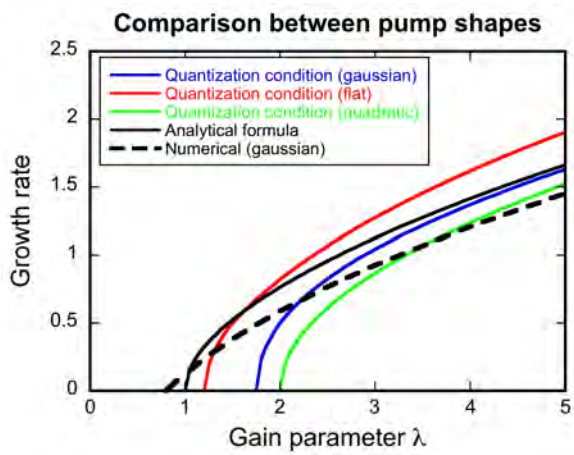

Figure 10.2: Growth rate of the fundamental mode ($n = 0$) vs λ. This plot shows a comparison between the WKB quantization condition applied to a gaussian, top-hat ("flat"), and parabolic pump profiles evaluated numerically; the analytical formula obtained assuming a parabolic pump in the infinite pump-strength limit, Eq. (10.34); and the numerical simulations using a gaussian pump.

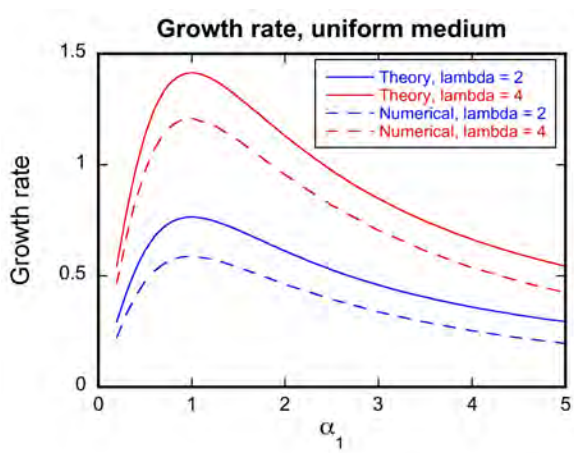

Figure 10.3: Normalized growth rate, $\bar{K}$, of the fundamental mode ($n = 0$) vs α_1.

The growth rate in the parabolic pump approximation was obtained by Sushchik in Ref. [67].

10.2.4 Mode Shape

The growth rate was calculated assuming a parabolic pump profile. For a more general pump profile $A_0(x)$, the numerical value of the growth rate will be slightly different but the nature of the eigenvalues will be the same, i.e. $k_z = \pm iK$, with K real. Then the "potential" $Q(x)$, Eq. (10.14), is purely real. Between the turning points, the fundamental mode ($n = 0$) has the form

$$a_1(x) \sim \cos \int_{x_1}^{x} \sqrt{Q(x')}\, dx'. \tag{10.37}$$

Outside of the pump, away from the turning points, the WKB solutions are

$$\begin{aligned} a_1 &\sim \exp \pm \int^{x} \sqrt{-Q}\, dx \\ &\sim A_0^{\pm 1/2} e^{\mp \frac{i}{2}(\alpha_1 - \alpha_2) k_z x}, \qquad |x| \gg 1. \end{aligned} \tag{10.38}$$

Putting everything together, we obtain the following expressions for the fundamental growing mode:

$$A_1(\bar{z}, \bar{x}) \sim \begin{cases} A_0(\bar{x})\, e^{\bar{K}(\bar{z} - \bar{x}/\alpha_2)} & \bar{x} \ll -1. \\ A_0^{1/2}(\bar{x}) e^{\bar{K}[\bar{z} + (\alpha_1 + \alpha_2)\bar{x}]} \cos \int_{\bar{x}_1}^{\bar{x}} \sqrt{Q(\bar{x}')}\, d\bar{x}' & -1 \ll \bar{x} \ll 1 \\ e^{\bar{K}(\bar{z} - \bar{x}/\alpha_1)} & \bar{x} \gg 1, \end{cases} \tag{10.39}$$

with $\bar{K} \approx \frac{2}{\alpha_1 - \alpha_2} \left(\lambda - \lambda^{1/2}\right)^{1/2}$. In this expression we have restored the "bars" denoting normalized x and z variables.

The fact that A_0 appears in the expression for $\bar{x} \ll -1$ explains that the signal mode be almost zero in that region. In the other side, where $\bar{x} \gg 1$, the mode is constant along the characteristics $\zeta = \bar{z} - \bar{x}/\alpha_1$.

10.2.5 Physical Interpretation

The Sushchik modes are laterally confined gain-guided modes. They constitute an absolute instability in the x-direction. Provided that the gain parameter λ is large enough, the waves grow even though they propagate in different directions. The signal wave, through its interaction with the pump, generates some idler, which in turn amplifies the signal: this self-sustaining process leads to an absolute instability. Fig. 10.4 illustrates this process.

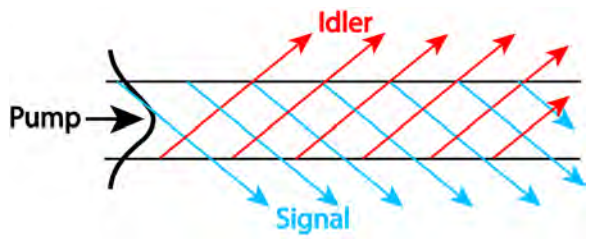

Figure 10.4: Physical picture behind confined noncollinear growing modes.

The waves amplified inside the pump "leak" and propagate along the characteristics $\bar{z} - \bar{x}/\alpha_{1,2}$. However, when the amplification large enough, the signal and idler are gain-guided by the pump.

On the other hand, if the gain parameter is too small, the growth is not large enough to make up for the losses due to the noncollinear propagation of the waves. This is the reason behind the threshold value.

10.2.6 Collinear Limit

To take the collinear limit, we must go back to the un-normalized variables. The physical growth rate is $K = \bar{K}/L_{NC}$, or

$$\lim_{L_{NC}\to\infty} K = \frac{2}{\alpha_1 - \alpha_2}\frac{\sqrt{\lambda}}{L_{NC}}. \tag{10.40}$$

In the collinear limit, $\alpha_1 \to 1$, $\alpha_2 \to -1$. Therefore we recover the collinear growth rate of a uniform medium, $K = \gamma_0$. The threshold vanishes, as it should in a collinear situation.

10.3 Noncollinear Interactions in a Non-Uniform Medium

10.3.1 Equation for Bound States

We now turn our attention to a non-uniform phase-matching medium. As before, we neglect diffraction. The equation describing the evolution of the signal wave is, from Eq. (10.9):

$$\mathcal{L}_1\mathcal{L}_2 A_1 - \lambda |A_0(x)|^2 A_1 - \left(i\kappa(z) + \alpha_2 \frac{d \ln A_0}{dx} \right) \mathcal{L}_1 A_1 = 0, \tag{10.41}$$

where $\kappa(z) = d\phi/dz$ is the phase-matching profile, and $\mathcal{L}_{1,2} = \partial/\partial z + \alpha_{1,2}\partial/\partial z$ as before.

In our discussion of the uniform medium, we saw that we could obtain the growth rate and mode shape in the infinite pump-strength limit. We therefore assume that it is valid to drop the term involving $(d/dx)\ln A_0$. We will also limit our discussion to the linear phase-matching profile, given by $\kappa(z) = \bar{\kappa}' z$.

Our solution in the case of a uniform medium was based on the separation of variables. However, numerical simulations (chapter 8) showed that in the case of a non-uniform medium this assumption is not valid. The phase, in particular, is a non-separable function of x and z, and was found to be constant along the characteristics $z - x/\alpha_{1,2}$. It turns out that it is possible to remove any dependence on z from the equation by using the following change of variables:

$$A_1(z,x) = B_1(z,x) \exp\left[i \frac{\alpha_1}{\alpha_1 - \alpha_2} \phi\left(z - x/\alpha_1\right) \right]. \tag{10.42}$$

Applying operators $\mathcal{L}_1$ and $\mathcal{L}_2$, we get

$$\mathcal{L}_1\mathcal{L}_2 A_1 = \mathcal{L}_1\mathcal{L}_2 B_1 + i\kappa\left(z - x/\alpha_1\right) \mathcal{L}_1 B_1. \tag{10.43}$$

After substitution into Eq. (10.41), we find that the coefficient of $\mathcal{L}_1 B_1$ involves $\kappa(z - x/\alpha_1) - \kappa(z) = -\bar{\kappa}' x/\alpha_1 = \alpha_2 \bar{\kappa}' x$. In the special case of a linear profile the

dependence on z disappears from the equation:

$$\mathcal{L}_1\mathcal{L}_2 B_1 - \lambda|A_0(x)|^2 B_1 + i\alpha_2\bar{\kappa}' x\mathcal{L}_1 B_1 = 0. \tag{10.44}$$

Now we can look for a solution which is separable in x and z.

The rest of the derivation is similar to that of a uniform medium. We take the Fourier transform in z:

$$\frac{d^2\widetilde{B}_1}{dx^2} + i\left[(\alpha_1+\alpha_2)k_z + \bar{\kappa}' x\right]\frac{d\widetilde{B}_1}{dx} + \left[k_z^2 + \lambda|A_0(x)|^2 - i\alpha_2\bar{\kappa}' x\right]\widetilde{B}_1 = 0, \tag{10.45}$$

We eliminate the first-order derivative using

$$\widetilde{B}_1(x) = b_1(x)\exp\left\{-\frac{i}{2}\left[(\alpha_1+\alpha_2)k_z x + \frac{\bar{\kappa}'}{2}x^2\right]\right\} \tag{10.46}$$

Then $b_1(x)$ satisfies a Shrodinger-like equation:

$$\frac{d^2 b_1}{dx^2} + Q(x)b_1(x) = 0, \tag{10.47}$$

with the "potential"

$$Q(x) = \lambda|A_0(x)|^2 + \frac{1}{4}\left[(\alpha_1-\alpha_2)k_z + \bar{\kappa}' x\right]^2 - \frac{i}{2}\bar{\kappa}'. \tag{10.48}$$

Since the curvature of the term $\bar{\kappa}'^2 x^2$ is positive while that of $\lambda|A_0|^2$ is negative, the chirp rate decreases the "strength" of the potential.

10.3.2 Growth Rate

The calculation of the eigenvalues k_z is similar to that carried out in the case of the uniform medium. We assume a parabolic pump profile, $|A_0|^2 = 1 - x^2$. The quantization condition, $\int_{x_1}^{x_2} Q^{1/2}dx = (n+1/2)\pi$, gives rise to

$$\sqrt{\lambda - \left(\frac{\bar{\kappa}'}{2}\right)^2}\left(\frac{\Delta}{2}\right)^2 = 2n+1, \tag{10.49}$$

where the distance between the turning points is given by

$$\Delta = \frac{1}{\lambda - (\bar{\kappa}'/2)^2}\sqrt{\lambda(\alpha_1-\alpha_2)^2 k_z^2 + 4\left[\lambda - \left(\frac{\bar{\kappa}'}{2}\right)^2\right]\left(\lambda - \frac{i\bar{\kappa}'}{2}\right)}. \tag{10.50}$$

Therefore the eigenvalue associated with confined mode n is

$$k_z = \frac{2i}{\alpha_1-\alpha_2}\sqrt{1-\frac{\bar{\kappa}'^2}{4\lambda}}\sqrt{\lambda - \frac{i\bar{\kappa}'}{2} - (2n+1)\sqrt{\lambda}\sqrt{1-\frac{\bar{\kappa}'^2}{4\lambda}}}. \tag{10.51}$$

The imaginary part of the k_z gives the growth rate. For the fundamental mode, the growth rate is approximately

$$\bar{K} = \frac{2}{\alpha_1-\alpha_2}\sqrt{1-\frac{\bar{\kappa}'^2}{4\lambda}}\sqrt{\lambda - \sqrt{\lambda}\sqrt{1-\frac{\bar{\kappa}'^2}{4\lambda}}}. \tag{10.52}$$

In physical units, $K = \bar{K}/L_{NC}$, so we obtain

$$K = \frac{2\gamma_0}{\alpha_1-\alpha_2}\sqrt{1-\frac{\lambda}{4\lambda_R^2}}\sqrt{1-\frac{1}{\sqrt{\lambda}}\sqrt{1-\frac{\lambda}{4\lambda_R^2}}}, \tag{10.53}$$

where $\lambda_R = \lambda^2/\bar{\kappa}' = \gamma_0^2/\kappa'$ is the Rosenbluth gain parameter.

As discussed in section 7.3, a useful way of representing the angular dependence of the growth rate is to plot $\bar{K}/\lambda = K/\gamma_0$ as a function of $1/\sqrt{\lambda} = |\tan\theta_1 \tan\theta_2|^{1/2}/\gamma_0 w_0$, for a fixed ratio of $\bar{\kappa}'/\lambda = \kappa'/\gamma_0^2 = 1/\lambda_R$. This plot is shown in Fig. 10.5. It should be compared with the growth rate obtained numerically, Fig. 8.27. Although the actual values differ, the shape of the curves and the trends are similar.

10.3.3 Physical Interpretation

The most important feature of Fig. 10.5 is the fact that gain-guided modes are allowed for sufficiently large noncollinear angles. This is a consequence of the lateral localization of the pump beam.

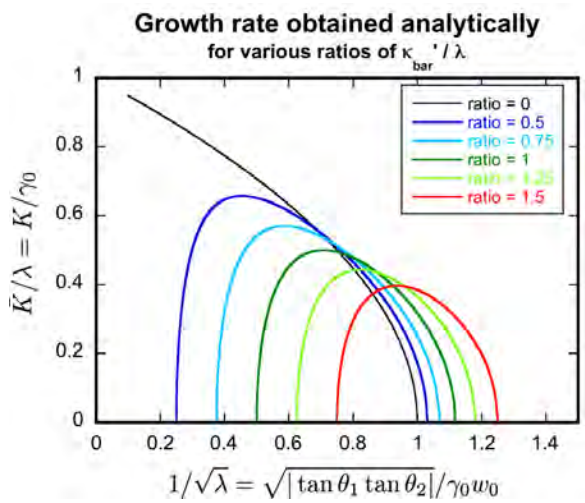

Figure 10.5: Angular dependence of the growth rate. This plot shows $\bar{K}/\lambda = K/\gamma_0$ as a function of $1/\sqrt{\lambda} = |\tan\theta_1 \tan\theta_2|^{1/2}/\gamma_0 w_0$, for fixed ratios of $\bar{\kappa}'/\lambda = \kappa'/\gamma_0^2 = 1/\lambda_R$ (where λ_R is the Rosenbluth gain parameter). This plot was obtained for the degenerate case $\alpha_1 = -\alpha_2 = 1$.

A physical interpretation of this result can be obtained by expressing the growth rate in terms of characteristic lengths. We introduce, as we did when discussing the Rosenbluth model, the dephasing length of a chirped grating,

$$L_{deph} = \frac{2\gamma_0}{\kappa'}. \tag{10.54}$$

We also consider the gain length of a uniform medium,

$$L_g = \frac{1}{\gamma_0}. \tag{10.55}$$

Finally, we recall our definition of the noncollinear length:

$$L_{NC} = \frac{w_0}{\sqrt{|\tan\theta_1 \tan\theta_2|}}. \tag{10.56}$$

The interpretation of the noncollinear length was given in chapter 7, as the length over which the noncollinear signal and idler waves escape the pump beam of radius

w_0. In terms of those characteristic lengths, the growth rate from Eq.(10.53) becomes

$$\frac{K}{\gamma_0} = \frac{2}{\sqrt{r} + 1/\sqrt{r}} \sqrt{1 - \left(\frac{L_{NC}}{L_{deph}}\right)^2} \sqrt{1 - \frac{L_g}{L_{NC}} \sqrt{1 - \left(\frac{L_{NC}}{L_{deph}}\right)^2}}. \tag{10.57}$$

The growth rate is real and positive only if $L_{NC} < L_{deph}$. In other words, growing modes exist (i.e. the chirp does not completely suppress the absolute instability) if the noncollinear length is *shorter* than the dephasing length.

Let us look at the various regimes successively. If $L_{NC} > L_{deph}$, the noncollinear length is longer than the dephasing length (i.e. the angle is small) and the waves remain in the interaction region sufficiently long to experience dephasing. In this case, the growth of the waves is suppressed. If the noncollinear length is shorter than the dephasing length (i.e. if the noncollinear angle is large enough), the waves leave the interaction region before experiencing significant dephasing, and as a consequence gain-guided modes can be established. However, if the angle is too large, the gain is low and is below the instability threshold. Fig. 10.6 illustrates this situation.

In the absence of lateral pump localization, ($w_0 \to \infty$), the noncollinear length becomes infinite (the waves never escape the interaction region). In this case, the absolute instability cannot exist. This explains why noncollinear growing modes could not be found in a 1-D model. Lateral pump localization is crucial to the existence of an absolute instability.

The results of this section bridge the gap between the Sushchik modes and the Rosenbluth model. Each case corresponds to a different limit of the problem: lateral localization of the pump but uniform medium in the case of Sushchik's work, and non-localized pump but non-uniform medium in the case of Rosenbluth's. In the present work we address the case where both lateral localization of the pump and non-uniformity of the medium are present. We find that when the collinear angle is small enough, the amplification stops because of dephasing, as in the Rosenbluth model. However, when the angle is large enough, Sushchik-like gain-guided modes can exist in spite of the non-uniformity. In other words, the instability, which is convective in the case of the Rosenbluth model, can become absolute when the pump

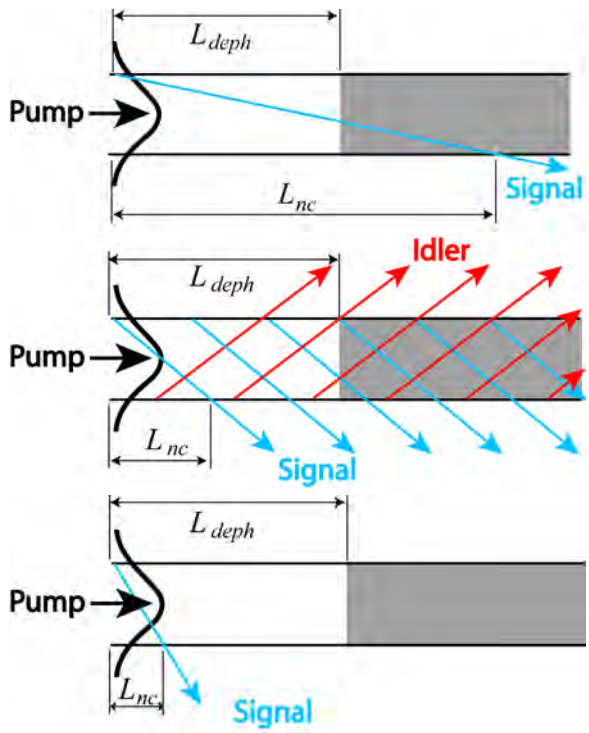

Figure 10.6: Physical picture behind confined noncollinear growing modes: when $L_{NC} > L_{deph}$, growing modes do not exist because they are suppressed by the dephasing (top); when $L_{NC} < L_{deph}$, growing modes exist because the waves escape the pump before experiencing dephasing (center); however, when the angle is too large growing modes do not exist because the instability is below threshold (bottom).

is confined laterally. A similar conclusion was reached in the case of *axial* localization of the pump in earlier work in the plasma physics literature [73, 74, 51].

10.4 Interactions in the Presence of Diffraction

10.4.1 Equation for Bound States

When the beams are tightly focused, or when the noncollinear angle is sufficiently small, diffraction is the dominant transverse effect. In this case the equation describing the evolution of the waves in the presence of dephasing, Eq. (10.9), becomes

$$\mathcal{L}_1\mathcal{L}_2 A_1 - \lambda |A_0(x)|^2 A_1 - i\kappa(z)\mathcal{L}_1 A_1 = 0, \tag{10.58}$$

with $\mathcal{L}_{1,2} = \partial/\partial z \mp i\beta_{1.2}\partial^2/\partial x^2$. As before, we neglected the terms involving $(d/dx)\ln A_0$. We also assume that $\beta_1, \beta_2 \ll 1$.

It is convenient to normalize the transverse dimension with respect to the pump width, as done above. However, in order leave the phase mismatch as an explicit parameter, we will leave the z-axis un-normalized. Therefore, the parameters appearing in Eq. (10.58) are defined differently than in previous sections, as

$$\beta_{1,2} = \frac{1}{2k_{1,2}w_0^2}, \tag{10.59}$$

$$\lambda = \gamma_0^2. \tag{10.60}$$

Eq. (10.58) is a PDE which is second order in z and fourth order in x. The method used earlier in this chapter, which consists in Fourier transforming in z and then finding the mode shape using WKB analysis in x, cannot be employed in this case.

An alternative solution technique is to solve the problem in the Fourier domain. This approach was used in the field of plasma physics, where the interaction is described by very complicated differential operators [75]. Assuming a parabolic pump profile, Eq. (10.58) has coefficients which are at most quadratic, which translates to a

second-order PDE in the Fourier domain. Thus working in k-space allows a reduction from 4 to 2 of the order of the differential equation.

For now we assume that the wave vector mismatch κ is constant. We consider a parabolic pump profile: $|A_0|^2 = 1 - x^2$. Taking Fourier transforms in z and x, Eq. (10.58) becomes

$$\left[-k_z^2 + (\beta_1 - \beta_2)k_z k_x^2 + \beta_1\beta_2 k_x^4\right] \widehat{\widetilde{A}}_1 - \lambda \left(1 + \frac{d^2}{dk_x^2}\right) \widehat{\widetilde{A}}_1 - \kappa \left(k_z - \beta_1 k_x^2\right) \widehat{\widetilde{A}}_1 = 0. \tag{10.61}$$

This can be written as

$$\frac{d^2\widehat{\widetilde{A}}_1}{dk_x^2} + \widehat{Q}(k_x)\widehat{\widetilde{A}}_1 = 0, \tag{10.62}$$

with the k-space "potential"

$$\widehat{Q}(k_x) = 1 + \frac{1}{\lambda}\left[k_z^2 - (\beta_1 - \beta_2)k_z k_x^2 - \beta_1\beta_2 k_x^4 + \kappa\left(k_z - \beta_1 k_x^2\right)\right]. \tag{10.63}$$

Here, k_z plays the role of the eigenvalue and k_x is the independent variable. $\widehat{Q}$ is a quartic potential. The solutions behave very differently depending on the sign of κ. We will examine successively the cases of κ positive and negative.

10.4.2 Positive Phase Mismatch

When $\kappa > 0$, the "potential" is

$$\widehat{Q}(k_x) = 1 + \frac{1}{\lambda}\left\{k_z^2 + |\kappa|k_z - \beta_1\beta_2 k_x^4 - \left[\beta_1|\kappa| + (\beta_1 - \beta_2)k_z\right]k_x^2\right\}. \tag{10.64}$$

The coefficients of k_x^4 and k_x^2 are both negative; they reinforce each other. In the limit of small β's, we can neglect the quartic term because the eigenmode will be localized around the origin in k_x-space.

The turning points (solutions of $\widehat{Q} = 0$) are separated by a distance

$$\Delta = 2\sqrt{\frac{\lambda + k_z(k_z + |\kappa|)}{\beta_1|\kappa| + (\beta_1 - \beta_2)k_z}}. \tag{10.65}$$

Application of the quantization condition, $\int_{k_{x1}}^{k_{x2}} \widehat{Q}^{1/2}\, dk_x = (n+1/2)\pi$, leads to

$$\sqrt{\frac{\beta_1|\kappa| + (\beta_1 - \beta_2)k_z}{\lambda}} \left(\frac{\Delta}{2}\right)^2 \frac{\pi}{2} = \left(n + \frac{1}{2}\right)\pi \tag{10.66}$$

In the limit of $\beta_{1,2} \to 0$, this equation leads to

$$k_z^2 + |\kappa| k_z + \lambda = 0, \tag{10.67}$$

which gives

$$k_z = \frac{|\kappa|}{2} \pm i\sqrt{\lambda - \left(\frac{\kappa}{2}\right)^2}. \tag{10.68}$$

We recover the results from the Rosenbluth model. If the phase mismatch is larger than $2\lambda^{1/2} = 2\gamma_0$, the eigenvalue k_z is purely real and the solutions do not grow. Diffraction is only a small perturbation; it does not modify the nature of the solutions.

10.4.3 Negative Phase Mismatch

When $\kappa < 0$, the "potential" is

$$\widehat{Q}(k_x) = 1 + \frac{1}{\lambda}\left\{k_z^2 - |\kappa| k_z - \beta_1\beta_2 k_x^4 + \left[\beta_1|\kappa| - (\beta_1 - \beta_2)k_z\right] k_x^2\right\}. \tag{10.69}$$

The coefficients of k_x^4 and k_x^2 have opposite signs. The function $\widehat{Q}$ has two local maxima, located at

$$k_x^{*\pm} = \pm\sqrt{\frac{\beta_1|\kappa| - \delta\beta k_z}{2\beta_1\beta_2}}, \tag{10.70}$$

where $\delta\beta = \beta_1 - \beta_2$. To each of these maxima correspond a pair of turning points. Application of the quantization condition for either maximum yields an equation for the eigenvalue k_z:

$$k_z^2 - |\kappa| k_z + \lambda + \frac{1}{4\beta_1\beta_2}\left(\beta_1|\kappa| - \delta\beta k_z\right)^2 = (2n+1)\sqrt{2\lambda}\sqrt{\beta_1|\kappa| - \delta\beta k_z}. \tag{10.71}$$

In the limit $\beta_{1,2} \to 0$, the solutions are

$$k_z = \frac{\beta_1}{2\bar{\beta}}|\kappa| \pm i\frac{\sqrt{\beta_1\beta_2}}{\bar{\beta}}\sqrt{\lambda}, \tag{10.72}$$

where $\bar{\beta} = (\beta_1 + \beta_2)/2$. The eigenvalues are complex. The imaginary part gives the growth rate:

$$K = \frac{\sqrt{\beta_1\beta_2}}{\bar{\beta}}\sqrt{\lambda}. \tag{10.73}$$

Substituting the eigenvalue into the expression for k_x^*, we find the location of the eigenmodes:

$$k_x^{*\pm} \approx \pm\sqrt{\frac{|\kappa|}{2\bar{\beta}}}. \tag{10.74}$$

(provided $|\kappa| \gg \lambda^{1/2}$). Assuming a symmetric mode, we sum contributions from both locations:

$$\widehat{\widetilde{A}}_1 = \widehat{b}(k_x - k_x^{*+}) + \widehat{b}(k_x - k_x^{*-}), \tag{10.75}$$

where $\widehat{b}(k_x)$ is the shape in k-space of the mode located around either of $k_x^{*\pm}$. The width of the mode $\widehat{b}$ is given approximately by the separation between the turning points,

$$\Delta = \left(\frac{\bar{\beta}\lambda}{2\beta_1\beta_2|\kappa|}\right)^{1/4}. \tag{10.76}$$

Finally, we come back to real space. The mode profile is given by

$$\widetilde{A}_1(k_z, x) = \cos\left(k_x^* x\right) b(x), \tag{10.77}$$

where $b(x)$ is the mode envelope. The mode is oscillatory, with a period of $1/k_x^* = (2\bar{\beta}/|\kappa|)^{1/2}$. The width of the envelope is of the order of $1/\Delta = (2\beta_1\beta_2|\kappa|/\bar{\beta}\lambda)^{1/4}$.

10.4.4 First Interpretation: Noncollinear Phase-Matching

The spectral content of growing modes in the presence of negative phase mismatch consists of two contributions, located at $k_x^{*\pm}$. This can be interpreted by a phase-matching argument.

Noncollinear phase matching was discussed in chapter 7. The phase-matching angles θ_1 and θ_2 satisfy

$$k_2 \sin\theta_1 - k_2 \sin\theta_2 = 0 \tag{10.78}$$

$$k_1 \cos\theta_1 + k_2 \cos\theta_2 = k_p - K_{g0} - |\kappa|, \tag{10.79}$$

where K_{g0} is the grating period which ensures *collinear* phase matching when $\kappa = 0$, i.e. $k_p - K_{g0} = k_1 + k_2$. In the small-angle approximation, the phase-matching angles are

$$\theta_{1,2} = \pm\sqrt{\frac{k_{2,1}}{k_{1,2}}}\sqrt{\frac{2|\kappa|}{k_1 + k_2}}. \tag{10.80}$$

The transverse components of the wave vectors are $k_{\perp 1,2} = k_{1,2}\theta_{1,2}$. Expressing the wave vectors $k_{1,2}$ in terms of $\beta_{1,2}$ using Eq. (10.59), we obtain

$$k_{\perp 1,2} = \pm\frac{1}{w_0}\sqrt{\frac{|\kappa|}{\beta_1 + \beta_2}} \tag{10.81}$$

In normalized x-units, the transverse components of the wave vectors are $\bar{k}_{1,2} = w_0 k_{1,2}$. So we find that the transverse wave vectors ensuring phase-matching are

$$\bar{k}_{\perp 1,2} = \pm\sqrt{\frac{|\kappa|}{2\bar{\beta}}}, \tag{10.82}$$

which is precisely equal to $k_x^{*\pm}$. The growing modes consist in the superposition of two noncollinearly phase-matched plane waves (for each of $\pm\theta_1$). Since they propagate at equal but opposite angles, they establish a standing-wave pattern in the x-direction, which explains why in physical space the mode is oscillatory. Fig. 10.7 illustrates this situation.

Growing modes do not exist when the phase mismatch is positive (and larger than $2\gamma_0$) because noncollinear phase-matching is not possible in this case. Eqs. (10.78) and (10.79) admit (real) solutions only when $\kappa < 0$.

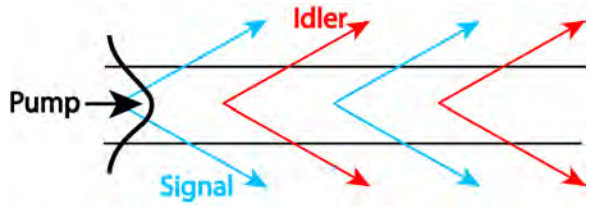

Figure 10.7: Physical picture: growing modes consist of two noncollinear phase-matched interactions.

10.4.5 Second Interpretation: Balance between Diffraction and Phase Deaccumulation

Another interpretation is that amplification occurs because diffraction cancels the phase accumulation due to the non-uniformity. This is illustrated by the following argument.

Let us rewrite the two coupled equations including diffraction and dephasing, but for simplicity let us ignore the localization of the pump and assume that $\beta_1 = \beta_2 = \beta$:

$$\left(\frac{\partial}{\partial z} - i\beta\frac{\partial^2}{\partial x^2}\right) A_1 = i\gamma_0 A_2^* e^{i\phi} \tag{10.83}$$

$$\left(\frac{\partial}{\partial z} + i\beta\frac{\partial^2}{\partial x^2}\right) A_2^* = -i\gamma_0 A_1 e^{-i\phi}. \tag{10.84}$$

We perform the substitution $A_{1,2} = a_{1,2}e^{i\phi/2}$. The equations become

$$\left(\frac{\partial}{\partial z} - i\beta\frac{\partial^2}{\partial x^2} + \frac{i}{2}\kappa\right) a_1 = i\gamma_0 a_2^* \tag{10.85}$$

$$\left(\frac{\partial}{\partial z} + i\beta\frac{\partial^2}{\partial x^2} - \frac{i}{2}\kappa\right) a_2^* = -i\gamma_0 a_1, \tag{10.86}$$

where $\kappa = d\phi/dz$ is assumed to be constant for simplicity. The effect of phase mismatch is contained in the term $i\kappa/2$. We now take the Fourier transform in x:

$$\left(\frac{\partial}{\partial z} + i\beta k_x^2 + \frac{i}{2}\kappa\right) \widetilde{a}_1 = i\gamma_0 a_2^* \tag{10.87}$$

$$\left(\frac{\partial}{\partial z} - i\beta k_x^2 - \frac{i}{2}\kappa\right) \widetilde{a}_2^* = -i\gamma_0 a_1. \tag{10.88}$$

Diffraction and dephasing can offset each other if the dephasing rate is negative. In particular, for $k_x = \sqrt{|\kappa|/2\beta}$, diffraction perfectly cancels the phase accumulation.

This shows that we can look at this situation from the point of view of noncollinear phase-matching or as a balance between diffraction and dephasing. These interpretations are in fact equivalent since phase matching is a consequence of cancellation of phase accumulation.

10.4.6 Non-Uniform Medium

In the analysis presented above, we assumed that the mismatch κ was constant. When this is not the case, the solution based on the separation of variables is not valid. In the case of a non-uniform medium in a noncollinear geometry, we solved this difficulty by using a change of variables that removes the z-dependence from the equation. However we have not yet found a similar change of variables for Eq. (10.58).

In the case of a linear phase-matching profile, we can assume that the general features of the solution remain globally the same and evolve in z. This assumption is supported by the numerical results shown in chapter 8. In particular, the location of the mode in k_x-space now varies with the square root of position, as shown in Fig. 8.35:

$$k_x^{*\pm}(z) = \pm\sqrt{\frac{|\kappa'|(z - z_{pm})}{2\bar{\beta}}} \tag{10.89}$$

The reduction of growth rate due to the chirp rate was observed numerically but could not be obtained analytically here. Another feature unaccounted by the uniform-medium solutions is the threshold length. The present calculation describes the existing mode but not their dynamics; it says nothing about how the growing modes are established. Heuristically, we can imagine that the mode established around $k_x = 0$ couples to the noncollinear direction $k_x^{*\pm}$, but that a certain distance is required before the amplitude of the noncollinear modes dominates; this distance is the threshold length. In chapter 8, we found numerically that the threshold length is given by

$$L_{th} = \frac{1}{8\beta}\left(\frac{\kappa'}{\lambda}\right)^2 = \frac{1}{8\beta\lambda_R^2} = \frac{kw_0^2}{4\lambda_R^2}, \tag{10.90}$$

where as usual $\lambda_R = \gamma_0^2/\kappa'$ is the Rosenbluth gain parameter.

Chapter 11

Design Guidelines

As discussed in chapter 2, chirped QPM gratings provide a way of engineering the amplification bandwidth of OPAs. This relies on the assumption that the Rosenbluth model is valid, i.e. that the amplification is localized in the vicinity of the phase-matched point. In this case, the gain depends on the local chirp rate, according to the Rosenbluth gain formula.

Transverse effects can destroy the desired behavior of chirped QPM OPAs in two ways. First, the parametric fluorescence due to noncollinear gain-guided modes can be large enough to spoil the beam contrast. Second, noncollinear interactions seeded by diffraction in negatively-chirped QPM gratings can destroy the Rosenbluth gain by allowing amplification over a longer distance. In this chapter we address these two issues and give design guidelines to suppress the undesired transverse effects.

We first obtain the noncollinear gain spectra of uniform and chirped QPM OPAs. Real amplifiers have a finite length, and, in the case of chirped QPM gratings, the frequency dependence of the phase-matched point needs to be taken into account. Then we use the noncollinear gain spectrum to calculate the power level of the parametric fluorescence.

Finally, we formulate design guidelines. First, we describe a procedure to control the parametric fluorescence due to noncollinear gain-guided modes. Second, we give a criterion to suppress the parasitic amplification occurring in the case of negative chirp rates. Both approaches rely on the use of a sufficiently wide pump beam.

Using wide pump beams eliminates the role played by the transverse dimension. This effectively transforms the 2-D model into a 1-D model. It is therefore not surprising that wide pump beams provide a way of suppressing transverse effects.

11.1 Noncollinear Gain Spectrum

The goal of this section is to understand the conditions under which the desired Rosenbluth gain dominates the undesired noncollinear gain. To accomplish that, we calculate the noncollinear gain of uniform and chirped QPM OPAs.

11.1.1 Uniform QPM Grating

For a uniform QPM grating, the growth rate of noncollinear gain-guided modes (Sushchik modes) is given by Eq. (10.36), which in the small-angle approximation becomes:

$$K_{pm}(\theta) = \frac{2\gamma_0}{\sqrt{r} + 1/\sqrt{r}} \sqrt{1 - \frac{\sqrt{r}|\theta|}{\gamma_0 w_0}}, \tag{11.1}$$

where $r = k_{s0}/k_{i0}$, γ_0 is the coupling coefficient, w_0 is the half-width of the pump beam and θ is the noncollinear angle. To obtain this result, we used Eqs. (7.30) and (7.31) to express α_1 and α_2 in terms of r. According to Eq. (11.1), for small angles the growth rate decreases linearly with θ.

Eq. (11.1) gives the growth rate of a perfectly phase-matched interaction. Shifting the signal wavelength away from the phase-matching wavelength introduces phase mismatch and reduces the gain. Using a parabolic approximation, the growth rate as a function of wavelength is

$$K(\theta, \lambda_s) = K_{pm}(\theta) - \left[\frac{\lambda_s - \lambda_{pm}(\theta)}{\Delta\lambda_{BW}}\right]^2, \tag{11.2}$$

where

$$\Delta\lambda_{BW} = \frac{\lambda_{pm}^2}{2\pi c} \frac{4\gamma_0}{|1/v_s - 1/v_i|} \tag{11.3}$$

is the amplification bandwidth expressed in wavelengths, obtained using Eq. (2.30).

The phase-matching wavelength is related to the angle by Eq. (7.17):

$$\lambda_{pm}(\theta) = \lambda_{s0}\left[1 + \frac{n_{s0}}{2c\,(1/v_s - 1/v_i)}\theta^2\right], \tag{11.4}$$

where λ_{s0} is the collinear phase-matching wavelength.

Now that we have the growth rate, let us calculate the actual gain. The (power) gain spectrum of a uniform-QPM OPA is given by

$$G(\theta, \lambda_s) = \frac{1}{2}e^{2K(\theta,\lambda_s)L}, \tag{11.5}$$

where L is the length of the uniform grating. Fig. 11.1 shows the angular and spectral dependence of the gain. It illustrates the wavelength shift and gain reduction associated with the noncollinear angle.

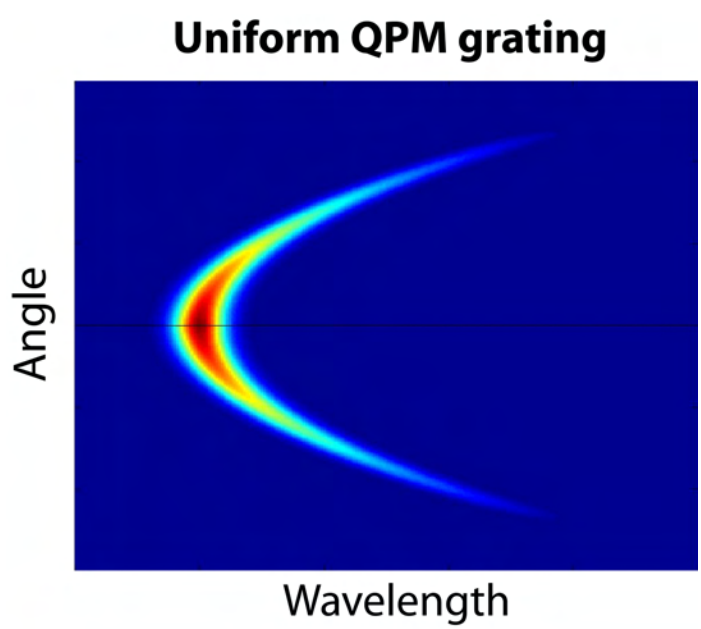

Figure 11.1: Diagram illustrating the noncollinear gain spectrum of uniform QPM gratings. Here it was assumed that $v_s > v_i$.

11.1.2 Chirped QPM Grating

The growth rate of noncollinear gain-guided modes in chirped QPM gratings was given in Eq. (10.53):

$$K_{pm}(\theta) = \frac{2\gamma_0}{\sqrt{r}+1/\sqrt{r}}\sqrt{1-\frac{\lambda}{4\lambda_R^2}}\sqrt{1-\frac{1}{\sqrt{\lambda}}\sqrt{1-\frac{\lambda}{4\lambda_R^2}}}, \tag{11.6}$$

where $\lambda_R = \lambda^2/\bar{\kappa}' = \gamma_0^2/\kappa'$ is the Rosenbluth gain parameter and $\lambda = (\gamma_0 L_{NC})^2$. The angular dependence of the growth rate is plotted in Fig. 8.27. Growing modes exist for a range of angles, as illustrated in Fig. 8.28.

Let us define λ_{s1} and λ_{s2} the edges of the phase-matching bandwidth ($\lambda_{s1} < \lambda_{s2}$). At a noncollinear angle θ, they are shifted from the collinear wavelengths λ_{s01} and λ_{s02} according to

$$\lambda_{s1}(\theta) = \lambda_{s01}\left[1+\frac{n_{s01}}{2c\,(1/v_s-1/v_i)}\theta^2\right], \tag{11.7}$$

$$\lambda_{s2}(\theta) = \lambda_{s02}\left[1+\frac{n_{s02}}{2c\,(1/v_s-1/v_i)}\theta^2\right], \tag{11.8}$$

where λ_{s01} and λ_{s02} denote the edges of the *collinear* bandwidth. A signal wavelength λ_s incident at angle θ is phase-matched somewhere inside the grating if it falls between λ_{s1} and λ_{s2}, and therefore the growth rate is given by

$$K(\theta,\lambda_s) = \begin{cases} K_{pm}(\theta) & \text{if } \lambda_{s1} < \lambda_s < \lambda_{s2} \\ 0 & \text{otherwise} \end{cases} \tag{11.9}$$

In the case of a linear grating profile, the position of the perfect phase-matching point is a linear function of wavelength:

$$z_{pm}(\lambda_s) = \begin{cases} L\frac{\lambda_s-\lambda_{s,1}}{\lambda_{s,2}-\lambda_{s,1}} & \text{if } \kappa'>0 \text{ and } 1/v_s<1/v_i \text{ or } \kappa'<0 \text{ and } 1/v_s>1/v_i \\ L\frac{\lambda_{s,2}-\lambda_s}{\lambda_{s,2}-\lambda_{s,1}} & \text{if } \kappa'<0 \text{ and } 1/v_s<1/v_i \text{ or } \kappa'>0 \text{ and } 1/v_s>1/v_i \end{cases}. \tag{11.10}$$

This expression reflects the fact that, if for instance the chirp rate is positive and the

dispersion relation is such that $1/v_s < 1/v_i$, wavelength λ_{s1} is phase matched at the beginning of the grating while λ_{s2} is phase matched at the end. A gain-guided mode established at z_{pm} grows for a distance $L - z_{pm}$; the total (power) gain is therefore

$$G(\theta, \lambda_s) = \frac{1}{2} \exp \left\{ 2K(\theta, \lambda_s) \left[L - z_{pm}(\lambda_s) \right] \right\}. \tag{11.11}$$

Fig. 11.2 shows the angular and spectral dependence of the noncollinear gain of a chirped QPM grating. It illustrates the fact that growing modes exist for sufficiently large angles only. It also shows the shift of phase-matching wavelengths associated with a noncollinear angle. At a fixed angle, the gain is function of wavelength because the position of the phase-matched point varies with wavelength.

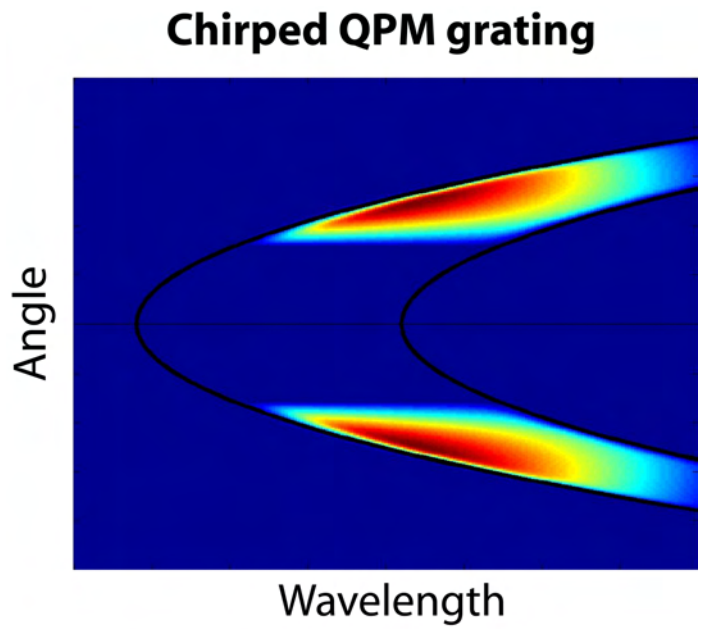

Figure 11.2: Diagram illustrating the noncollinear gain spectrum of chirped QPM gratings. Here it was assumed that $v_s > v_i$.

This plot explains why the fluorescence spectrum observed experimentally (Fig. 5.1) was shifted towards longer wavelengths, appearing only over the long-wavelength side of the spectrum.

As shown in Fig. 11.2, noncollinear growing modes exist only for sufficiently large

angles. When the angle is too small, gain-guided modes are suppressed by the dephasing. In this case, the amplification is limited to the vicinity of the phase-matched point and is given by the Rosenbluth gain formula (see chapter 2):

$$G_R(\theta, \lambda_s) = \begin{cases} e^{2\pi\lambda_R} & \text{if } \lambda_{s1}(\theta) < \lambda_s < \lambda_{s2}(\theta) \\ 0 & \text{otherwise} \end{cases} . \tag{11.12}$$

This is actually the desired behavior of chirped QPM OPAs.

11.2 Parametric Fluorescence

Now that we have calculated the gain as a function of wavelength and angle, we are in position to calculate the parametric fluorescence spectrum.

The theory of parametric fluorescence is described in Refs. [27, 28, 61, 62, 63, 64, 44]. Following Byer and Harris [44], we assume that the amplifier is seeded by one signal photon per mode:

$$d^2 I_{in}(\omega, \theta) = \frac{\hbar\omega}{4\pi^2} k_\perp \, dk_\perp d\omega, \tag{11.13}$$

where $k_\perp$ is the perpendicular component of the k-vector. Using $\theta = k_\perp/k$, and $k = n\omega/c$, we obtain the following expression for the intensity of the parametric "noise" seeding the amplifier per unit solid angle and frequency:

$$d^2 I_{in}(\omega, \theta) = \frac{\hbar\omega^3 n^2}{4\pi^2 c^2} \theta \, d\theta d\omega. \tag{11.14}$$

The total intensity of the amplified parametric fluorescence is obtained by multiplying by the power gain spectrum and integrating over all angles and frequencies:

$$I_{out} = F_0 \int G(\theta, \omega)\theta \, d\theta d\omega, \tag{11.15}$$

where

$$F_0 = \frac{\hbar\omega_s^3 n_s^2}{4\pi^2 c^2} \tag{11.16}$$

is the fluence associated with the parametric noise seeding the amplifier. For the experiment described in chapter 9, the fluence F_0 is equal to 24.7 pJ/cm^2.

For a uniform grating, evaluating the integrals using the gain spectrum given in Eq. (11.5) yields

$$I_{out} = \frac{1}{4} F_0 e^{2\gamma_0 L} \Delta\theta^2 \sqrt{\pi} \Delta\omega_{BW}, \tag{11.17}$$

where

$$\Delta\theta = \frac{\sqrt{r} + 1/\sqrt{r}}{2} \frac{w_0}{\sqrt{r} L} \tag{11.18}$$

and $\Delta\omega$ are the angular and spectral gain bandwidths, respectively. For the experiment described in chapters 4 and 9, Eq. (11.17) gives an equivalent input energy (i.e. at zero pump intensity) due to the parametric noise of 6.0×10^{-18} J (or a peak power of 7.5 nW). This is in reasonable agreement with the value of 3.9×10^{-18} J measured experimentally (see chapter 9). The logarithm of the fluorescence output power is proportional to $2\gamma_0 L$. This fact was used in chapter 9 to measure the coupling coefficient.

Let us now turn our attention to chirped QPM gratings. We substitute the gain given in Eq. (11.11) into (11.15). Evaluating the integral in ω first, we find:

$$\int_0^{\Delta\omega_{BW}} e^{2K(\theta)L\delta\omega/\Delta\omega_{BW}} \, d\delta\omega = \frac{\Delta\omega_{BW}}{2K(\theta)L} \left(e^{2K(\theta)L} - 1 \right), \tag{11.19}$$

where $\Delta\omega_{BW}$ is the amplification bandwidth. The integral in θ can then be evaluated approximately around the angle of maximum gain. The amplified fluorescence is given by

$$I_{out} = \frac{F_0 e^{2K(\theta^*)L} \theta^* \Delta\theta \Delta\omega_{BW}}{2K(\theta^*)L}, \tag{11.20}$$

where θ^* is the angle corresponding to maximum gain and $\Delta\theta$ is the range of angles over which amplification is possible. As indicated in Fig. 8.27, $K(\theta^*)$, θ^* and $\Delta\theta$ all depend on the chirp rate through the Rosenbluth gain parameter, $\lambda_R = \gamma_0^2/\kappa'$. Compared to uniform gratings, chirped gratings offer a wider angular and spectral bandwidth but a reduced growth rate. We will use this result in section 11.3) to set limits on the minimum signal power required to dominate the parametric emission.

11.3 Suppression of Parametric Fluorescence

The parametric fluorescence can be ignored when the power level of the amplified signal in the collinear OPA is much higher than that of the fluorescence caused by noncollinear gain-guided modes. This condition can be expressed as

$$P_{in}e^{2\pi\gamma_0^2/\kappa'} \gg P_{noise}e^{2K(\theta^*)L}, \tag{11.21}$$

where P_{in} and P_{noise} are the the power levels of the input signal and of the "equivalent input noise", respectively. The equivalent input noise is given by (using Eq. (11.20))

$$P_{noise} = \frac{F_0\theta^*\Delta\theta\Delta\omega_{BW}\pi w_0^2}{2K(\theta^*)L}, \tag{11.22}$$

where w_0 is the radius of the pump beam. P_{noise} is typically of the order of nanowatts, but depends on the bandwidth and angular range of the parametric emission. The factor appearing on the left-hand-side is the Rosenbluth gain factor. That on the right-hand-side is the gain of the noncollinear mode at the angle offering the largest growth rate. The maximal growth rate $K(\theta^*)$ can be difficult to estimate; however it will always be lower than the collinear growth rate γ_0. Therefore a more stringent, but safer, design guideline is

$$P_{in}e^{2\pi\gamma_0^2/\kappa'} \gg P_{noise}e^{2\gamma_0 L}. \tag{11.23}$$

If the input signal power level is not large enough to dominate the fluorescence, then control of the parametric emission can be achieved using a sufficiently wide pump beam. Let us recall that noncollinear growing modes exist for a range of normalized gain parameters. We label $1/\sqrt{\lambda^*}$ the lower limit of that range (see Fig. 8.27). The angle associated with this value is

$$\theta_{min} = \frac{\gamma_0 w_0}{\sqrt{r\lambda^*}}. \tag{11.24}$$

Therefore, increasing the pump width w_0 means that the parametric fluorescence will

be emitted at larger angles. This has two consequences which can be exploited in actual devices. First, if the angle is sufficiently large the parametric emission can be eliminated using angular filtering. Second, an increase of the noncollinear angle causes a shift of the phase-matching wavelength. If the angle is sufficiently large, the spectral range of parametric emission can be shifted outside of the amplification bandwidth, where it can be eliminated using spectral filtering.

Let us summarize the design procedure for cases where the input power is insufficient to dominate the parametric emission (i.e. when the criterion given in Eq. (11.21) is not satisfied). The first step is to choose the minimum tolerable wavelength shift, $\Delta\lambda_s$, of the parametric fluorescence. Typically, $\Delta\lambda_s$ would be large enough to shift the parametric fluorescence outside the useful wavelength range of the amplifier, and would therefore be at least as large as the amplification bandwidth. This choice determines the minimum noncollinear angle required:

$$\theta_{min} = \sqrt{\frac{2c\,(1/v_s - 1/v_i)}{n_s}\Delta\lambda_s}\ . \tag{11.25}$$

Conversely, one can choose the angle of parametric emission, θ_{min}, large enough so that it falls outside the divergence angle of the signal beam (i.e. $\theta_{min} > \lambda_s/\pi w_{0s}$, where λ_s is the signal wavelength and w_{0s} is the signal spot size). In this case, filtering could be carried out entirely in the angular domain without the need for any spectral filtering.

Once θ_{min} is determined, we choose the width of the pump beam large enough so that noncollinear modes with angles smaller than θ_{min} are suppressed by the chirp of the grating. This is realized when $1/\sqrt{\lambda} < 1/\sqrt{\lambda^*}$, i.e. when the normalized gain parameter falls outside of the range of existence of noncollinear growing modes. The pump width ensuring this condition is

$$w_0 > \frac{\sqrt{r\lambda^*}\theta_{min}}{\gamma_0}, \tag{11.26}$$

where $1/\lambda^*$ is the lower limit of the range of existence of noncolliear modes.

By means of illustration, let us consider a chirped QPM grating made of periodically-poled lithium niobate, designed to provide an amplification bandwidth of 100 nm around 1550 nm, similar to the experiment reported in chapters 5 and 9. The chirp rate required is $\kappa' = 1.5 \times 10^5$ m^{-2}. Let us suppose a power gain of 40 dB, corresponding to a Rosenbluth gain parameter $\lambda_R = 1.46$. The coupling coefficient required is $\gamma_0 = 474$ m^{-1}. According to Fig. 8.27, when $1/\lambda_R \approx 0.7$, the lower limit of the range of noncollinear modes is $1/\sqrt{\lambda^*} = 0.2$. The angle required to shift the phase-matching wavelength by 100 nm (so that the fluorescence be emitted outside of the 1500 - 1600-nm range) is $\theta = 2.4$ ^{O}. According to Eq. (11.26), the pump half-width corresponding to a maximum growth rate at this angle is $w_0 = 620$ μm. Therefore, using a pump beam half-width greater than 620 μm ensures that the parametric fluorescence will be emitted outside of the useful spectral range of the amplifier. Assuming that the signal beam has the same width (620 μm), its divergence is around 0.05^{O}, much smaller than the angle of emission of the parametric fluorescence (2.4^{O}). In this example, using angular filtering would lead to a less stringent criterion for the pump beam width. In general, whether angular or spectral filtering allows for the smallest spot size depends on which one leads to the largest angle of parametric emission.

The method described here consists in eliminating the parametric fluorescence at the output of the amplifier. It does not address the problem of pump depletion, which can affect the performance of the OPA if the gain of the noncollinear gain-guided modes is sufficiently large.

11.4 Negative Chirp Rate

Our numerical and theoretical investigations showed that amplification beyond the phase-matched region can occur when the chirp rate is negative. When this happens, the waves that are generated at the phase-matched point can grow until they reach the end of the grating; their growth length is potentially as large as $L - z_{pm}(\lambda_s)$, where $z_{pm}(\lambda_s)$ is the phase-matched point given by Eq. (11.10). This explains why the gain of negatively chirped gratings varies strongly across the spectrum, as shown in Figs. 5.7 and 9.8, since shifting the phase-matched point changes the gain length.

According to the numerical investigations (chapter 8), there is a certain distance, the threshold length, required before the noncollinear modes dominate. We found that the threshold length is given by

$$L_{th} = \frac{k_1 w_0^2}{4\lambda_R^2} \tag{11.27}$$

with $\lambda_R = \gamma_0^2/\kappa'$. This condition is valid at degeneracy, but nevertheless provides a guideline for non-degenerate wavelengths.

The growth of noncollinear modes can be suppressed using a sufficiently wide pump beam so that the threshold length is larger than the crystal length. This is accomplished when

$$w_0 > 4\lambda_R \sqrt{\frac{L}{k_1}}. \tag{11.28}$$

In terms of the diffraction length, $L_{diff} = \frac{1}{2}k_1 w_0^2$, the condition for suppression of noncollinear growing modes is

$$L_{diff} > 2\lambda_R^2 L. \tag{11.29}$$

Let us consider the design example given above: a PPLN chirped QPM OPA providing a 100-nm bandwidth around 1550 nm. A gain of 40 dB requires $\lambda_R = 1.46$. For a 5-cm-long grating, the pump half-width ensuring suppression of noncollinear growing modes is $w_0 = 445$ μm.

11.5 Summary of Design Procedures

With the results of this chapter, we see that it is possible to suppress transverse effects using a sufficiently wide pump beam. The typical beam diameters required exceed the aperture of the samples we had available at the time these experiments were carried out, but are within the range that can be supported in commercially available periodically poled crystals.

Experimental tests of these assumptions, such as measurements of amplification spectra using wider and wider pump beam diameters (while keeping the peak intensity constant) would be valuable to test the design criteria developed here.

Chapter 12

Conclusion

Chirped quasi-phase-matching (QPM) gratings provide a way of engineering the gain spectrum of optical parametric amplifiers (OPAs). In the case of a linear chirp, the gain is essentially flat over the entire spectrum. The bandwidth can be made as large as desired by adjusting the chirp rate or the grating length. The amplification is given by the Rosenbluth gain formula. According to this result, the logarithmic gain is proportional to the intensity of the pump beam and inversely proportional to the chirp rate. There is a trade-off between gain and bandwidth: increasing the chirp rate increases the bandwidth but reduces the gain, and vice-versa.

The gain and phase spectrum of chirped QPM gratings are affected by a significant amount of ripple. This ripple is due to the abrupt turn-on and turn-off of the interaction at the edges of the grating. It can be reduced by tapering the gain at the edges of the grating.

By using non-uniform chirp rates, it is possible to obtain more general gain spectra. Engineering of the gain profile is possible because the gain at a given wavelength is related to the local chirp rate at the phase-matched point.

Chirped QPM gratings also provide a way to introduce additional dispersion at the idler wavelength. While the group delay of the signal wave remains essentially unaffected by the amplification process, that of the idler is related to the location of the phase-matching point, which is itself a function of the input frequency. The fact that the dispersion of the idler wave can be controlled by the QPM grating profile

was used in a tandem-grating design to obtain at the same time a constant gain and constant group delay across the spectrum of the amplifier.

The basic properties of chirped-QPM OPAs discussed above (gain, bandwidth, group delay) were obtained in the frequency domain. In this work we also solved the space-time problem to calculate the shape of the amplified pulses. We obtained an integral representation for the Green's functions of the signal and idler waves, and examined their asymptotic behavior in various regimes. Then we used these Green's functions to obtain the actual shape of amplified pulses. We considered two regimes, long and short pulses, depending on the duration of the input pulse relative to the accumulated delay between the waves. Long pulses are amplified without distortion. However, in the short-pulse regime, the amplified waves contain precursors and trailing pulses. These distortions are manifestations of the ripple affecting the gain and phase spectrum and can be reduced by apodization techniques.

The fact that chirped QPM gratings provide flat gain over a broad bandwidth, as well as the basic scalings predicted by the theory, were confirmed experimentally in the case of positive chirp rate. However the experiment revealed two unexpected phenomena. First, the parametric fluorescence was much more intense than expected. Second, negatively-chirped QPM gratings behaved drastically differently, offering a large gain variation across the spectrum. These measurements revealed the existence of high-gain processes unaccounted for by the simple 1-D model.

We believe that the large parametric fluorescence is due to noncollinear gain-guided modes. The existence of these modes is critically depends on the pump beam being laterally localized. Analogous modes in plasmas have been studied in the literature in the case of uniform phase-matching media. In this work, we demonstrated analytically and experimentally that noncollinear gain-guided modes can also exist in non-uniform phase-matching media.

The unexpected behavior of negatively-chirped QPM gratings is due to the cancellation of phase due to nonuniformity where the effects of diffraction and decreasing phase accumulation due to negative chirp are neutralized. Another way of looking at this is that because of diffraction, noncollinear phase-matching is possible when the chirp rate is negative. As a result, amplification is possible over the entire length

after the perfect phase-matching point and the gain is strongly dependent on the input wavelength.

As far as broadband OPAs are concerned, those two unexpected processes can be hindrances. If the input signal level is sufficiently high, the parametric fluorescence caused by noncollinear gain-guided modes may be ignorable. If this is not the case, the paramatric fluorescence can be controlled by making the pump beam wide enough. This will shift the fluorescence emission outside the range of wavelengths or angles where the amplification of the signal occurs, thus making it easy to separate or filter. The amplification due to the balance between diffraction and decreasing phase accumulation when the chirp rate is negative can also be controlled by using a sufficiently wide pump beam.

Future work might consist in finding uses for the noncollinear gain-guided modes. Possible applications include broadband noncollinear OPAs and broadband sources of parametric fluorescent light.

Another promising area is the space-time analog of the noncollinear gain-guided modes. Instead of a laterally-localized pump beam, we can imagine a temporally-localized short pump pulse. If the signal and idler group velocities are in opposite directions relative to the pump, then temporally growing modes should exist in spite of the phase mismatch introduced by the chirped QPM grating. Synchronously-pumped optical parametric oscillators using uniform QPM gratings have been demonstrated [76]; it would be interesting to see whether the wide amplification bandwidth offered by chirped QPM gratings could be exploited in this context.

Bibliography

[1] S. Backus, C. G. D. III, M. M. Murnane, and H. C. Kapteyn, "High power ultrafast lasers," Rev. Sci. Instrum. **69**, 1207 (1998).

[2] I. C. G. Durfee, S. Backus, M. M. Murnane, and H. C. Kapteyn, "Design and implementation of a TW-class high-average power laser system," IEEE J. Sel. Top. Quantum Electron. **4**, 395 (1988).

[3] P. Maine, D. Strickland, P. Bado, M. Pessot, and G. Mourou, "Generation of ultrahigh peak power pulses by chirped pulse amplification'," IEEE J. Quantum Electron. **24**, 398 (1988).

[4] W. Joosen, P. Agostini, G. Petite, J. P. Chambaret, and A. Antonetti, "Broadband femtosecond infrared parametric amplification in β-BaB_2O_4," Opt. Lett. **17**, 133 (1992).

[5] G. M. Gale, M. Cavallari, T. J. Driscoll, and F. Hache, "Sub-20-fs tunable pulses in the visible from an 82-MHz optical parametric oscillator," Opt. Lett. **20**, 1562 (1995).

[6] G. M. Gale, F. Hache, and M. Cavallari, "Broad-bandwidth parametric amplification in the visible: femtosecond experiments and simulations," IEEE Journal of Selected Topics in Quantum Electronics **4**(2), 224–229 (1998).

[7] A. Dubietis, G. Jonusauskas, and A. Piskarskas, "Powerful femtosecond pulse generation by chirped and stretched pulse parametric amplification in BBO crystal," Optics Comm. **88**, 437 (1992).

[8] I. Jovanovic, C. Ebbers, and C. P. J. Barty, "Hybrid chirped-pulse amplification," Optics Letters **27**(18), 1622–1624 (2002).

[9] I. Jovanovic, B. J. Comaskey, C. A. Ebbers, R. A. Bonner, D. M. Pennington, and E. C. Morse, "Optical Parametric chirped-pulse amplifier as an alternative to Ti:sapphire regenerative amplifiers," Applied Optics **41**(15), 2923–2929 (2002).

[10] I. Jovanovic, C. G. Brown, C. A. Ebbers, C. P. J. Barty, N. Forget, and C. L. Blanc, "Generation of high-contrast millijoule pulses by optical parametric chirped-pulse amplification in periodically poled $KTiOPO_4$," Opt. Lett. **30**, 1036 (2005).

[11] A. Shirakawa and T. Kobayashi, "Noncollinearly phase-matched femtosecond optical parametric amplification with a 2000 cm^{-1} bandwidth," Appl. Phys. Lett. **72**, 147 (1998).

[12] A. Shirakawa, I. Sakane, M. Takasaka, and T. Kobayashi, "Sub-5-fs visible pulse generation by pulse-front-matched noncollinear optical parametric amplification," Applied Physics Letters **74**(16), 2268–2270 (1999).

[13] T. Kobayashi and A. Baltuska, "Sub-5-fs pulse generation from a noncollinear optical parametric amplifier," Meas. Sci. Technol. **13**, 1671 (2002).

[14] M. M. Fejer, G. A. Magel, D. H. Jundt, and R. L. Byer, "Quasi-phase-matched second harmonic generation: tuning and tolerances," IEEE J. Quantum Electron. **28**, 2631 (1992).

[15] A. Galvanauskas, M. A. Arbore, M. M. Fejer, M. E. Fermann, and D. Harter, "Fiber-laser-based femtosecond parametric generator in bulk periodically poled lithium niobate," Optics Letters (1997).

[16] A. Galvanauskas, A. Hariharan, D. Harter, M. A. Arbore, and M. M. Fejer, "High-energy femtosecond pulse amplification in a quasi-phase-matched parametric amplifier," Opt. Lett. **23**, 210 (1998).

[17] A. Galvanauskas, D. Harter, M. A. Arbore, M. H. Chou, and M. M. Fejer, "Chirped-pulse-amplification circuits for fiber amplifiers, based on chirped-period quasi-phase-matching gratings," Optics Letters **23**(21), 1695–1697 (1998).

[18] T. Suhara and H. Nishihara, "Theoretical analysis of waveguide second-harmonic generation phase matched with uniform and chirped gratings," IEEE J. Quantum Electron **26**, 1265 (1990).

[19] M. A. Arbore, A. Galvanauskas, D. Harter, M. H. Chou, and M. M. Fejer, "Engineerable compression of ultrashort pulses by use of second-harmonic generation in chirped-period-poled lithium niobate," Optics Letters **22**(17), 1341–1343 (1997).

[20] M. A. Arbore, O. Marco, and M. M. Fejer, "Pulse compression during second-harmonic generation in aperiodic quasi-phase-matching gratings," Opt. Lett. **22**, 865 (1997).

[21] G. Imeshev, A. Galvanauskas, D. Harter, M. A. Arbore, M. Proctor, and M. M. Fejer, "Engineerable femtosecond pulse shaping by second-harmonic generation with Fourier synthetic quasi-phase-matching gratings," Opt. Lett. **23**, 864 (1998).

[22] G. Imeshev, M. A. Arbore, M. M. Fejer, A. Galvanauskas, M. Fermann, and D. Harter, "Ultrashort-pulse second-harmonic generation with longitudinally nonuniform quasi-phase-matching gratings: pulse compression and shaping," J. Opt. Soc. Am. B **17**, 304 (2000).

[23] G. Imeshev, M. M. Fejer, A. Galvanauskas, and D. Harter, "Pulse shaping by difference-frequency mixing with quasi-phase-matching gratings," J. Opt. Soc. Am. B **18**, 534 (2001).

[24] K. L. Baker, "Single-pass gain in a chirped quasi-phase-matched optical parametric oscillator," Appl. Phys. Lett. **82**, 3841 (2003).

[25] T. Beddard, M. Ebrahimzadeh, T. D. Reid, and W. Sibbett, "Five-optical-cycle pulse generation in the mid infrared from an optical parametric oscillator based on aperiodically poled lithium niobate," Opt. Lett. **25**, 1052 (2000).

[26] M. Charbonneau-Lefort, M. M. Fejer, and B. Afeyan, "Tandem chirped quasi-phase-matching grating optical parametric amplifier design for simultaneous group delay and gain control," Opt. Lett. **30**, 634 (2005).

[27] R. L. Byer, *Nonlinear Optics* (P. G. Harper and B. S. Wherrett eds, Academic Press, 1977).

[28] Y. R. Shen, *The Principles of Nonlinear Optics* (John Wiley and Sons, 1984).

[29] J. Heading, *An introduction to phase-integral methods* (Wiley, 1962).

[30] M. V. Berry and K. E. Mount, "Semiclassical approximations in wave mechanics," Rep. Prog. Phys. **35**, 315 (1972).

[31] K. G. Budden, *The Propagation of Radio Waves* (Cambridge University Press, 1988).

[32] M. N. Rosenbluth, "Parametric instabilities in inhomogeneous media," Phys. Rev. Lett. **29**, 565 (1972).

[33] J. Huang, X. P. Xie, C. Langrock, R. V. Roussev, D. S. Hum, and M. M. Fejer, "Amplitude modulation and apodization of quasi-phase-matched interactions," Opt. Lett. **31**, 604 (2006).

[34] C. M. Bender and S. A. Orszag, *Advanced Mathematical Methods for Scientists and Engineers* (Springer-Verlag New York Inc., 1999).

[35] R. B. White, *Asymptotic Analysis of Differential Equations* (Imperial College Press, 2005).

[36] L. D. Landau, Phys. Z. Sowjet **2**, 46 (1932).

[37] C. Zener, "Non-adiabatic crossing of energy levels," Proc. Roy. Soc. London A **37**, 696 (1932).

[38] E. C. G. Stueckelberg, Helv. Phys. Acta **5**, 369 (1932).

[39] F. W. Chambers, Ph.D. thesis, Massachusetts Institute of Technology (1975).

[40] M. N. Rosenbluth, R. B. White, and C. S. Liu, "Temporal evolution of a three-wave parametric instability," Phys. Rev. Lett. **31**, 1190 (1973).

[41] R. W. Short and A. Simon, "Theory of three-wave parametric instabilities in inhomogeneous plasmas revisited," Phys. Plasmas **11**, 5335 (2004).

[42] B. Afeyan and M. M. Fejer, "Short Pulse Optical Parametric Processes with Group velocity Mismatch and Quasi-Phase Matching," in *Proceedings of NLO* (2002).

[43] D. L. Bobroff and H. A. Haus, "Impulse Response of Active Coupled Wave Systems," J. Appl. Phys. **38**, 390 (1967).

[44] R. L. Byer and S. E. Harris, "Power and Bandwidth of Spontaneous Parametric Emission," Phys. Rev. **168**, 1064 (1968).

[45] J. A. Armstrong, S. S. Jha, and N. S. Shiren, "Some effects of group-velocity dispersion on parametric interactions," IEEE J. Quantum Electron. **6**, 123 (1970).

[46] E. M. Lifshitz and L. P. Pitaevskii, *Physical Kinetics* (Butterworth-Heinemann Ltd., 1981).

[47] A. Bers, *Basic Plasma Physics I* (A. A. Galeev and R. N. Sudan eds, North-Holland Publishing Company, 1983).

[48] M. Abramovitz and I. A. Stegun, *Handbook of Mathematical Functions* (Dover Publications Inc., 1970).

[49] G. Picard and T. W. Johnston, "Absolute Parametric Instabilities in Inhomogeneous Plasmas," Phys. Rev. Lett. **51**, 574 (1983).

[50] E. A. Williams, J. R. Albritton, and M. N. Rosenbluth, "Effect of Spatial Turbulence on Parametric Instabilities," Phys. Fluids **22**, 139 (1979).

[51] F. W. Chambers and A. Bers, "Parametric interactions in an inhomogeneous medium of finite extent with abrupt boundaries," Phys. Fluids **20**, 466 (1977).

[52] Y. Furukawa, K. Kitamura, S. Takekawa, A. Miyamoto, M. Terao, and N. Suda, "Protorefraction in $LiNbO_3$ as a function of [Li]/[Nb] and MgO concentrations," Appl. Phys. Lett. **77**, 2494 (2000).

[53] Y. Furukawa, K. Kitamura, A. Alexandrovski, R. K. Route, M. M. Fejer, and G. Foulon, "Green-induced infrared absorption in MgO doped $LiNbO_3$," Appl. Phys. Lett. **78**, 1970 (2001).

[54] D. H. Jundt, "Temperature-dependent Sellmeier equation for the index of refraction, n_e, in congruent lithium niobate," Optics Letters **22**, 1553 (1997).

[55] G. D. Miller, "Periodically poled lithium niobate: modeling, fabrication, and nonlinear-optical performance," Ph.D. thesis, Stanford University (1998).

[56] G. D. Miller, R. G. Batchko, W. M. Tulloch, D. R. Weise, M. M. Fejer, and R. L. Byer, "42%-efficient single-pass cw second-harmonic generation in periodically poled lithium niobate," Opt. Lett. **22**, 1834 (1997).

[57] V. Shur, E. Rumyantsev, R. Batchko, G. D. Miller, M. M. Fejer, and R. L. Byer, "Physical basis of the domain engineering in the bulk ferroelectrics," Ferroelectrics **221**, 157 (1999).

[58] V. Y. Shur, E. L. Rumyantsev, R. G. Batchko, G. D. Miller, M. M. Fejer, and R. L. Byer, "Domain kinetics in the formation of a periodic domain structure in lithium niobate," Phys. solid state **41**, 1681 (1999).

[59] V. Y. Shur, E. L. Rumyantsev, E. V. Nikolaeva, E. I. Shishkin, R. G. Batchko, G. D. Miller, M. M. Fejer, and R. L. Byer, "Regular Ferroelectric Domain Array in Lithium Niobate Crystals for Nonlinear Optics Applications," Ferroelectrics **236**, 129 (2001).

[60] V. Y. Shur, E. L. Rumyantsev, E. V. Nikolaeva, E. I. Shishkin, R. G. Batchko, M. M. Fejer, and R. L. Byer, "Recent Achievements in Domain Engineering in Lithium Niobate and Lithium Tantalate," Ferroelectrics **257**, 191 (2001).

[61] W. H. Louisell, A. Yariv, and A. E. Siegman, "Quantum Fluctuations and Noise in Parametric Processes. I." Phys. Rev. **124**, 1646 (1961).

[62] J. A. Armstrong, N. Bloembergen, J. Ducuing, and P. S. Pershan, "Interactions between Light Waves in a Nonlinear Dielectric," Phys. Rev. **127**, 1918 (1962).

[63] S. E. Harris, M. K. Oshman, and R. L. Byer, "Observation of tunable optical parametric fluorescence," Phys. Rev. Lett. **18**, 732 (1967).

[64] D. A. Kleinman, "Theory of Optical Parametric Noise," Phys. Rev. **174**, 1027 (1968).

[65] A. M. Schober, "Parametric Interactions of Short Optical Pulses in Quasi-Phase-Matched Nonlinear Devices," Ph.D. thesis, Stanford University (2005).

[66] *COMSOL - Multiphysics Modeling*. URL `http://www.comsol.com/`.

[67] M. M. Sushchik and G. I. Freidman, "The effect of nonuniformity of the amplitude and phase distribution of the pumping radiation on the spatial locking of parametrically amplified waves," Radiofizika **13**, 1354 (1970).

[68] S. E. Harris, "Proposed backward wave oscillator in the infrared," Appl. Phys. Lett. **9**, 114 (1966).

[69] G. P. Agrawal, *Nonlinear Fiber Optics* (Academic Press, 1995).

[70] M. M. Sushchik, V. M. Fortus, and G. I. Freidman, "Trapping of parametrically coupled waves by pulses and beams of pump radiation," Radiofizika **12**, 235 (1969).

[71] M. M. Sushchik, V. M. Fortus, and G. I. Freidman, "Excitation of parametrically amplified waves during spatial capture by pumping-radiation wave packets," Radiofizika **13**, 192 (1970).

[72] L. D. Landau and E. M. Lifshitz, *Quantum Mechanics* (Butterworth-Heinemann Ltd., 1977).

[73] D. Pesme, G. Laval, and R. Pellat, "Parametric Instabilities in Bounded Plasmas," Phys. Rev. Lett. **31**, 203 (1973).

[74] D. F. DuBois, D. W. Forslund, and E. A. Williams, "Parametric Instabilities in Finite Inhomogeneous Media," Phys. Rev. Lett. **33**, 1013 (1974).

[75] B. B. Afeyan and E. A. Williams, "Stimulated Raman sidescattering with the effects of oblique incidence," Phys. Fluids **28**, 3397 (1985).

[76] S. Lecomte, R. Paschotta, M. Golling, D. Ebling, and U. Keller, "Synchronously pumped optical parametric oscillators in the 1.5-μm spectral region with a repetition rate of 10 GHz," J. Opt. Soc. Am. B **21**, 844 (2004).